NANYANG TECHNOLOGICAL UNIVERSITY

# Surface Modification and Corrosion Properties of Mg Based Alloys for Bio-implant Application

**Sara Kaabi Falahieh Asl**

**School of Mechanical and Aerospace Engineering**

**A thesis submitted to Nanyang Technological University in partial fulfillment of the requirements for the degree of Doctor of Philosophy**

**2016**

# Abstract

The use of implants for bone repair has a considerable and successful history. Traditionally, metallic implants have been used in such a way that the implant would be surgically removed after sufficient bone healing has been achieved. During the last decade, interest in biodegradable magnesium (Mg) implants has increased dramatically. The use of Mg is based on the fact that Mg is one of the essential elements for human metabolism, and the density and elastic modulus of Mg are close to the human bone, thus, avoiding stress shielding effect. However, Mg alloys corrodes too rapidly, resulting in hydrogen evolution and consequently, local alkalization close to the surgery region as well as premature degradation in the implant's mechanical integrity before bone healing occurred. All these factors impede the practical applications of Mg implants.

In this study, a hydrothermal coating process was used to provide, uniform and biodegradable inorganic calcium-phosphate (Ca-P) and calcium-phosphate/polymer (Ca-P/Polymer) composite coatings on AZ31 magnesium substrate that slow the corrosion of Mg and to meet different requirements for implant application. In the current study two different types of novel Ca-P/Polymer composites coatings were successfully deposited for the first time on AZ31 magnesium alloy to reduce Ca-P material brittleness by using polyacrylic acid and carboxymethyl cellulose polymers. The results showed, crystal phase and coating's morphology could be successfully controlled by the type and concentration of polymer used which could affect the coating's degradation rate as well. Incorporation of polymer in the Ca-P coatings reduced the coating elastic modulus bringing it close to that of Mg and that of human bone. Apart from mechanical properties, cell proliferation studies indicated that composite coatings induced better cell attachment compared to the purely inorganic Ca-P coating.

Moreover, in order to inhibit bacterial adhesion and prevent implant-associated infection, anti-infective coatings with local drug delivery ability were successfully deposited on AZ31 magnesium substrate.

The corrosion performance of coatings were comprehensively studied with potentiodynamic, electrochemical impedance spectroscopy (EIS) as well as long-term immersion tests. The obtained coating could decrease the corrosion rate of AZ31 substrate by 100-10,000 fold.

A detailed investigation was performed in order to understand the deposition mechanism of coatings on different metallic substrates during hydrothermal process to determine the various steps in the coating formation and growth. It was found that successful coating deposition is strongly dependent on substrate-solution interface and resulted from substrate corrosion in the first step of deposition process.

The obtained coatings could be promising candidates for surface protection of Mg for implant application with the multiple functions of corrosion protection and cell attachment/cell growth promotion.

# Acknowledgments

I would like to express my deepest gratitude to my supervisors, Prof. Tan Ming Jen and Dr. Nemeth Sandor for their encouragement, supervision and patient guidance to my PhD project. I would also like to thank Prof. Aldo R. Boccaccini from Friedrich-Alexander-Universität Erlangen-Nürnberg for all his guidance during my attachment program in Germany.

I would also like to thank Prof. Wolfgang Goldmann from Friedrich-Alexander-Universität Erlangen-Nürnberg and Dr. Saeed Maleksaeedi from SIMTech for their useful suggestions.

I would like to express my sincere thanks to Dr. Chan Wing Yue for his training and professional guidance on cell culture and in vitro tests.

I sincerely thank the technician of Materials Laboratories 1 and 2, Ms. Yong Mei Yoke, Mr. Lew Sui Leung, Mr. Leong Kwok Phui and many other technicians for training and technical assistance during my PhD program.

Finally, I would like to acknowledge Nanyang Technological University, especially School of Mechanical and Aerospace Engineering, Singapore International Graduate Award (SINGA) and Singapore Institute of Manufacturing Technology (SIMTech) for giving me this opportunity to pursue my postgraduate studies.

# Table of Contents

# List of Tables

# List of Figures

# List of Abbreviations

| Abbreviation | Meaning |
|---|---|
| $Ca(NO_3)_2$ | Calcium nitrate |
| $Ca_{2.86}Mg_{0.14}(PO_4)_2$ | Whitlockite |
| $Ca_2P_2O_7$ | Calcium pyrophosphate |
| $Ca_3(PO_4)_2$ | Tricalcium phosphate |
| $CaHPO_4$ | Monetite |
| Ca-P | Calcium-Phosphate |
| Ca-P/Polymer | Calcium-Phosphate/Polymer |
| $C_{dl}$ | Double layer capacitance |
| $C_f$ | Oxide film capacitance |
| COF | Friction coefficients |
| $COO^-$ | Carboxylate |
| $E_{corr}$ | Corrosion potential |
| EDS | Energy-dispersive X-ray spectroscopy |
| EIS | Electrochemical impedance spectroscopy |
| EMEM | Eagle's Minimum Essential Medium |
| $F_f$ | Friction force |
| FTIR | Fourier transform infrared spectroscopy |
| HA | Hydroxyapatite |
| HE160°C-3hr | Ca-P coating deposited at 160°C (deposition time:3 hour) |
| HEPAA | Composite coating with PAA addition |
| HESCMS | Composite coating with SCMS addition |
| $i_{corr}$ | Corrosion current density |

| | |
|---|---|
| ICP | Inductively coupled plasma atomic emission spectrometer |
| L | Inductance |
| MAO | Micro arc oxidation |
| $Mg(OH)_2$ | Magnesium hydroxide |
| $Mg_2SiO_4$ | Forsterite |
| MgO | Magnesium oxide |
| $NH_4H_2PO_4$ | Ammonium dihydrogen phosphate |
| OCP | Open circuit potential |
| PAA | Polyacrylic acid |
| P-B | Pilling-Bedworth |
| PBS | Phosphate buffered saline |
| PCL | Polycaprolactone |
| PEO | Plasma electrolytic anodizing |
| PLA | Polylactic acid |
| PLGA | Poly(lactic-co-glycolic acid) |
| $R_{ct}$ | Charge transfer resistance |
| $R_p$ | Polarization resistance |
| $R_{pns}$ | Newly formed surface polarization resistance |
| SBF | Simulated body fluid |
| SCMS | Sodium carboxymethyl cellulose |
| SEM | Scanning electron microscopy |
| TCH | Tetracycline |
| TGA | Thermo-gravimetric analysis |
| UV-Vis | Ultraviolet–visible spectroscopy |
| XRD | X-ray diffractometer |
| \|Z\| | Absolute impedance value |

# Chapter 1

# Introduction

## 1.1 Background

Currently, there is a huge demand in the hard-tissue replacement implant markets around the world. Current permanent metallic implants are made of commercially pure titanium (Ti) or Ti-6Al-4V alloy, 316L stainless steel (SS), and cobalt-chromium (Co-Cr) alloys, which are widely used for bone fracture fixation. These metallic implants have a serious drawback of stress shielding effect due to the mismatch in mechanical properties between implant materials (Young's modulus 100-200 GPa) and human bone (Young's modulus 10-30 GPa) as reported in Table 1-1. Bone stress shielding is due to a high load being carried by the implant due to its high modulus for a given strain value. Stress shielding effect results in a number of critical clinical issues such as implant loosening, delay in healing process and damaged bone growth. Also, normally metallic implants need to be removed after the bone has healed within the first two years after the first surgery. Therefore, another surgical operation is necessary with all the personal, medical, social, economic consequences and costs. Biodegradable implant can be an ideal solution to overcome these challenges [1-8].

**Table 1-1.Summary of the properties of various implants in comparison to natural bone [9]**

| Properties | Bone | Mg | Ti | Co-Cr | SS | HA |
|---|---|---|---|---|---|---|
| **Density($g/cm^2$)** | 1.8-2.1 | 1.7-2.04 | 4-4.5 | 8.3-9.2 | 7.9-8.1 | 3.1 |
| **Elastic modules (GPa)** | 3-20 | 41-45 | 110-117 | 230 | 189-205 | 73-117 |
| **Compressive yield (MPa)** | 130-180 | 65-100 | 758-1117 | 450-1000 | 170-310 | 600 |
| **Fracture toughness ($MPa.m^{1/2}$)** | 3-6 | 15-40 | 55-115 | NA | 50-200 | 0.7 |

Currently, biodegradable implants are mainly made of polymers, such as poly-L-Lactic acid (PLLA). These polymer based implants usually do not have a satisfactory mechanical strength. Metals are more suitable for load-bearing applications compared

with polymeric materials due to their combination of high mechanical strength and fracture toughness. Mg and its alloys could be an ideal alternative for implant material due to its non-toxic nature. The use of Mg is based on the fact that Mg takes part in many metabolic and biological reactions and shows excellent biocompatibility. Moreover, density and elastic modulus of Mg are close to the human bone, which avoids stress shielding effect. Mg implants can also dissolve in the body, thus eliminating the need for a second surgery for implant removal. However, it was found that Mg alloys corroded too rapidly, resulting in hydrogen evolution and consequently, local alkalization close to the surgery region as well as failure in the implant's mechanical integrity before bone healing occurred; all these factors retard the practical applications of Mg implants [7, 10].

In general, a biodegradable material should have a controllable dissolution rate, and maintain its mechanical integrity before the surgical region recovers or heals. After bone healing, the implant should gradually dissolve, be consumed or be absorbed [10]. Obviously, a suitable corrosion rate becomes critical for biodegradable Mg implant in this scenario. To put Mg to practical use, it is necessary to deal with its shortcomings and improve its performance through alloying or surface modification. Corrosion rate of Mg can be enhanced by adding suitable alloying elements. These elements must be non-toxic and harmless to the human body. Common alloying elements used are zinc (Zn) and calcium (Ca). However, the amount of alloying elements is limited in order to maintain desired mechanical properties and reduce their potential toxicity. In addition, surface modification of Mg could also decrease the corrosion rate. The coating layer can block the access of body fluids to the Mg surface. Consequently, reducing corrosion rate [5, 11-13]. Since the interaction between the cells and tissues with biomaterials at the tissue-implant interface is a surface phenomenon; therefore surface properties of the implant play a major role in determining the biological response to implants and the material response to the physiological conditions, which the current project is aimed to focus on that.

## 1.2 Objectives and Scope

Based on the gaps in the previous studies, the objectives of the current research were defined as:

1- To develop novel hydrothermally deposited biodegradable and biocompatible coatings for Mg alloys to achieve controllable and uniform degradation rate in order to protect Mg substrate until bone healing occurs.

2- To adjust mechanical performance of coatings by incorporating biodegradable and biocompatible organic phases into the coating structure.

3- To develop an anti-infective coating with drug delivery ability in order to inhibit bacterial adhesion and prevent implant associate infection.

4- To understand the deposition mechanism of the coating during hydrothermal deposition process.

To this end the scope of this study includes:

- Development of biodegradable Ca-P coatings by means of hydrothermal process and understanding the effect of deposition temperature and deposition time on coatings properties such as chemical composition, surface morphology, coating's adhesion and thickness.
- Development of composite coatings (Ca-P/Polymer) by hydrothermal method, in order to overcome the Ca-P coating's drawbacks such as brittleness and to adjust the mechanical properties of coating by incorporating polymers into the coating structure.
- Study the effect of polymer addition on crack formation tendency, hardness and Young's modulus by using nano-indentation and scratch tests.

- Study the corrosion properties of the inorganic and composite coatings using different electrochemical techniques like potentiodynamic and electrochemical impedance spectroscopy tests.
- Study the biodegradation behavior of coatings by performing an immersion test in simulated body fluid solution.
- Study the effect of polymer addition on the biodegradation rate of the composite coatings.
- Study the deposition mechanism of coatings on different metallic substrates using different techniques such as Raman spectroscopy, Fourier transform infrared spectroscopy, X-ray Diffraction, field emission scanning electron microscopy and energy dispersive spectroscopy to determine the various steps in the coating formation and growth.
- Investigation of the coating's biocompatibility by conducting direct and in direct in vitro tests in the present of MG63 cell line.
- Study the drug release profile and anti-bacterial activity of coatings using Ultraviolet–visible spectroscopy and agar disk diffusion test.

## 1.3 Organization of the Thesis

The organization of the rest of this thesis is as follows:

Chapter 2 is focusing on literatures and reviewing previous research in the field of biodegradable Mg implants.

Chapter 3 is focusing on materials and experimental details and describing different techniques which were used during this project for characterization of deposited coatings.

Chapter 4 is focusing on deposition of inorganic Ca-P and novel Ca-P/Polymer composite coatings and analyzing the coatings in detail by using different techniques.

Chapter 5 is focusing on the deposition mechanism of inorganic and composite coatings and comparing the deposition process during hydrothermal process for different metallic substrates.

Chapter 6 provides comprehensive results for evaluating corrosion and mechanical performance of inorganic and composite coatings.

Chapter 7 describes the in vitro performance and cytotoxicity of coatings. The second section of this chapter is focusing on deposition of anti-infective coatings with drug delivery ability.

Chapter 8 summarized the obtained results of the current project and provides some recommendations for future works.

# Chapter 2

# Literature Review

## 2.1 Introduction

The use of implants for bone repair has a considerable and generally successful history. Currently used metallic implants are usually made of Ti or Ti-6Al-4V alloy, 316L stainless steel and Co-Cr alloys. These metallic implants have the serious drawback of stress shielding effect due to the mismatch in mechanical properties between implant materials (Young's modulus 100–200 GPa) and human bone (Young's modulus 10–30 GPa) [5, 14]. This phenomenon causes stress concentration at bone-implant interfaces. Bone as a living tissue, is constantly remodeling and adapting to the stress imposed upon it. This process of remodeling can lead to the phenomena of stress shielding when an implant is present. If the implant carries a large fraction of the applied load as compared to the bone beneath, the bone experiences a reduced load, which results in reduced bone density. In the case of conventional implant materials, each metal alloy used has a significantly higher modulus of elasticity, which in turn leads to the implant carrying a greater portion of the load and runs the risk of causing stress shielding of the bone as shown in Fig.2-1 [8, 15]. Stress shielding can cause critical clinical issues such as implant loosening, delay in healing process and consequently, damaged bone growth, as well as skeleton thickening, and chronic inflammation. Eventually, the implant will fail to satisfy the requirement of load-bearing fixation. In addition, the release of toxic ions by corrosion or mechanical wear from these metallic implants can cause further harm, inflammation and less bone formation [16-18]. Also, after bone healing, second surgery may be required for the implant removal.

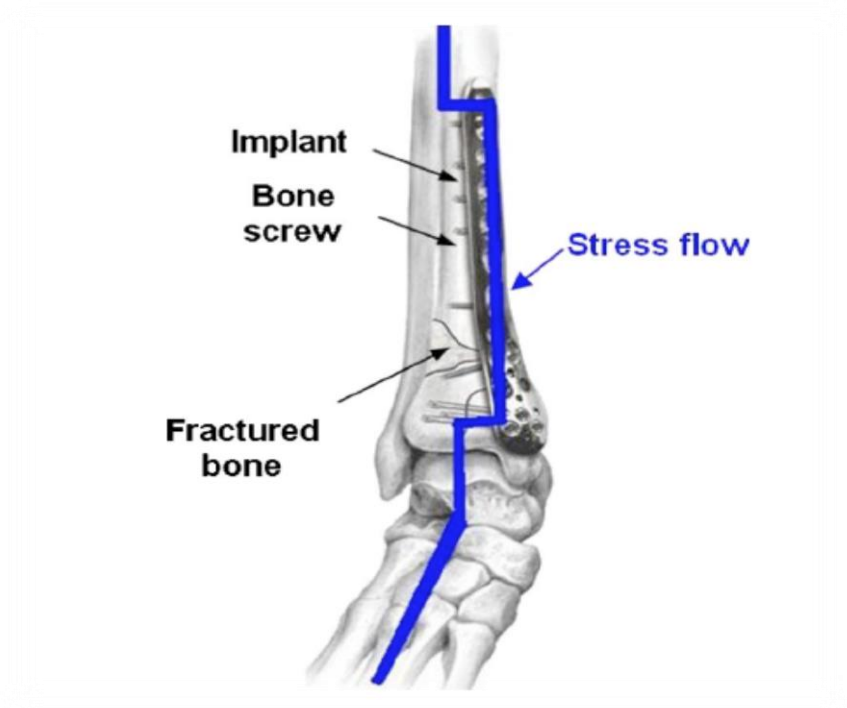


**Figure 2-1. Stress shielding effect on fixing fractures [8]**

However, more recently the use of biodegradable implant materials including biodegradable metals, have become a key research area striving to combine improved mechanical properties and biocompatibility [5, 14].

During the last decade, interest in biodegradable Mg implants has increased dramatically since Mg is an essential element for human metabolism, and the density and elastic modulus of Mg alloys (density: 1.7-2.04 g/cm$^3$, Young's modulus: 41-45 GPa) are close to that of human bone (density: 1.8-2.1 g/cm$^3$, Young's modulus: 10-30 GPa), thus avoiding stress shielding effect [1, 5, 14]. However, Mg alloys suffer from high corrosion rate, resulting in hydrogen evolution and consequently, local alkalization close to the surgery region as well as premature degradation in the implant's mechanical integrity before bone healing can occur. The degradation rate of Mg and its alloys in the initial stages of implantation would play a significant role in the newly formed tissue response. If the early degradation rate of Mg-based implants

is too rapid, pre-implantation and osteolysis reaction would take place. Consequently, this would negatively affect the bone tissue regeneration and healing process [11, 19-21]. To put Mg to practical use, it is necessary to improve its corrosion performance through alloying or surface modification. Corrosion resistance of Mg can be enhanced by adding non-toxic alloying elements such as Zn and Ca which also are essential elements in human metabolism. However, the amounts of alloying elements are limited in order to maintain desired mechanical properties and sufficient improvement in corrosion properties as well as to reduce their potential toxicity when present in high concentrations. The alternative is surface modification of Mg that could also decrease the corrosion rate, potentially to a higher extent [22, 23].

## 2.2 Mg and Its Alloys as Biomaterials

The biodegradability of Mg and its alloys and their mechanical properties (which are quite similar to the human bone) is an attractive combination for orthopedic applications. This combination makes Mg a promising candidate for bio-medical application. The use of Mg based implants could avoid or minimize the stress shielding effect. Moreover, using Mg alloys as an implant material remove the necessity for second removal surgeries, thereby, decreasing health risks, costs and scarring.

The use of Mg is based on the fact that Mg takes part in many metabolic reactions and is a constituent of bones and muscles with high daily intake. Normally, the human body requires 300-400 mg/day of Mg [24, 25]. Moreover, Mg ions assist in the growth of new bone and shorten the healing process time. For all above reasons, Mg and its alloys can be used as a scaffold or as a plate and screw for bone fracture fixation. However, an undesirable high degradation rate of Mg and its alloys is a major concern for using it as an implant material and retards its practical application [5, 26, 27]. The high corrosion rate results in the formation of harmful hydrogen gas pocket in the

interface of bone and implant causing failure of the surgery before bone healing, as the gas pocket can cause separation of implant and tissue and may also lead to infection [28]. In addition, due to the high degradation rate of Mg, the implant's mechanical stability fails during the healing process. Therefore, this is important to control the corrosion performance of Mg based implants for two reasons: firstly, the implant material must maintain its mechanical integrity and remain in the body for a specific period for the bone to heal and secondly, the corrosion must be sufficiently slow so as to not affect the healing process [29-33].

## 2.3 Corrosion Mechanisms of Mg and Its Alloys

Mg and its alloys possess a low corrosion resistance in aqueous solutions that limit their engineering applications, and for safe use surface modification might be required. However, this limitation is a significant blessing for biodegradable implant application [4, 34, 35]. Corrosion mechanism of Mg in aqueous solutions takes place according to Eq.2-1 which is the sum of the following reactions (Eqs.2-2~2-4) and leads to evolution of hydrogen gas and formation of magnesium hydroxide ($Mg(OH)_2$) [36].

$$\mathbf{Mg(s) + 2H_2O(aq) \rightarrow Mg(OH)_2(s) + H_2(g)} \quad \textbf{(2-1)}$$

$$\mathbf{Mg(s) \rightarrow Mg^{2+} + 2e^-} \quad \textbf{(2-2)}$$

$$\mathbf{2H_2O + 2e^- \rightarrow H_2 + 2OH^-} \quad \textbf{(2-3)}$$

$$\mathbf{Mg^{2+} + 2OH^- \rightarrow Mg(OH)_2} \quad \textbf{(2-4)}$$

According to Pourbaix diagram in Fig.2-2 Mg dissolves below a pH value of approximately 11.5 while above pH value 11.5 a passive layer of $Mg(OH)_2$ could form which is normally not fully protective [37]. In the human body, blood pH value is around 7.3~7.4; therefore, Mg is actively dissolved [37, 38]. The high reactivity of Mg is due to the fact that the standard electrode potential of Mg (-2.37 V vs. SHE) is very

negative and it is more active than most metals. Thus, in most situations Mg acts as an anode [38].

Due to the strongly negative electrode potential, Mg is highly susceptible to galvanic corrosion. Galvanic corrosion of Mg and its alloys is caused by impurities and secondary phases that act as cathode [10, 36]. Cathodes can be external such as other metals in contact with Mg, or may be internal such as secondary or impurity phases as shown in Fig.2-3. In the case of internal galvanic corrosion, the presences of cathode regions are due to precipitation of continuous secondary phase along the grain boundaries. These continuous cathodes form galvanic cells with the purer Mg domains; consequently, corrosion starts and propagates along the matrix close to the grain boundaries [36].

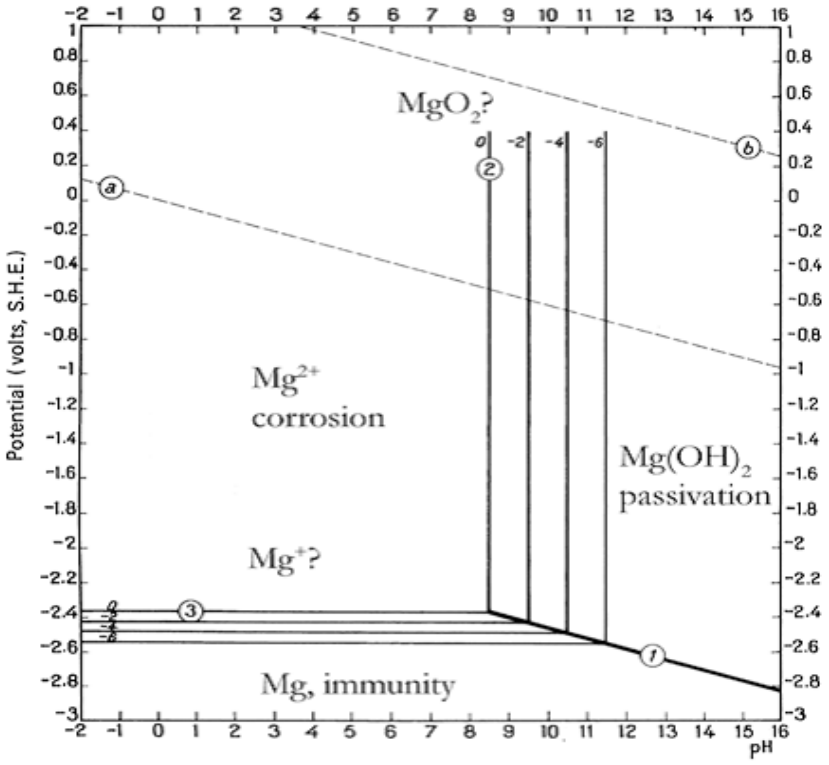


**Figure 2-2. Pourbaix diagram of Mg [37]**

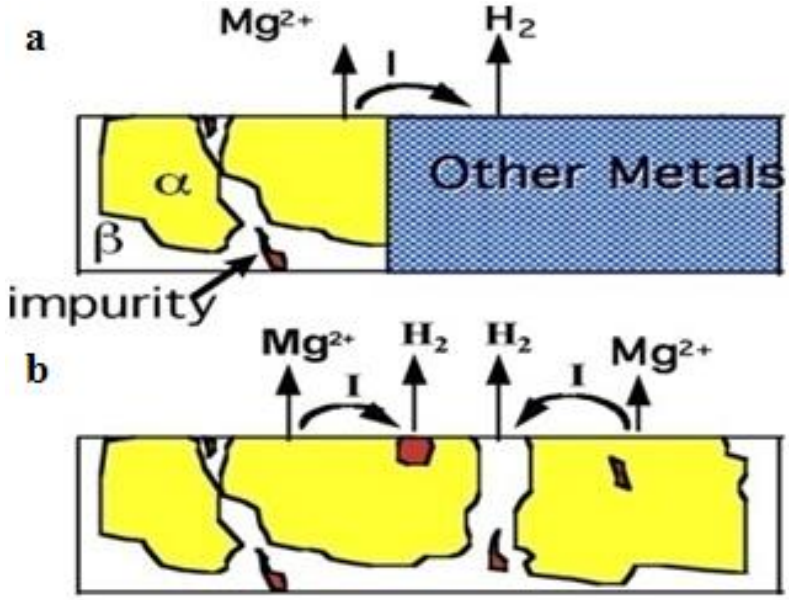


**Figure 2-3. a) Macro-galvanic corrosion and b) Micro-galvanic corrosion [36]**

Apart from galvanic corrosion, localized corrosion is another major corrosion mechanisms of Mg alloys in physiological environment [39].

Localized corrosion is identified by the non-homogeneous corrosion on the surface of the Mg and its severely corroded sites. Furthermore, a metastable and partially protective film, often, naturally forms on the Mg alloys and there is a tendency for selective attacks to happen at these susceptible sites when exposed to the solution [39]. Therefore, continuous localized corrosion at these sites often results in a non-uniformly corroded surface of the Mg alloy [40]. The surface of Mg is normally covered by a partially protective film. Galvanic corrosion can start as general corrosion that may transition to localized corrosion, and, in several cases, it can begin as a local galvanic attack depending on the metallic phase distribution and morphology, solution properties, agitation, temperature, and impurities [41].

However, the localized corrosion for Mg is different from autocatalytic pitting corrosion observed in stainless steels. When localized corrosion starts in Mg, irregular

pits tend to form that spread laterally and cover the whole surface without a tendency towards deep pitting.

Moreover, unlike stainless steel, the localized corrosion in Mg has an inherent tendency to be self limiting due to pH change. However, the intense localized corrosion would be expected to have produced high local pH values and high local concentrations of $Mg^{2+}$ so that it would be expected that most of the surface would indeed be covered by a film of corrosion products [42].

## 2.4 Mg Alloys for Bone Fixation

The most frequent types of fracture in the skeleton can be classified into four groups: fracture in neck, back and spine, head, and the extremities. In the fractured bone, the fragment loses its alignment in the form of displacement. In this case, implants can be used to hold a fracture reduction [43]. Different types of implants such as plates, screws and nails are used for the bone fracture fixation. These implants must only remain in the body until bone healing is completed and therefore, have a temporary function. The temporary implant must provide a good mechanical stability until the bone is healed and then gradually dissolve afterwards [9, 14, 30, 44]. Biodegradable implants have the advantage that a second surgery for removal of the implant is not necessary, saving cost to the health system and being beneficial for the patient. In addition, degradable implants are also applicable in pediatrics cases, where the body is still in a growth process, and permanent implants would have to be changed to match the growth. Moreover, the healing and remodeling process of the injured tissue is stimulated by degradable implants due to a gradual load transfer from the implant to the tissue, as depicted in Fig.2-4. After an injury, the fractured bone needs support from the implant for healing. With time the implant degrades; its strength diminishes and hence, the load is gradually transferred to the bone until the tissue has healed and reached its full strength while the implant has dissolved. The optimal degradation

performance of a biodegradable orthopedic implant is initially slow to provide mechanical integrity and increases with time once the injured tissue has healed sufficiently [10, 26, 30, 32, 45]. Mg alloys as potential biodegradable materials providing both biocompatibility and suitable mechanical properties can be used for this purpose [5].

To evaluate the in vivo degradation of Mg, Li et al. [45] used Mg-Ca alloy, and Ti pins for bone fixation of rabbit femoral, and they found that the Mg-Ca alloy did not induce any toxicity in the cells. After 3 months of implantation, the Mg-Ca alloy was completely absorbed in the body while the new bone was formed around the alloy. However, they did not find any new bone formation around the Ti pin during the experimental period.

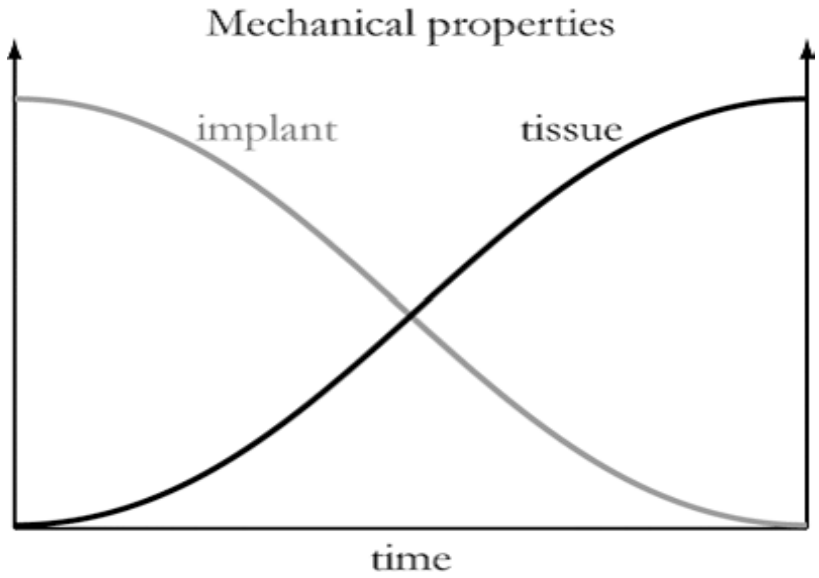


**Figure 2-4. Schematic diagram of the ideal change in strength over time of an implant and healing bone tissue [46]**

Likewise, Thomann et al. [47] compared the degradation of LAE442 magnesium alloy and Mg-0.8 wt.% Ca in the rabbit model for 12 months implantation. Based on their

result, Mg-0.8 wt.% Ca showed osteogenic effect, and the bone-implant contact was much stronger than for the LAE442 (89.6% Mg, 4.0% Li, 3.9% Al, 2.2% Se, 0.2% Mn) magnesium alloy. However, the Mg-0.8 wt.% Ca alloy showed higher degradation rate in comparison with LAE442 alloy [47, 48]. Another report found the byproduct of implant degradation for Mg-0.8 wt.% Ca is benign since Mg and Ca are natural components of the organism. On the other hand, the corrosion product of LAE442 alloy that consist of rare earth elements was hard to resorb by the body [48].

## 2.5 Improving the Mechanical and Corrosion Properties of Mg with Alloying

Pure Mg has many shortcomings such as insufficient strength, elongation and heat resistance as well as poor corrosion resistance. Hence, it is necessary to enhance the performance of Mg before using it in practical applications. Adding alloying elements to pure Mg can improve its mechanical properties. In addition, the corrosion resistance of Mg can be changed with alloying as well. From a medical point of view, there are only few suitable alloying elements for making biodegradable Mg alloys such as manganese (Mn), Zn, Ca, strontium (Sr), zirconium (Zr) and yttrium (Y) [7, 49-52]. Generally, these alloying elements affect the mechanical and corrosion properties of Mg alloys. Some of these alloying elements are discussed below in some details.

### 2.5.1 Zinc (Zn)

Zn is an essential trace element for human body and biological functions [53]. Zn contributes to mechanical strength due to the solid solution strengthening mechanism [26, 54]. Zn can improve corrosion resistance and decrease the hydrogen evolution rate as shown in Fig.2-5. Moreover, Zn addition can change the corrosion type from

localized to general form due to the presence of a higher amount of Zn in the corrosion protective layer as compared to Mg [12, 13, 55].

From a mechanical property standpoint, Zn is known to be a good solid solution and precipitation-strengthening agent in Mg alloys. It is one of the most commonly and effectively used alloying elements in Mg. Since Zn has a relatively high solid solubility in Mg at high temperatures, good mechanical properties can be achieved by solid solution strengthening mechanism. The effect of Sr and Zn addition to Mg on its mechanical properties was reported by Brar et al. [26] and according to their findings, an increase in Sr content in the binary alloying system had a minor effect on the strength of the alloys, but the addition of Zn significantly improved the mechanical properties of the alloys. Based on their result Mg-6.0 wt.% Zn-0.5 wt.% Sr alloys showed highest yield strength (YS) and ultimate tensile strength (UTS), due to grain refinement properties of Sr resulting in growth restriction effect, and consequently, improved corrosion resistance by formation of a passive layer on the surface.

In the same way, Zhang Yin et al. [56] reported the effect of Zn addition on Mg-Zn-Mn alloy. Zn element can significantly refine the grain size of Mg alloys, because Zn shows relatively high growth restriction factor (GRF) compared to other elements such as Al, Sr and Y.

The mechanical properties of Mg, especially the yield strength are grain sensitive. Therefore, the tensile and yield strength both increased slightly with an increase in Zn content due to the refinement effect of Zn. However, when the Zn content is increased to 3 wt.%, a serious drop in elongation was found [56].

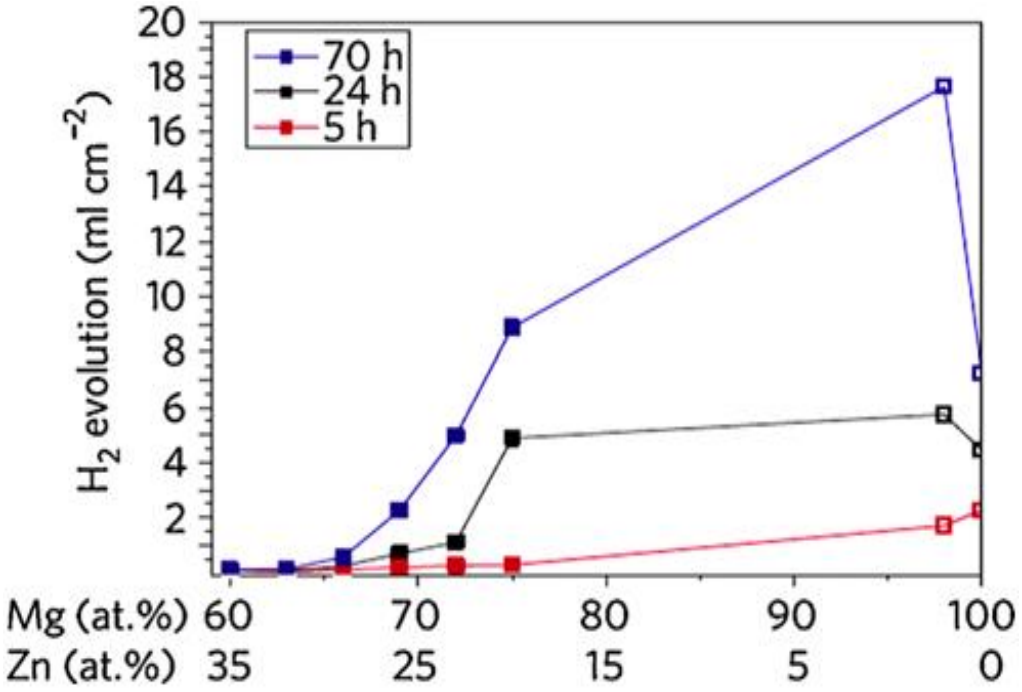


**Figure 2-5. The hydrogen evolution rate in SBF [55]**

### 2.5.2 Calcium (Ca)

Besides Zn, Ca is also a vital nutrient in the human body and very important for bone strength. Ninety-nine percent of Ca is stored in the human bone. Ca contributes to solid solution and precipitation strengthening in Mg alloys. Using Ca with low density (1.55 $g/cm^3$) produces the Mg-Ca systems with the density very close to the bone. Ca can improve both the corrosion and mechanical properties [8, 45].

Due to the above reasons, some researchers worked on Mg-Ca alloys. Among them, Wan et al. [57] reported an improvement in compressive strength and elastic modulus when Ca was incorporated into pure Mg. This phenomenon can be readily interpreted by the amount of precipitates such as $Mg_2Ca$ within the Mg-Ca alloys.

Similarly, Li et al. [45] fabricated different Mg-xCa (x=1-3 wt.%) alloys and they reported the obtained alloys mainly consisted of α-Mg and $Mg_2Ca$ phases while the $Mg_2Ca$ phase precipitated along the grain boundaries. The mechanical properties of

alloys degraded with increasing Ca content. Among the different alloys, the Mg-1wt.% Ca did not show toxicity effect. Based on their results, corrosion and mechanical properties of Mg-Ca alloys could be adjusted by controlling the Ca content and processing treatment.

### 2.5.3 Yttrium (Y)

Some researchers reported that adding Y as an alloying element resulted in a net shift in the corrosion current density ($i_{corr}$) to higher values; due to the formation of $Mg_{24}Y_5$ intermetallic phase that increases with increasing amount of Y (from 2 wt.% to 18 wt.%) added to the pure Mg as shown in Fig.2-6 [36]. Briefly, the effect of adding the different alloying elements on corrosion rate, cathodic and anodic branches shift is presented in Fig.2-7 [20].

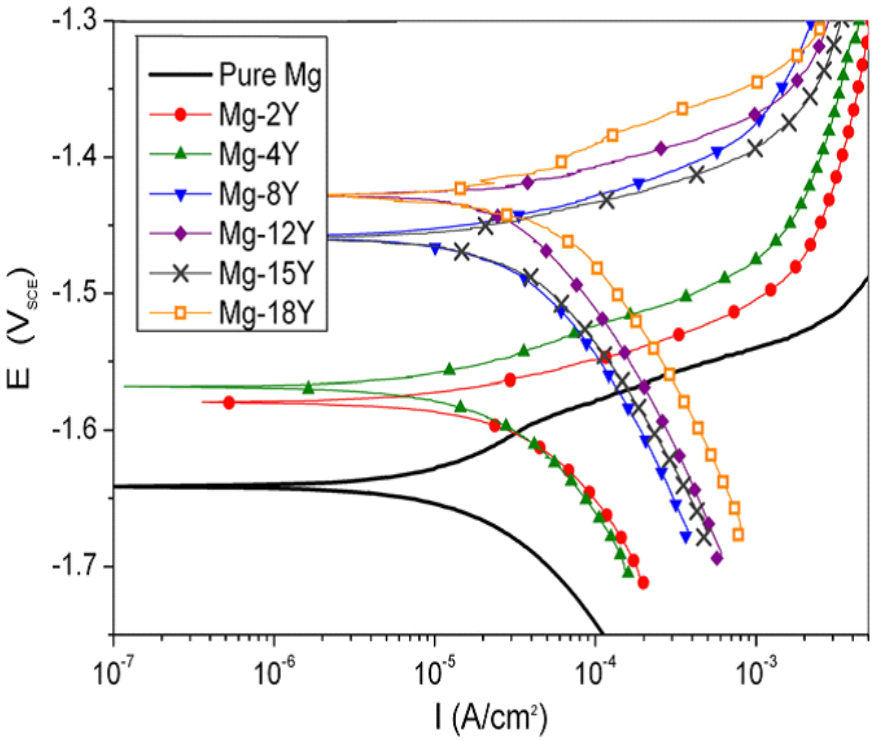


**Figure 2-6. Representative potentiodynamic polarization curves for binary Mg–Y alloys [36]**

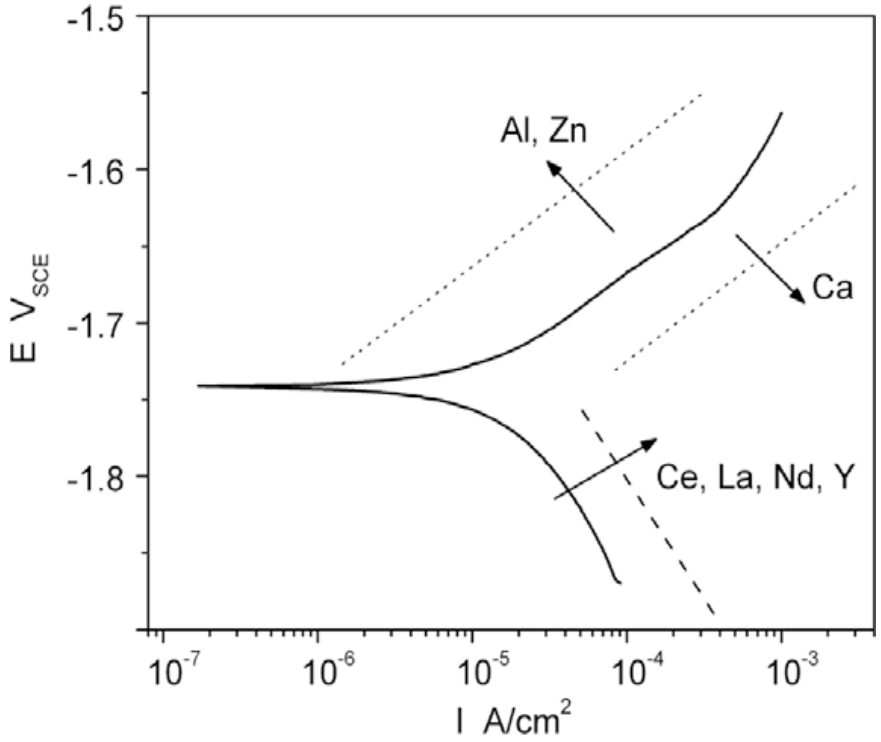


**Figure 2-7. Effect of different alloying elements on Mg corrosion behavior [20]**

## 2.6 Surface Modification of Mg Alloys

Extremely high degradation rate of Mg alloys result in a rapid loss of implant mechanical integrity in the human body environments, limiting practical applications. Considering the fact that the interaction between the cells and tissues with biomaterials at the tissue-implant interface is a surface phenomenon, implant surface properties play a major role in determining both the biological response to implants and the material response to the physiological condition [58, 59]. Hence, the ability to modify the surface properties while preserving the bulk properties is important. Therefore, surface modification to form a hard, biocompatible and corrosion resistant layer has always been an interesting topic in the biomaterial field. A corrosion resistant coating can significantly delay the initiation of biodegradation. A delayed degradation process is critical to a biodegradable implant, as the implant needs to be fully functional for a

certain period before the surgery region starts healing. Ideally, the corrosion resistant film formed on the Mg implant should also be wear resistant, so the film will not be damaged by scratching during implanting. In addition, since Mg possesses a low melting point, some of the coating methods such as physical vapor deposition is less practical for surface modification of Mg [11, 22, 30, 36, 60, 61].

Generally, coatings can be classified as conversion and deposited coatings. The in situ grown coatings are called conversion coatings. In conversion coating, some parts of the surface are converted into the coating as an oxide layer with a chemical or electrochemical process between the substrate and the solution [62-64]. On the other hand, deposited coatings can be divided into organic, inorganic and metallic materials. Different coating methods are discussed below.

### 2.6.1 Chemical Conversion Coatings

Fluoride conversion coating and anodized coatings exhibit an effective barrier to improve the corrosion resistance of Mg alloys, and they can be used as a pre-treatment in a bi-layer coating to enhance the coating adhesion. The adhesion of conversion coatings to the substrate tends to be very good due to in situ growth [3, 62, 65, 66].

#### 2.6.1.1 Fluoride Conversion Coatings

Fluoride treatment is well known as one of the useful methods to inhibit the corrosion of Mg and its alloys and acceptable for the medical purpose due to several advantages such as economy, non-toxicity, chemical inertness, convenience, and easy processing. Mg is regarded as one of the most resistant metals to hydrofluoric acid because of the formation of a dense protective fluoride film that can protect the underlying metal and prevent corrosion [29, 67]. Several researchers investigated the corrosion protective aspect of fluoride coatings.

Pereda et al. [67] developed 4 different fluoride conversion coatings on Mg substrate using different concentrations (0.01 M-0.3 M) of potassium fluoride (KF) solution and further investigated the effect of chloride ions ($Cl^-$) on the corrosion performance of different conversion coatings. According to their result in the presence of $Cl^-$, fluoride content in the conversion coatings gradually drop and consequently the magnesium fluoride ($MgF_2$) layer gradually dissolves, resulting in a decrease in corrosion resistance.

Apart from that, Chiu et al. [29] obtained a thin (1.5 μm) and compact fluoride conversion coating on pure Mg substrate after 24 hours immersion in 48% hydrofluoric acid (HF) solution which was mainly composed of $MgF_2$ phase. According to their results the conversion coating provided moderate improvement in corrosion resistance (around 40 times) in Hanks' solution. Still, the obtained coating could be use as pre-coat for subsequent coating method.

Likewise, Ren et al. [68] used $MgF_2$ conversion coating as pre-coat on AZ31 alloy for the sol-gel process in order to develop a double layers coating of Ca-P/$MgF_2$. According to their report the good adhesion strength between the coating and AZ31 substrate prevented coating cracking and peeling off during the immersion of samples in simulated body fluid (SBF) solution which prolonged the protection period of coating on AZ31 alloy until 18 days.

In another research, Van Phuong et al. [69] compared zinc phosphate and magnesium phosphate conversion coatings which formed on AZ31 by immersion in zinc phosphate and magnesium phosphate solutions respectively. Their results showed although zinc phosphate layer possessed a higher thickness compared with a magnesium phosphate layer, but a magnesium phosphate coating offered better corrosion resistance due to the presence of less porosity in the coating nature.

In the same way, Witte et al. [70] investigated the corrosion behavior of extruded LAE442 magnesium alloy with and without fluoride treatment as a biodegradable

implant in a rabbit model. A favorable corrosion resistance of LAE442 magnesium alloy in vivo was observed; moreover, they found the evolution of hydrogen gas was remarkably restricted after fluoride treatment.

#### 2.6.1.2 Anodizing of Mg

Anodizing is also classified as a conversion coating method. In anodizing method, the metal makes the anode in the electrical circuit with the aim to passivate the surface and increase the thickness of oxide layer in order to enhance the corrosion and wear resistance of substrate. Anodizing can take place in different solutions, such as alkaline baths based on potassium hydroxide, phosphate-fluoride or even silicate-containing electrolytes [44]. Anodizing of Mg in 0.25M sodium hydroxide and 0.1M sodium silicate solution at room temperature can improve corrosion resistance of Mg substrate. The coating composition mostly consisted of a mixture of magnesium oxide (MgO) and forsterite ($Mg_2SiO_4$). Moreover, The high molar volume of $Mg_2SiO_4$ could smoothen and uniform the anodized coating shrinkage caused by the formation of low molar volume MgO [44].

Guang et al. [71] reported that the ceramic like anodized coating formed on the surface of Mg could slow down the degradation rate of Mg and therefore, result in slower hydrogen evolution and solution alkalization process. The results indicate that an anodized Mg alloy might be used as a biodegradable implant material.

On the other hand, Shi et al. [72] used micro arc oxidation (MAO) method followed by $TiO_2$ sol–gel coating for surface modification of Mg substrate. The porous MAO coating layer with a thickness about 12 μm was sealed by $TiO_2$ layer which resulted in slightly improvement of Mg corrosion resistance (30 times).

In brief, one of the challenges in anodizing of Mg alloys is to obtain thick and compact layers with a low Pilling-Bedworth (P-B) ratio for making oxide/hydroxide layers.

High P-B ratio leads to high internal stress and can cause cracking in the growing oxide layer [73, 74]. Another anodizing method is called plasma electrolytic anodizing (PEO) which forms the oxide layers on Mg substrate above the breakdown voltage. This method can produce stable and hard coating with high resistance to corrosion and abrasion [75-77].

Vu et al. [78] reported formation of porous anodized film on AZ91D alloys by using plasma electrolytic anodizing process at constant current density (20 $mA/cm^2$), using classical electrolytic bath ( KOH, KF and $K_2HPO_4$) with addition of CaO (1-3 g/L). According to their report obtained coating was composed of $Mg(OH)_2$, MgO, $MgAl_2O_4$, and Ca and P elements. The result showed that small addition of CaO (1 g/L) to the deposition electrolyte could optimize coating corrosion performance in SBF solution. The enhancement in corrosion performance was resulted from precipitation of Ca/P containing layer in SBF solution and its sealing effect. However, adding higher amount of CaO (3 g/L) resulted in a crack formation in the anodic oxide film and subsequently negatively affected the corrosion performance of coating layer.

The drawbacks of PEO coatings are their brittleness and their electrical isolation properties, which make this technique unsuitable for later processing by electrochemical methods [3].

#### 2.6.1.3 Biomimetic Ca-P Conversion Coatings

An apatite layer can form on the substrate in the biomimetic process, during the immersion in SBF solution. SBF is a supersaturated solution of Ca and P ions. The deposition solution's concentration can vary between SBF and 10xSBF (the concentration of ions in this solution is ten times of normal SBF solution). This process is carried out at pH 7.4, temperature 37 °C and for an immersion period of about 14-28 days with replenishment of SBF solution [33, 79]. Different compositions of surface layers such as amorphous carbonate, Ca-P, Mg-P and a mixture of Ca/Mg-P can form

on the surface by changing the bath composition. The thickness of these layers is more than 20 µm, reportedly extremely permeable, and exhibit many cracks [80].

Cui et al. [81] reported the formation of non-uniform and porous Ca-P coatings on Mg substrates. Releases of hydrogen bubble on Mg substrate and consequently formation of Ca-P layer around these bubbles resulted in a porous and non-compact coating.

Apart from that, Zhang et al. [23] developed homogenous bone-like biomimetic apatite coating on Mg substrate using high supersaturated SBF solution (3xSBF) without any surface pre-treatment at 42 ºC for 24 and 48 hours. The obtained coating showed good bioactivity and decreased the corrosion rate of Mg substrate. Formation of an apatite coating resulted from a high level of supersaturation of SBF solution and a sharp increase of solution's pH as a result of Mg substrate corrosion.

Similarly, Chen et al. [82] studied the possibility of a formation of biomimetic coating on Mg-x% Ca and Mg-3Zn–y% Ca alloys. The 5 µm thick biomimetic coatings were formed on Mg alloy substrates during two steps of immersion in solution at 65 ºC for 2 minutes followed by post-treatment in a 10 g/L NaOH solution at 80 ºC for 4 hours. The obtained coatings were loose and rough with a mixture of Ca-P and $Mg(OH)_2$ phases. The results confirmed that the level of corrosion protection of coatings strongly depends on Ca content in the substrate. Coating could form on Mg-5Ca (Ca content in the substrate was around 5 wt.%) and Mg-3Zn substrates, however, the obtained coatings were not provided remarkable corrosion protection.

Likewise, Duan et al. [83] reported a formation of multi layers biomimetic Ca-P coatings on Ti, SS, Co-Cr-Mo, and tantalum (Ta) substrates without using high supersaturated solution. The coating process consists of multi steps of immersion samples in SBF solutions, taking out the samples and drying in room temperature. A crystalline Ca-P coating completely covered the surfaces after several dip and dry processes which reportedly helped formation of a compact coating layer. Dipping the sample in supersaturated solution left a wet Ca-P layer on the sample surface. During

the drying step, the solvent gradually evaporated from Ca-P layer, which resulted in an increase in supersaturation level on the top of samples. This increase in supersaturation level may assist the nucleation of Ca-P crystals during the next immersion step and consequently, increase the surface coverage and supported the subsequent growth of Ca-P coatings due to their similarities in structures and compositions.

Silva et al. [84] used a different approach for the deposition of biomimetic coating on bio-inert silicon nitride ceramic in order to improve their bioactivity. Coating process was done in two steps: first silicon nitride substrate was immersed into sodium silicate solution at 37 °C for 7 days followed by immersion of substrate into 1.5xSBF solution at 37 °C for 6 days. As they reported, the successful deposition of a hydroxyapatite (HA) layer resulted from adsorption of silicates ions on the surface in the first step which provide a desirable area for nucleation and growth of the HA layer.

### 2.6.2 Deposited Coatings

Another group of coatings is classified as deposited coatings. This group includes metallic, inorganic, and organic based coatings. These types of coatings can be applied by different methods such as electrodeposition, electrophoresis and plasma spray techniques. Among these coatings, the use of metallic coating on the Mg surface is a big technological challenge. Since Mg has one of the highest chemical reactivity and lowest electrode potential in comparison with other metals, it usually acts as an anode in contact with other metals. Therefore, any damage in the metallic coating layer leads to galvanic corrosion and a rapid degradation of the Mg substrate [3].

#### 2.6.2.1 HA and Ca-P Electrodeposited Coatings

HA is a main inorganic constituent of natural bone and can speed up bone growth. However, due to its poor mechanical strength, it cannot be used in load-bearing applications [85]; nevertheless, HA could be used as a coating layer in order to improve biocompatibility of metallic implants [86]. The previous literature indicated that electrodeposition of HA results in better properties than the chemical conversion method. However, for electrodeposition, the deposition parameters need to be adjusted carefully. Moreover, the deposited coating is not always pure due to the presence of trace amounts of the substrate material that is mixed into the coating. This induces the formation of new phases in the surface layer [87-92]. Song et al. [87] applied HA coating on AZ91 by electrodeposition and found that HA layer can decrease the degradation rate of Mg alloy substrate. The coating morphologies after corrosion also showed that the HA coating could potentially offer protection to the Mg alloy substrate. The $i_{corr}$ for the HA coating was reported $3.65*10^{-5}$ A/cm$^2$, which was almost ten times lower than that of Mg substrate ($2.97*10^{-4}$ A/cm$^2$). Other research results showed reduced hydrogen evolution after applying the HA coating [87, 90]. Similarly, Guan et al. [90] reported that after applying HA coating the corrosion potential ($E_{corr}$) of coated sample was higher in comparison with the uncoated sample, indicating that the coated sample would be more corrosion resistant. However, in the electrodeposition method, the release of a hydrogen bubble on the Mg surface creates imperfections in the coating, resulting in a poor adherence and a non-uniform layer, since the hydrogen bubbles adhere to the surface and prevent the nucleation and deposition of coating [87, 90, 93]. Some researchers, compared the deposition of Ca-P coatings with pulse and direct current deposition, and reported that by using the pulse current method the coated alloy showed higher polarization ($R_p$) resistance and lower corrosion rate. This improvement in corrosion resistance can be related to a decrease in anodic dissolution and a more uniform coating morphology resulting from the pulse current method [94, 95].

Kannan et al. [96] used potentiostatic pulse-potential and constant-potential methods for deposition of Ca-P on AZ91 substrate in order to improve substrate's corrosion performance. The obtained coating from the pulse-potential deposition method showed better corrosion resistance (around 3 times improvement in Rp) compared to the obtained coating from constant-potential deposition method. The better performance of a pulse-potential deposited coating resulted from compact surface morphology of Ca-P coating, even though, the coating thickness was lower for this coating (7 μm) compared to a deposited coating by the constant-potential method (12 μm).

Similarly, Qin et al. [97] deposited a silicon (Si) doped Ca-P coating on AZ31 substrate by the pulse electrodeposition method in an attempt to enhance bioactivity, corrosion performance and osseointegration of substrate. It was believed that an inadequate Si amount in the body decreases osteoblast formation and influences the rate of bone repair. An incorporation of Si into the Ca-P coating resulted in a higher osteogenic activity, osteoblast differentiation as well as a higher apatite layer formation which confirmed its better bioactivity. Moreover, the obtained coatings could improve the corrosion performance of the Mg substrate approximately ten fold ($i_{corr}$ of the coating: $1.51 * 10^{-6}$ A/cm$^2$, $i_{corr}$ of the bare substrate $7.42 * 10^{-5}$ A/cm$^2$).

Apart from that, Kannan et al. [98] investigated the effect of adding a polylactic acid (PLA) polymer layer on top of Ca-P deposited coating in attempt to control the coating porosity and the corrosion performance, since the porosity is a major problem in electrodeposition of the Ca-P coating on Mg substrate due to hydrogen evolution. The results showed adding a polymer layer can enhance Rp of Ca-P coating to one order of magnitude. However, while the bare alloy and Ca-P coating alloy exhibited patches of localized degradation, there was no evidence of a localized attack on the alloy with the polymer top layer.

Roy et al. [95] also deposited thick porous Ca-P and Si-Ca-P coatings on the Mg surface with sol-gel method, but the degradation results did not show any significant improvement in corrosion resistance due to the coating's porous nature as well as presence of cracks in the coating layer. However, their cytocompatibility studies on coated and uncoated samples confirmed that bioactivity of Mg substrate improved after applying the coating.

Apart from that, Jo et al. [99] deposited a double layers HA/$MgF_2$ coating with an aerosol deposition method on the Mg substrate in order to increase the coating adhesion and reduce the corrosion rate. The $MgF_2$ layer was used as a bi-layer in their study. Based on their observation, double layers of a HA/$MgF_2$ coating significantly improved the corrosion resistance. The $Mg^{2+}$ ion released during the immersion test after 70 hours for uncoated Mg was reported 350 ppm, while in the case of coated substrate it decreased to 100 ppm. In addition, the coating adhesion was reported around 25 MPa that fulfilled the coating material requirement.

Likewise, Alabbasi et al. [100] reported a deposition of a two layer corrosion protective coating (with total thickness of 37±4 μm) on Mg substrate. The coating composed of a layer of rough silicate-based coating which followed by deposition of a smooth Ca-P layer by electrodeposition method. According to their report, the obtained coating significantly enhanced the substrate corrosion performance. Two-order of magnitudes increase in Rp and a remarkable decrease in $i_{corr}$ (~96%) was observed.

Grubac et al. [101] deposited HA coating on AZ91D in two steps: first a deposition of a calcium hydrogen phosphate ($CaHPO_4$) layer with a constant potential electrodeposition method (voltage: -1.90 V to -2.10 V), followed by a conversion of $CaHPO_4$ layer to HA through alkaline treatment. The deposited coating decreased $i_{corr}$ of substrate from 32 μA/$cm^2$ to 4 μA/$cm^2$ in Hanks' solution; the increase in corrosion

performance was depended on deposition voltage and increased by increasing cathodic potential and deposition time.

Ren et al. [102] reported a simple method for deposition of a uniform calcium deficient hydroxyapatite (CDHA) coating on AZ31 substrate in a short period of time (less than 10 min in two steps) by using a microwave assisted coating technology layer. However, the decrease in corrosion rate was not significant.

#### 2.6.2.2 Organic Coatings

Organic coatings (as a part of the deposited coatings class) are very attractive for biomedical applications because they offer great flexibility in the chemical functional groups that can be combined on the implant surface (to control tissue-implant interactions). Additionally, the polymer coatings have mechanical properties that are comparable to soft biological tissues. The relative ease of processing is another reason for the extensive interest in organic thin films. Moreover, these coatings are attractive as they can offer drug delivery capability [3, 103, 104].

For example, Xu et al. [6] used biodegradable PLA and polycaprolactone (PCL) polymer film to modify the surface of Mg and reported that the polymer films can significantly improve the cytocompatibility and decrease $Mg^{2+}$ release during the cell culture tests. The decrease in $Mg^{2+}$ release is an indication that the corrosion resistance of Mg substrate is enhanced by applying the different organic films. Other researchers reported that by applying chitosan coating on Mg alloy the corrosion resistance increased and higher volumes of new bone growth were observed on the polymer-coated samples [105, 106]. Thicker coatings may improve corrosion resistance; such as increasing thickness of PLA organic film which increases the polarization resistance. However, increasing the coating thickness also showed a deleterious effect on the coating adhesion [107]. Cai et al. [108] fabricated a multilayer organic coating by

using a layer-by-layer method. The cytocompatible multilayer coating increased the $R_p$ of AZ31 magnesium substrate by 3.45 times

In the same way, Abdal-hay et al. [61] deposited polyvinyl acetate (PVA) on the AM50 magnesium substrate by using different solvents. Based on their observations, the solvent type has a significant effect on the coating porosity, and therefore, coating performance. The presence of porosity in the PVA film improved the cell attachment in cell culture test. However, the corrosion rate increased after applying the PVA coating due to the porous coating morphology. On the other hand, in vitro degradation testing of PLA coating on AZ91 magnesium alloy using the spin coating method proved to be beneficial for enhancing the degradation resistance of the alloy [61, 105].

Likewise, Wong et al. [105] reported deposition of layer-by-layer PCL and dichloromethane coating on Mg substrate by a spraying method, the obtained coating had a porous nature mainly due to the process of phase separation and solvent evaporation during the drying process, although, this porous layer could reduce the substrate degradation rate without showing any toxicity and any inflammation effect.

Similarly, Oosterbeek et al. [109] deposited a PLA polymer and ceramic-polymer composite coatings on a Mg substrate with a combination of biomimetic and dip coating methods. The obtained coating did not show remarkable corrosion protection due to the presence of porosity and cracks in the coating. Moreover, ceramic-polymer composite coatings showed lower adhesion strength to the substrate compared to the PLA coating resulted from poor bonding between the ceramic layer and the Mg substrate. This reduced the coating's adhesion strength which leads to earlier coating cracking during the corrosion test, demonstrating poorer performance of the coating.

#### 2.6.2.3 Composite Coatings

The main issues for HA coatings are their brittleness and low adhesive strength between the coatings and substrates that lead to early failure of the bone-implant interface. Composites can be formed by the combination of HA and bioresorbable polymers that can be an effective method to overcome the HA mechanical problems [103, 110-116]. In addition, human bone is a composite of HA and collagen. From the viewpoint of bionics, if the composition and structure of implants are similar to the human bone, it will be favorable for cells to adhere and proliferate to the bone. These composites usually have weak mechanical properties; accordingly, they cannot be used in load bearing application. However, composites such as HA/collagen can be used as coating for metals substrate. In this case, the presence of collagen in the HA/collagen composite coating increases the metals-implant biocompatibility in comparison with HA coating [112, 115, 117, 118]. Shi et al. [119] coated AZ80 magnesium alloy with a MAO/Ca-P layer in two steps: first development of MAO layer followed by electrodeposition of Ca-P layer. They reported a decrease in hydrogen evolution rate from 0.07 ml/cm$^2$/day for uncoated substrate to 0.01 ml/cm$^2$/day for the coated sample, indicating that MAO/Ca-P layer can decrease the corrosion rate. Also, Zhang et al. [120] worked on HA/stearic acid composite coating by using the combination of electrodeposition and solution methods. The resulting coating was porous, although according to Electrochemical Impedance Spectroscopy (EIS) results, the coating showed higher corrosion resistance compared to the bare substrate. They suggested this porous coating might improve the growth of osseous tissue.

Likewise, Li et al. [121] applied a layer of PCL coating on MAO pre-treated Mg substrate, in attempt to seal the porous structure of MAO and improve the corrosion performance. According to their results MAO layer could not provide sufficient corrosion protection for Mg substrate due to the porous nature, however, applying a layer of PCL with dip coating method on MAO layer (PCL thickness: 9 μm) could

decrease the $i_{corr}$ of MAO coated substrate from 1.14 $\mu A/cm^2$ to 0.0045 $\mu A/cm^2$. Although deposition of a relatively thin PCL layer (600 nm) did not have significant effect of corrosion performance ($i_{corr}$: 0.81 $\mu A/cm^2$).

Ian et al. [122] reported deposition of a composite coating of poly(lactic-co-glycolic acid) (PLGA) and nanostructured hydroxyapatite (nHA) [nHA/PLGA coating] on Mg substrate using the spin coating method in order to control its corrosion rate. Pure PLGA coating was used as control as well. The results showed that corrosion performance of Mg substrate ($i_{corr}$: $4.71*10^{-3}$ $A/cm^2$) was relatively improved after applying PLGA ($i_{corr}$: $9.17*10^{-4}$ $A/cm^2$) and nHA/PLGA coatings ($i_{corr}$: $8.23*10^{-5}$ $A/cm^2$). However, the coating layers showed a delamination from the Mg substrate during an immersion in a SBF solution, resulted from a release of $H_2$ gas.

For comparison a summary of different common coatings for surface modification of magnesium is reported in Table 2-1.

**Table 2-1. A summary of common surface modification for magnesium substrate**

| Substrate | Coating | Coating method | Results | Ref. |
|---|---|---|---|---|
| AZ91 | Polycaprolactone | Spraying | Coating reduced the corrosion rate of substrate; Coating aided in retaining the mechanical strength of the substrate; Coating showed good biocompatibility | [105] |
| AZ91D | HA | Electrodeposition | Improve the biodegradation rate; Parts of the flake-like HA coating were dissolved into SBF | [87, 123, 124] |
| AZ31 | Ca-P | Biomimetic | Coating improved the corrosion resistance | [23, 30, 33, 125] |
| Mg–Zn–Ca | MgO/HA | Micro arc /electrochemical | Improved the corrosion resistance of the substrate ;Coating showed good bioactivity Coating decreased the loss of mechanical integrity in SBF solution | [113] |
| Pure Mg | MgO | Micro arc /Anodizing | Coatings improved the corrosion resistance; coating not supported cell growth; The biocompatibility improved by a series of post surface treatments in cell-culturing medium | [126] |
| AZ91 | PLA | Spin coating | Coating improved the corrosion resistance of substrate; Increase in coating thickness decreased the adhesion; Coatings degradation resistance decreased with increase in SBF exposure time | [107] |
| AZ31 | $MgF_2$/PAN | Dip coating | Interfacial reaction between the polymer and the substrate improved the coating to substrate adhesion; coating decreased the corrosion rate | [32] |
| Mg–Nd–Zn–Zr | Brushite | Chemical deposition | Coating enhanced corrosion resistance; Coating reduced haemolysis Coating produced less gas; Coating showed good surface bioactivity | [127] |
| Mg-Zn-RE | Ti-O/HA | Sputtering | Coating improved the corrosion resistance | [128] |
| Mg | Zinc | Ion implantation | The corrosion rate increased because of the galvanic effect between the Zn rich surface and magnesium | [129] |

## 2.7 Summary

Up to date different types of coatings such as anodizing, electrodeposition, fluoride conversion and biomimetic coatings have been used to control the corrosion of Mg alloys. Based on a literature survey, a wide range of coatings on Mg and Mg alloys can increase the corrosion resistance. However, the problem is that different research groups performed their experiment under different conditions including the use of a different deposition solution or using different deposition parameters selection. Therefore, their results are not comparable. Generally in vitro and in vivo tests have indicated that most of the coatings improved the corrosion performance of Mg substrate at a different level. However, the control of phases and the formation of cracks is still unsatisfactory. For example, biomimetic and anodized coatings are reportedly rather permeable and exhibited many cracks [3, 11].

On the other hand, a relatively thin and dense coating can be made of $MgF_2$ as a conversion coating, but it gradually dissolves when the sample is transferred to fluoride-free solutions precluding long-term protection [3, 11].

An issue that is normally neglected is for coated samples corrosion may start at defects present in the coating, and therefore, it is non-uniform in nature and flaking of coating could take place. Moreover, most studies did not investigate the coating adhesion to substrate or only focused on corrosion analysis.

Thus, no suitable coating seems to exist for Mg implant application and there is a need for a novel coating that is dense and able to provide superior corrosion protection. In addition, the coating must be biodegradable and biocompatible as the biological response of implant materials strongly depends on the implant's surface properties, since interactions between the cells and biomaterials takes place at the tissue-implant interface [61]. In order to obtain a denser and fault-free protective layer on Mg, it would be necessary to prepare the layer in such a way that any porosity would be

healed during the coating process. It was expected that a process that gradually grows the coating material may fulfill this requirement. Such a known process is hydrothermal growth of particles that increases the size of crystals gradually until either overlap of crystals, or exhaustion of ions to build the crystals, is reached. Surface modification of Mg alloy by hydrothermally deposited coatings is the main objective of the current work, which will be discussed in detail in the next chapters.

# Chapter 3

# Experimental Procedures

This chapter describes the hydrothermal method for deposition of inorganic coatings, composite coatings as well as anti-infective coatings. Moreover, characterization methods for deposited coating layers in terms of surface properties, corrosion and mechanical performance are also summarized in this chapter.

## 3.1 Materials and Methods

### 3.1.1 Materials

AZ31 magnesium alloy was used as substrate for the coating process allowing comparison with previous literature reports. Disks were prepared with 25 mm diameter and 2 mm thickness using commercial AZ31 rod. The nominal chemical composition of AZ31 is listed in Table 3-1. Prior to the coating process, an AZ31 substrate was prepared up to 2400 with grit abrasive paper, and then ultrasonically cleaned in acetone for 20 minutes.

**Table 3-1. Chemical composition of AZ31**

| Ingredient | Weight % |
|---|---|
| Magnesium (Mg) | 94.8-97 |
| Aluminium (Al) | 2.4-3.6 |
| Zinc (Zn) | 0.5-1.5 |
| Manganese (Mn) | 0.02-0.1 |

Moreover, in the current work the possibility of deposition of Ca-P inorganic coatings on Al free Mg alloy substrates was also checked. For this purpose a hydrothermal deposition process was done on WE54 (chemical composition: 4.75-5.5 wt.% Y; 1.5-

2 wt.% Neodymium; 1-2 wt.% Rare Earths and 0.4 wt.% Zr) and Mg-Ca alloys for comparison purposes too.

For the hydrothermal process, calcium nitrate [$Ca(NO_3)_2$] with 99.98% purity and ammonium dihydrogen phosphate ($NH_4H_2PO_4$) with 98% purity were obtained from Alfa Aesar. Sodium carboxymethyl cellulose (SCMC) with molecular weight 700,000 units (degree of substitution: 0.9) and polyacrylic acid (PAA) with molecular weight 450000 **units** were used in this study due to their biocompatibility and biodegradability. PAA and SCMC polymers were purchased from Sigma-Aldrich.

## 3.1.2 Deposition Methods

### 3.1.2.1 Deposition Process of Ca-P and Ca-P/Polymer Coatings

In order to deposit a Ca-P coating on the AZ31 magnesium substrate, hydrothermal processes were used. A solution containing of $NH_4H_2PO_4$ (0.06 M) and $Ca(NO_3)_2$ (0.1M) was prepared. The pH of solution was adjusted to 3.9-4.0 by using ammonia, the AZ31 samples were sealed in the autoclave with the deposition solution and heated in an electric oven at varied temperatures (100 ºC, 130 ºC, 160 ºC and 190 ºC) for 3 hours (Note: Under some conditions, Mg may corrode in the autoclave, potentially generating hydrogen gas that may increase the pressure significantly. Such potential pressure increase and the pressure rating of the autoclave should be taken into account for safe operation of autoclave.). The samples henceforth were named as HE100 ºC-3hr, HE130 ºC-3hr, HE160 ºC-3hr and HE190 ºC-3hr, respectively. For the 190 ºC deposition temperature, heating durations of 1 and 2 hours were used as well.

Moreover, a hydrothermal deposition process was performed on WE54 and Mg-Ca substrates at 160 ºC for 3 hours as well, and samples henceforth were named as WE54 substrate and MgCa substrate respectively.

In the next step hydrothermal process was used for deposition of Ca-P/PAA and Ca-P/SCMC composite coatings which were denoted as HEPAA and HESCMS composite coatings from now on respectively. For the hydrothermal deposition process first, a stock solution of $Ca(NO_3)_2$ (0.1M) and a stock solution of $NH_4H_2PO_4$ (0.06 M) were prepared, then different amount of PAA (0.1, 0.2, 0.3, 0.4, 0.5 and 0.6 wt.%) was fully dissolved in 100 ml of $NH_4H_2PO_4$ stock solution. A further 100 ml of $Ca(NO_3)_2$ stock solution was added to the first solution ($NH_4H_2PO_4$ + PAA) and the pH was adjusted to 3.9-4.0. Next, AZ31 samples were sealed in the autoclave with the deposition solution and heated in an electric oven at 160 ºC for 3 hours. The samples henceforth were named as HEPAA(0.1%), HEPAA(0.2%), HEPAA(0.3%), HEPAA(0.4%), HEPAA(0.5%) and HEPAA(0.6%) respectively.

The same procedure was repeated for SCMC by replacing PAA with SCMS and samples were named as HESCMC (0.1%), HESCMC(0.2%), HESCMC(0.3%), HESCMC(0.4%), HESCMC(0.5%), and HESCMC(0.6%) respectively.

#### 3.1.2.2 Deposition of Anti-infective Coating with Incorporation of Antibiotic

Anti-infective coatings with a local drug delivery ability could be prepared by incorporating the antibiotics into the coating. One of the effective and widely used antibiotics is tetracycline (TCH). TCH is well known to have a binding affinity to the bone and could prevent biofilm formation and consequently infection.

In this work, different concentrations of TCH were incorporated into inorganic and composite coatings [Ca-P and HEPAA(0.2%) coatings were hydrothermally prepared before antibiotic's incorporation] by means of the electrophoretic deposition (EPD) method.

The processes of TCH incorporation in the coatings are summarized below:

Two solutions were used in order to incorporate TCH into hydrothermally pre-coated samples:

1- A solution of SCMS polymer (0.2% w/V)

2- A solution of SCMS + TCH (5mg/ml)

Incorporation of TCH into the coating was done in 3 steps:

1- Deposition of a layer of SCMS/TCH for 2 minutes at 10 Volts by means of EPD on the hydrothermally pre-deposited coatings; followed by drying in room temperature for 15 minutes.

2- Deposition of an intermediate layer of SCMS polymer for 2 minutes at 10 Volts by EPD, followed by drying in room temperature for 15 minutes (this intermediate layer was applied to control the drug's release profile).

3- Deposition of a layer of SCMS/TCH for 2 minutes at 10 Volts by EPD followed by drying in room temperature for 15 minutes.

In the case of HEPAA, TCH was incorporated in other concentrations as well (2.5 and 10 mg/ml).

## 3.2 Characterization of Coatings

### 3.2.1 X-Ray Diffractometer (XRD) Analysis

The surface phases of the coated samples were characterized by XRD (XRD, Panalytical Empyrean, DY2t), by using Cu-Kα1 radiation (wavelength λ= 1.5406 Å). The diffraction patterns were collected in the 2θ range $10^{o}$–$80^{o}$, with a step size of $0.02^{o}$. Scanning rate was 0.5°/min.

### 3.2.2 Surface Morphology Observation

The surface morphology and the chemical compositions of samples were analyzed by means of scanning electron microscopy (JEOL JSM 5600 SEM) with an EDS (INCA system, Oxford Instruments, UK).

### 3.2.3 Fourier Transform Infrared Spectroscopy (FTIR) Measurement

FTIR (VERTEX 80V) measurements were carried out to verify the deposition of Ca-P coatings. First, the coating layer was carefully scraped from the AZ31 substrate, and then mixed with potassium bromide (KBr) powder in 1:50 weight ratio, and then the mixture was compressed into a disc for characterization. Analyses were performed in the 400 to 4000 $cm^{-1}$ wave number range.

### 3.2.4 Raman Scattering Measurement

The Raman scattering measurements were performed using a Raman microprobe instrument (RENISHAW-in Via Raman Microscope) in order to investigate the deposition mechanism of coating during hydrothermal process. Raman spectra were collected over the frequency range 100-1500 $cm^{-1}$ with 1 $cm^{-1}$ spectral resolution. The 488 nm line of an $Ar^{+}$ laser was used as excitation source. Raman measurements were done through the coating cross section. For this purpose, samples were cold mounted and after cutting the samples the cross section were prepared with up to 4000 grit abrasive paper, and mechanically polished up to 0.5 micron using alumina slurry.

### 3.2.5 Coatings Degradation Evaluation

#### 3.2.5.1 Immersion Tests and Mg Ions Release Measurements

Immersion tests were conducted in simulated body fluid (SBF) standard solution according to a reported procedure [130] at pH 7.2-7.4 for up to 28 days in order to assess the early corrosion performance of the coated and uncoated substrates. After each immersion period samples take out from SBF solution and the mass loss was measured.

$Mg^{2+}$ ions release from the substrate was measured using an inductively coupled plasma atomic emission spectrometer (ICP-MS7700, Agilent). After each immersion period, 5 ml of solution was analyzed in order to determine the $Mg^{+2}$ release from the bare and coated samples.

#### 3.2.5.2 Electrochemical Tests

The electrochemical behavior of uncoated and coated samples was investigated by a potentiodynamic polarization test using a Solartron potentiostat (Model SI 1287) conducted in SBF solution. For the electrochemical tests, a three-electrode cell was used with the sample as working electrode, saturated calomel electrode (SCE (sat. KCl)) was used as the reference, and graphite as the counter electrode. An area of 1 $cm^2$ of the working electrode was exposed to the solution. A 1 mV/s scanning rate was applied during the potentiodynamic polarization test. Prior to the polarization test, samples were equilibrated in SBF solution for 30 minutes.

An EIS test was performed in order to investigate the corrosion behavior of coatings in SBF solution using a Solartron potentiostat (Model SI 1260). The EIS tests were

conducted at the open circuit potential (OCP) in the frequency range of 100 kHz to 10 mHz using 10 mV amplitude of signal's perturbation.

It is worth noting that the electrochemical techniques are widely used for the evaluation of the corrosion of Mg alloys because it is a quick and easy technique. The Tafel extrapolation method is essentially an instantaneous technique, which provides a measurement of the corrosion rate at a particular time over which the measurement was carried out. In contrast, the weight loss measurement evaluates the corrosion rate as an average value over the exposure period. Possible issues with the Tafel extrapolation method for Mg alloys are that the corroding area (or topography) is different during immersion test and measurement of the polarization curve. Thus short-term tests may provide measurements that do not agree with long-term tests. An important issue is, thus, that the short-term tests do not provide adequate prediction of long-term behavior [131].

The most beneficial aspect of a polarization test is that it allows quantification of the relative rates of the anodic and cathodic reaction over a range of potentials, while weight loss experiments do not reveal the mechanisms involved in the corrosion process [132].

### 3.2.6 Mechanical Performance Measurements

#### 3.2.6.1 Compression Test

In order to evaluate the degradation of mechanical integrity of uncoated and coated specimens after various immersion periods in SBF solution due to corrosion, cylindrical samples with 15 mm height and 10 mm diameter were used and tested via a compression test. After each immersion period, samples were removed from SBF solution and their compressive strength was measured using Instron 5569 testing

machine using 1 mm/min crosshead speed. The displacement speed was controlled with an Instron machine.

#### 3.2.6.2 Pull Off Adhesion Test

Adhesive strength between the coating layer and AZ31 substrate was evaluated based on ISO 13779-4 test method. Coating adhesion strength was determined by applying a uniaxial tensile load to a cylindrical test assembly composed of one coated specimen bonded to an uncoated component. The tests were carried out by using Instron 5569 testing machine at a crosshead speed of 1 mm/min.

#### 3.2.6.3 Nano-indentation Measurement

For characterizing the mechanical response, nano-indentation experiments were conducted using a Berkovich diamond indenter (Hysitron). A maximum load of up to 4000 μN was used.

#### 3.2.6.4 Scratch Test

A scratch test was performed using a micro scratch tester (CETR multifunction tribometer), by applying a constant increasing force from 0 to 1500 g to the sample. A diamond indenter with the point radius of 200 μm was used. The scratch speed was 5 mm/min, and the scan length was 6 mm.

### 3.2.7 Contact Angle Measurement

Contact angle measurements were carried out using a VCA Optima (VCA-2500XE, AST products, Inc.) Contact Angle System using ultrapure water at room temperature. The volume of the water drop was 0.5 µl and the measurements were repeated three times.

### 3.2.8 Thermo-Gravimetric Analysis (TGA)

The polymer loading in the coating structure was determined by means of TGA (TGA Q500). First, the coating layer was carefully scraped from the AZ31 substrate and powders were heated in nitrogen atmosphere from 20 ºC to 600 ºC, then the gas was switched to air for continued heating from 600 ºC to 950 ºC at a heating rate 10 ºC/min. The mass of composite coating during heating was recorded as a function of time and temperature. The mass loss of inorganic Ca-P coating was measured as the control.

### 3.2.9 *In Vitro* Tests

The in vitro tests were done by means of direct and indirect tests in order to analyze the cell-coating interactions as well as coatings biocompatibility. Cell morphology observation was used for the direct test. For the indirect test, cell viability was used to assess the cytotoxicity of bare and coated samples. The MG63 (human osteosarcoma) cell line was obtained from American Type Culture Collection (ATCC, Rockville, MD) and cultured in a standard culture medium containing Eagle's Minimum Essential Medium (EMEM, Sigma-Aldrich) supplemented with 10% fetal calf serum (FCS, Sigma Aldrich) and 1% penicillin/streptomycin (Sigma-Aldrich) at 37 °C in a humidified atmosphere of 5% $CO_2$.

#### 3.2.9.1 Direct *In Vitro* Test

For the direct test, samples (1x1cm$^2$) were UV sterilized for one hour prior to the test. Samples were placed in 24 wells and 2 ml complete culture medium including $10^5$ cells/ml (3 samples for each group was used) were added to each well and cultured for 1 and 7 days. On day 1 and 7, samples were taken out, rinsed twice with sterile phosphate buffered saline (PBS) solution and fixed with 4% formaldehyde solution and freeze dried. Cell morphology was observed under SEM.

#### 3.2.9.2 Indirect *In Vitro* Test (Cell Viability Measurement by Extract Assay)

Bare substrate, inorganic and composite coatings were immersed in culture medium with the sample surface exposed to the culture medium at 1ml/1cm$^2$ level and incubated at 37 ºC at 5% $CO_2$ for 3 days. After 3 days, supernatant fluids (extracts) were collected and stored at 4 ºC prior to the cytotoxicity test.

MG63 cells at density of 1.2*$10^3$ cells were cultured on a 96 well culture plate and incubated for 1 and 7 days for cytotoxicity test. After each incubation time, cell viabilities were measured by MTS assay [3-(4,5-dimethylthiazol-2-yl)-5-(3-carboxymethoxyphenyl)-2-(4-sulfophenyl)-2H-tetra-zolium] according to company instructions (Promega). Briefly, a MTS working solution was prepared by mixing 1 part of MTS reagent and 4 parts of culture media. Cells were incubated with the working solution for 3 hours in an incubator and absorbance of the product solution was measured by a microplate reader (Tecan Ultra Evolution) at a wavelength of 492 nm. The cell viabilities of the test media (mean ± SD, in %) were calculated relative to negative control (fresh culture medium).

### 3.2.10 Drug Release Measurements and Antibacterial Test

The effect of antibiotic's incorporation into anti-infective coatings on the viable counts of gram positive S. aureus bacteria (ATCC 25923) was investigated by conducting agar disk diffusion tests, in order to evaluate the antibacterial activity of the coatings according to literature [133]. Prior to the study, coatings were sterilized by UV treatment for 45 min each side. Four samples of each series were immersed at 37 ºC in PBS solution at pH 7.4 for 10 days. The sample surface area to solution ratio was $1cm^2$/5ml. At pre-determined time intervals (1, 3, 7 an d 10 days) aliquots (5 µl) of each series were removed and applied to paper discs and placed on the surface of Mueller–Hinton agar plates seeded with S. aureus through a modification of the agar disk diffusion method of CLSI (CLSI 2010) [The bacterial cells were incubated overnight and the solution was then diluted to an optical density OD600 (optical density of a sample measured at a wavelength of 600 nm) of 0.01. After that 50 µl diluted bacteria solution were inoculated on Mueller-Hinton agar plates.]. After 24 hours of incubation at 37 ºC agar plates were checked and the size of inhibition zone was measured.

The release of TCH from the coatings into the PBS solution was measured using the Ultraviolet–visible spectroscopy (UV-Vis) at 360 nm over a period of 10 days.

# Chapter 4

# Deposition of Protective Inorganic Ca-P and Novel Ca-P/Polymer Composite Coatings by Hydrothermal Method

## 4.1 Introduction

For practical application of Mg as an implant material, there is a need for a novel coating that is dense and able to provide superior corrosion protection. In order to obtain a denser and protective layer on the Mg substrate, it would be necessary to prepare the coating in such a way that any porosity would be healed during the coating process. It was expected that a process that gradually grows the coating material may fulfill this requirement. Such a known process is hydrothermal growth of particles that increase the size of crystals gradually until either overlap of the crystals or exhaustion of ions to build the crystals is reached. Producing Ca-P crystals by hydrothermal process has a successful history [134-138]. However, there are not many publications on the deposition of Ca-P crystals directly on metal substrates. Liu et al. [139] reported deposition of a fairly uniform crystalline hydroxyapatite (HA) layer on metal substrates such as Ti, Al, copper (Cu) and SS by seeded hydrothermal deposition method. The process was done in two steps, first, deposition of a seed layer by means of an electrochemical method, followed by a hydrothermal process. Successful deposition resulted from deposition of a primary seed layer. However, corrosion performance of the obtained coating were not investigated. Similarly, Onoki et al. [140, 141] used a double layered capsule hydrothermal hot-pressing technique for developing HA coating on Ti and Mg substrates with good adhesion properties (4-5.5 MPa). Hiromoto et al. [142] used hydrothermal method to deposit HA and octacalcium phosphate in a wide range of pH conditions, although the improvement in corrosion performance was not remarkable (ten-fold improvement in corrosion rate of substrate), due to the presence of porosity in the coating structure.

Apart from this, formation of a $Mg(OH)_2$ layer as a corrosion protective layer by means of hydrothermal process for surface modification of a Mg substrate was investigated by different researchers [66, 143, 144]. Although a $Mg(OH)_2$ layer can improve the

corrosion performance of Mg substrate, it is not preferred in biomedical applications unlike the biodegradable and biocompatible Ca-P coatings. Additionally, since the aim of surface modification of Mg is to delay the degradation of Mg only for a specific period of time until bone healing takes place, therefore, coating solubility is a critical factor. Thus, other resorbable Ca-P phases like monetite or tricalcium phosphate are more suitable for surface modification of Mg compared to a HA phase, due to their higher solubility and resorption rate [145-147]. Hence, a hydrothermal method is reported here that is able to produce dense, adherent and biodegradable coatings over a large surface area (the sample surface area is depended on the autoclave size. In this experiment a total surface area of 16 $cm^2$ could be coated in one run) of Mg substrate even with irregular substrate geometry. In this chapter the feasibility of deposition of inorganic Ca-P (in sections 4.2) and Ca-P/Polymer composite coatings (in section 4.3) on AZ31 magnesium substrate will be discussed.

## 4.2 Deposition of Inorganic Ca-P Coating

The successful deposition of Ca-P layer on the AZ31 substrate during a hydrothermal process resulted from an increase in the solution's supersaturation. Increasing the temperature reduced Ca-P salt solubility and consequently the solution becomes supersaturated resulting in Ca-P mineral deposition. Fig.4-1 shows a photograph of hydrothermally deposited coatings on AZ31 substrate. From Fig.4-1 it is clear that the Ca-P coating successfully deposited on AZ31 substrate and fully covered the substrate. The surface morphology of the coatings will be discussed in the next section.

Increasing the deposition temperature resulted in color changes in deposited coatings. Coating's color was changed from gray to white by increasing deposition temperature from 100 ºC to 190 ºC, which might be due to the change in the coating's chemical composition. This aspect will be discussed in more details in the next sections.

Moreover, the deposition of Ca-P coating was successful for other Mg substrates (WE45 and MgCa) as well regardless of substrate chemical composition as shown in Fig.4-2.

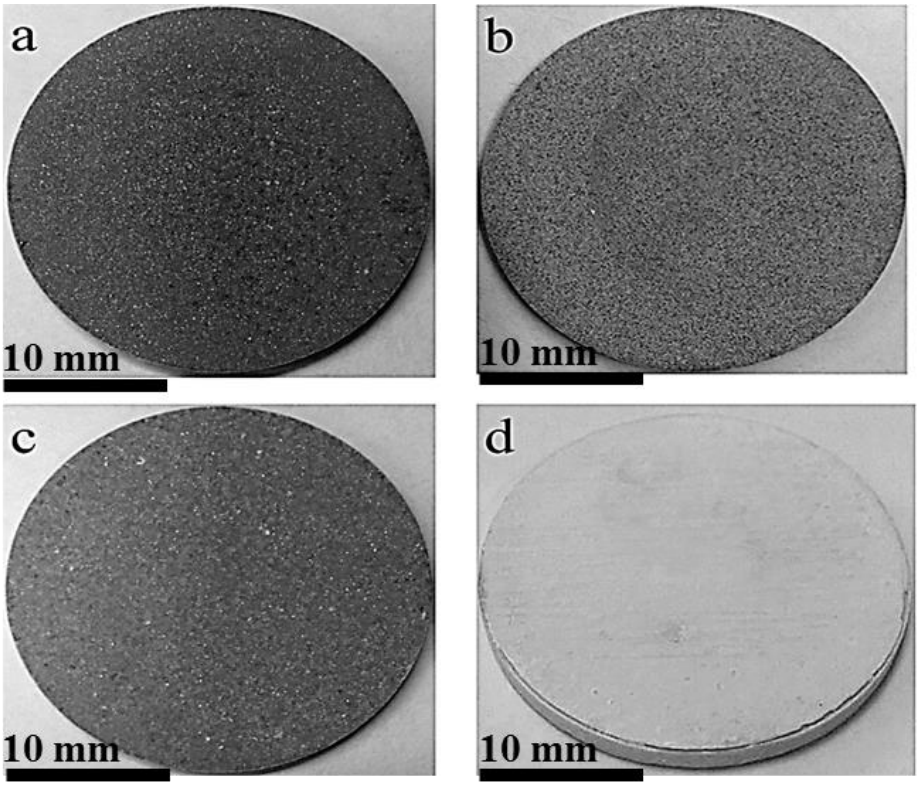


**Figure 4-1. Photographs of hydrothermally deposited coatings: a) HE100 ºC-3hr, b) HE130 ºC-3hr, c) HE160 ºC-3hr and d) HE190 ºC-3hr**

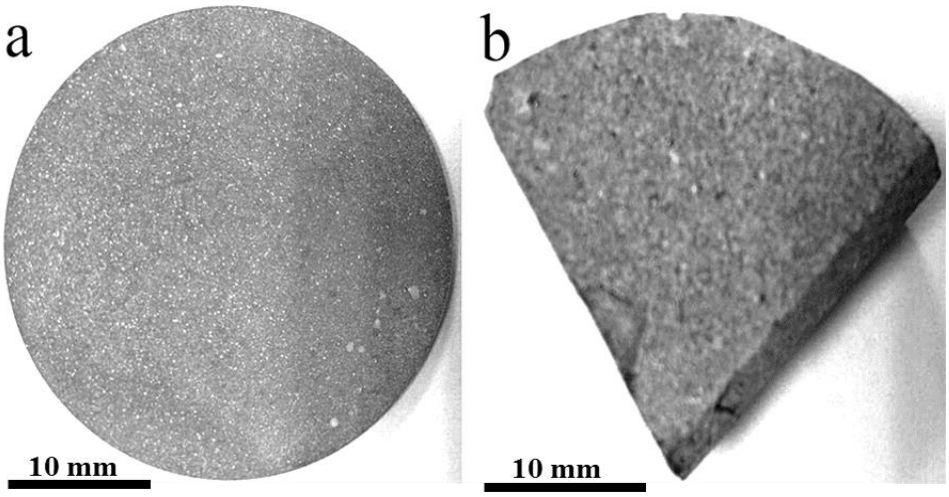


**Figure 4-2. Photographs of: a) Ca-P coating on WE54 and b) Ca-P coating on MgCa substrate**

## 4.2.1 Structure and Chemical Composition of Coatings

### 4.2.1.1 XRD and FTIR Studies of Deposited Ca-P Layer

XRD analysis indicated that the deposited Ca-P coatings were a mixture of monetite ($CaHPO_4$), tricalcium phosphate with a small amount of Mg substitution ($Ca_{2.86}Mg_{0.14}(PO_4)_2$, also known as whitlockite), and calcium pyrophosphate ($Ca_2P_2O_7$) phases as shown in Fig.4-3. XRD analysis confirmed that by changing the deposition temperature coating's composition varied from a monetite phase, to a mixture of monetite and whitlockite phases.

At 100 °C and 130 °C deposition temperatures, the coating composed of a monetite phase. In XRD pattern the peak at $2\theta = 13.08°$ is a characteristic of the monetite phase. The XRD patterns showed diffraction peaks with minimal line broadening and high intensity confirming the presence of the crystalline phases. The stronger diffraction peak at the [112] direction can be ascribed to the preferential growth in [112] orientation. Further increase in deposition temperature resulted in coatings

compositional changes. By increasing the temperature from 130 °C to 190 °C, whitlockite and calcium pyrophosphate peaks appeared in the XRD patterns. For the sample coated at 190 °C, the peak intensities of the whitlockite phase increased while the monetite peak height decreased slightly.

The XRD pattern of Ca-P coating deposited at 190 ºC is given in Fig.4-4. For the coating deposited at 190 °C-1hr, the coating composition was a mixture of monetite and whitlockite. By increasing the deposition time to 2 and 3 hours the peak intensity of whitlockite phase increased significantly. A schematic of crystal structures of monetite and tricalcium phosphate phases is shown in Fig.4-5. Monetite has a triclinic structure (a: 6.91, b: 6.62, c: 6.99; α: 96.34, β: 103.82 and γ: 88.33) while whitlockite has a rhombohedral structure (a = b: 10.40 and c: 37.316).

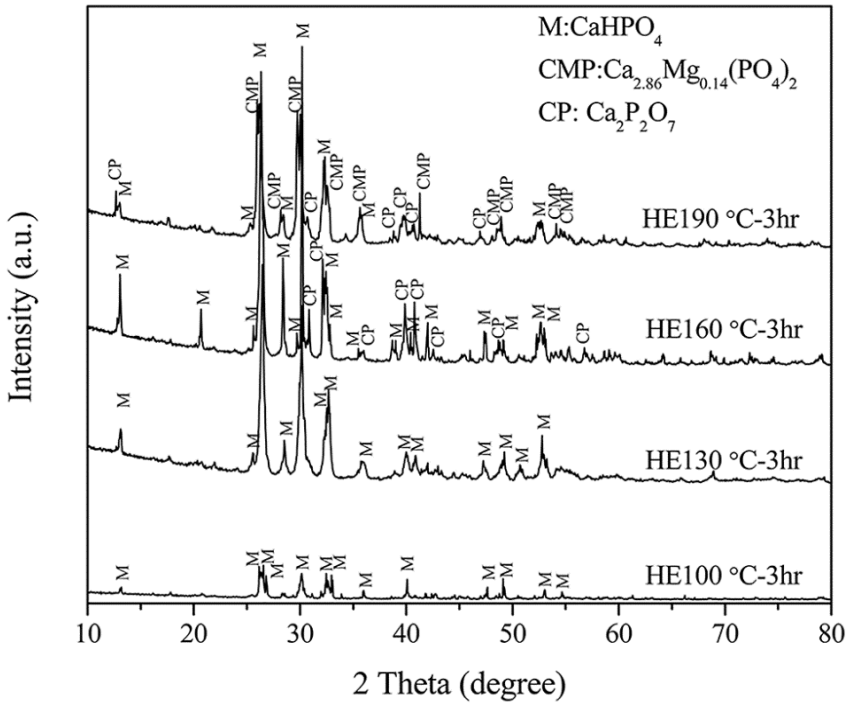


**Figure 4-3. X-ray diffraction pattern of coated samples at different temperatures**

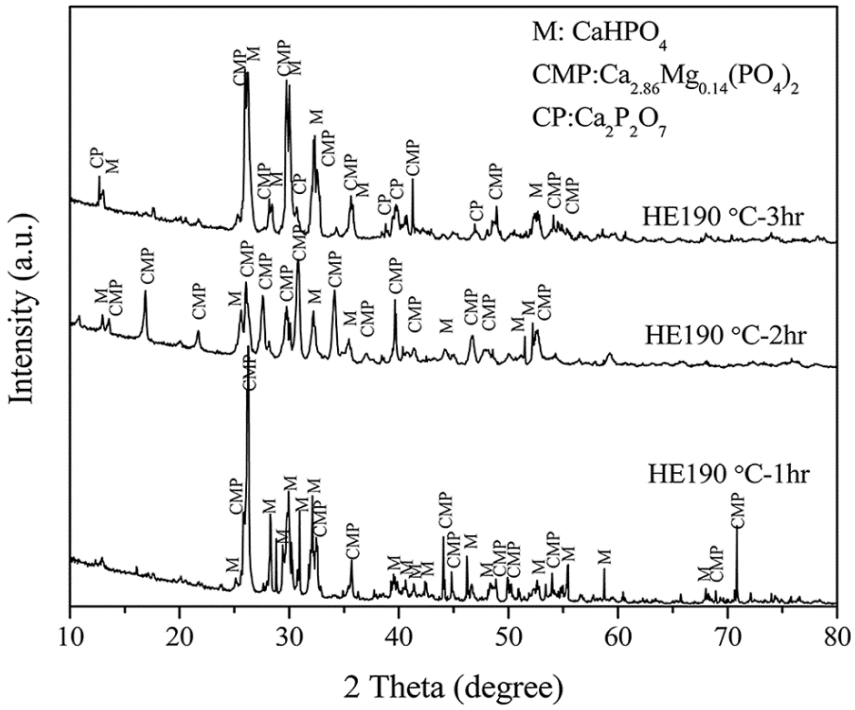


**Figure 4-4. X-ray diffraction pattern of coated samples at 190 °C for different deposition time**

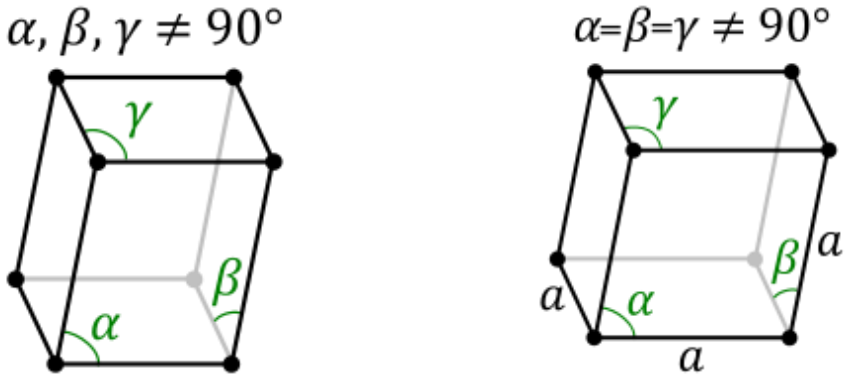


(a) (b)

**Figure 4-5. Schematic of crystal structure of: a) monetite phase and b) whitlockite phase**

The FTIR spectra for Ca-P coating layers deposited at different temperatures, Ca-P coating layers deposited at 190 ºC for different deposition times and FTIR spectra for Ca-P coating deposited on different Mg substrates are given in Fig.4-6 to Fig.4-8

respectively. They show all the vibration bands corresponding to P-O stretching, P-O(H) stretching, O-P-O(H) and O-P-O in the range of 400-1400 $cm^{-1}$. These bands are characteristics for monetite structure [148, 149]. The peaks at 960 $cm^{-1}$ and 1087 $cm^{-1}$ were assigned to P-O-P band in calcium pyrophosphate structure [150]. The peaks at 443 $cm^{-1}$, 548 $cm^{-1}$, 605 $cm^{-1}$ and 1127 $cm^{-1}$ represent the vibrational band of $PO_4^{3-}$ in tricalcium phosphate structure. The observed bands were in general agreement with the literature [151, 152]. The vibrational bands are summarized in Table 4-1. These results agree well with analysis obtained from X-ray diffraction data, which confirmed the formation of monetite and tricalcium phosphate phases under acidic conditions during hydrothermal process.

The chemical composition of deposited Ca-P coating on different Mg substrates was similar and composed of monetite phase which was confirmed by FTIR analysis (Fig.4-8). This is confirmed that for different Mg alloy substrates deposition of Ca-P was mainly controlled by deposition temperature and deposition solution's pH. Therefore, the rest of the project was carried out on AZ31 substrate.

**Table 4-1. FTIR bands for the Ca-P coatings**

| Wave number ($cm^{-1}$) | Assignment | Structure |
|---|---|---|
| 421 | O-P-O | Monetite |
| 528 | P-O bending mode | Monetite |
| 577 | O-P-O(H) | Monetite |
| 888 | P-O(H) stretching | Monetite |
| 992 | P-O stretching | Monetite |
| 1016 | P-O | Monetite |
| 1065 | P-O stretching | Monetite |
| 1131 | P-O stretching | Monetite |
| 1392 | P-O-H in plane bending | Monetite |
| 960 | ν P-O-P asymmetric | Calcium pyro phosphate |
| 1087 | ν P-O-P asymmetric | Calcium pyro phosphate |
| 433 | $PO4^{3-}$ | Tricalcium phosphate |
| 553 | $PO4^{3-}$ | Tricalcium phosphate |
| 605 | $PO4^{3-}$ | Tricalcium phosphate |
| 1127 | $PO4^{3-}$ | Tricalcium phosphate |

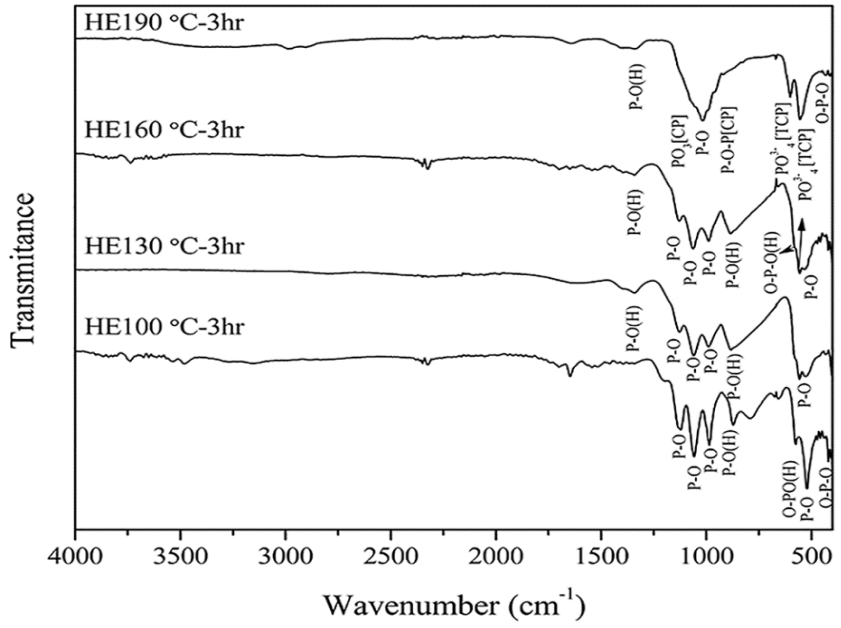


**Figure 4-6. FTIR spectra for coating deposited at different deposition temperature**

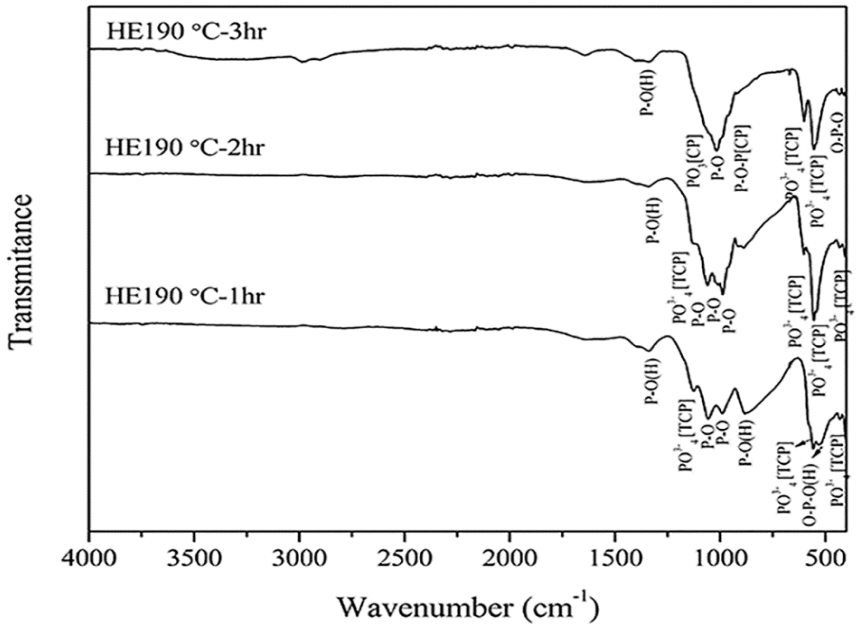


**Figure 4-7. FTIR spectra for coating deposited at 190 ºC for different deposition time**

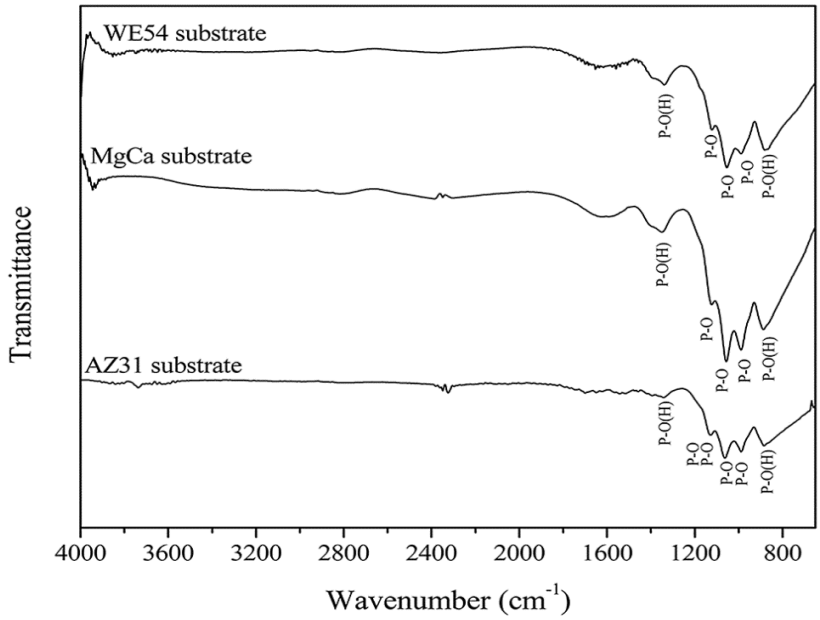


**Figure 4-8. FTIR spectrum of deposited Ca-P layer on different Mg alloy substrate**

#### 4.2.1.2 Surface Morphology Studies of Deposited Coatings

Figure.4-9 shows the morphologies of Ca-P coatings obtained from the hydrothermal process. The coating's morphologies are quite compact, and the crystals clearly show the triclinic structure. The coated sample at 100 ºC deposition temperature clearly showed a two layer coating, the under layer is nodular like and the top layer showed a plate like morphology. By increasing the temperature, the gap size between crystals decreased and the coating became denser. The amount of deposited Ca-P and the size of crystals increased significantly with increase in the deposition temperature. The solubility of Ca-P decreases with increasing temperature, consequently, a higher amount of Ca-P is deposited on the substrate. Additionally, diffusion rate of ions increases by increasing the deposition temperature, hence the reactants move to the substrate more readily accelerating crystal growth to larger dimensions [139]. During the hydrothermal process, the deposition solution (pH: 3.9-4.0) etches the Mg substrate

and forms a rough metal surface as seen on the substrate after removing the coating layer which may act as nucleation sites for Ca-P deposition and growth.

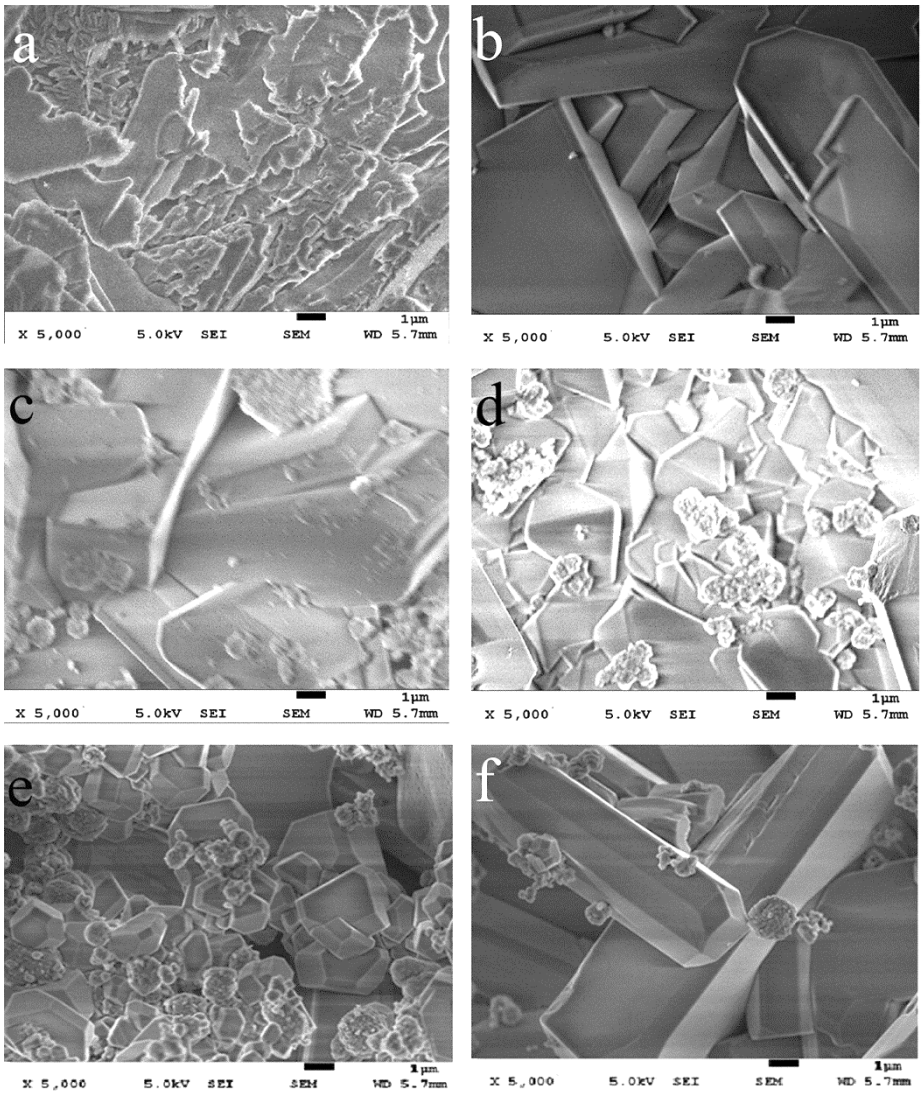


**Figure 4-9. SEM micrographs of coatings: a) HE100 ºC-3hr, b) HE130 ºC-3hr, c) HE160 ºC-3hr, d) HE190 ºC-3hr, e) HE190 ºC-2hr and f) HE190 ºC-1hr**

The semi-quantitative analysis of coating layers obtained from EDS analysis is summarized in Table 4-2. The results showed that Ca to P atomic ratio varied from 0.93 to 1.26 corroborating the findings from the XRD studies.

**Table 4-2. EDS result for Ca-P coated samples**

| Sample | Ca (at. %) | P (at. %) | Ca/P ratio |
|---|---|---|---|
| HE100 °C-3hr | 16.42 | 17.35 | 0.93 |
| HE130 °C-3hr | 17.39 | 16.52 | 1.05 |
| HE160 °C-3hr | 11.98 | 10.7 | 1.11 |
| HE190 °C-3hr | 12.49 | 11 | 1.13 |
| HE190 °C-2hr | 28.35 | 22.45 | 1.26 |
| HE190 °C-1hr | 18.09 | 16.53 | 1.09 |

At the pH lower than 5, biocompatible and biodegradable monetite and calcium pyrophosphate are the most stable phases. However, the presence of Mg ions can stabilize the tricalcium phosphate phase. The stabilizing effect of Mg is attributed to the markedly smaller ionic radius of $Mg^{2+}$ (0.65 Å) compared to $Ca^{2+}$ (0.99 Å) [153-155]. Deposition of Ca-P phases during hydrothermal process might take place according to Eq.4-1 to Eq.4-3 [156, 157]. Based on the phase transformation route in the Ca-P family, the thermodynamic stable phase eventually forms. Transformation of monetite to calcium pyrophosphate most likely occurred by a dissolution- re-precipitation process as indicated by Eq.4-3.

$$\mathbf{Ca^{2+} + HPO_4^{2-} \rightarrow CaHPO_4} \quad \textbf{(4-1)}$$

$$\mathbf{3Ca^{2+} + 2PO_4^{3-} \rightarrow Ca_3(PO_4)_2} \quad \textbf{(4-2)}$$

$$\mathbf{2CaHPO_4 \rightarrow Ca_2P_2O_7 + H_2O} \quad \textbf{(4-3)}$$

When the surface in contact with body fluid is Ca-P, resorption or transformation into the other, more stable Ca-P phase can happen [146]. Monetite with triclinic crystallographic structure has high aqueous solubility around the physiological pH values compared to other Ca-P phases and it can be easily resorbed unlike HA [158, 159]. Moreover, recent studies confirmed that monetite possess good osteoblastic activity and osteoconductivity [160, 161] with a significant dissolution rate which is

able to be rapidly replaced by new bone and also resulted in greater new bone volume formation [162]. Therefore, monetite is a preferred material for resorbable coating on Mg. Since the aim of the Mg surface modification is to delay the degradation of Mg only for a specific period of time until bone healing takes place (around 4-5 months, depending on fracture type) and therefore, an optimum coating solubility is a requirement.

### 4.2.2 Coating Thickness and Adhesion Measurements

The coating thickness was measured by an eddy current probe and was checked with the cross sectioning method which is shown in Fig.4-10. The result showed that deposition temperature had significant effect on the coating thickness. The coating thickness increased slightly from 20 µm at 100 ºC deposition temperature to around 61 µm at 160 ºC, which was followed by a sharp increase to 400 µm at 190 ºC.

The coating adhesion to substrate was measured by the pull-off test. During the pull-off test no delamination was observed for coating layers as it is clear from Fig.4-11.a. The SEM micrograph of coating (Fig.4-11.b) after pull-off test clearly showed that coating still remained on the substrate for all samples without exposing any magnesium, confirming cohesive failure. This cohesive failure confirmed that adhesion strength of the coating to the AZ31 substrate was higher than the cohesion strength between the Ca-P crystals [163].

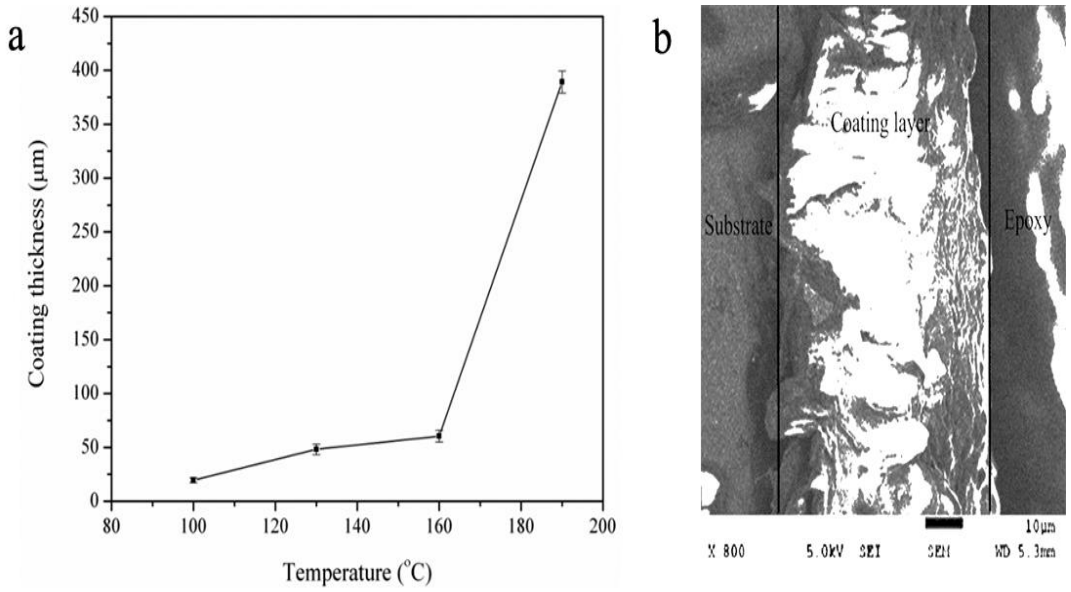


**Figure 4-10. a) Coating thickness variation with deposition temperature and b) Coating thicknes measurment with cross sectioning method for HE160 ºC-3hr coating**

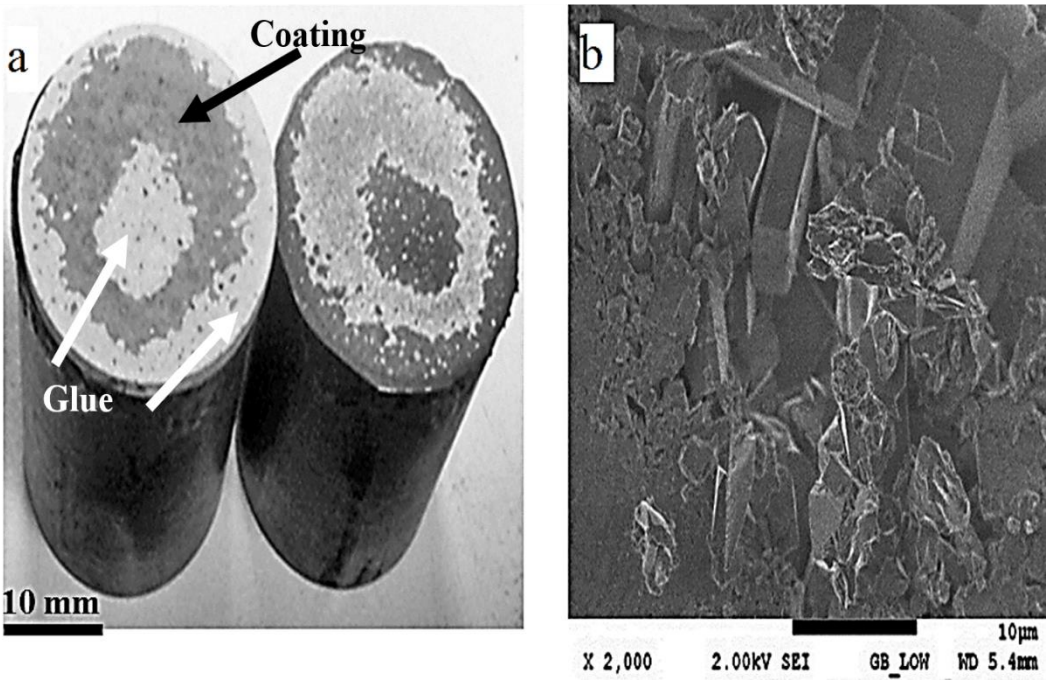


**Figure 4-11. a) Photograph of coated sample surface and b) SEM micrograph of coated sample surface after adhesion test**

The stress-displacement curves obtained from a pull-out adhesion test is shown in Fig.4-12. For the samples treated at 100 ºC, 130 ºC and 160 ºC, the coatings failed by cohesive failure between 5.2 to 5.8 MPa. Further increasing the deposition temperature to 190 ºC, the coated sample failed at 3.1 MPa. The lower failure stress may be due to the increase in coating thickness and possibly higher residual stress in the coating layer. Alternatively, changes in the coating composition could have contributed to the lower strength.

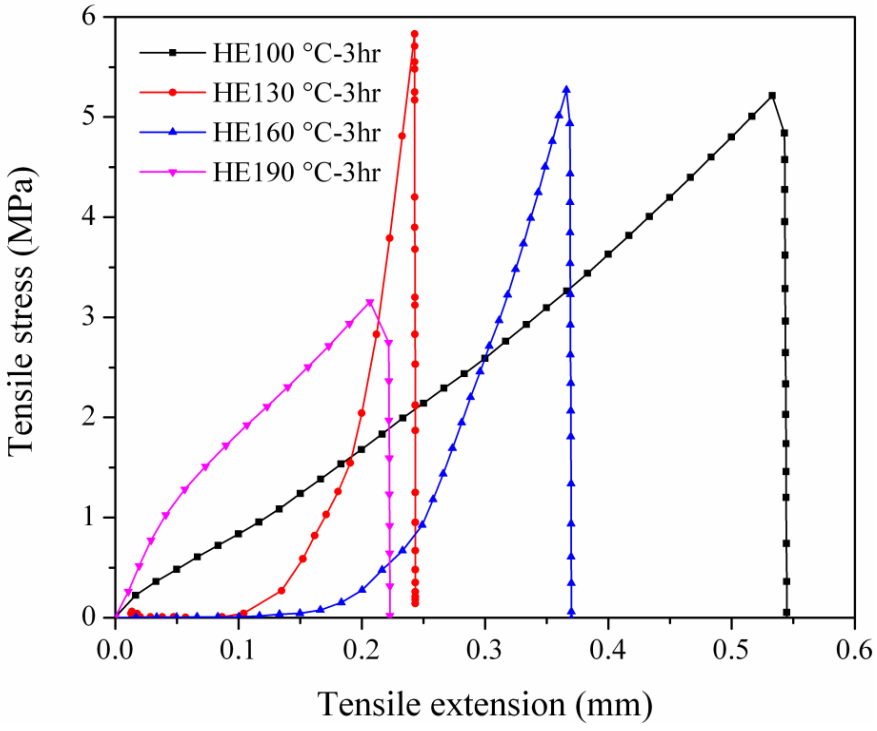


**Figure 4-12. The stress-displacement curves obtained from pull-out adhesion test**

The data measured from the pull-off test present the stiffness (based on the slope of the loading part of the curves) and separation force of the samples. The same substrate and glue were used for all the experiments. The stiffness indicated in the plot is the stiffness of the whole assembly (substrate, glue, coating, perhaps even the grip). The

relatively large extension before the failure suggests that the whole assembly is elongated and consequently, the observed stiffness is primarily determined by the parts other than the coating. Thus, it is not possible to derive reliable data on the coating modulus or stiffness from this experiment. The coating modulus was measured by nano-indentation.

## 4.3 Deposition of Novel Ca-P/Polymer Composite Coatings

The main issue for Ca-P coatings is their brittleness, potentially leading to early failure of the bone-implant interface. Composite coatings can be an ideal approach to overcome this issue and they can be formed by a combination of Ca-P as inorganic part and bioresorbable polymers as organic component [103, 110-116]. Apart from mechanical properties consideration, cell proliferation and cell attachment to the implant material is another aspect to be considered. Human bone is a composite of Ca-P and collagen. From the viewpoint of bionics, if the composition and structure of implant are similar to the human bone, it will be favorable for cells to adhere to and proliferate to form bone tissue [112, 115, 117, 118].

According to the literatures, biologically active composite coatings with a combination of ceramic and polymeric materials are generally developed in multistep processes [68, 109, 121, 122, 140]. However, the complexity of the coating preparation usually reduces their practical usefulness. Therefore, there is a clear need to deposit high performance composite coatings in one step.

### 4.3.1 Structure and Chemical Composition of Coatings

In order to address the current issues of coating deposition complexity and adjustment of coating mechanical properties, novel biodegradable composite coatings consisting

of Ca-P with either PAA or SCMS polymers were prepared in a single step by means of hydrothermal deposition process, reported here for the first time.

PAA and SCMS have been used due to their biocompatibility and biodegradability. The use of these polymers have a successful history [164-167]. The availability and reactivity of PAA surface carboxylic groups for the covalent bonding of molecules that are able to promote the osseointegration is another reason for their wide use [164, 165]. Likewise, SCMS have been used due to its high chemical stability, non-toxic nature, hydrophilicity, biocompatibility, and biodegradability [168]. Fig.4-13 shows a photograph of hydrothermally deposited composite coatings (temperature: 160 °C duration: 3 hours, polymer concentration 0.2 wt. %) which confirmed the successful deposition of uniform and compact composite coating by hydrothermal process.

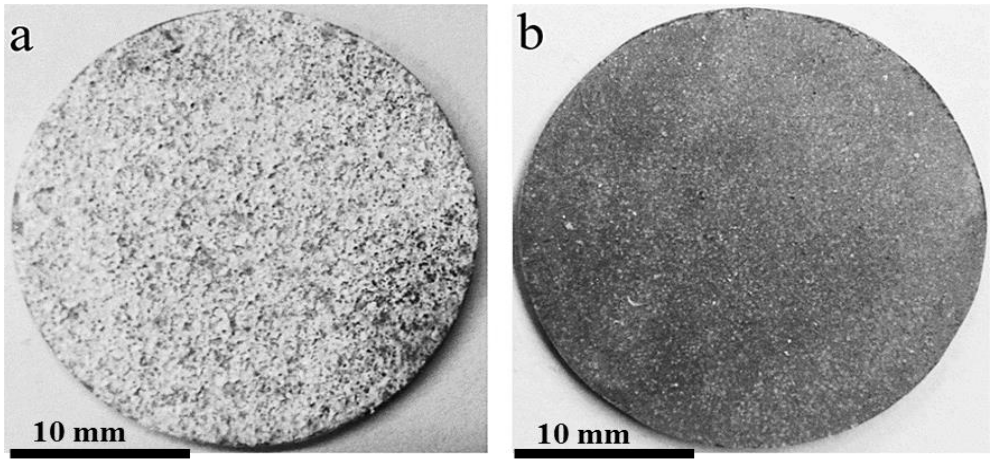


**Figure 4-13. Photographs of hydrothermally deposited composite coatings: a) HEPAA(0.2%) and b) HESCMS(0.2%)**

#### 4.3.1.1 XRD and FTIR Studies of Composite Coatings

The XRD patterns of HEPAA and HESCMS composite coatings are given in Fig.4-14 and Fig.4-15 respectively which includes the XRD pattern of a Ca-P inorganic coating as a reference. The inorganic coating shows diffraction peaks with minimal line broadening and high intensity relating to the crystalline phase. The inorganic coating is mainly composed of a monetite phase. Incorporation of PAA in the coating structure caused the peaks to become wider and peak intensities to decrease significantly. Moreover, a second crystalline phase, tricalcium phosphate, appeared along with monetite. These results showed that incorporation of PAA in the coating changed the phase formation route during the hydrothermal process. By increasing the PAA concentration, the signal strength of tricalcium phosphate phase increased in the coating while the XRD peak intensities related to monetite phases decreased.

For the HESCMS composite coatings (Fig.4-15) the main phase remained as monetite even with an increasing polymer concentration but an incorporation of SCMS in the coating caused the diffraction peaks to become wider with reduced peak intensities compared to the inorganic coating. A further increase in SCMS concentration to 0.5 wt.% and 0.6 wt.%, the intensity of tricalcium phosphate phase, started to increase in the coating structure.

For the HESCMS coatings, the intensities of the diffraction peaks corresponding to the (112) and (200) planes of monetite phase decreased significantly suggesting that SCMS interacts and adsorbs on these planes resulting in reduction of crystallinity. SCMS adsorption on these planes can act as a barrier and therefore decreases diffusion of $Ca^{2+}$ ions and reduces its incorporation into the crystals, thus inhibiting crystal growth. The morphological change due to adsorption of polymer on crystalline plane had been observed and reported for other Ca-P phase as well [169].

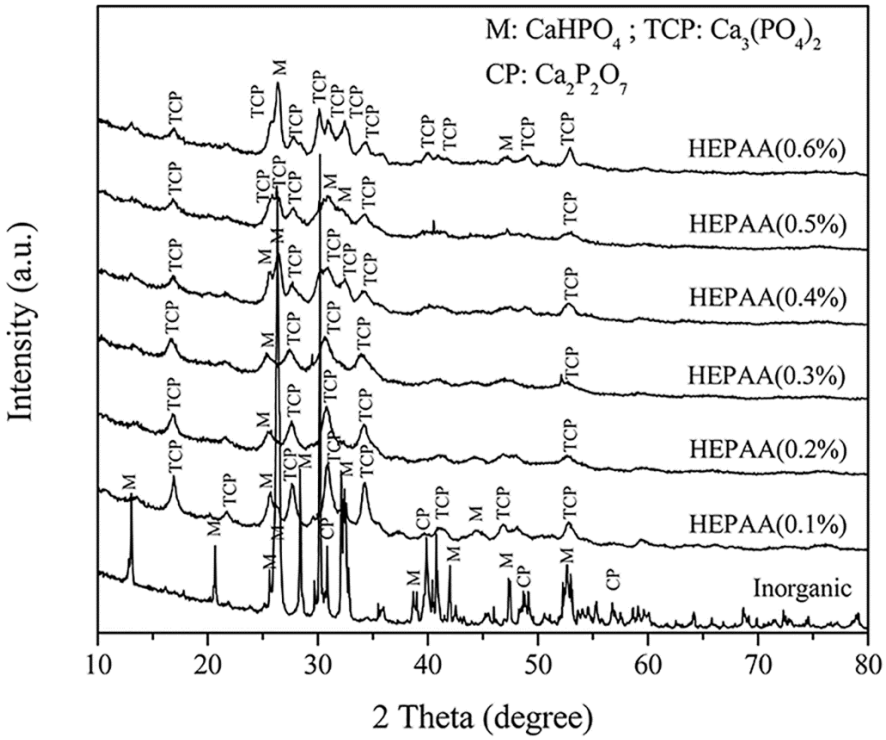


**Figure 4-14. XRD pattern of HEPAA composite coatings**

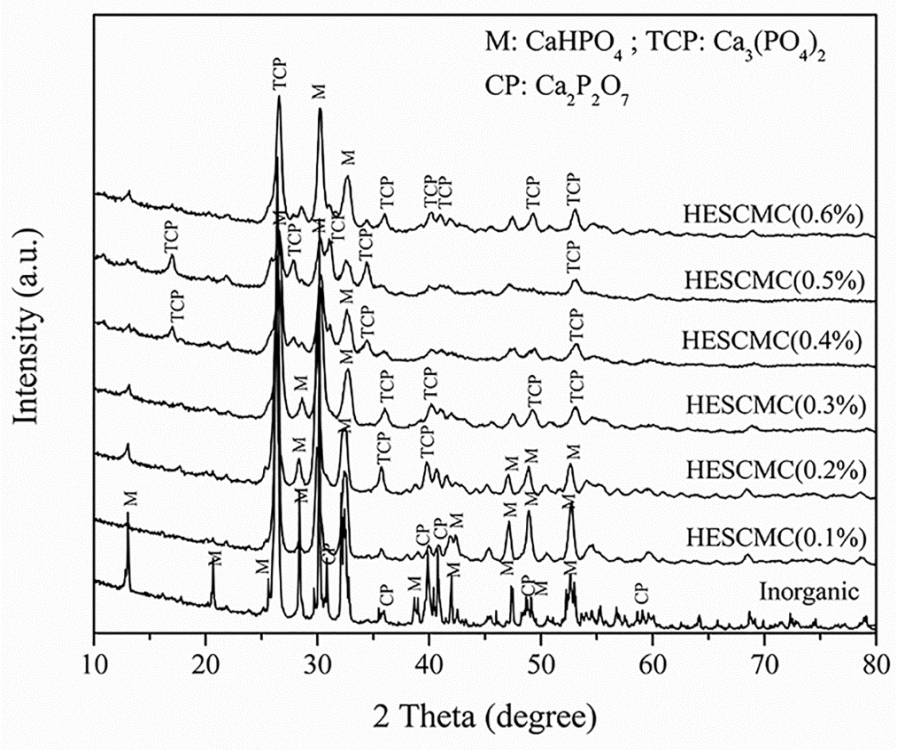


**Figure 4-15. XRD pattern of HESCMS composite coatings**

The FTIR spectra of HEPAA and HESCMS composite coatings are given in Fig.4-16 and Fig.4-17 respectively. They show all the vibration bands corresponding to P-O stretching, P-O(H) stretching, O-P-O(H) and O-P-O in the range of 400-1400 $cm^{-1}$. These bands are characteristic for monetite structure [148, 149]. The peaks at 443 $cm^{-1}$, 548 $cm^{-1}$, 605 $cm^{-1}$ and 1127 $cm^{-1}$ represent the vibrational band of $PO_4^{3-}$ in tricalcium phosphate structure. The observed bands were in general agreement with literature reports [151, 152]. Apart from the vibrational bands related to the monetite and tricalcium phosphate phases, extra vibrational bands appeared in the composite coatings spectra related to the $CH_2$, CH-CO and COOH and $COO^-$ groups which confirmed the co-deposition of Ca-P and polymers and formation of composite coating during the hydrothermal process. By increasing the polymer concentration in the deposition bath, the peak intensities related to $CH_2$, CH-CO and COOH and $COO^-$ also increased, which is in agreement with analysis obtained from X-ray diffraction data.

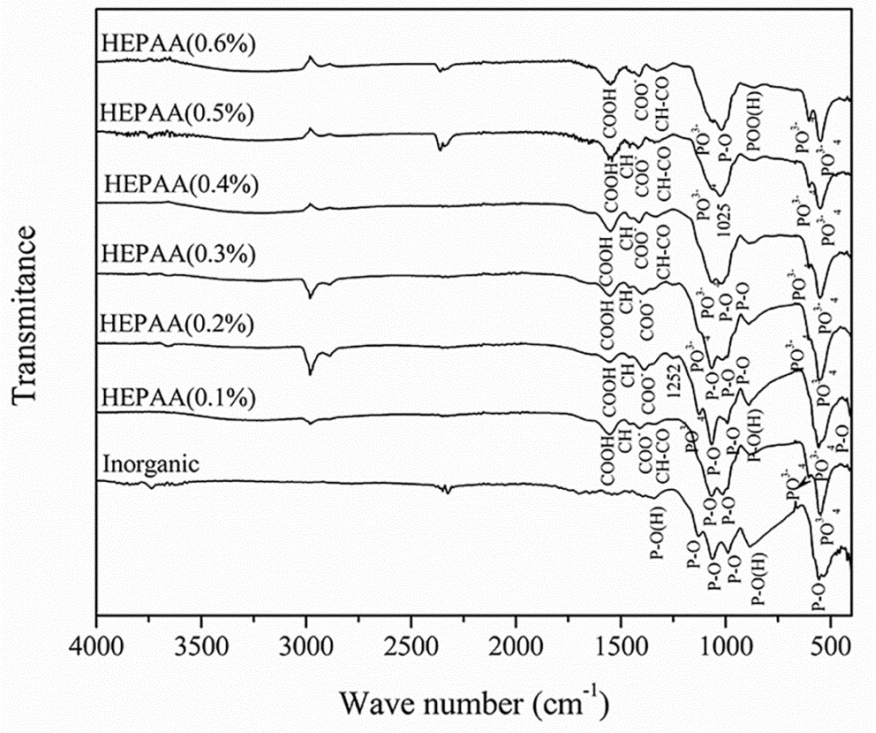


**Figure 4-16. FTIR spectrum of HEPAA composite coatings**

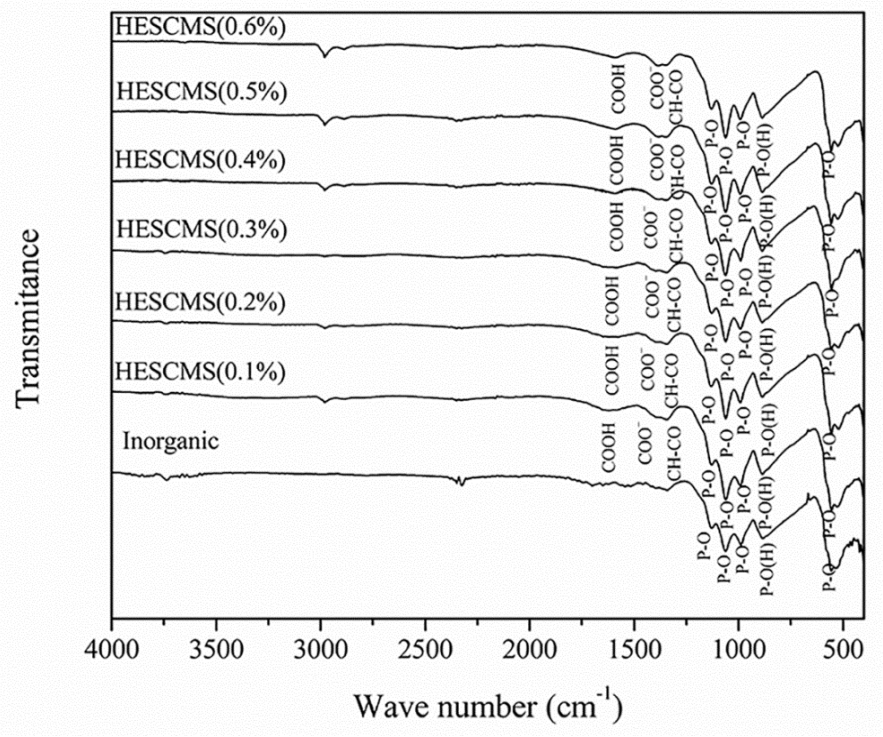


**Figure 4-17. FTIR spectrum of HESCMS composite coatings**

#### 4.3.1.2 Surface Morphology Studies of Composite Coatings

SEM micrographs of HEPAA and HESCMS composite coatings are depicted in Fig.4-18 and Fig.4-19 respectively. The crystals of the inorganic coating were fairly well developed, while the crystals in the HEPAA composite coating were significantly modified in appearance, showing a nodular morphology. Granule-shape Ca-P was formed at the surface of the Mg substrate which is a typical result of the strong interaction between the carboxyl ($COO^-$) acid groups and $Ca^{2+}$ [170] due to the chelation of $Ca^{2+}$ ions and a decrease in their diffusion rate caused by electrostatic interaction between $Ca^{2+}$ and $COO^-$ functional groups. The formation of the chelate structure of $COO^-$ groups and $Ca^{2+}$ ions decreases the activation energy for Ca-P nucleation due to an increase in the local super saturation level. Similar nodular

morphology is also reported for $CaCO_3$ in the presence of poly(methacrylic acid) (PMAA) [170].

Incorporation of SCMS in the coating mainly affects the crystal size, unlike in the case of PAA addition which also changed the morphology. Adsorption of SCMS on (112) and (200) planes suppresses the crystal growth. By increasing the SCMS concentration sufficiently, signs of nodular morphology appeared in the HESCMS coating as well, probably due to the increase of $COO^-$ functional group concentration. The difference in coating morphology in the presence of PAA and SCMS polymers could be resulted from significantly higher concentration of $COO^-$ functional group in PAA structure as compared to SCMS. The results showed that SCMS acts as a crystal habit modifier for crystal growth and it was found that the critical amount of SCMS needed to change the crystal phase from monetite to tricalcium phosphate is higher compared to PAA.

It is reported that formation of crystalline phases are affected by the degree of super saturation in the Ca-P system. The crystalline phases of Ca-P could be changed, depending on the functional groups present in the deposition system because functional groups might change the degree of super saturation required for nucleation [29, 170]. $COO^-$ is the functional group in PAA structure which is negatively charged and attracts $Ca^{2+}$. Chelate formation between $Ca^{2+}$ and $COO^-$ functional groups induces heterogeneous nucleation and increases the local concentration of $Ca^{2+}$ which can provide local super saturation and accelerate the formation of tricalcium phosphate phase [169].

The higher concentration of tricalcium phosphate in the HEPAA coatings compared to the HESCMS coatings correlates with the presence of higher concentration of $COO^-$ functional group in the PAA structure compared to the SCMS polymer. According to the PAA and SCMS chemical structure, the $COO^-$ concentration in PAA is around 62% while it is only around 18% for the SCMS. The coating process involves cross linking

of $COO^-$ groups in PAA and SCMS structure by the $Ca^{2+}$ ions and co-deposition of Ca-P and polymer [170]. It is well known that if a polymer lowers the interface energy of a specific polymorph (and the interface energy is lowered already below the critical surface coverage), it is this polymorph which is specifically nucleated. This concept is consistent with the recent finding that $COO^-$ containing copolymers were able to initiate the vaterite nucleation from stable supersaturated solutions through binding of the $Ca^{2+}$ ions at the ionized $COO^-$ groups [170]. It appears that the formation of chelate structure of $COO^-$ groups and $Ca^{2+}$ decreases the activation energy for tricalcium phosphate nucleation. The change in the crystalline phase of the Ca-P in the presence of functional groups is reported in literature. Yokoi et al. [171] reported that octacalcium phosphate was changed to HA in the presence of $COO^-$ groups in the solution due to a decrease in the activation energy of Ca-P formation by presence of a chelate structure involving $Ca^{2+}$and $COO^-$ groups.

Organic molecules can act as “templates”, accelerating the nucleation and controlling the crystal growth and morphology via providing preferential sites for nucleation and determining the orientation of the resulting crystals. The organic macromolecule behaves as foreign surface and accelerates the nucleation. Acceleration of nucleation is ascribed to reduced interfacial energy between a crystal nuclei and the foreign substrate compared to the interfacial energy between crystal nuclei and solution. Additionally, the organic material provides a set of chemical functionalities that promotes strong bonding to the nucleus, the enthalpy contribution to the interfacial free energy becomes small and nucleation occurs preferentially on the corresponding crystal plane [169, 171].

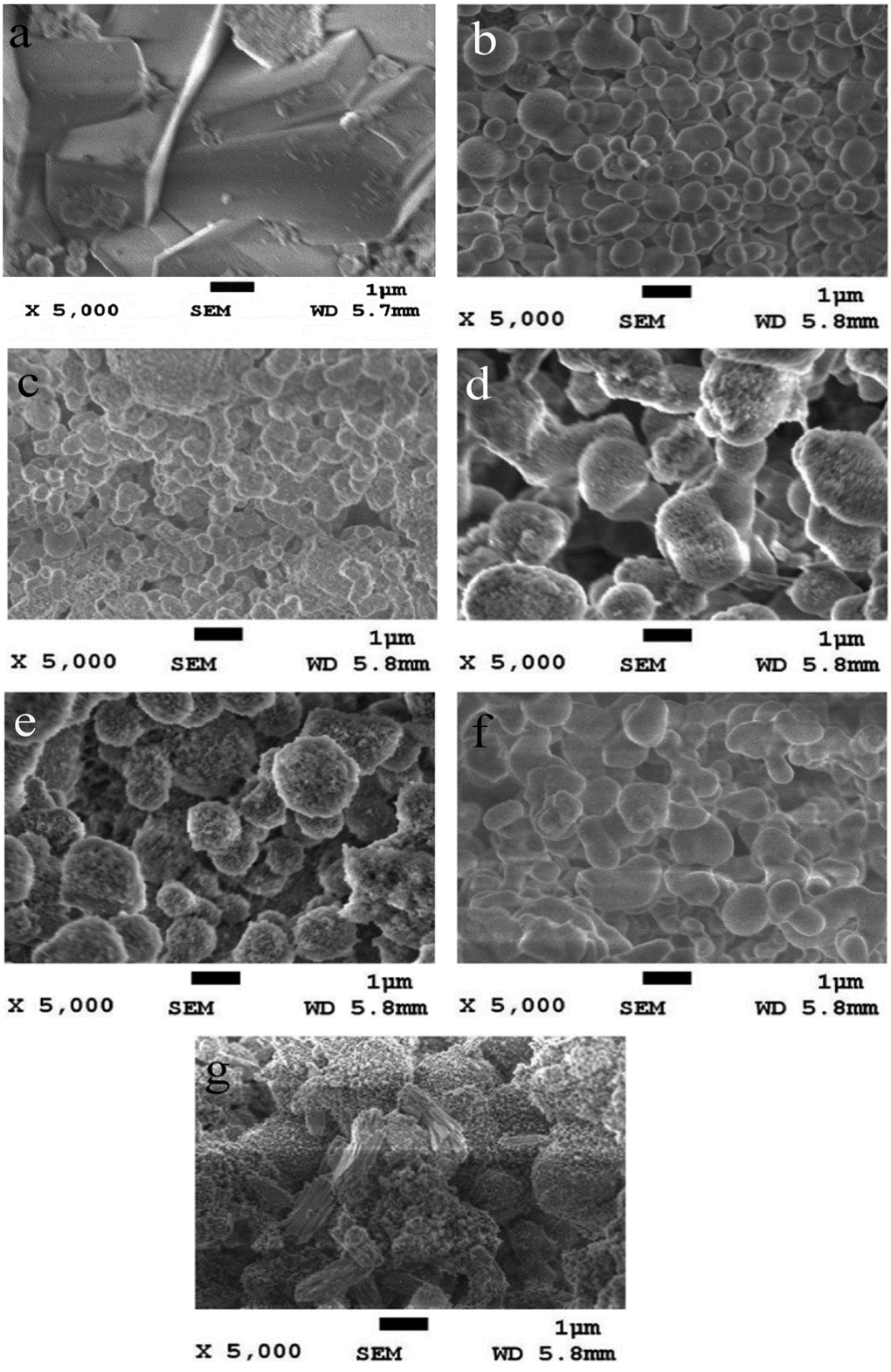


**Figure 4-18. SEM micrographs: a) inorganic coating, b) HEPAA(0.1%), c) HEPAA(0.2%), d) HEPAA(0.3%), e) HEPAA(0.4%), f) HEPAA(0.5%) and g) HEPAA(0.6%)**

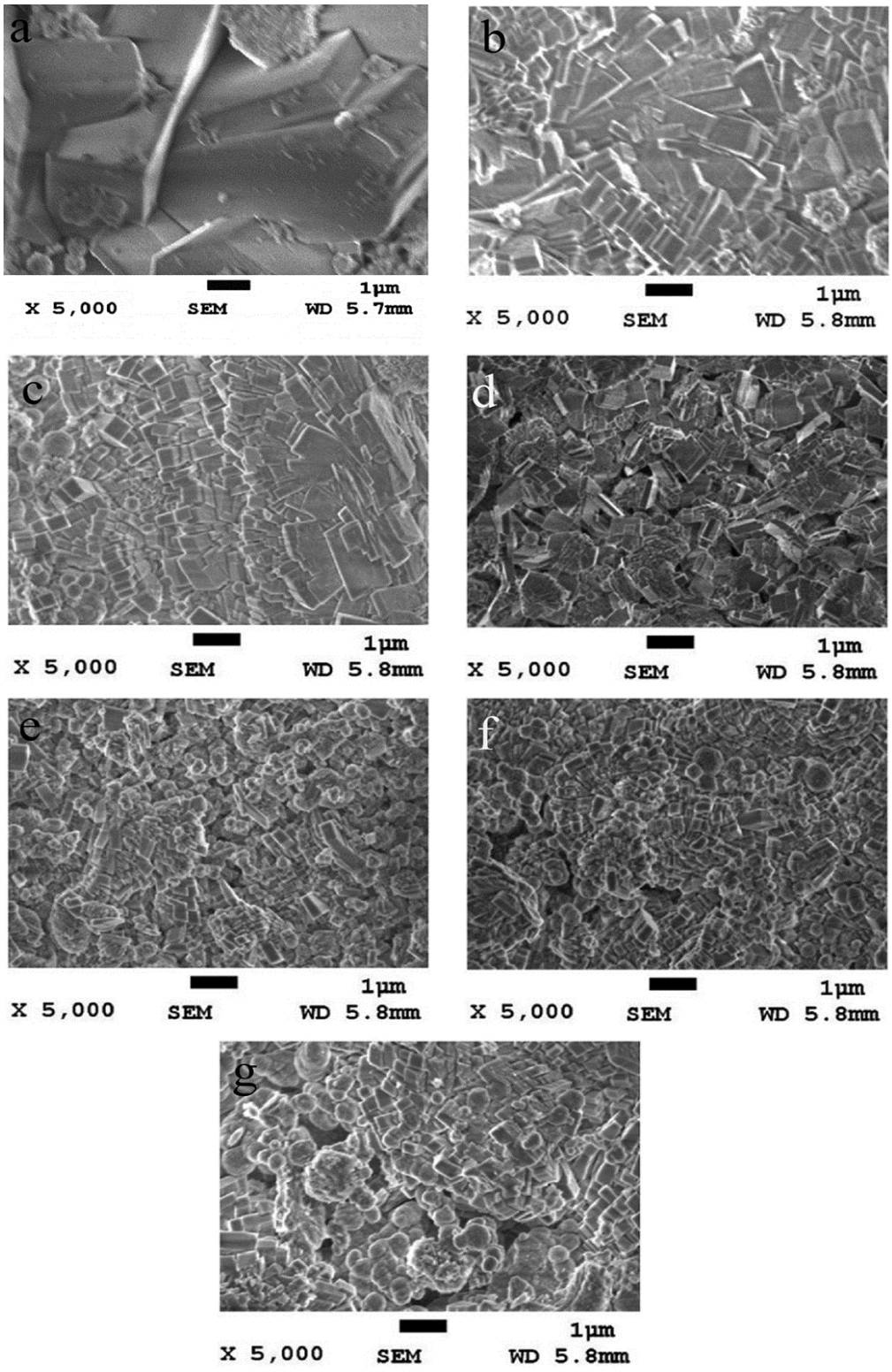


**Figure 4-19. SEM micrographs: a) inorganic coating, b) HESCMS(0.1%), c) HESCMS(0.2%), d) HESCMS(0.3%), e) HESCMS(0.4%), f) HESCMS(0.5%) and g) HESCMS(0.6%)**

### 4.3.2 Thermogravimetric Analysis of Composite Coatings

The amount of polymers incorporated into the coating structures were measured by the TGA technique and inorganic coating was used as the reference. TGA results of HEPAA and HESCMS composite coatings are given in Fig.4-20 and Fig.4-21 respectively.

The total mass loss for inorganic coating in the range of 30- 900˚C was 9.4 wt.%; while it was 15.8 wt.% for the HEPAA(0.1%), and reached to 40.1 wt.% for the HEPAA(0.6%). Therefore, the PAA loading in the HEPAA composite coatings was between 6.87 wt.% to 33.81 wt.%. In the case of HESCMS composite coatings, the SCMS loading in the HESCMS composite coating was between 3.44 wt.% to 9.94 wt.%. The higher weight losses of composite coatings compared to the inorganic coating were attributed to polymer degradation.

According to literature, thermal degradation of PAA commences with a dehydration reaction occurring by intramolecular cyclisation of adjacent monomer units (below 120 ºC) to give six-member anhydride ring structures. Next, decarboxylation proceeds to give carbon dioxide product at about 250 ºC and both water and carbon dioxide continue to evolve on heating up to 500 ºC. A number of other volatile products, including monomers, are formed but only in trace amounts. Above 350 °C, the polymer residue mainly decomposes, which consists of short chain fragments derived from two or more original repeat units. These may contain only anhydride rings or both rings and carboxylic acid structures [172].

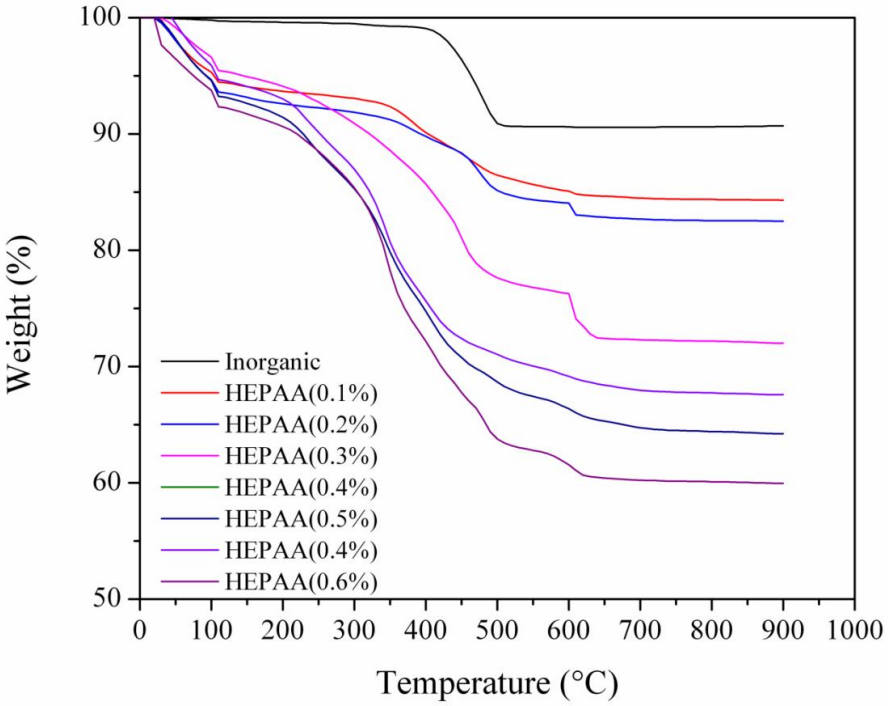


**Figure 4-20. TGA results for the HEPAA composite coatings**

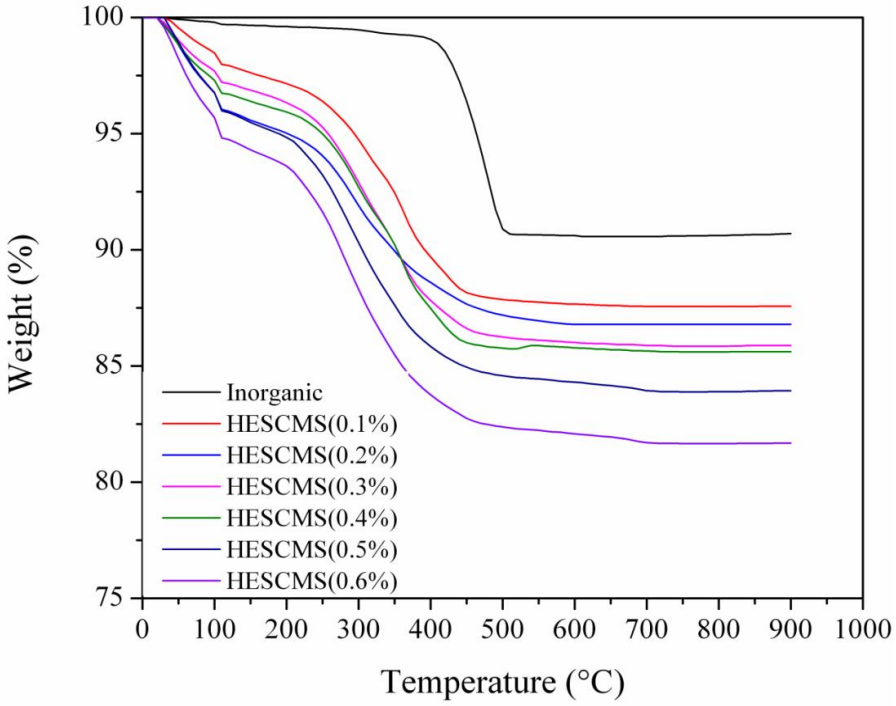


**Figure 4-21. TGA results for the HESCMS composite coatings**

In the case of SCMS, decomposition of SCMC starts (up to 150 ºC), with vaporization of the hydrated water which is bound in the internal surface area of the super molecular cellulosic structure. This is followed by weight loss above 150 ºC which could be attributed to breaking the bond associated with the functional groups along the polymer chain and weak groups within the chain [173].

## 4.4 Summary

Ca-P coatings were successfully deposited on AZ31 substrate by using hydrothermal method at different deposition temperatures (from 100 ºC to 190 ºC). By increasing the temperature and deposition time, coating compositions were changed to some extent. Lower process temperatures favored the formation of resorbable monetite together with some whitlockite, while high temperature promoted the deposition of some calcium pyrophosphate as well. The coating thickness was found to increase with deposition temperature significantly, and in a non-linear manner. Higher temperature promoted the growth of much thicker layers (at 190 °C).

On the other hand, novel Ca-P/Polymer composite coatings were successfully deposited on AZ31 substrate by a hydrothermal process for the first time. Inclusion of biocompatible PAA and SCMC polymers in the deposition solution resulted in the co-deposition of Ca-P crystalline phases and polymer molecules. The polymer molecules strongly modulated the morphology of the crystals. SCMC with low carboxylate group content reduced the Ca-P crystal size while PAA with high carboxylate content or high SCMC concentration resulted in the growth of nodular structures allowing the adjustment of surface morphology that is known to be an important factor in cell attachment and cell proliferation on surfaces.

# Chapter 5

# Deposition Mechanism of Hydrothermally Deposited Coatings

## 5.1 Introduction

As explained in Chapter 4, the hydrothermal process is a useful method for deposition of uniform inorganic Ca-P and Ca-P/Polymer composite coatings on the AZ31 substrate. Since the deposition mechanism determines the coating properties to a considerable extent, therefore the aim of this chapter is to present a thorough understanding of the deposition mechanism of inorganic and composite coatings on the AZ31 substrate during hydrothermal process by means of comparing deposition under different conditions. For comparison purposes and understanding the effect of substrate on deposition mechanism, Ca-P coating was also deposited on Ti, SS and Zn substrates at 160 ºC for 3 hours.

## 5.2 Deposition Mechanism of Inorganic Ca-P Coatings

### 5.2.1 Structure and Chemical Composition of Coatings

The hydrothermal process is a useful method for the deposition of the Ca-P and Ca-P /Polymer composite coatings on AZ31 substrate [174] as explained in Chapter 4, and other metallic substrates [139] which resulted from the solutions' supersaturation.

The XRD patterns of Ca-P coating layers deposited on different substrates is shown in Fig.5-1. XRD analysis shows that coated materials obtained from the hydrothermal process on AZ31 substrate are predominantly a mixture of monetite and whitlockite and the as-deposited coatings on SS and Zn substrates are pure monetite phase.

The morphologies of the coatings deposited on different substrates (at 160 ºC for 3 hours) are shown in Fig.5-2. Coatings were only found on AZ31, Zn, and partially on SS substrates. In the case of SS, the coating appeared to be visibly discontinuous. No coating was found on Ti substrates.

Coatings are deposited uniformly on AZ31 substrate and Zn substrates. However, in the case of the SS substrate, some parts of the substrate were not covered by the coating. For the Ti substrate, Ca-P crystals only deposited as separate islands on some parts of the metal surface, and the coating deposition was not successful in agreement with a study reported in the literature [175]. This confirmed that the substrate's chemistry plays an important role in successful deposition of Ca-P coatings.

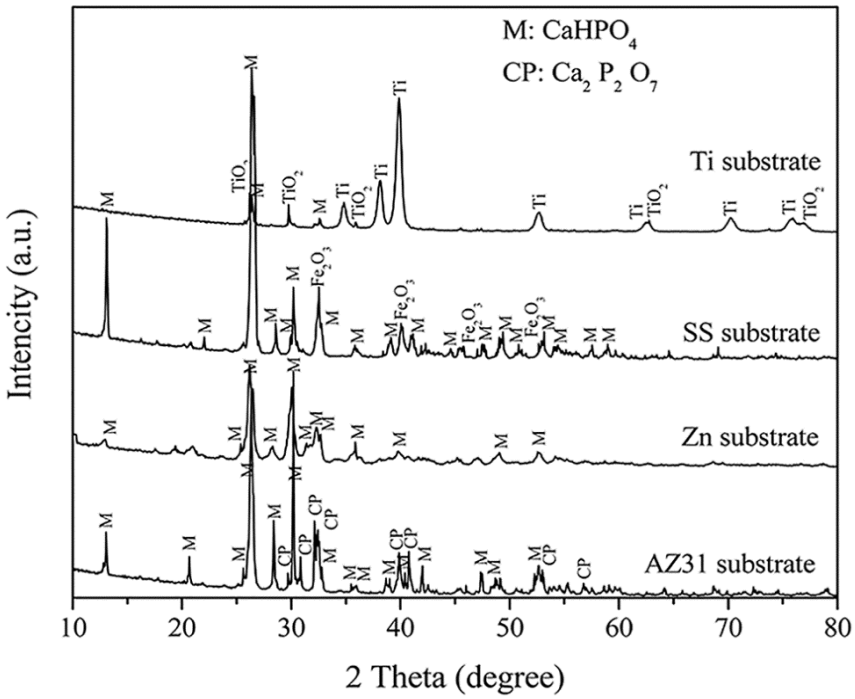


**Figure 5-1. XRD comparison of deposited coating on different substrates at 160 °C**

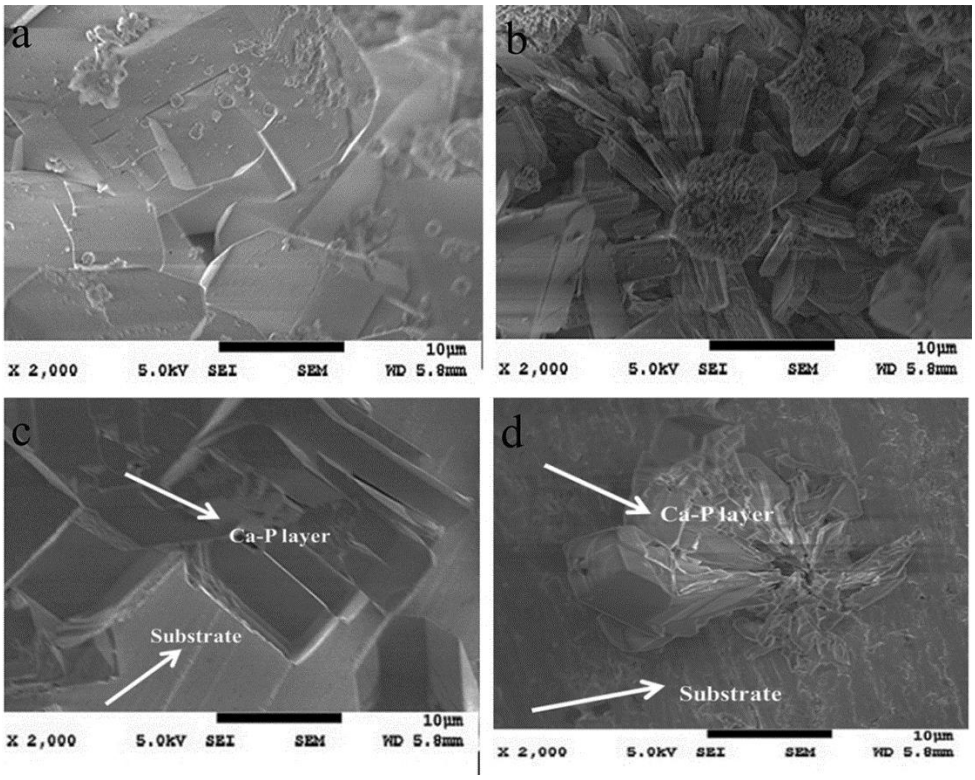


**Figure 5-2. SEM micrographs of coating on different substrates: a) AZ31 substrate, b) Zn substrate, c) SS substrate and d) Ti substrate**

### 5.2.2 Nature of Deposited Layers and Proposed Deposition Mechanism

In order to understand the deposition mechanism of Ca-P, Raman spectroscopy studies were conducted through the coating cross section for Ca-P layers deposited at different temperatures on AZ31 substrate, as well as deposited Ca-P layers on Zn and SS substrates. In the case of AZ31 substrate, the Raman spectroscopy results for deposition temperatures from 100-160 ºC were similar (deposited coatings at 190 ºC showed different deposition mechanism which will be discussed separately in the next section). Therefore, only one Raman spectroscopy mapping analysis is reported through the cross section by selecting the sample coated at 160 ºC as given in Fig.5-3. Deposition of Ca-P on the Zn substrate showed the same mechanism as on AZ31 substrate as shown in Fig.5-4. However, the coating layer was thinner compared to the

coating layer deposited on AZ31 substrate (approximately 50 µm for the Zn substrate and 60 µm for the AZ31 substrate). This may be resulted from less reactivity of Zn substrate compare to AZ31 substrate, which affects the corrosion rate of substrate and subsequently pH change close to the substrate.

Based on the cross section studies noted that the coatings are composed of two different layers, which can be distinguished through their main corresponding Raman peaks. The layer adjacent to the AZ31 (or Zn) substrate contains predominantly tricalcium phosphate or to be more precise whitlockite phase with the main Raman peak at 970 $cm^{-1}$. This layer started to deposit on the AZ31 substrate at the early stages of coating formation. This was followed by the deposition of a second layer mainly consisting of monetite phase with the main Raman peak at 987 $cm^{-1}$.

Increasing distance from the AZ31 substrate indicated decrease in the peak intensity related to tricalcium phosphate while the intensity of monetite phase increased. The observed Raman peaks are summarized in Table-5-1. There were some small differences (shift in the range of 1-2 $cm^{-1}$) in the positions of the observed bands found in the coating and reported in the literature. This finding could be attributed to the partial substitution of $Ca^{2+}$ by $Mg^{2+}$ in the tricalcium phosphate structure.

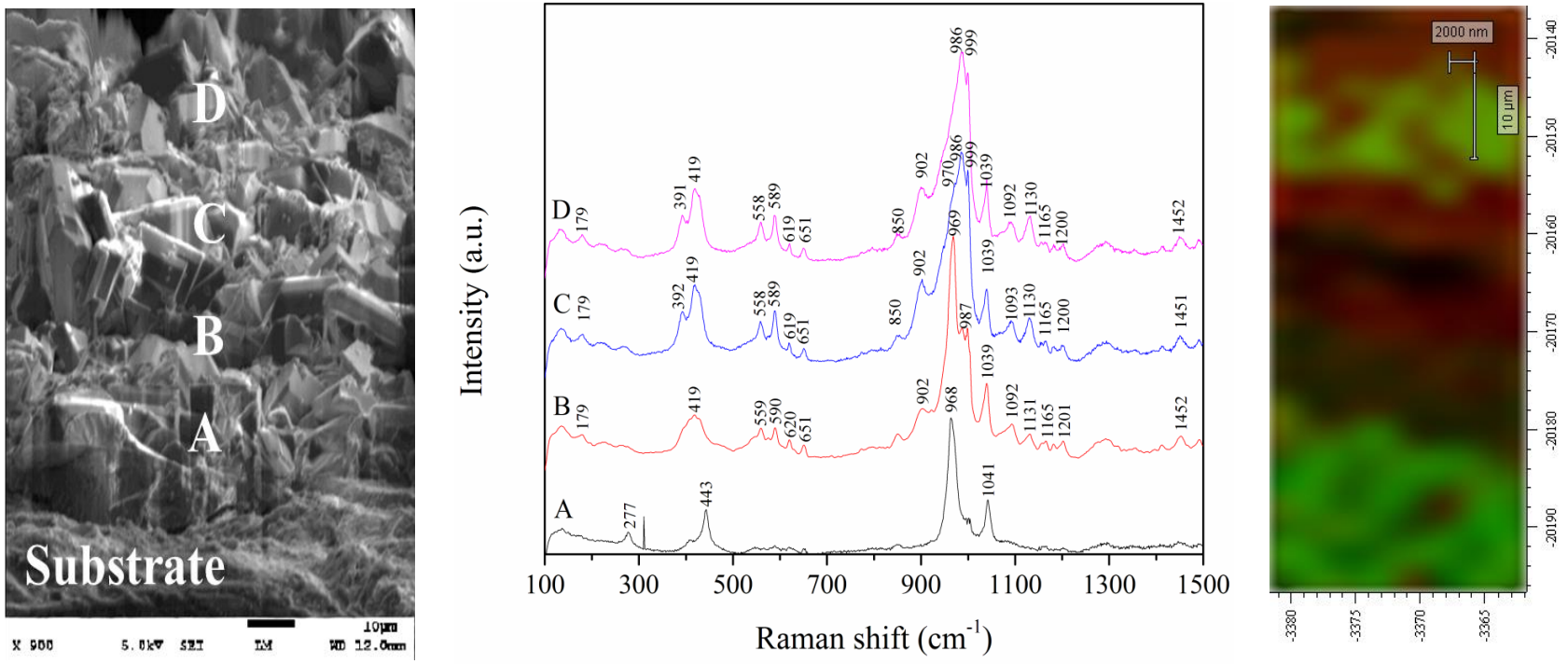


a b c

Red color represents the monetite phase ; Green color represents the tricalcium phosphate phase

**Figure 5-3. a) SEM cross section, b) Raman pattern through the cross section, c) Raman map review through the cross section on AZ31 substrate (T:160 °C)**

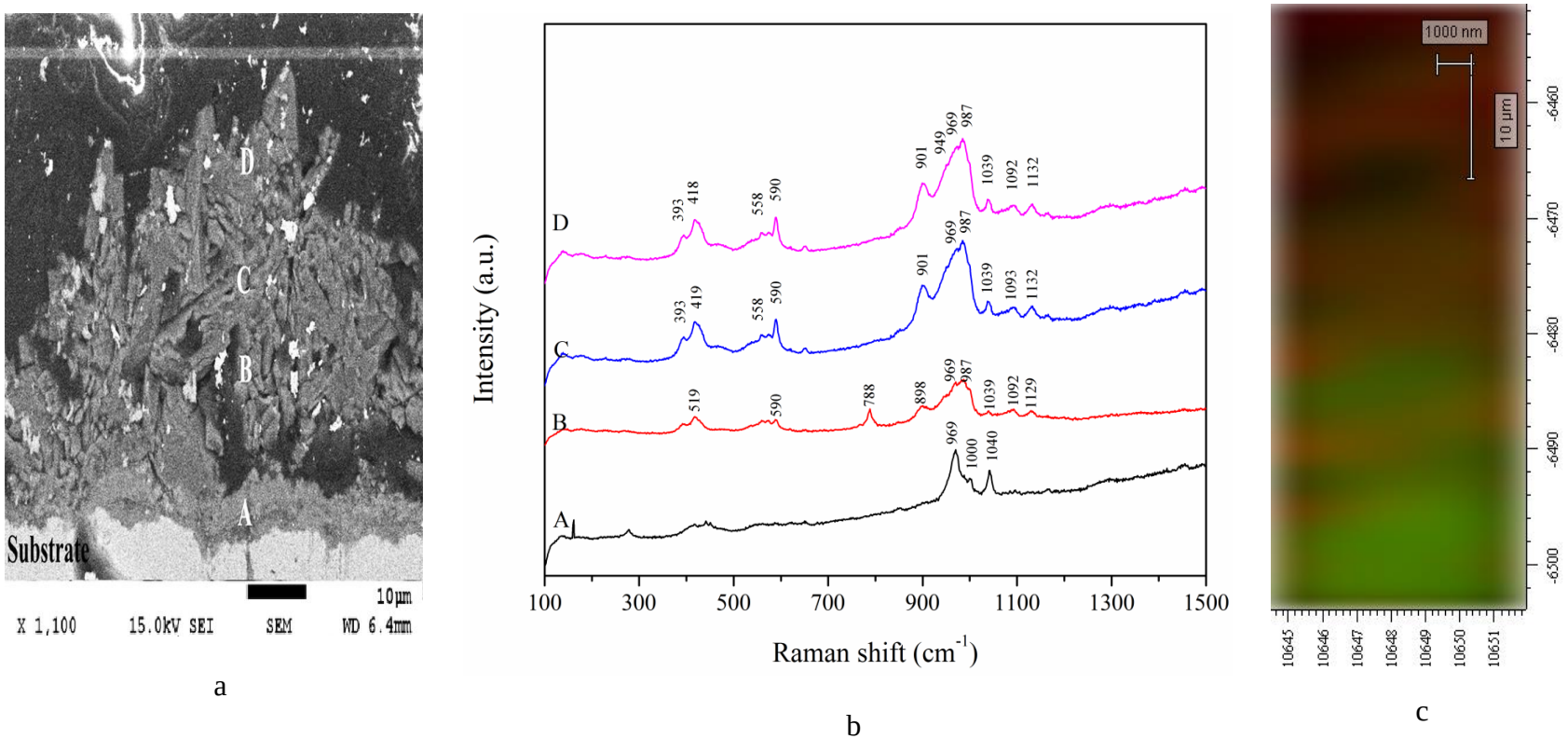


Red color represents the monetite phase ; Green color represents the tricalcium phosphate phase

**Figure 5-4. a) SEM cross section, b) Raman pattern through the cross section, c) Raman map review through the cross section on the Zn substrate**

**Table 5-1. Raman bands for Ca-P coatings**

| Raman Shift ($cm^{-1}$) | Assignment | Phase |
|---|---|---|
| 177 | Lattice mode | Monetite |
| 277 | …. | Magnesium hydroxide |
| 391 | POH | Monetite |
| 413-417 | POH | Monetite |
| 444 | MOH bend | Magnesium hydroxide |
| 559 | POH | Monetite |
| 589 | $\nu_4\ PO_4^{3-}$ | Tricalcium phosphate |
| 619 | ν POP (symmetric) | Calcium pyrophosphate |
| 850 | …. | Carbonated apatite |
| 946 | $\nu_1\ PO_4^{3-}$; POH | Tricalcium phosphate; Monetite |
| 968-970 | $\nu_1\ PO_4^{3-}$ | Tricalcium phosphate |
| 890 | POH | Monetite |
| 987 | POH | Monetite |
| 999 | $\nu PO_3$(asymmetric) | Calcium pyrophosphate |
| 1039 | $\nu_3\ PO_4^{3}$ | Tricalcium phosphate |
| 1090 | $\nu_3\ PO_4^{3-}$, ; POH | Tricalcium phosphate; Monetite |
| 1157 | $\nu PO_3$ (asymmetric) | Calcium pyrophosphate |
| 1180 | $\nu PO_3$ (asymmetric) | Calcium pyrophosphate |
| 1202 | POH | Monetite |
| 1293 | POH | Monetite |
| 1450 | POH | Monetite |

Mg (and Zn) actively corrodes at low pH; as a result of substrate corrosion, released hydrogen ions are converted into hydrogen gas, and consequently, the local pH close to the substrate surface increases. The rise in the local pH can exceed the pH stability range of tricalcium phosphate which results in the solution's super saturation and promotes the deposition of tricalcium phosphate crystals as a first deposited layer according to Eq.5-1.

$$\mathbf{Ca^{2+} + PO_4^{3-} \rightarrow Ca_3(PO_4)_2} \qquad \textbf{(5-1)}$$

Moreover, the presence of $Mg^{2+}$ (released through substrate corrosion) can stabilize the tricalcium phosphate phase as well. The stabilizing effect of Mg is attributed to the

markedly smaller ionic radius of $Mg^{2+}$ (0.65 Å) compared to $Ca^{2+}$ (0.99 Å) [153-155]. Mg ions reside in the Ca(4) and Ca(5) sites in the tricalcium phosphate structure, which can accommodate divalent cations and stabilize the structure [176].

The EDS analysis through the cross section of coated sample at 160 °C on AZ31 substrate confirms that $Mg^{2+}$ contributed to the coating layer with high abundance near the substrate. However, the $Mg^{2+}$ diminished as the distance from the substrate increased, as shown in Fig.5-5.

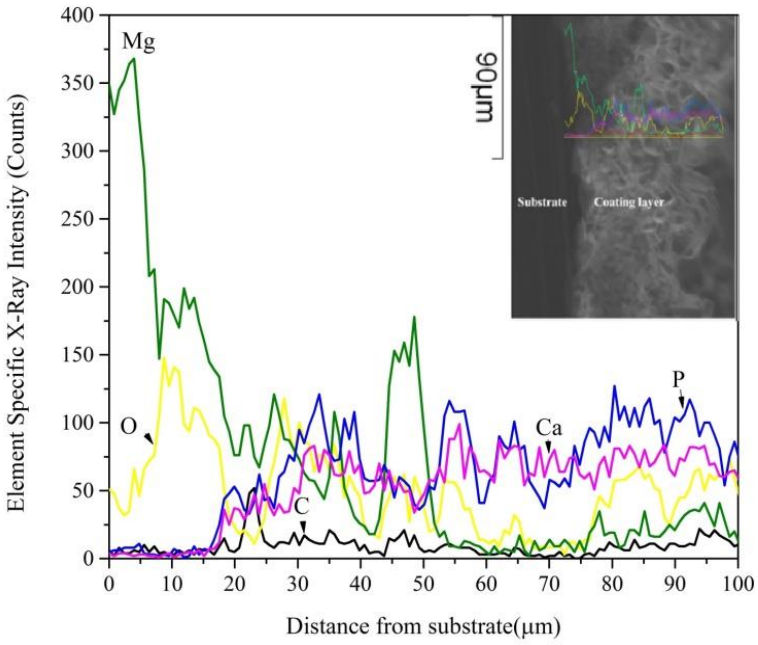


**Figure 5-5. EDS analyses through the coating cross section for Ca-P layer on AZ31 substrate deposited at 160 °C**

Initial deposition of tricalcium phosphate on the AZ31 substrate can isolate the metal substrate from the direct contact with the solution. Thus, after a thin tricalcium phosphate coating layer is formed, the effect of substrate corrosion on the local pH of the solution is reduced. Further Ca-P deposition is influenced only by the solution's pH (pH is 3.9 to 4.0) that is more conducive for monetite phase formation on top of the tricalcium phosphate layer. Therefore, the coating was composed of two different

crystalline layers (tricalcium phosphate and monetite). The tricalcium phosphate layer can dissolve partially at low pH and it can be converted to monetite as well. This means that the deposition of the monetite phase could happen through two different mechanisms according to Eq.5-2 and Eq.5-3 [157, 158, 177].

$$\mathbf{Ca_3(PO_4)_2 + 2HPO_4^- \rightarrow 3CaHPO_4 + \ HPO_4^{2-}} \quad (5\text{-}2)$$

$$\mathbf{Ca^{2+} + HPO_4^{2-} \rightarrow CaHPO_4} \quad (5\text{-}3)$$

Firstly, partial dissolution of the tricalcium phosphate phase and re-precipitation as a monetite phase may occur. Secondly, direct deposition of monetite from the solution bath is likely.

By increasing the deposition temperature to 190 ºC, the coating thickness on AZ31 substrate increased significantly (approximately from 60 µm to 400 µm), and the deposition mechanism also changed as will be discussed comprehensively in the next section.

### 5.2.3 Deposition Mechanism of Ca-P Coating at 190 °C

By increasing the deposition temperature from 160 ºC to 190 ºC using an AZ31 substrate, the coating thickness increased sharply and the deposition mechanism was found to be different. Cross sections of coatings deposited at 190 ºC show two distinct layers as shown in Fig.5-6. The coating is composed of a thick layer of $Mg(OH)_2$ adjacent to the substrate and mixed with a minor amount of tricalcium phosphate and a second crystalline layer with a mixture of monetite and whitlockite phases forming the outer layer of the coating. The coating geometry seemed to suggest that first a $Mg(OH)_2$ layer was formed on the substrate followed by deposition of Ca-P layers.

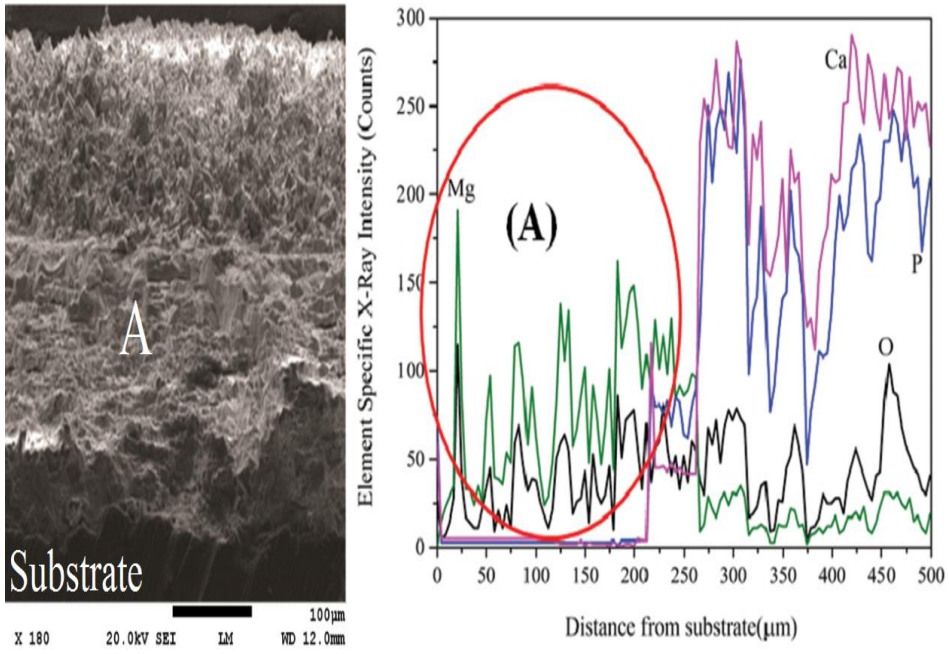


**Figure 5-6. SEM image (left) and EDS profile (right) through the cross section of coated sample at 190 °C for 3 hours**

However, comparison studies through the cross section of samples coated at varied deposition times at 190 ºC confirmed that the first deposited layer is a non-compact and crystalline whitlockite phase.

SEM micrographs of the top surface and cross sections of coated samples deposited at 190 °C for different deposition times are shown in Fig.5-7. Fig.5-7.b shows that the coated sample at 190 °C-1hr is only composed of a crystalline layer and the SEM micrograph from top surface of this coating showed that the coating is non-compact (Fig.5-7.a).

Due to imperfections in the initially formed whitlockite layer, the AZ31 substrate was still exposed to corrosive electrolyte, and $Mg(OH)_2$ started to deposit under the whitlockite layer. Since the Mg converted primarily into $Mg(OH)_2$, the results suggest that mostly water was able to penetrate through the first whitlockite layer, and

phosphates (as well as Ca ions) had lower penetration rate through the coating to the metal. This observation is supported by the fact that at increased deposition temperature the water vapor pressure as well as the activity of water increases significantly, thus providing a driving force for the water to penetrate the coating.

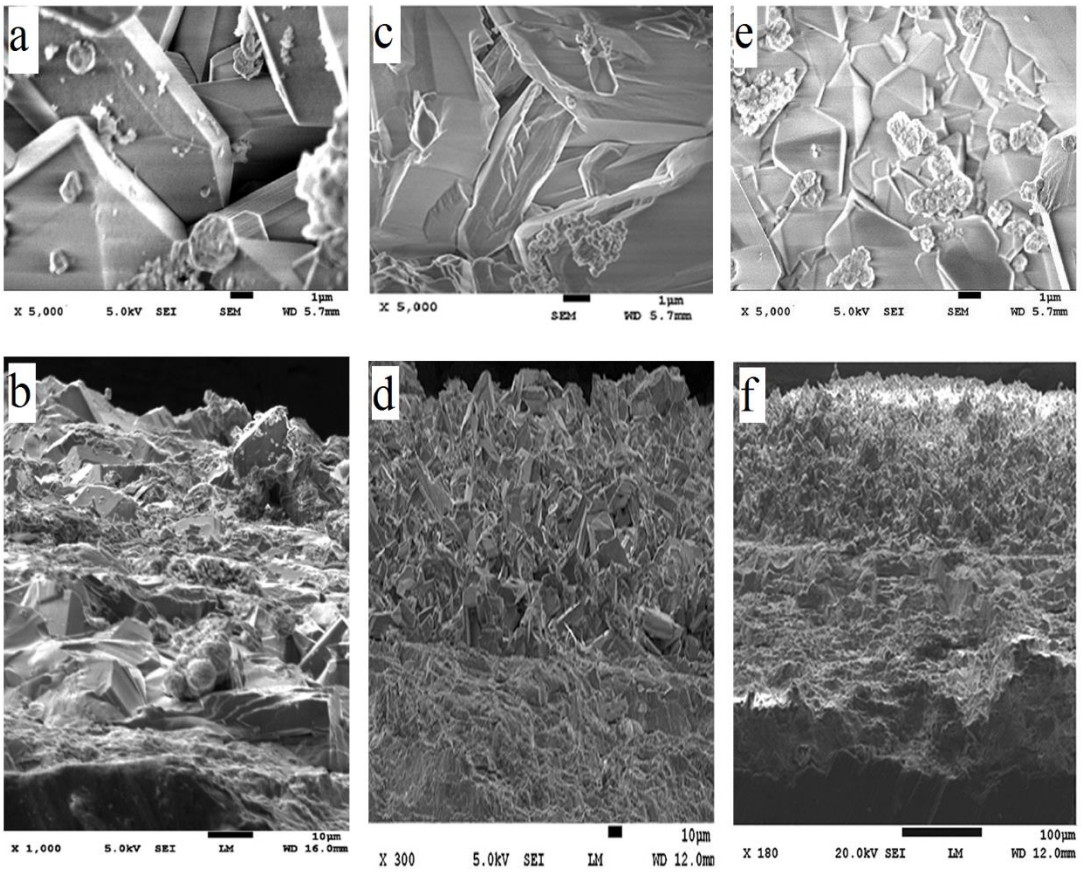


**Figure 5-7. SEM micrographs of coated samples at 190 ˚C: a) HE190 °C-1hr top surface, b) HE190 °C-1hr cross section, c) HE190 °C-2hr top surface, d) HE190 °C-2hr cross section, e) HE190 °C-3hr top surface and f) HE190 °C-3hr cross section**

The continued corrosion of the AZ31 substrate at high temperature (190 °C) hydrothermal coating deposition process also leads to the release of increased amount of $Mg^{2+}$ as shown in Fig.5-8. As a result of fast degradation of AZ31, the thickness of

the coating increased significantly during the high temperature deposition through the formation of $Mg(OH)_2$.

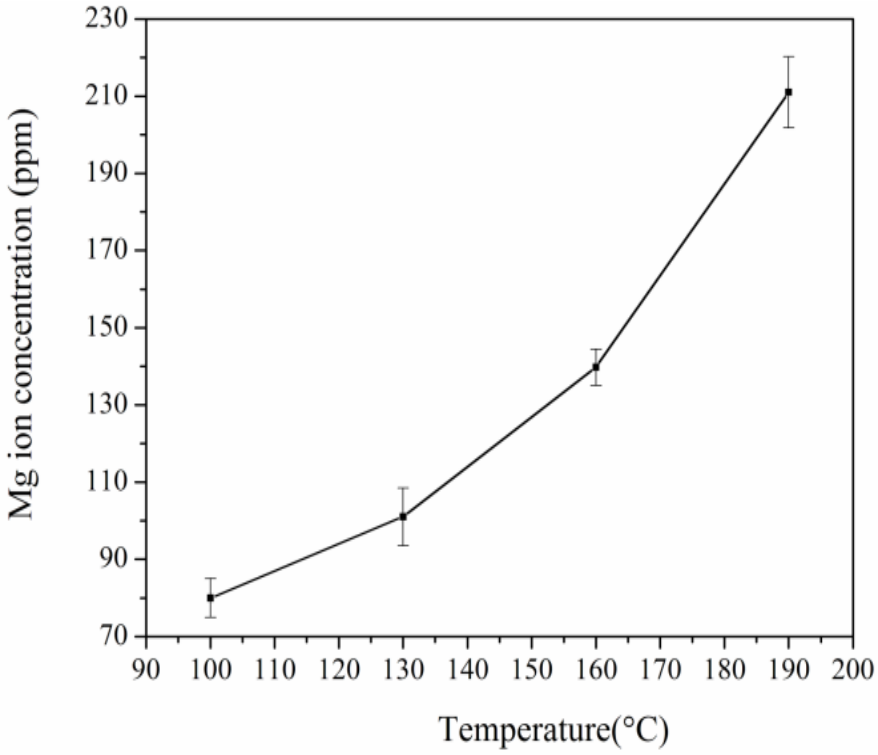


**Figure 5-8. $Mg^{2+}$ concentration in the deposition batch after hydrothermal process for different deposition temperature**

The Raman spectroscopy of deposited coating at 190 ºC for different deposition times are given in Fig.5-9, Fig.5-10 and Fig.5-11 respectively. Raman spectroscopy studies also confirmed that at the first step Ca-P phase started to deposit and then $Mg(OH)_2$ layer started to deposit under the crystalline layer.

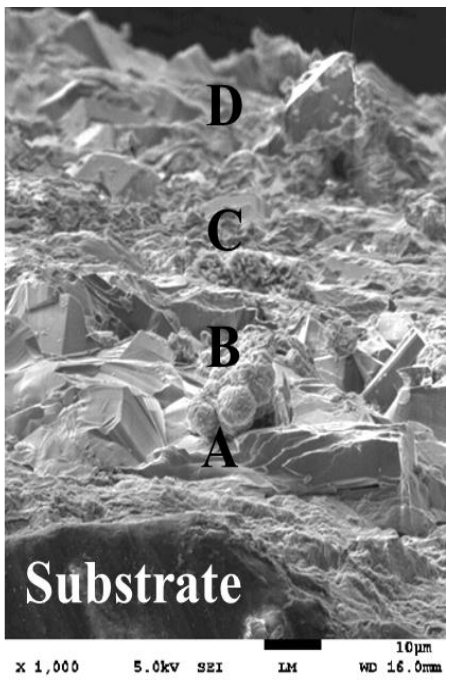


a

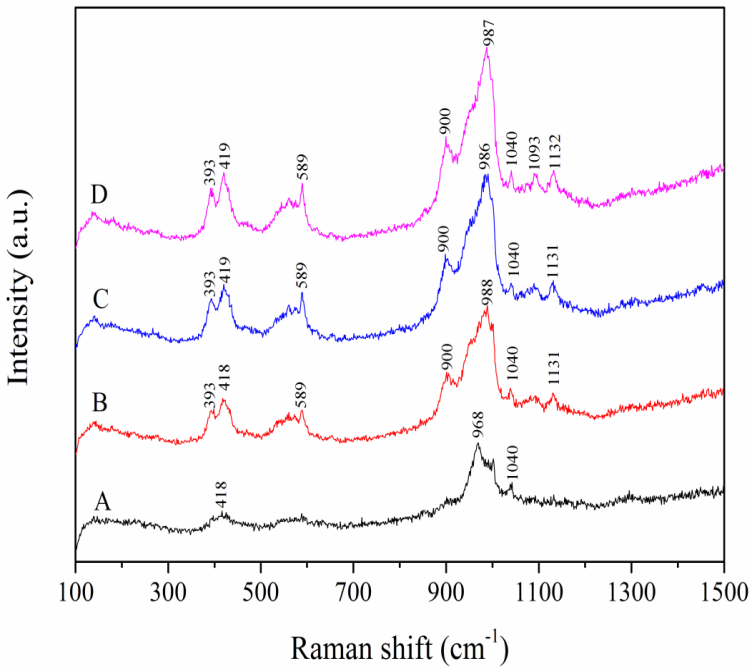


b

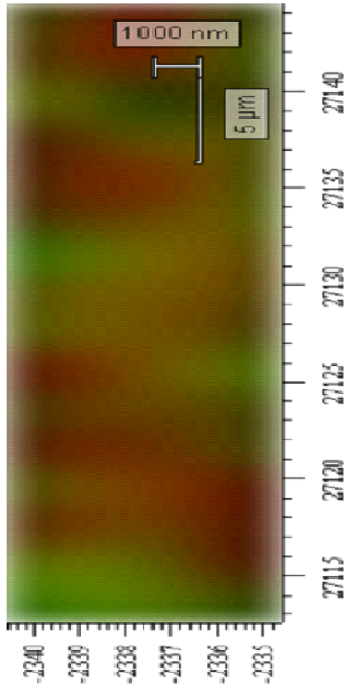


c

Red color represents the monetite phase ; Green color represents the tricalcium phosphate phase

**Figure 5-9. a) SEM cross section, b) Raman pattern through the cross section, c) Raman map review through the cross section for HE190 ºC-1 hr**

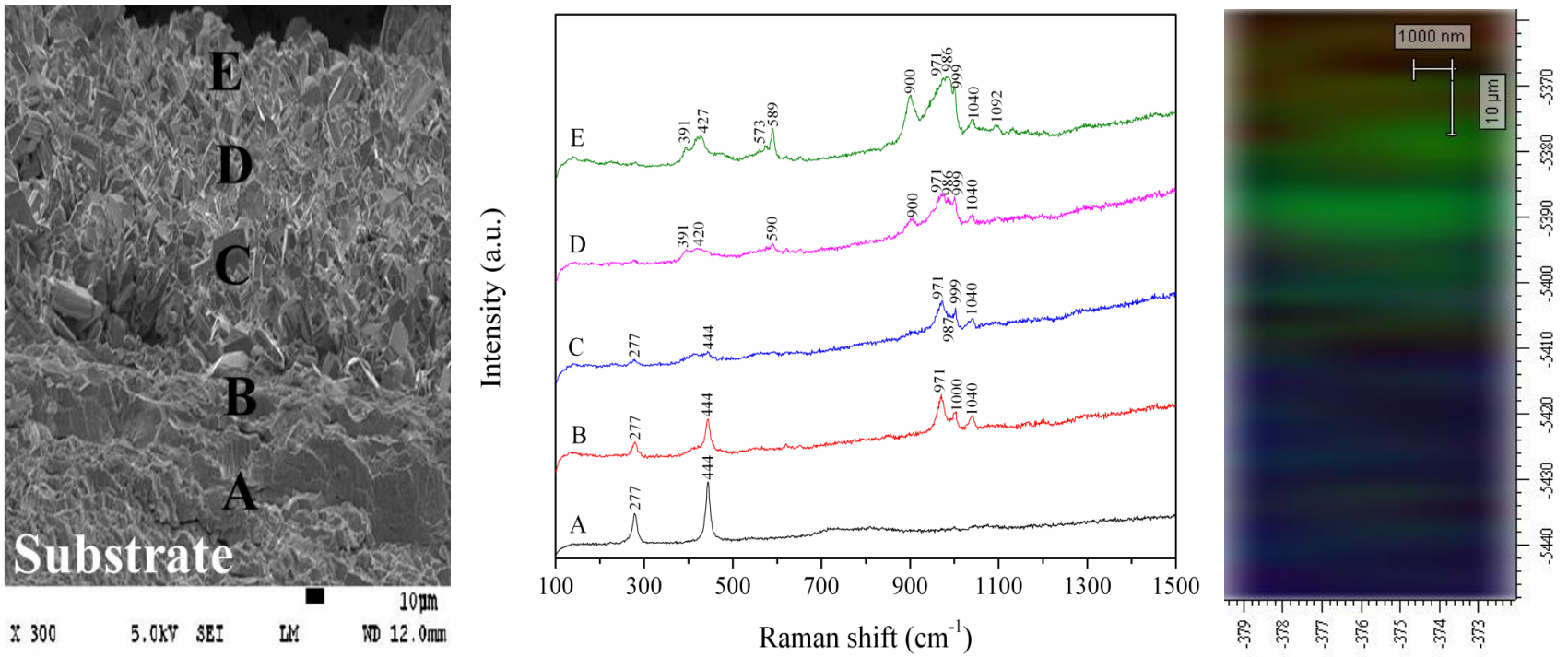


a b c

Red color represents the monetite phase ; Green color represents the tricalcium phosphate phase; Blue color represent the magnesium hydroxide phase

**Figure 5-10. a) SEM cross section, b) Raman pattern through the cross section, c) Raman map review through the cross section for HE190 ºC-2 hr**

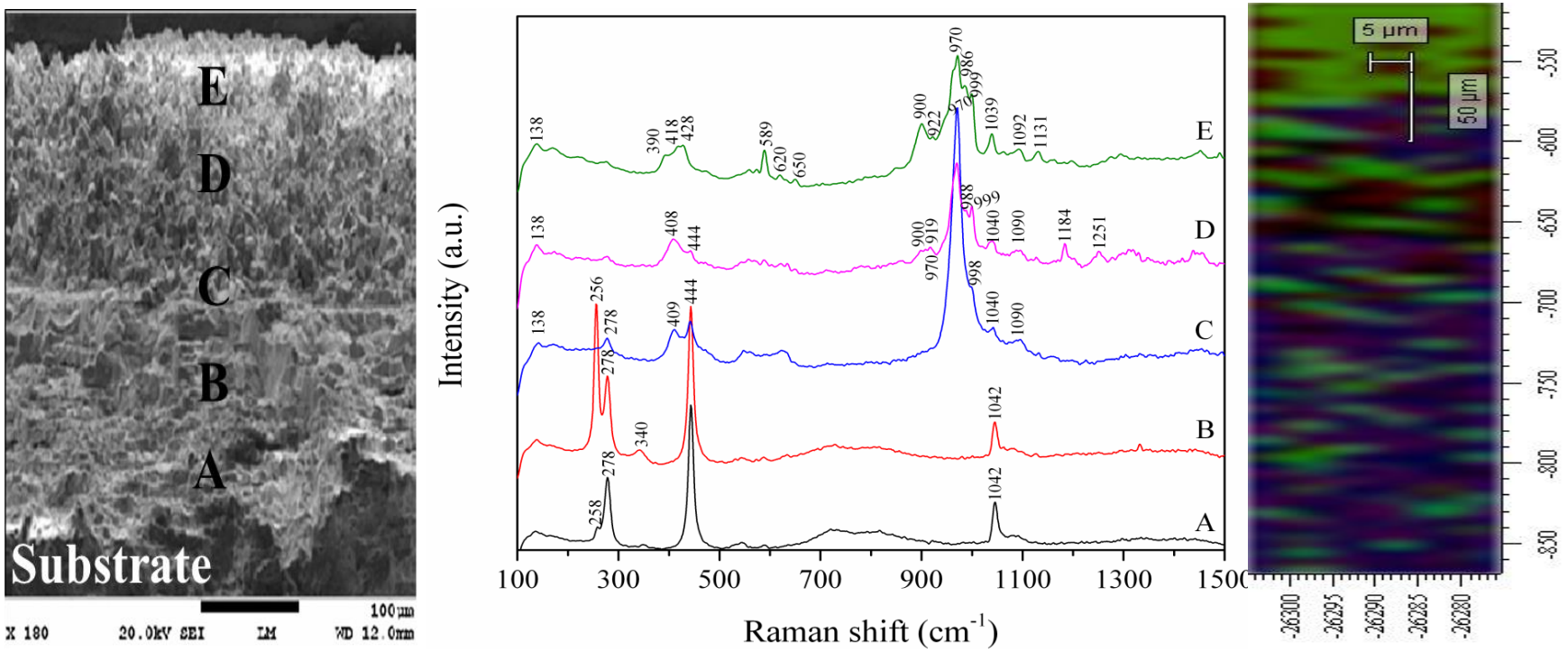


a b c

Red color represents the monetite phase ; Green color represents the tricalcium phosphate phase; Blue color represent the magnesium hydroxide phase

**Figure 5-11. a) SEM cross section, b) Raman pattern through the cross section, c) Raman map review through the cross section for HE190 ºC-3 hr**

### 5.2.4 Deposition Mechanism on SS Substrate

Deposition of Ca-P on SS substrate showed different mechanism. A thin layer of Ca-P partially deposited on the SS substrate but, some parts of the surface remained uncoated. **The** monetite phase directly nucleates and grows on the SS substrate during the hydrothermal process as shown in Fig.5-12. The deposition of some monetite on the SS substrate might be a result from the deposition of the pre-formed monetite crystals from the deposition bath. The obtained results confirmed that interface reaction has a critical role in the coating deposition.

According to Liu et al. [139] inertness of Ti and SS substrate in deposition solution prevent the deposition of Ca-P on these substrates; according to their report even after 15 hours hydrothermal deposition at 200 °C (solutions' pH 10) no coating was observed on Ti and SS substrates. Only a few scattered crystals were deposited on substrates. The dissolution behavior of metal substrates is an important factor which affects the successful deposition of Ca-P coating [139, 175, 178]. According to Xiong et al. [179] a relatively successful deposition of HA particles at high temperature (200 ˚C) on TiNb substrate might be related to formation of negatively charged Ti-OH and Nb-OH functional groups on the alloy surface during hydrothermal process. The negative charge can absorb $Ca^{2+}$ and promote heterogeneous nucleation.

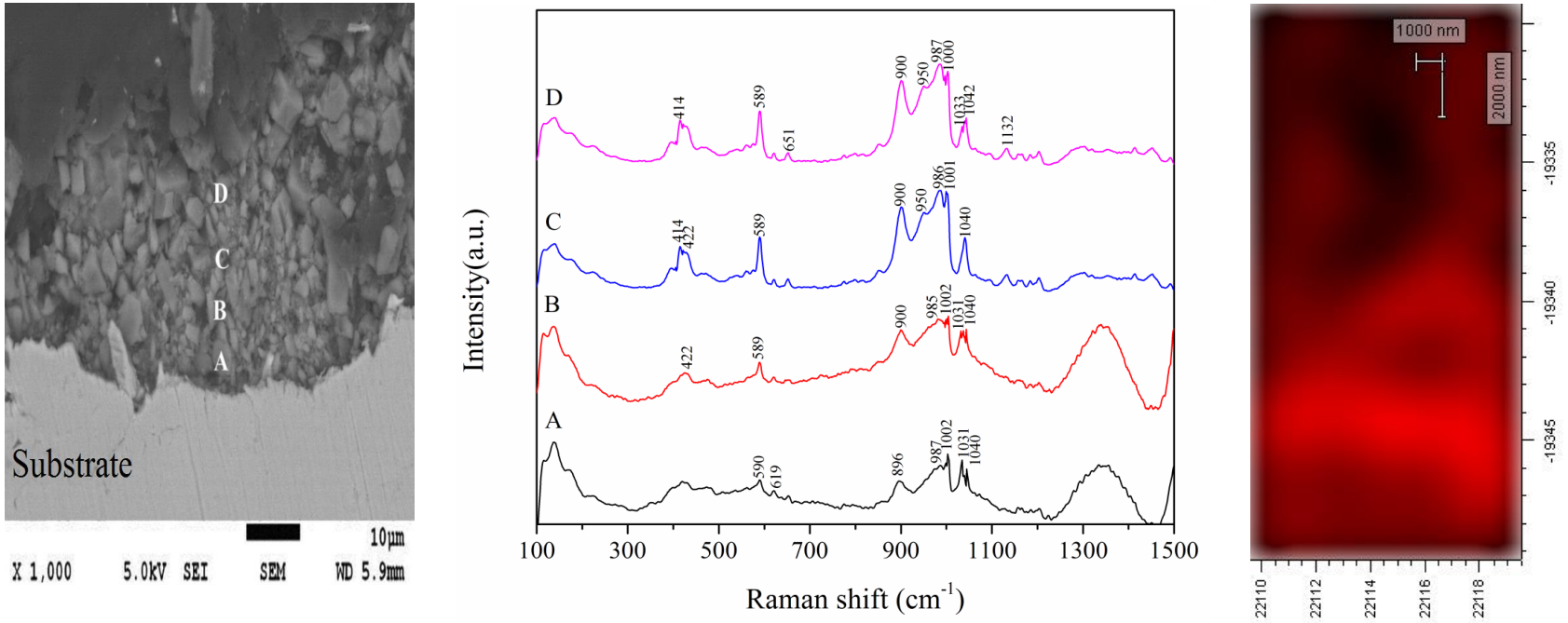


a b c

Red color represents the monetite phase

**Figure 5-12. a) SEM cross section, b) Raman pattern through the cross section, c) Raman map review through the cross section for coated sample on SS**

### 5.2.5 Causes of Unsuccessful Ca-P Deposition on Ti and Discontinuous Coating Formation on SS Substrates

In order to understand the reason why deposition of the Ca-P coating was not successful for some substrates, the electrode potentials of different substrates were monitored for one hour in Ca-P deposition solution and the results showed more active electrode potentials for AZ31and Zn substrates than Ti and SS substrates as shown in Fig.5-13. The obtained potentials for each substrate were transferred to their respective Pourbaix diagram as illustrated in Fig.5-14 (Note: these Pourbaix diagrams are used for comparison purposes. The presence of some ions may change the Pourbaix diagram). The Pourbaix diagram of Zn is based on a standard calomel electrode, therefore the conversion between hydrogen standard electrode and calomel standard electrode had been done).

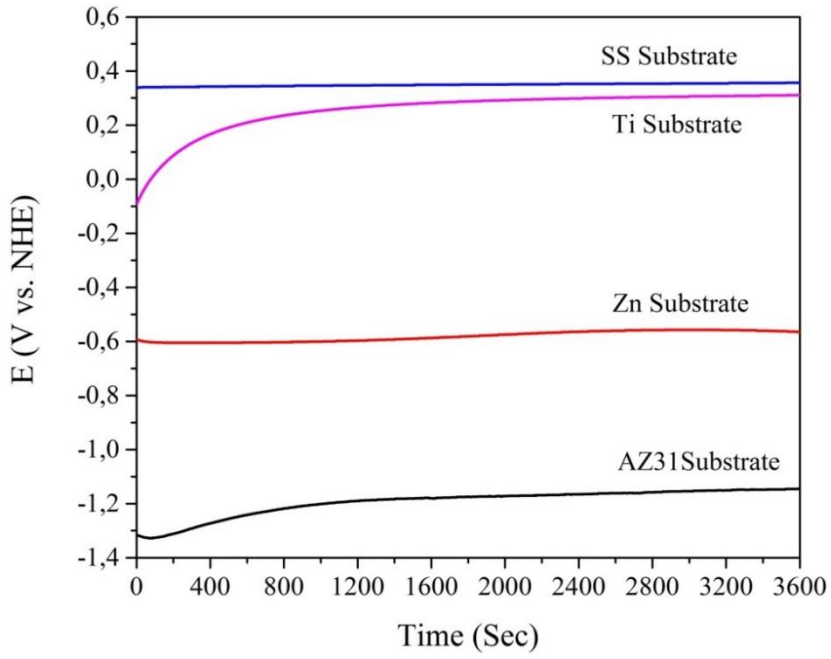


**Figure 5-13. Change in electrode potential vs. time in a Ca-P solution for different substrates**

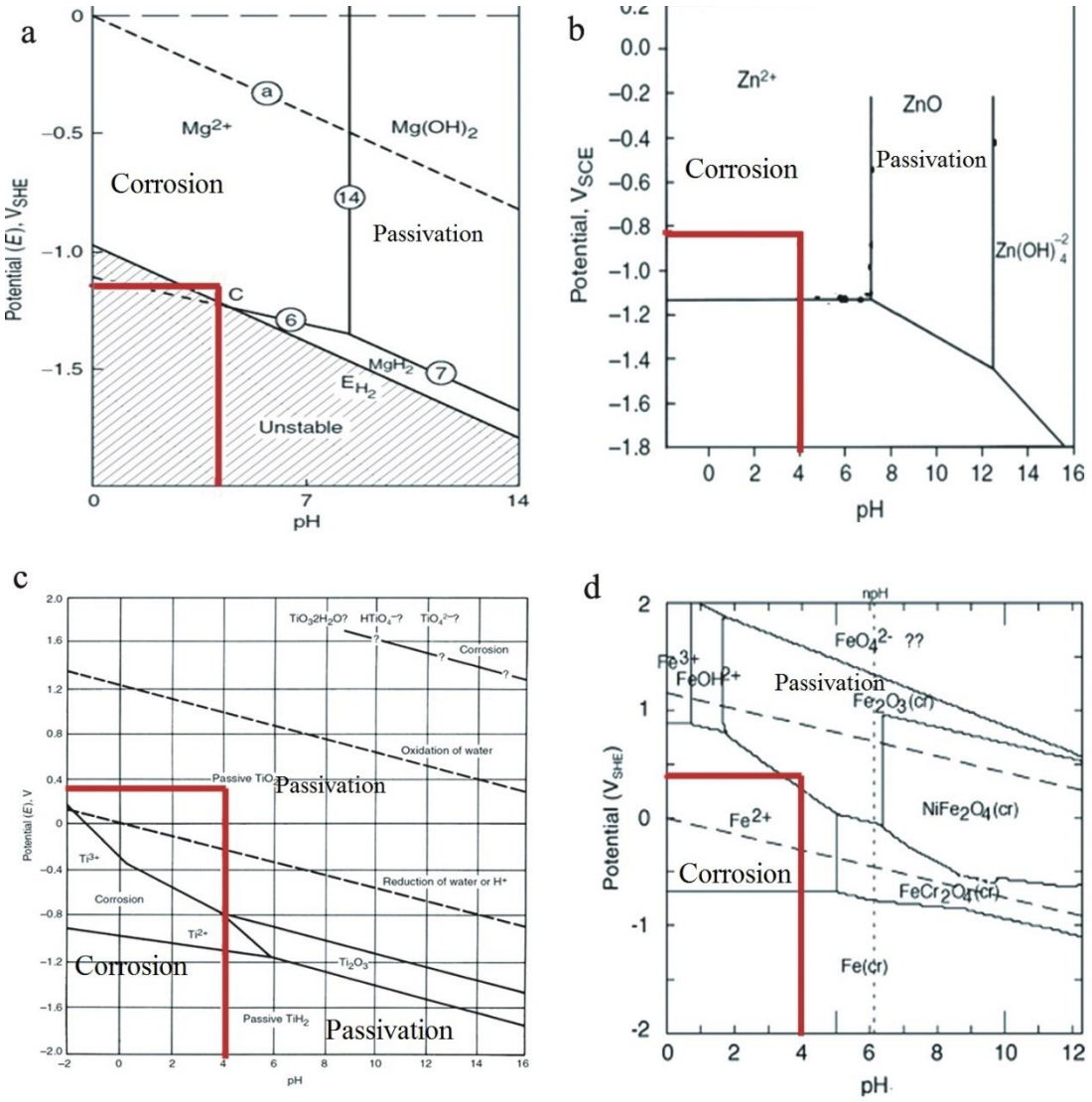


**Figure 5-14. Pourbaix diagram for a) AZ31 substrate [180] , b) Zn substrate [181] , c) Ti substrate [182], and d) SS substrate [183]**

According to the Pourbaix diagrams, AZ31 and Zn actively corrode at potentials developed in the deposition solution. This corrosion process is described by Eq.5-6 [184] and Eq.5-7. However, SS and Ti form oxide layers at those potentials according to Eq.5-8 and Eq.5-9.

$$Mg + 2H^+ \rightarrow Mg^{2+} + H_2 \quad (5\text{-}4)$$

$$Zn + 2H^+ \rightarrow Zn^{2+} + H_2 \quad (5\text{-}5)$$

$$2Fe^{2+} + 3H_2O \rightarrow Fe_2O_3 + 6H^+ + 2e^- \quad (5\text{-}6)$$

$$Ti + 2H_2O \rightarrow TiO_2 + 4H^+ + 4e^- \quad (5\text{-}7)$$

Based on the measured electrode potentials and Pourbaix diagrams, it seems that the interface reaction between substrate and solution is a key driver for successful deposition of Ca-P layer. As a result of corrosion of AZ31 and Zn substrates, solution's pH increases in the vicinity of the metal which helps to locally supersaturate the solution and consequently, Ca-P mineral starts to deposits from solution. Conversely, in the case of Ti and SS substrates, any corrosion and corresponding oxide layer formation results in the release of hydrogen ions decreasing the pH. The lower pH delays or prevents the deposition process. According to SS's Pourbaix diagram the release of $H^+$ and concomitant decrease in solution's pH shifts the metal into the corrosion area with ferrous ion ($Fe^{2+}$) release as a result of iron corrosion. Since, the atomic radius of $Fe^{2+}$ (0.62 Å) is smaller than $Ca^{2+}$ (0.99 Å), $Ca^{2+}$ can be substituted by $Fe^{2+}$ in the Ca-P structure; therefore, release of $Fe^{2+}$ ions might help to speed up the deposition of the Ca-P on the SS substrate as compared to the Ti substrate where no stabilizing effect is expected.

The pH values of deposition solutions were measured after the hydrothermal process and found to be in the range of 3.2-3.4 pH when using AZ31 or Zn, while it decreased to pH: 2.5 when SS or Ti substrate was used.

#### 5.2.5.1 Effect of Wettability

Apart from substrate corrosion, substrate wetting is also an important interface phenomenon during nucleation process. It has been confirmed that wettability of a

substrate is favorable for the heterogeneous crystal nucleation [185-188]. According to Wang et al. [186] a decrease in wetting angle significantly decreases the critical nucleus radius and critical nucleation energy, which remarkably accelerates heterogeneous crystal nucleation on the substrate. Chevalier [185] studied the effect of substrate wettability on calcium carbonate heterogeneous nucleation and he reported that an increase in hydrophilicity for silanized glass substrate resulted in higher crystal nucleation rate. It has also been reported that surfaces with step-like structures display strong wettability by an aqueous $NH_4Cl$ solution and, therefore the nucleation density of $NH_4Cl$ on such a substrate is significantly higher than smooth surfaces which shows that the geometrical morphology features can have important effects on both the wettability and the nucleation behavior [188, 189].

The water contact angle on different substrates is reported in Table 5-2, measured at room temperature. The SS substrate showed the lowest contact angle and highest wettability in comparison to the other substrates, though the contact angles may change at higher temperature. Despite the lower contact angle and its potential effect of decreasing the energy barrier for heterogeneous nucleation, the deposits did not form a continuous film on SS implying that the metal corrosion (for Mg and Zn) is the dominant factor in promoting nucleation.

**Table 5-2. Water contact angle data for different substrates**

| Substrate | Contact angel (degree) |
|---|---|
| AZ31 Substrate | 59±3 |
| Zn Substrate | 74±2 |
| SS Substrate | 33±4 |
| Ti Substrate | 66±2 |

## 5.3 Deposition Mechanism of Composite Coatings

As reported in Chapter 4, incorporation of polymers (PAA and SCMC) in the deposition solution of calcium and hydrogen phosphate ions had a different effect on deposition process in terms of the coating's chemical composition and morphology.

In order to better understand the difference between deposition of inorganic Ca-P and Ca-P/Polymer composite coatings, a deposition process was done only for 15 minutes for each coating in order to understand the initial step of deposition. The prepared samples were further analyzed by Raman spectroscopy technique. Interestingly results showed in the case of HEPAA composite coating, in the beginning of the deposition process a layer of polymer (PAA) was adsorbed on the AZ31 surface as shown in Fig.5-15, it means that we have a $COO^-$ functionalized surface which has a strong negative charge. This adsorbed polymer layer protected the AZ31 substrate from further corrosion as well, which means that the deposition process cannot be affected by corrosion of the AZ31 substrate and local pH increase and deposition following a different route [190].

In this case, a negatively charged surfaces attract $Ca^{2+}$ ions easily from solution and resulted in high concentration of $Ca^{2+}$ on the surface. Consequently at the same time many nuclei formed, by formation a layer of nuclei on the substrate and isolating the substrate deposition it is most likely followed by deposition of nuclei formed in the solution [191].

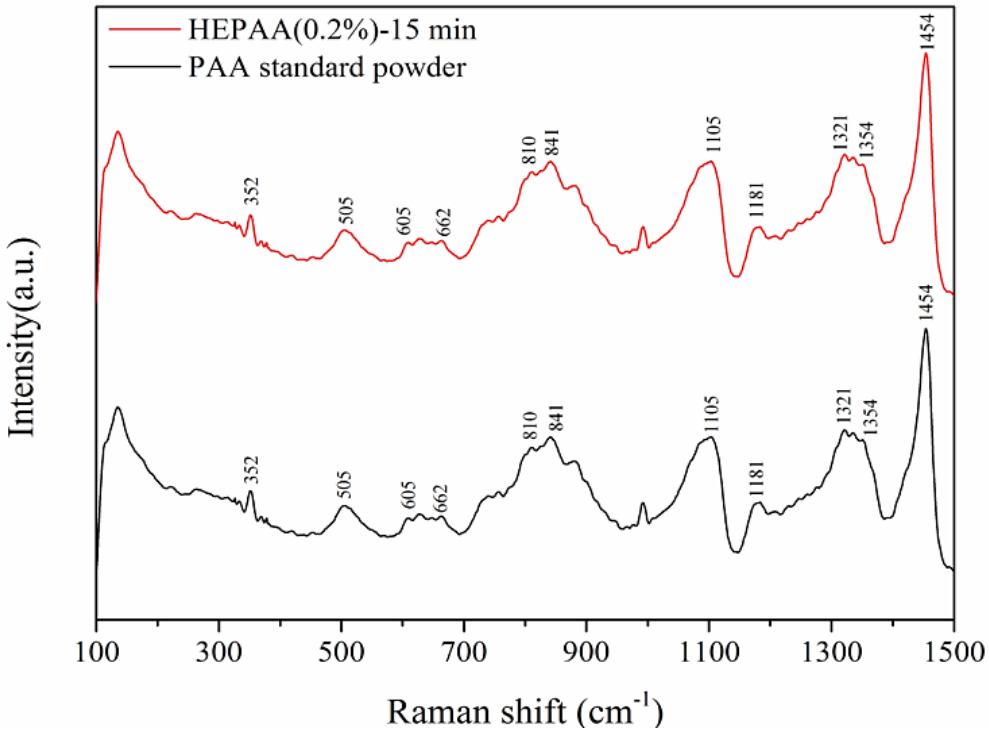


**Figure 5-15. Raman spectrum of HEPAA composite coatings after 15 min deposition**

By passing time, decreasing the amount of polymer in the solution and dropping the supersaturation of solution, monetite phases started to deposit. This concept is confirmed by Raman spectroscopy through the cross section of HEPAA(0.2%) as shown in Fig.5-16. From the Fig.5-16 by increasing distance from substrate, a monetite phase is started to appear in the coating layer. The deposition of monetite is confirmed by appearing the peak at 987 $cm^{-1}$.

However, the findings showed that the initial step of coating deposition for the HESCMS composite coatings was different. The coated sample for 15 minutes showed no sign of polymer adsorption on the surface of AZ31 substrate and the deposition mechanism of HESCMS composite in the initial step was similar to inorganic Ca-P coating as shown in Fig.5-17. The Raman result showed that tricalcium phosphate is deposited in the beginning of deposition, however, the formation of tricalcium

phosphate in this case most probably followed the pH induce deposition mechanism [190]. As it reported earlier Mg is actively corroded at low pH, as a result of Mg corrosion, hydrogen gas releases and consequently, the pH close to the substrate surface increases and should reach the pH stability range of tricalcium phosphate which results in the solution's super saturation, and promotes the deposition of tricalcium phosphate as a first deposited layer [190].

The role of SCMS in this case was limited to interaction and adsorption on the crystal plane and, consequently, slows down the growth process.

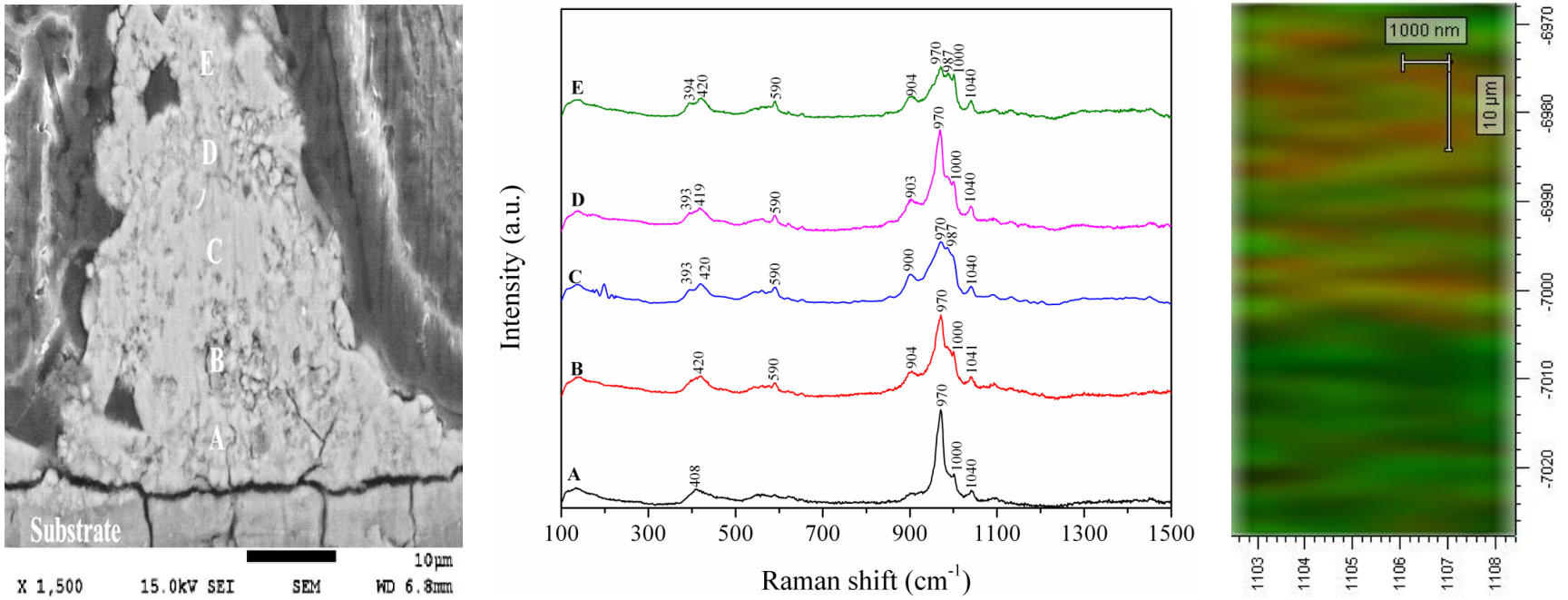


a b c

Red color represents the monetite phase; Green color represents the tricalcium phosphate phase.

**Figure 5-16. a) SEM cross section, b) Raman pattern through the cross section, c) Raman map review through the cross section for HEPAA (0.2%) coating**

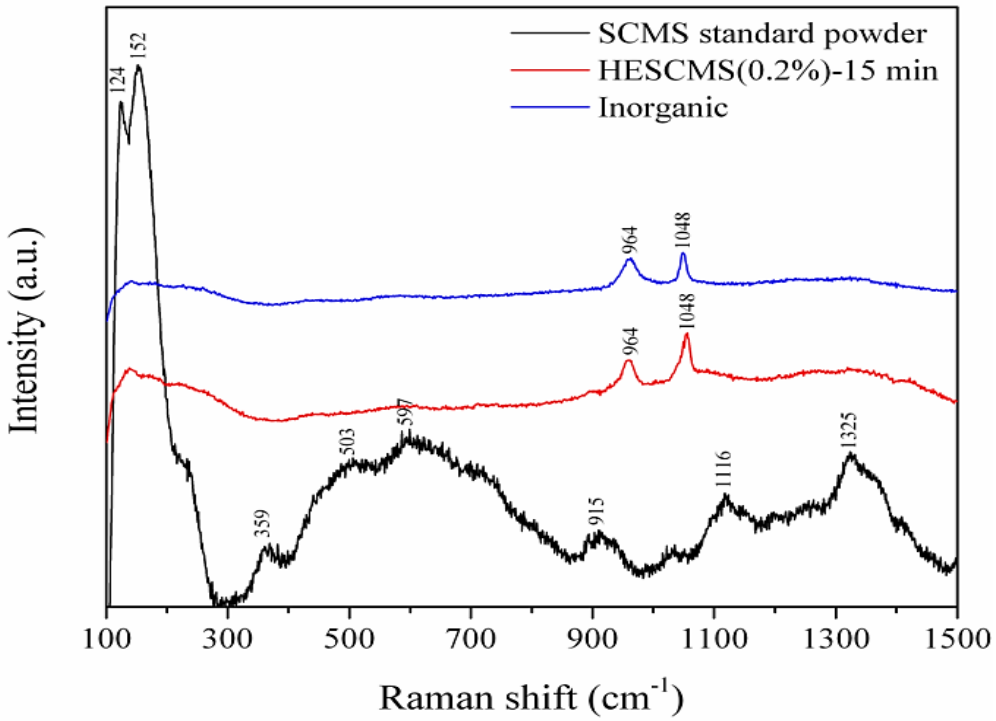


**Figure 5-17. Raman spectrum of inorganic and HESCM composite coating after 15 min deposition**

A schematic comparison of deposition of HEPAA and HESCMS composite coatings are shown in Fig.5-18 and Fig.5-19. In both cases deposition occurs due to super saturation of the solution but the mechanism of super saturation is different in the presence of the two different polymers. PAA polymer adsorption increases local calcium concentration near the surface while in the case of SCMC the effect of AZ31 on the local pH shifts the solution into the super saturated range. The figures explain the difference in deposition mechanism which was affected by polymer adsorption on the AZ31 substrate.

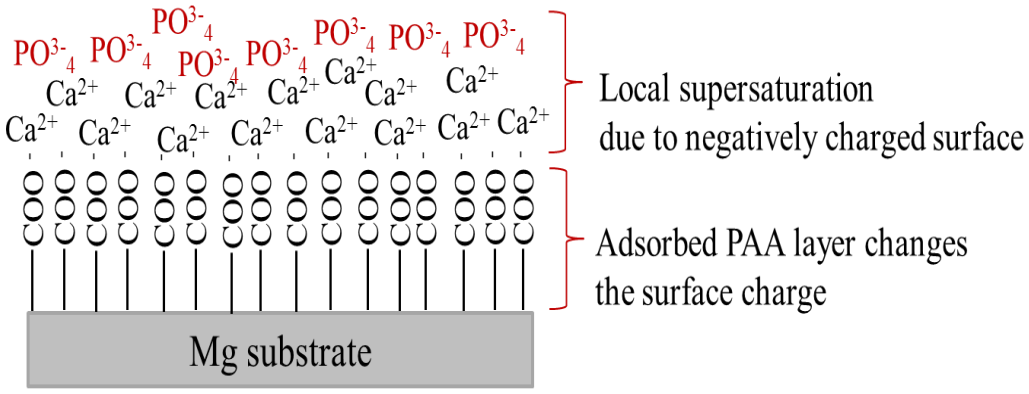


**Figure 5-18. A schematic of HEPAA composite coating deposition**

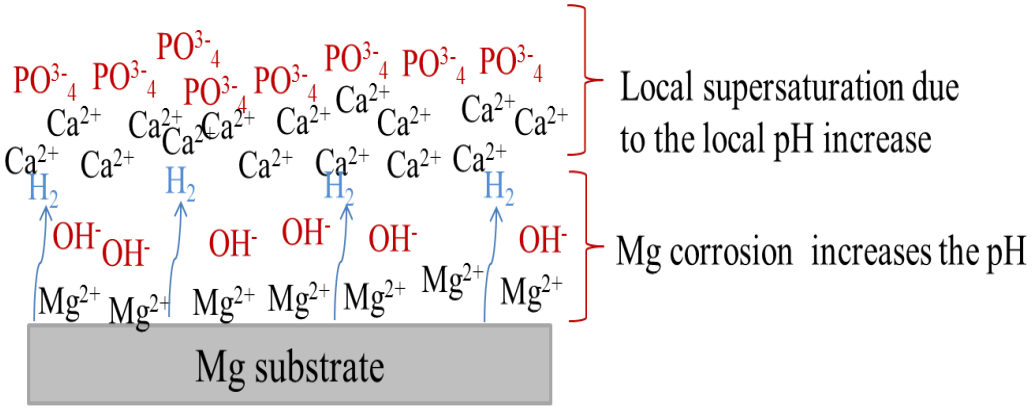


**Figure 5-19. A schematic of inorganic and HESCM composite coating deposition**

## 5.4 Summary

Ca-P coatings were successfully deposited on the AZ31 and Zn substrates using a hydrothermal process. Comparisons to unsuccessful and partially successful deposition on Ti and SS, respectively, indicated that metal-electrolyte interface reactions played a dominant role in the deposition mechanism. The Corrosion of substrate in the first step of the deposition process resulted in inducing a pH change in the vicinity of the metal and promoting Ca-P precipitation on the surface. This finding

was corroborated by the observation that AZ31 and Zn substrates had coatings composed of two different layers. The formation of the first deposited layer adjacent to the substrate (tricalcium phosphate) is promoted by increased local pH by the interface reaction while the second layer (monetite) is deposited at the lower bulk solution pH.

Moreover, deposition temperature had a significant effect on the deposition mechanism. By increasing the temperature, the deposition mechanism changed for the Mg substrate and the coating composed of a thick $Mg(OH)_2$ layer on the substrate capped by a mixture of tricalcium phosphate and monetite. The formation of a thick $Mg(OH)_2$ layer resulted from a permeable and not fully protective initial tricalcium phosphate layer which allowed access and penetration of water to the AZ31 substrate during the 190°C deposition process, resulting from increased water vapor pressure. Fast degradation of the AZ31 substrate was found and it accelerated the formation of a thick $Mg(OH)_2$ layer.

On the other hand, the polymer incorporation in the deposition solution also affected the deposition mechanism. In the case of composite coatings, PAA polymer adsorption on AZ31 substrate in the initial step of deposition had changed the deposition mechanism. In this case, an increase in the local calcium concentration near the surface accelerated the deposition of the Ca-P coating. While, HESCMS composite coatings had followed the same deposition mechanism as inorganic Ca-P coatings.

# Chapter 6

# Corrosion Performance and Mechanical Properties of Hydrothermally Deposited Coatings

## 6.1 Introduction

Despite the high potential of using Mg alloys as temporary and biodegradable implants, their applications are not widespread. Yet as the corrosion rate of Mg alloys is too high (resulting in excessive hydrogen evolution and local alkalization close to the surgery region), premature degradation in the implant's mechanical integrity before sufficient bone healing can occur [3].

The corrosion properties of obtained coating as well as their mechanical performance are reported in this chapter.

## 6.2 Corrosion Performance of Coatings

### 6.2.1 Corrosion Performance of Inorganic Ca-P Coatings

The variation of open circuit potential (OCP) over time can be used as a criterion to understand the interface stability of coating and substrate. OCP curves for uncoated and coated samples are illustrated in Fig.6-1. The OCP of the coated samples shifted to nobler potential as compared to the bare alloy. The OCP of coated sample deposited at 190 ºC increased by 1.72 V compared to AZ31 bare substrate, while 1.22 V increase was seen for a coated sample at 160 ºC. The positive shift of OCP due to the presence of coating indicates the formation of a stable Ca-P/AZ31 interface [93, 192]. The much nobler behavior of the coated sample at 190 ºC and the stable OCP over a 30 minutes period can be attributed to the improved stability of the coated alloy surface that may be related to high coating thickness, and a more complicated path of electrolyte penetration into the coating layer due to its compact morphology. The observations

indicated that the Ca-P layer has a protective nature and could provide good protection for the Mg substrate.

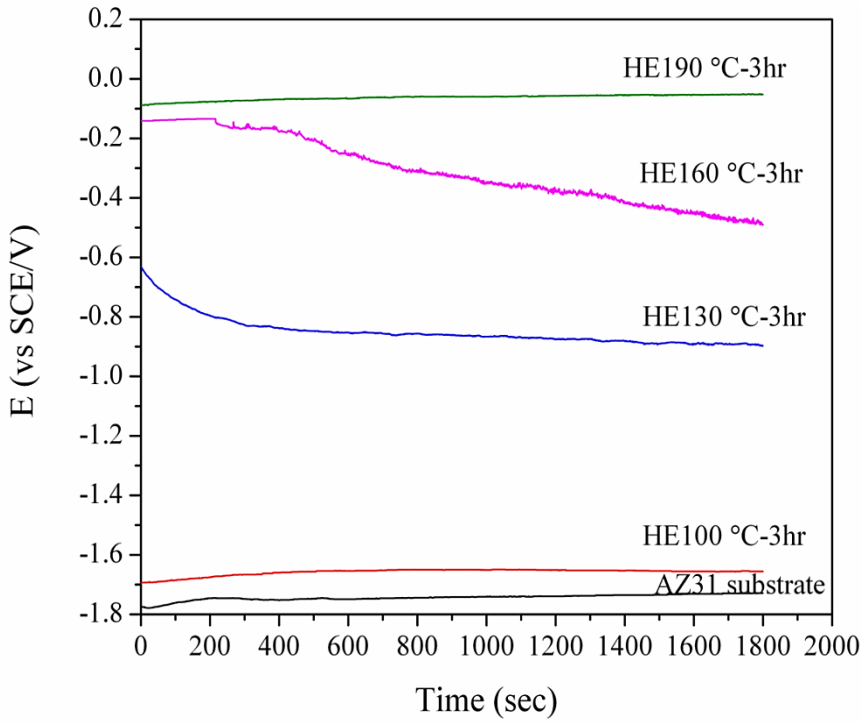


**Figure 6-1. Open circuit potential curves of uncoated and coated samples for different deposition temperature in simulated body fluid (SBF) solution**

Fig.6-2 shows the potentiodynamic curves for coated samples deposited at varied temperatures for 3 hours. The $E_{corr}$ and $i_{corr}$ were derived from the polarization curves by means of the Tafel extrapolation method, and the results are summarized in Table 6-1. According to the data, the corrosion rate of coated samples decreased significantly compared to the uncoated sample. The corrosion rate was reduced by increasing the hydrothermal deposition process temperature. This was likely due to an increase in the coating thickness and changes in coating morphology. However, the corrosion resistance did not change uniformly with coating thickness. Mg and its alloys are

known to suffer from pitting corrosion manifesting in rapid increase in the anodic current over small polarization potential range in potentiodynamic scans which can be seen clearly in Fig.6-2 for the bare substrate and coated sample at 100 ºC. On the other hand, samples coated at 130 ºC and 160 ºC, the polarization curves show an abrupt increase in anodic current followed by a quasi-passive region at around $10^{-5}$ A/cm$^2$, while coated sample at 190 ºC only had a quasi-passive region in polarization curve at around $5*10^{-7}$A/cm$^2$.

The corrosion improvement can be better understood by considering the corrosion process of the metal. Mg reacts with SBF solution immediately upon contact and starts to corrode according to Eqs 6-1 to 6-3 [193]:

$$\mathbf{Mg \rightarrow Mg^{2+} + 2e^-} \quad (6\text{-}1)$$

$$\mathbf{2H_2O + 2e^- \rightarrow H_2 + 2OH^-} \quad (6\text{-}2)$$

$$\mathbf{Mg^{2+} + 2OH^- \rightarrow Mg(OH)_2} \quad (6\text{-}3)$$

The presence of a coating layer can prevent or delay the access of electrolyte to the Mg substrate and retard the initiation of corrosion process by limiting the availability of water needed for hydrogen generation according to Eq.6-2. Thus, by increasing the coating thickness and improving the coating morphology, the corrosion rate can be decreased [192].

The change in corrosion rate of the sample coated at 190 ºC was examined for different deposition durations from 1 to 3 hours, as shown in Fig.6-3. By increasing the deposition time, the protective nature of the coating improved, most likely due to the increase in coating thickness and formation of a more compact morphology.

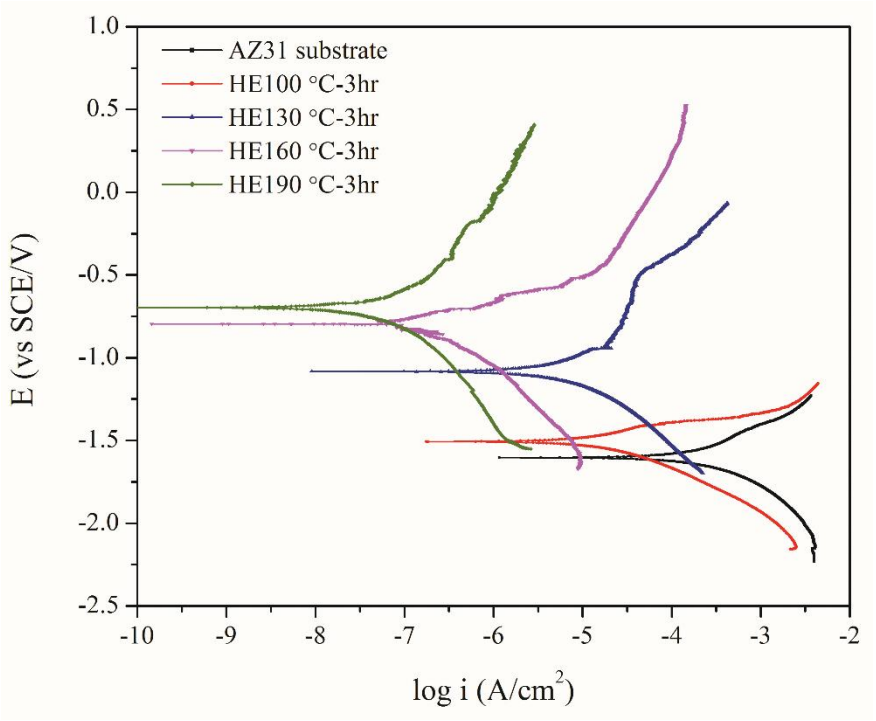


**Figure 6-2. Potentiodynamic curves of uncoated and coated samples for different deposition temperature in SBF solution**

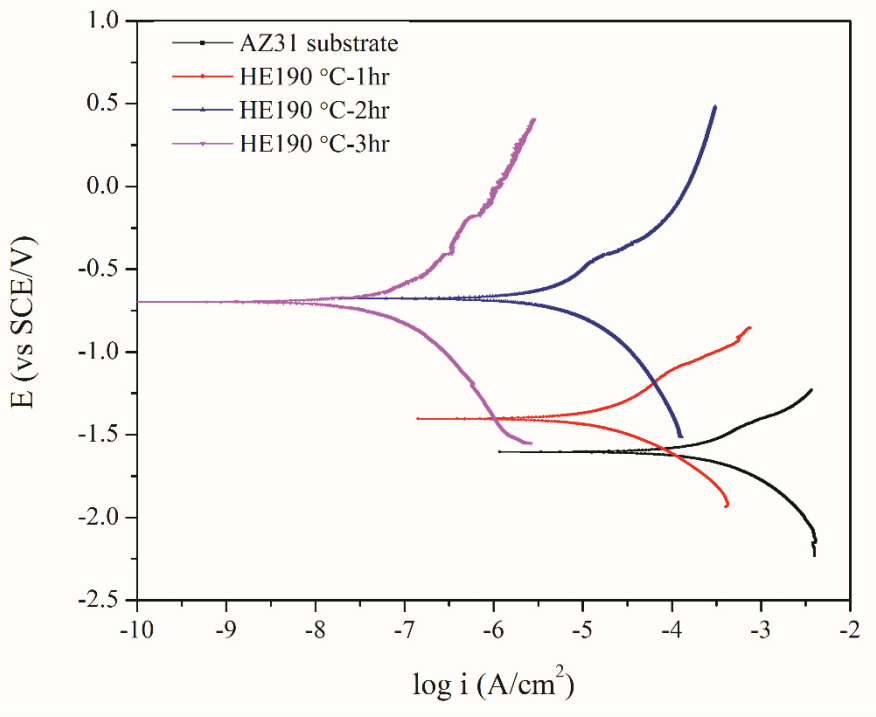


**Figure 6-3. Potentiodynamic curves of uncoated and coated samples at 190 °C**

**Table 6-1. Coating thickness and potentiodynamic polarization curve parameters**

| Sample | Coating Thickness (µm) | $i_{corr}$ (A/cm$^2$) | $E_{corr}$ (V vs. SCE) |
|---|---|---|---|
| AZ31 Substrate | 0 | $1.2*10^{-4}$ | -1.5 |
| HE100 ºC-3hr | 20 ±2.4 | $1.2*10^{-5}$ | -1.5 |
| HE130 ºC-3hr | 48 ± 4.8 | $2.8*10^{-6}$ | -1.1 |
| HE160 ºC-3hr | 61 ± 5.4 | $1.1*10^{-7}$ | -0.8 |
| HE190 ºC-3hr | 389 ± 10.2 | $2.3*10^{-8}$ | -0.7 |
| HE190 ºC-2hr | 150 ± 8.3 | $4.2*10^{-6}$ | -0.7 |
| HE190 ºC-1hr | 58 ± 3.7 | $2.2*10^{-5}$ | -1.4 |

### 6.2.2 Corrosion Performance of Composite Coatings

Fig.6-4 and Fig.6-5 show the potentiodynamic curves for HEPAA and HESCMS composite coatings respectively. The $E_{corr}$ of coated samples increased significantly (between 500 mV-1000 mV, depending on coating composition) compared to the AZ31 bare substrate which indicates the formation of a stable coating/substrate interface [93, 192]. Moreover, composite coatings showed higher corrosion resistance compared to the bare substrate. The corrosion resistance of AZ31 substrate was enhanced approximately 1000 fold by applying composite coatings. In the case of the HEPAA composite coatings, the variation in polymer concentrations has no significant effect on the corrosion performance. However, in the case of the HESCMS composite coatings, an increased polymer concentration slightly decreased the corrosion performance of the coatings. This was due to change in the coating morphology, as the coating become slightly porous with higher polymer content (Fig.4-19).

Fig.6-6 shows a comparison between corrosion performance of inorganic (HE160°C-3hr) and composite coatings indicating comparable corrosion resistance. The results showed that a HEPAA composite coating with porous structure has comparable corrosion resistance with HESCMS, this might be due to the adsorption of a polymer

layer (PAA) on the surface of the AZ31 substrate in the initial step of deposition of the HEPAA composite coating (as shown in the Fig.5-15) which could protect the substrate from solution attack.

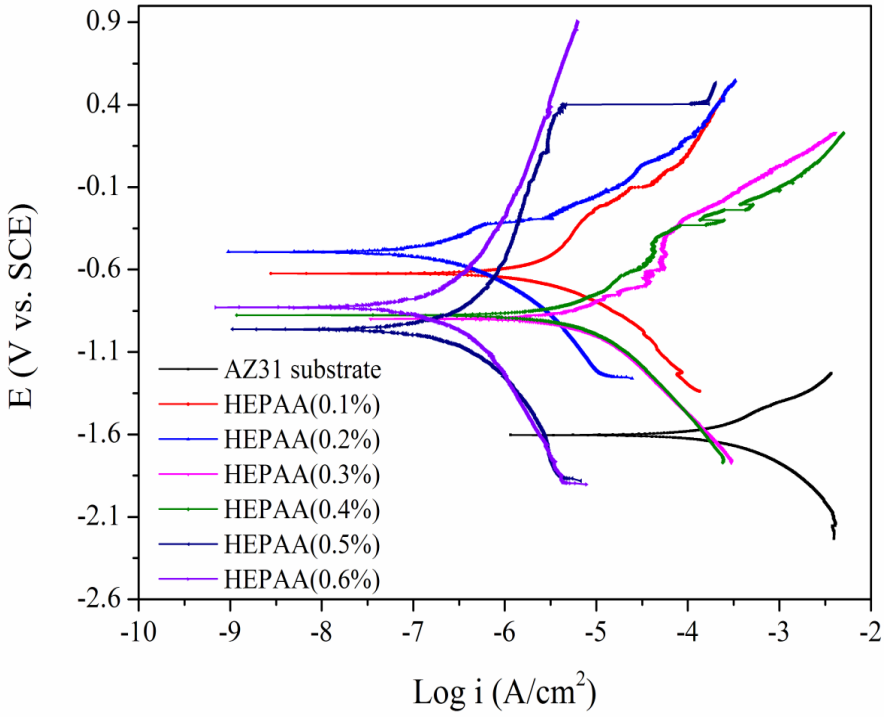


**Figure 6-4.Corrosion performance of HEPAA composite coating measured by potentiodynamic polarization**

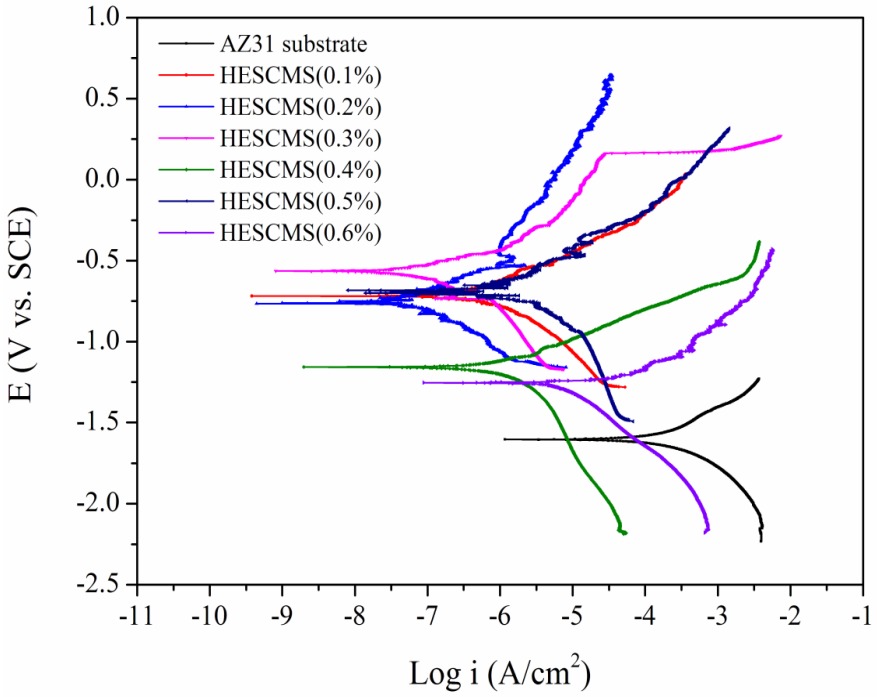


**Figure 6-5.Corrosion performance of HESCMS composite coating measured by potentiodynamic polarization**

The presence of a coating layer can prevent or delay the access of electrolyte to the Mg substrate and retard the initiation of corrosion process by limiting the availability of water needed for hydrogen generation. Thus, by applying coating and improving the coating morphology, the corrosion rate can be decreased [192]. The observations indicated that coating layers have a protective nature and could provide good protection for the AZ31 substrate.

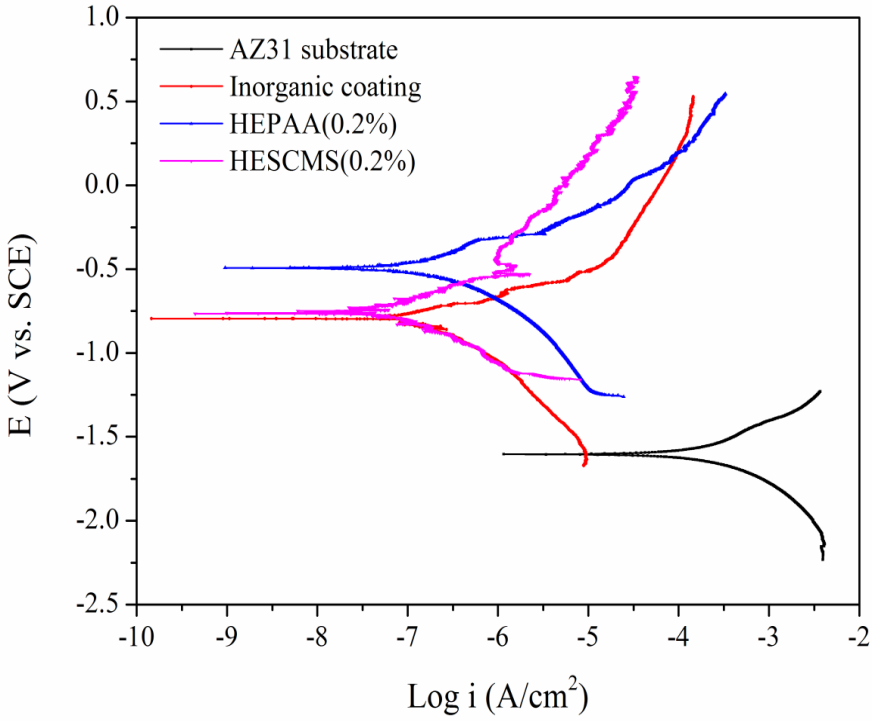


**Figure 6-6. A comparison between corrosion of inorganic and composite coatings measured by potentiodynamic polarization**

### 6.2.3 Electrochemical Impedance Spectroscopy (EIS) Results

EIS measurements were done to understand the corrosion behavior and performance of coated and uncoated substrate in a SBF solution. EIS measurements were analyzed by two methods: Nyquist impedance spectroscopy and Bode graphs. The Nyquist graph for the bare and coated samples with inorganic Ca-P layer is given in Fig.6-7. It was clearly observed that the Nyquist graph for a bare sample composed of two capacitive semi-circuits at medium and low frequency, followed by an inductive loop in the low frequency region. The Bode phase graph of a bare sample showed two phase maxima at low and medium frequency. The time constant at medium frequency can be attributed to the partially protective oxide layer, and the semi-circle at low frequency may be related to the charge transfer resistance ($R_{ct}$) and double layer capacitance ($C_{dl}$)

at the surface of substrate [184]. The calculated results from EIS graphs are reported in Table 6-2. The appearance of an inductive loop at low frequency is probably due to film weakening and pit incubation. Coated samples at 100 ºC, 130 ºC and 160 ºC only showed a capacitance loop at medium frequency. The capacitive loop at medium frequency may be attributed to the coating layer $R_p$. The calculated capacitances for these time constants were in the range of 4-12 µF. Since the double layer capacitance is normally between 20-50 µF [194], the appearance of the semi-circle is related to coating layer resistance. The size of capacitance loops were increased by increasing the deposition temperature. This is in parallel to the increase in charge transfer and polarization resistance which is a criterion for corrosion resistance enhancement [195].

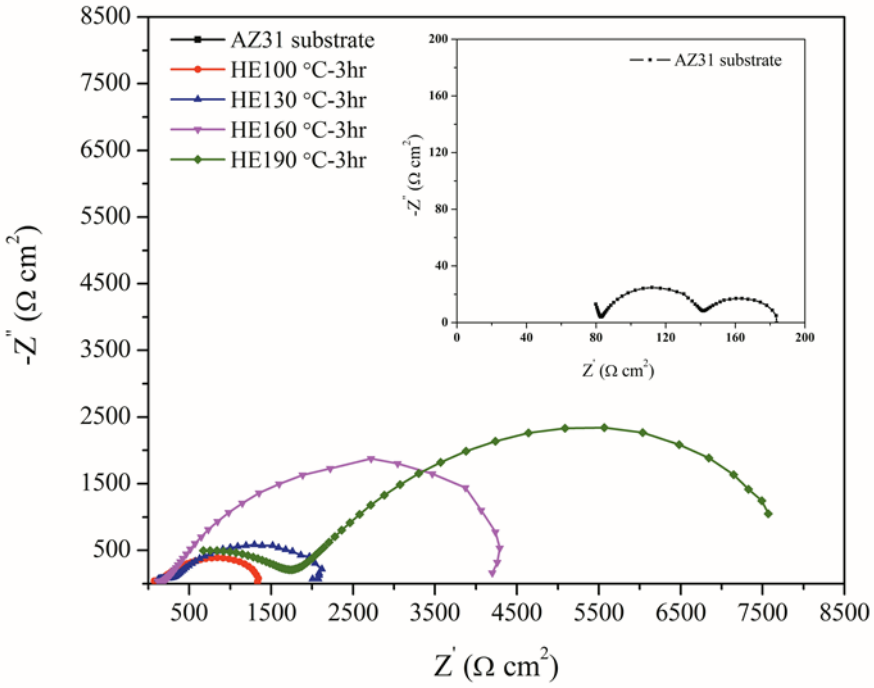


**Figure 6-7. Nyquist of uncoated and coated samples in SBF solution (Insert is AZ31 Nyquist graph)**

**Table 6-2. EIS parameters derived from impedance spectra**

| ***Sample*** | $R_{ct}$ $(\Omega.cm^2)$ | $R_p$ $(\Omega.cm^2)$ | $R_{ns}$ $(\Omega.cm^2)$ | $\|Z\|$ $(\Omega.cm^2)$ | $C_{dl}$ $(\mu F/cm^2)$ | $C_f$ $(\mu F/cm^2)$ | $C_{ns}$ $(nF/cm^2)$ |
|---|---|---|---|---|---|---|---|
| AZ31 substrate | 47.1 | 61.5 | … | 141 | 20.6 | 8.2 | … |
| HE100 °C-3hr | … | 1981 | … | 1421 | … | 3.9 | … |
| HE130 °C-3hr | … | 2143 | … | 2088 | … | 4.1 | … |
| HE160 °C-3hr | … | 4182 | … | 3305 | … | 9.6 | … |
| HE190 °C-3hr | … | 6478.9 | 2748 | 7712 | … | 12.3 | 0.58 |

The sample coated at 190 ºC showed a different behavior. The Nyquist graph was composed of two capacitive loops at high and medium frequency. The high frequency time constant can be related to the coating layer resistance and the presence of a capacitive loop at a medium frequency range can be related to the new surface formation at the electrode surface as a result of partial delamination of top surface of coating [196]. This result is in agreement with the potentiodynamic test data. According to Fig.6-1 and Fig.6-2 there is a significant difference between the OCP value for the coated sample at 190 ºC and its corrosion potential. Normally the values of these two potentials are close. However, the formation of a new surface during corrosion process can result in the shift of these potentials.

Since the deposited coating at 190 ºC was the thickest, the high thickness may result in increased residual stress and delamination of the top layer of coating resulting in the emergence of the second capacitive loop at medium frequency range as shown in Fig.6-8. However, for the coated sample at 190 ºC, the diameter of the capacitive loop at medium frequency was significantly larger than that of other coatings, which confirmed that this coating possesses a higher corrosion resistance compared to other coatings.

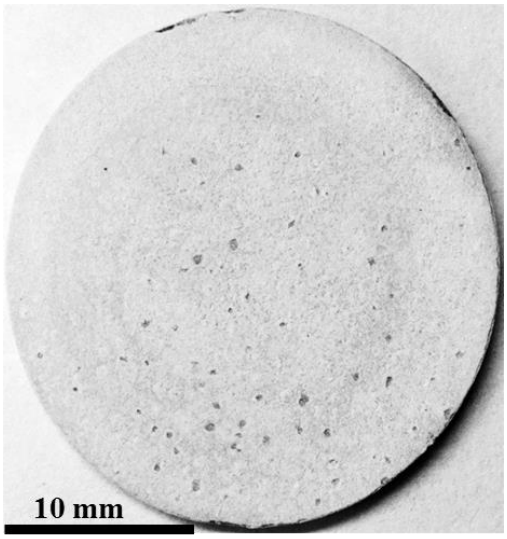


**Figure 6-8. Photograph of coated sample at 190 ºC after corrosion test**

Bode plot (Fig.6-9), shows that coated substrates have larger impedance (|Z|) values compared to the bare substrate, which means the corrosion performance of coated sample is much better than bare substrate [192]. The absolute impedance value (|Z|) increases by increasing the deposition temperature. The EIS results are thus in a good agreement with potentiodynamic results and confirmed that by increasing deposition temperature, the corrosion performance of coated samples improved.

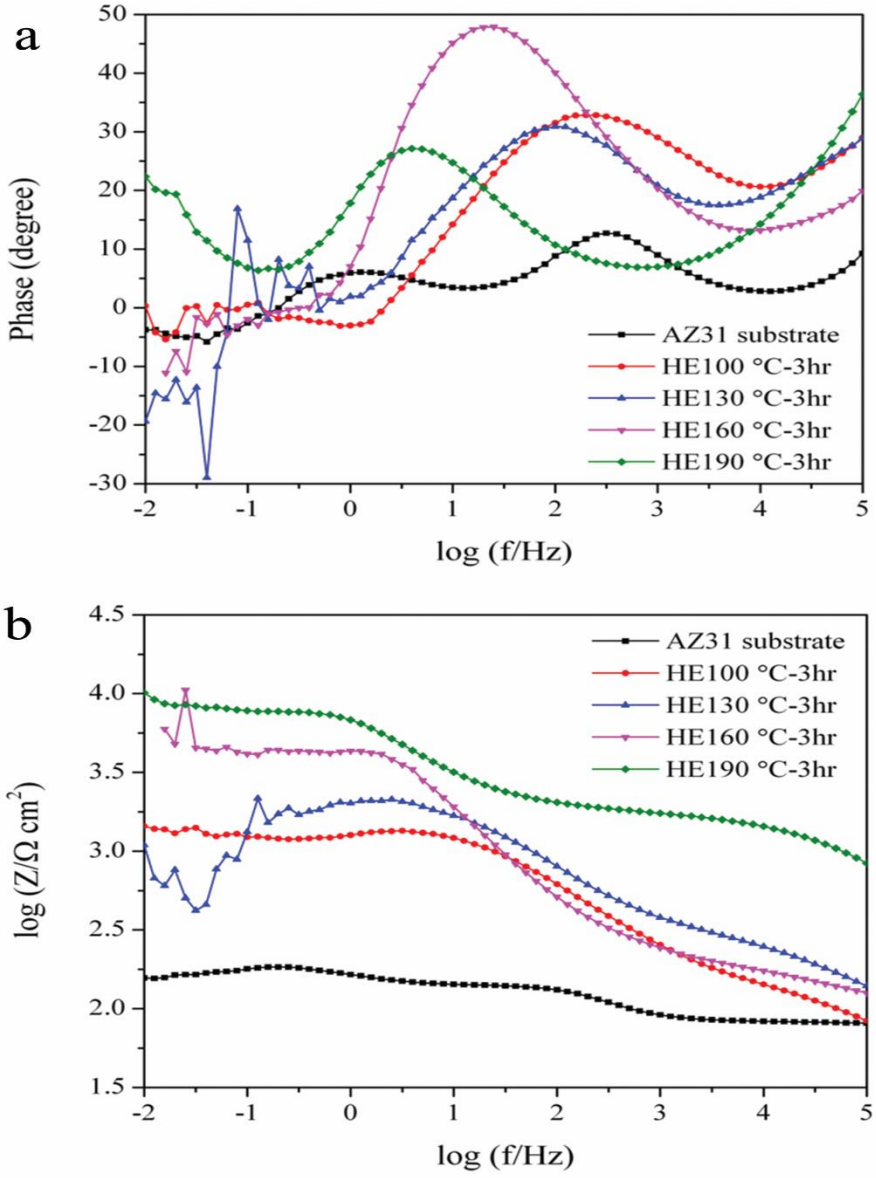


**Figure 6-9. a) Bode phase graph and b) Bode plot graph for uncoated and coated samples in SBF solution**

The impedance data for the bare and coated samples were fitted to theoretical models as shown in Fig.6-10. For the bare substrate, $C_f$ is considered as oxide film capacitance, while in the case of the coated sample it is related to the coating layer capacitance. $C_{ns}$ is related to the newly formed surface at the surface of coated sample at 190 ºC. $R_p$ and $R_{pns}$ represent the coating layer and newly formed surface polarization resistance

respectively. $R_{ct}$ represents the charge transfer resistance at the surface of substrate, $C_{dl}$ shows the double layer capacitance at the surface of electrode and L represents an inductance. The fitting results were in good agreement with the original impedance graphs.

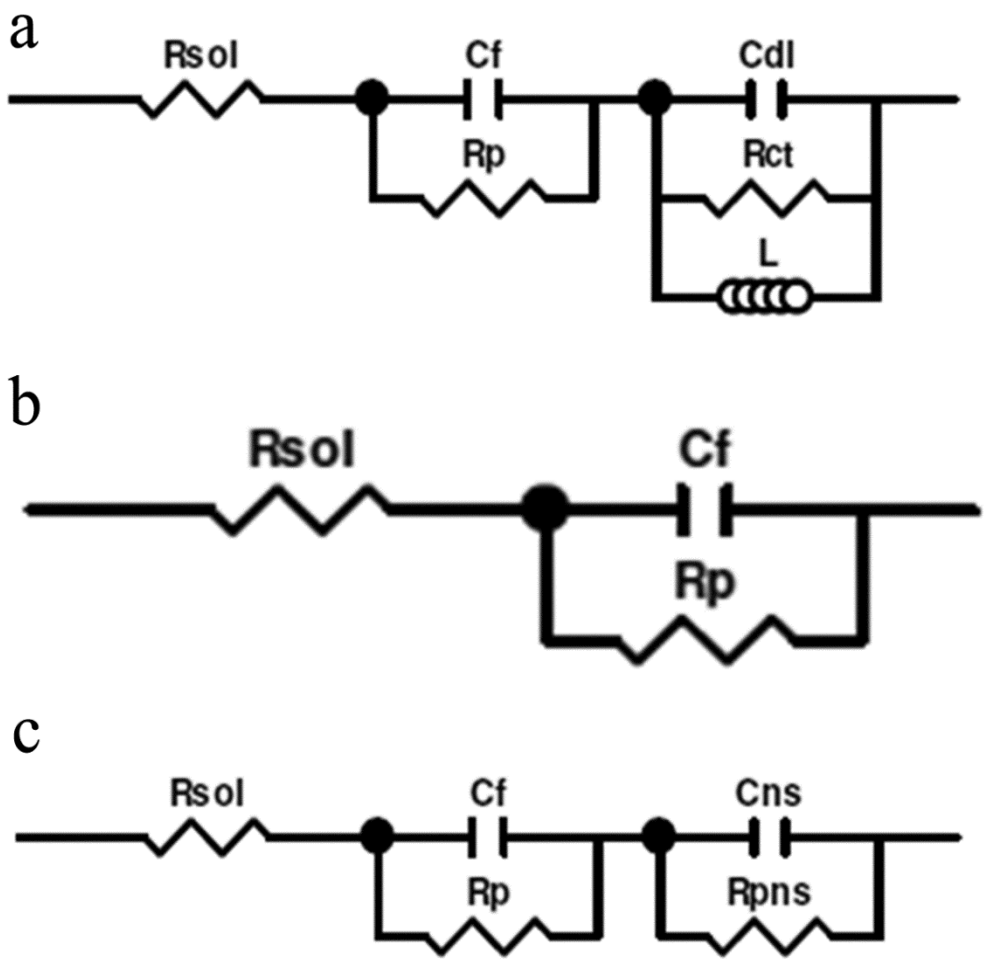


**Figure 6-10. Equivalent circuits for: a) uncoated substrate, b) coated samples at 100 °C, 130 °C and 160 °C and c) coated sample at 190 °C**

## 6.3 Long Term Corrosion Performance Evaluation by Immersion Test

The mass loss is a common test for evaluating corrosion performance as reported in literature [197, 198]. In this study, the mass loss of bare and coated samples was monitored during immersion in SBF solution as shown in Fig.6-11. After each immersion time, samples were extracted and corrosion products were removed by using chromic acid and silver nitrate according to the method described in the literature [199]. After removal of corrosion products, the samples were further cleaned with ethanol, and left in a dry box for one week to fully dry and remove adsorbed water from the coating. After drying, the mass loss for each sample was calculated by measuring the mass of sample before and after immersion in SBF solution using Eq.6-4.

$$\textbf{Mass loss} = \frac{(\mathbf{m_0 - m_1})}{\mathbf{S}} \quad \textbf{(}6\text{-}4\textbf{)}$$

$m_0$: mass of sample before immersion test

$m_1$: mass of sample after immersion test

S: sample's surface area

As soon as Mg is immersed in the SBF solution, corrosion takes place which results in the release of hydrogen gas and consequently formation of $Mg(OH)_2$ on the surface of Mg according to Eq.6-3. Since SBF solution contains aggressive ions such as chloride ($Cl^-$), the $Mg(OH)_2$ layer can convert into soluble $MgCl_2$ according to Eq.6-5 [200]. The soluble $MgCl_2$ cannot protect the surface of Mg, consequently the mass loss of the sample increases as the immersion time becomes longer resulting from Mg dissolution.

$$\mathbf{Mg(OH)_2 + 2Cl^- \rightarrow Mg(Cl)_2 + 2OH^-} \quad \textbf{(6-5)}$$

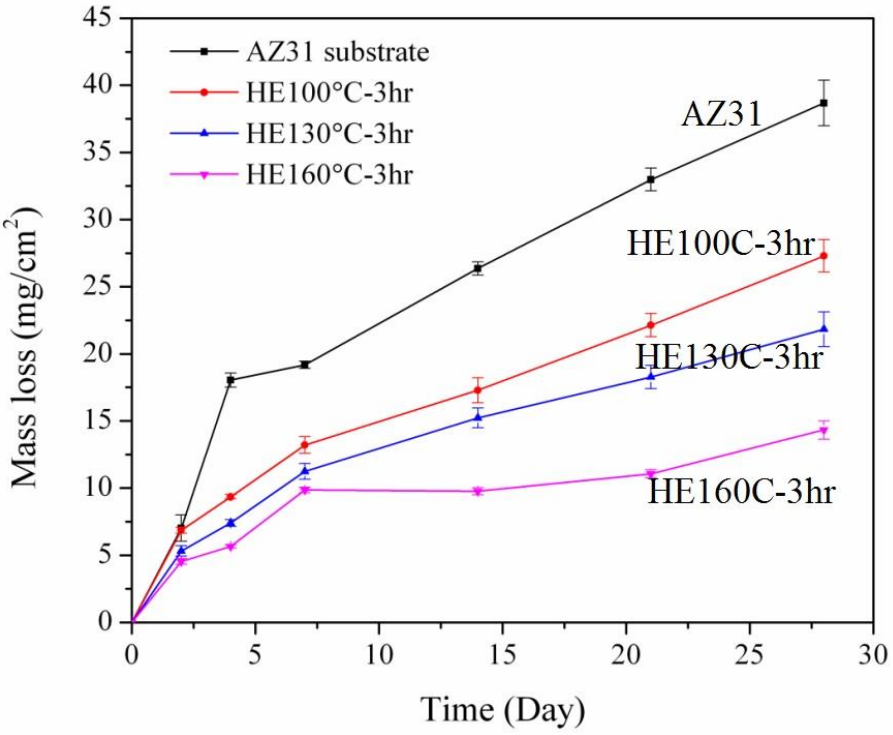


**Figure 6-11. Mass loss as a function of immersion time in SBF solution for uncoated and coated samples**

Conversely, coated samples would be expected to lose mass due to dissolution of the coating layer as well as corrosion of the Mg once it is exposed to the electrolyte via either existing coating defects or coating dissolution. In order to estimate the maximum contribution to mass loss due to coating dissolution, the coating weight can be calculated. Using the theoretical density of monetite and tricalcium phosphate based on their crystal structure parameters (the theoretical density of monetite is 2.93 g/cm$^3$ and the theoretical density of tricalcium phosphate is 3.13 g/cm$^3$), the coating density can be estimated to be in the range of 2.9 g/cm$^3$ to 3.1 g/cm$^3$. Taking the coating density as 3 g/cm$^3$ and assuming no porosity in the coatings based on the OCP results and previously coating morphology studies, this translates to approximately 3 mg/cm$^2$ coating weight for each 10 µm coating thickness.

The total mass loss from the uncoated AZ31 was 38.7 mg/cm$^2$ after 28 days immersion in a SBF solution, while samples coated at 160 ºC had mass loss of 14.3 mg/cm$^2$ compared to the estimated 18 mg/cm$^2$ original coating weight. In the case of samples coated at 100 ºC and 130 ºC, the mass loss after 28 days immersion in SBF solution was 27.3 mg/cm$^2$ (estimated 6 mg/cm$^2$ original coating weight) and 21.4 mg/cm$^2$ (estimated 14 mg/cm$^2$ original coating weight), respectively, indicating that a significant amount of mass loss must have been due to metal corrosion of these samples. The degradation rate of the Mg samples in the 28 days immersion test decreased three-fold as measured by the combined mass loss from corrosion and coating dissolution when applying the coating at 160 ºC. The electrochemical tests indicated a much higher reduction of corrosion rate (approximately 1,000 fold for a coating deposited at 160 ºC). However, it is necessary to consider the different time scales of the electrochemical and immersion tests. While the electrochemical tests characterize the corrosion resistance in the presence of intact coating, the immersion tests take a much longer time, allowing some defects to develop on the coating and resulting in a localized attack on the substrate. Once such localized coating defects occur, the corrosion can accelerate at the defect site allowing the eventual degradation of the metal substrate. In fact, such behavior is desirable for implant application when the alloy is initially well protected from corrosion but it can degrade more readily once the bone healing process is underway (the bone healing process takes 6-12 weeks, depending on fracture type) .

A comparison of mass loss for the inorganic (HE160 °C-3hr) and composite coatings [HEPAA(0.2%) and HESCMS(0.2%)] is shown in Fig.6-12. The total mass loss for HEPAA(0.2%) and HESCMS(0.2%) after 28 days immersion in SBF solution were 17.43 mg/cm$^2$ and 16.5 mg/cm$^2$ respectively, while the mass loss for the inorganic coating was 14.32 mg/cm$^2$. The slightly higher mass loss for the composite coatings

compared to inorganic coating may be resulted from incorporation of a polymer into the coating structure. Polymers have higher degradation rate than Ca-P phases, therefore, incorporation of biodegradable polymers such as PAA and SCMS could increase the degradation rate of the coatings [201-203].

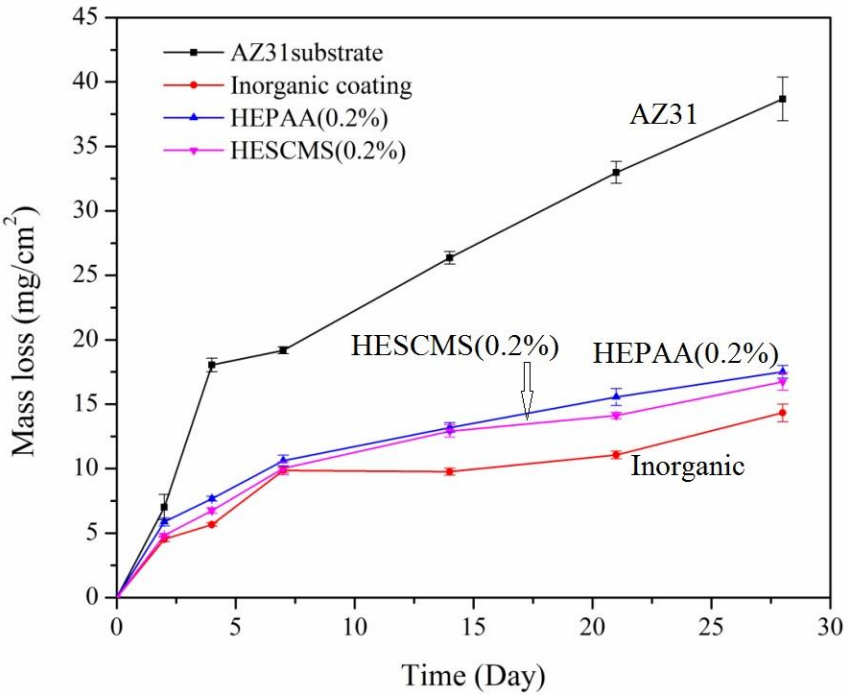


**Figure 6-12. A comparison of mass loss as a function of immersion time for inorganic and composite coating**

From the TGA analysis the PAA amount in the HEPAA(0.2%) composite coating (Fig.4-20) is 9.05 wt.% and in the case of HESCMS(0.2%) coating the SCMS amount in the coating (Fig.4-21) is 4.33 wt.%; therefore the higher degradation rate of HEPAA(0.2%) coating might be a result of a higher amount of incorporated polymer into the coating structure. Based on the literatures the resorption rate of tricalcium phosphate is much lower than monetite; the orders of relative solubility of Ca-P phases are as follows:

Amorphous calcium phosphate (ACP) > Monetite (DCP) > Tetracalcium phosphate (TTCP) > α-Tricalcium phosphate (α-TCP) > β-Tricalcium phosphate (β-TCP) >HA. However, a polymer addition into Ca-P structure had a significant effect on coating degradation. The increase in HA solubility with adding PAA is also reported in literature [204]. Besides that, polymer degradation by itself is dependent on polymer hydrophilicity, molecular weight and end functional group.

Generally, a polymer with a lower average molecular weight has a higher degradation rate [205]. The polymers that we used in this project had different molecular weight. PAA ($M_w$: 450000 units) has lower molecular weight compared to SCMS ($M_w$: 700000 units); therefore, PAA should has higher degradation rate and consequently affect and increase the HEPAA(0.2%) coating degradation rate.

Another factors that could affect degradation rate of coatings are their physical form, composition, crystal structure and crystal size [204]. The crystal size of HEPAA(0.2%) coating was smaller than HESCMS(0.2%) coating and also the HEPAA(0.2%) coating has a porous morphology. All these factors could affect the coating degradation rate and resulted in slightly higher degradation rate of HEPAA(0.2%) compared to HESCMS(0.2%) and inorganic coatings, unlike what was expected. It was expected that HEPAA(0.2%) coating shows lower degradation rate compared to other coatings, since HEPAA(0.2%) coating is mainly composed of tricalcium phosphate which is less soluble than monetite phase [HESCMS(0.2%) and inorganic coatings are mainly composed of monetite phase]. However, a combination of different factors like polymer content, polymer type, polymer molecular weight, coating's morphology and coating crystal size define the real dissolution rate of coating. The EDS analysis results of coated and uncoated samples after 28 days immersion test are given in Table 6-3.

**Table 6-3. EDS analysis after 28 days immersion test in simulated body fluid**

| Sample | Element (Wt.%) | | | | | |
|---|---|---|---|---|---|---|
| | C | O | Mg | P | Ca | Cl |
| AZ31 substrate | … | 57.46 | 23.14 | 6.47 | 9.08 | 3.85 |
| HE100 C-3hr | 3.49 | 48.91 | 14.19 | 10.21 | 14.44 | 8.75 |
| HE130 C-3hr | 7.79 | 53.46 | 5.41 | 12.86 | 20.49 | … |
| HE160 C-3hr | … | 58.14 | 1.32 | 16.42 | 24.13 | … |
| HEPAA(0.2%) | 15.76 | 29.37 | 3.88 | 29.64 | 21.34 | … |
| HESCMS(0.2%) | 10.91 | 16.93 | 3.92 | 17.97 | 50.26 | … |

### 6.3.1 Surface Morphology Study after Immersion Test

Photographs of tested samples after 28 days immersion in SBF solution are shown in Fig.6-13. As it can be seen from Fig.6-13, the uncoated Mg substrate undergoes severe and non-uniform corrosion. As immersion time increased to 28 days, the pits on the surface of Mg became wider and started to penetrate through the substrate thickness. In some parts of the substrates, pits propagated through the whole 2 mm substrate thickness leading to premature loss of mechanical integrity. On the other hand, the Ca-P coated samples at 130 ºC and 160 ºC as well as composite coatings displayed little change in the coatings and no obvious pits were observed on the coating surface.

Since the $Mg(OH)_2$ layer formed from the metal is not protective and can transform into soluble $MgCl_2$, the breakdown of $Mg(OH)_2$ layer can provide more active sites on the Mg surface, which accelerates the substrate corrosion. Moreover, the difference in electrochemical activities of different phases in the alloy results in the formation of microcells and consequently galvanic corrosion can happen after dissolution of protective layers resulting in the formation of a non-uniform corrosion process [200].

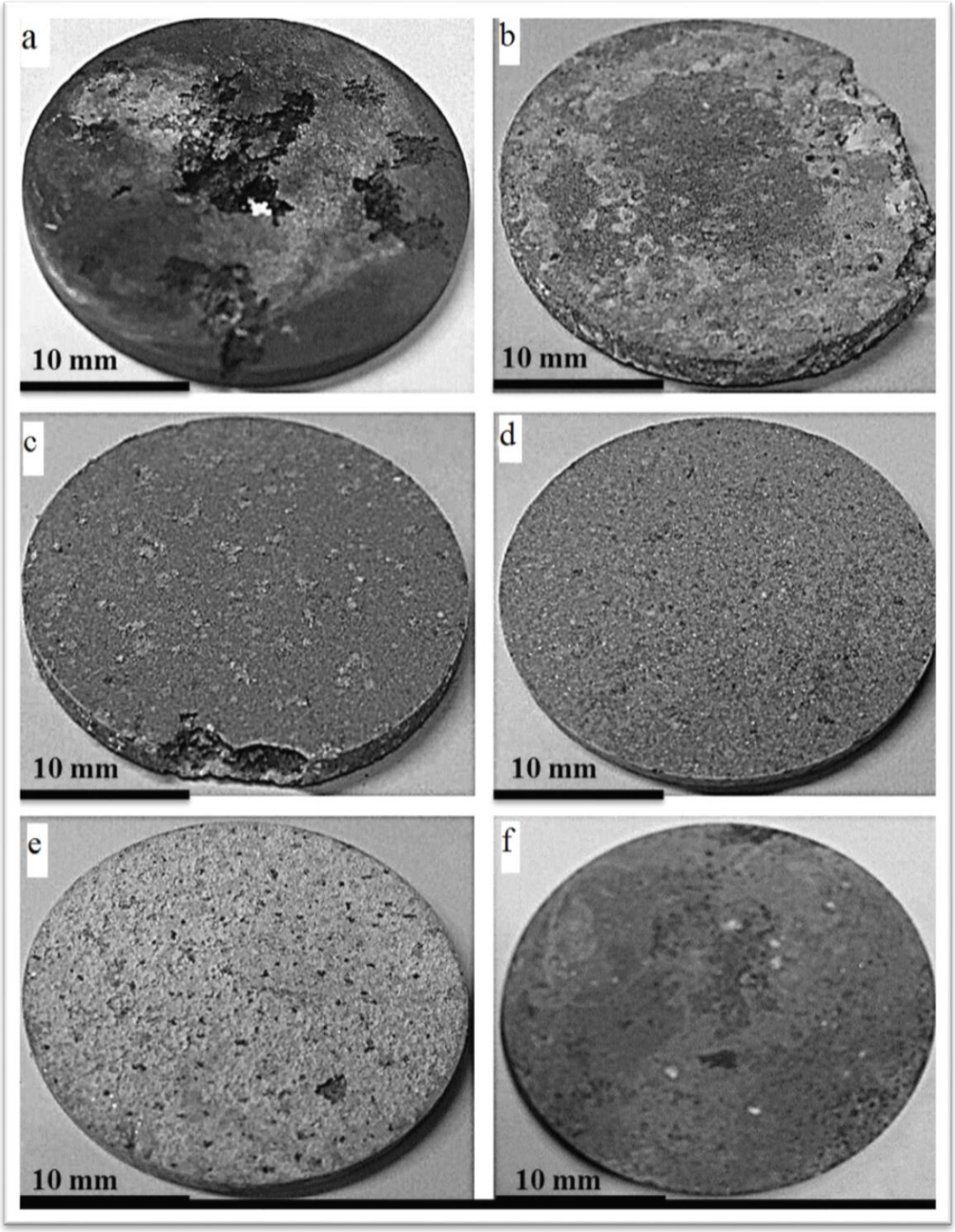


**Figure 6-13. Photographs of tested samples after 28 days immersion test: a) AZ31 substrate, b) HE100 °C-3hr, c) HE130 °C-3hr, d) HE160 °C-3hr, e) HEPAA(0.2%) and f) HESCMS(0.2%)**

SEM images of the bare and coated samples after 28 days immersion test are shown in Fig.6-14. It is clear that surfaces of bare AZ31 substrate and HE100 °C-3hr undergo severe corrosion and show a rough appearance. However, in the case of coated sample at 130, 160 ºC and HESCMS(0.2%) the coating layers still remained on the surface of substrate but Ca-P crystals started to dissolve as some pits appeared on their surfaces. Formation of pits on the surface of Ca-P crystals might be attributed to the dissolution of monetite. Monetite is a stable phase below pH value around 5. Since the pH was around 7.2-7.4 in the SBF solution, this higher pH could break down the thermodynamic equilibrium at the interface of monetite and solution and results in dissolution of monetite phase according to Eq.6-6 [206].

$$\mathbf{CaHPO_4 \rightarrow Ca^{2+} + HPO_4^{2-}} \qquad \textbf{(6-6)}$$

Even though the mass loss for the HEPAA(0.2%) composite coatings was slightly higher that HE160 °C-3hr, but no significant changes were observed in the coating morphology.

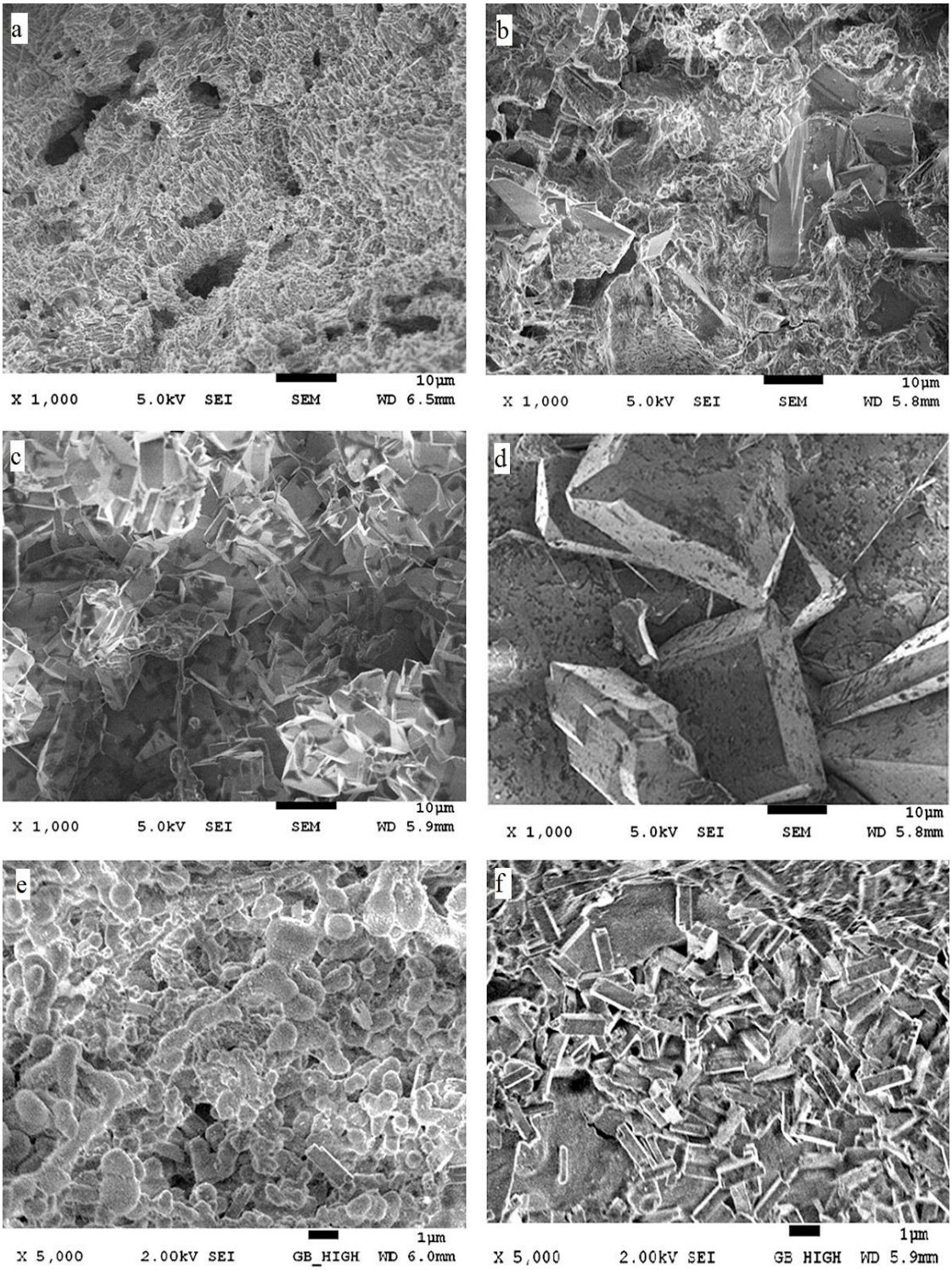


**Figure 6-14. SEM micrographs of tested samples after 28 days immersion test: a) AZ31 substrate, b) HE100 °C-3hr, c) HE130 °C-3hr, d) HE160 °C-3hr, e) HEPAA(0.2%) and f) HESCMS(0.2%)**

### 6.3.2 Ion Release Measurements and pH Monitoring

The Mg, Zn and Al ions release of uncoated and Ca-P coated samples were measured by means of ICP techniques. The results are shown in Fig.6-15 for Mg ions release. Cumulative Zn and Al release did not exceed 0.2 ppm/cm$^2$ for the 28 days immersion period. For the uncoated samples, the Mg ion release increased from 83 ppm/cm$^2$ after 2 days immersion to 174 ppm/cm$^2$ after 28 days immersion in SBF solution.

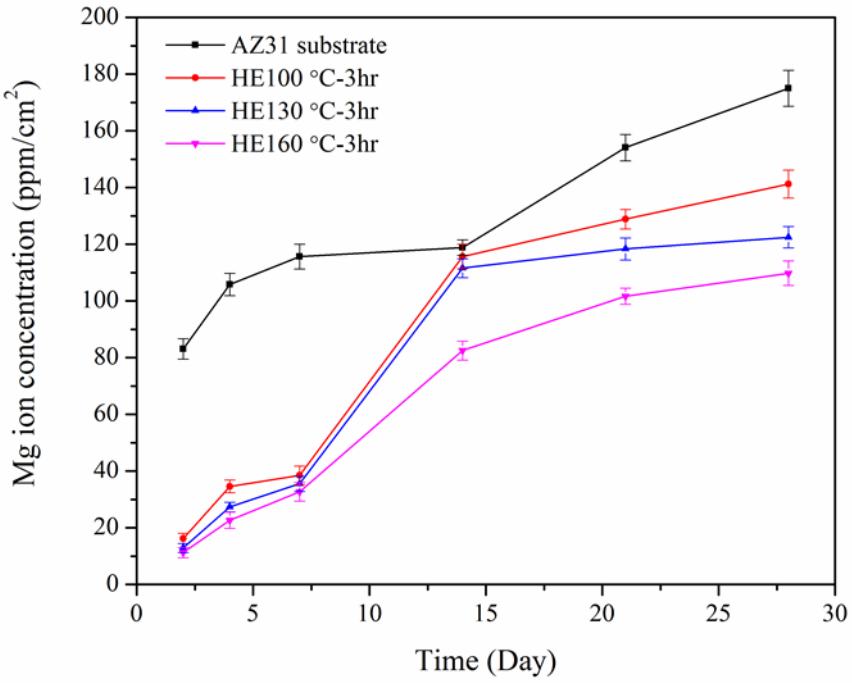


**Figure 6-15. Mg ion release from bare and Ca-P coated samples during immersion test (solution volume: 5 ml)**

The release of $Mg^{2+}$ from Ca-P coated samples was low compared to the uncoated sample. In the case of samples coated at 160 ºC, $Mg^{2+}$ release started from 11 ppm/cm$^2$ after 2 days of immersion and reached to 108 ppm/cm$^2$ after 28 days immersion in

SBF solution. The results show that Ca-P coatings can protect Mg substrate from corrosion and can decrease its degradation rate significantly.

A comparison of $Mg^{2+}$ release from inorganic and composite coatings is shown in Fig.6-16. In the case of HEPAA(0.2%) composite coating the $Mg^{2+}$ release started from 36 ppm/cm$^2$ after 2 days and reached to 140 ppm/cm$^2$ after 28 days immersion test. On the other hand, $Mg^{2+}$ release from HESCMS(0.2%) composite coating was in the range of 32-125 ppm/cm$^2$ during 28 days immersion in SBF solution.

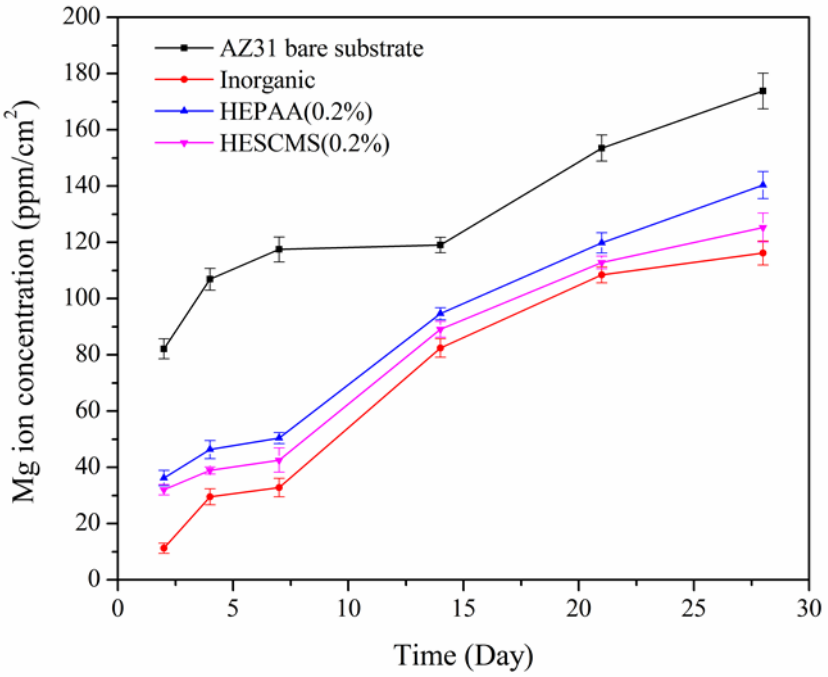


**Figure 6-16. Mg ion release from bare sample, inorganic and composite coatings during immersion test (solution volume: 5 ml)**

In general the $Mg^{2+}$ release from composite coatings was slightly higher compared to inorganic coating; however, the ion release was still lower than the bare substrate. The higher ion release from composite coatings could be a result from a slightly higher degradation rate of composite coatings compared to an inorganic coating as explained in the previous section; or it might be resulted from release of Mg ions that combined and chelated with $COO^-$ in a polymer structure.

Apart from $Mg^{2+}$ release, fast hydrogen evolution and consequently alkalization are critical issues resulting from Mg corrosion that may delay the healing process and adversely affect new tissue formation and cell proliferation. To see if the present coatings can overcome this problem, the change in pH over immersion time in SBF solution was monitored for uncoated and coated samples, and the results are shown in Fig.6-17. The initial measured pH value of the SBF solution was 7.35, and it increased significantly after one-day immersion to 8.4 and leveled out to 9.95 after 10 days immersion for uncoated sample. For the inorganic Ca-P coating (deposited at 160 ºC) the change in pH (to 7.42) was minor after one-day immersion and increased to 8.35 after 10 days immersion. The change in pH for composite coatings was almost similar as inorganic coating and it reached to 8.3 and 8.6 for HEPAA(0.2%) and HESCMS(0.2%) composite coatings respectively. The results confirmed that the present coating can moderate the pH increase induced by Mg corrosion.

The presence of a coating layer acts as a barrier to prevent access of electrolyte to the substrate. By increasing the immersion time, the solution can penetrate through the coating via pits and the substrate dissolution and pH increase start. However, the changes in the pH values were much smaller for coated samples than for bare substrate.

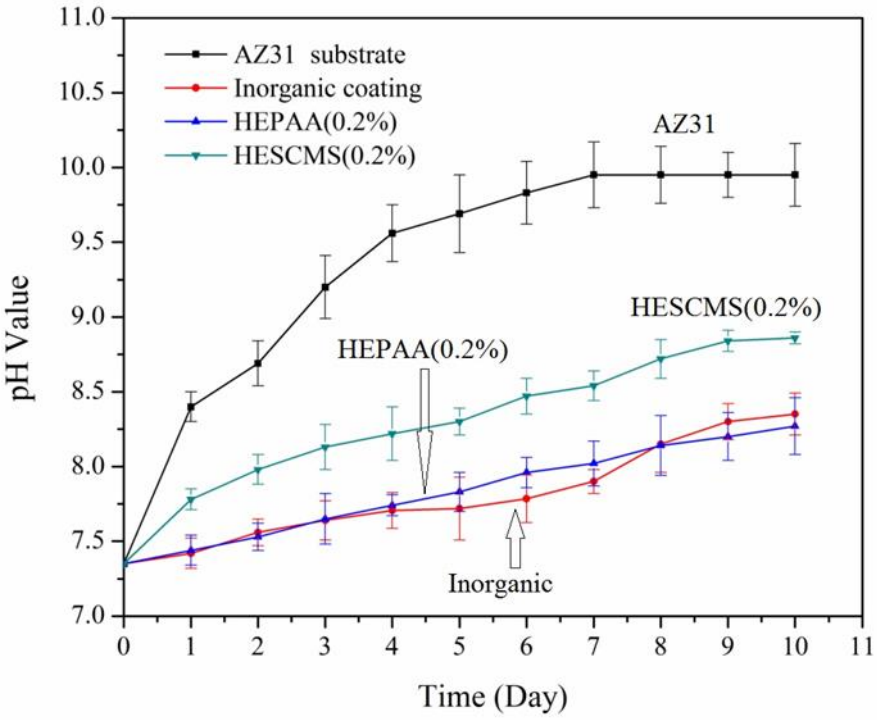


**Figure 6-17. Change in pH value after different immersion times**

This phenomenon might be explained by Eq.6-7 and Eq.6-8 describing the dissolution of the coating. As a result of dissolution of monetite or tricalcium phosphate phase, $HPO_4^{2-}$ or $PO_4^{3-}$ ions are released from the surface which can moderate the pH increase due to substrate dissolution.

$$\mathbf{CaHPO_4 \rightarrow Ca^{2+} + HPO_4^{2-}} \quad \textbf{(6-7)}$$

$$\mathbf{Ca_3(PO_4)_2 \rightarrow 3Ca^{2+} + 2PO_4^{3-}} \quad \textbf{(6-8)}$$

Moreover, during the immersion test in the SBF solution, coatings partially could convert to the HA phase through the dissolution-reprecipitation mechanism. The dissolution of coatings at this slightly alkaline pH and concurrent precipitation of $Ca^{2+}$ and $PO_4^{3-}$ ions due to their high concentration in SBF solution leads to eventual thermodynamic equilibrium by the conversion of coatings into HA. The conversion may be described by Eq.6-9 and Eq.6-10 [206]:

$$5Ca^{2+} + 3HPO_4^{2-} + OH^- \rightarrow Ca_5(PO_4)_3(OH) \quad \textbf{(6-9)}$$

$$5Ca^{2+} + 3PO_4^{2-} + OH^- \rightarrow Ca_5(PO_4)_3(OH) \quad \textbf{(6-10)}$$

As it can be seen from Eq.6-9 and Eq.6-10 some $OH^-$ ions are consumed during the formation of HA phase, which also helps to keep the solution's pH from rising rapidly.

## 6.4 Mechanical Properties of Coating

Ca-P coatings are known to be stiff and brittle which leads to early failure of the bone-implant interface. On the other hand, polymers exhibit relatively low mechanical strength and stiffness which do not meet the mechanical demands in bone regeneration applications. Composite coating with a combination of Ca-P as inorganic part and bioresorbable polymers as organic component can be an ideal approach to obtain adjustable mechanical properties [207] . Mechanical properties of coatings and the effect of polymer incorporation into the coating structure were evaluated by means of nano-indentation and scratch tests.

### 6.4.1 Nano-indentation Test Results

Figure.6-18 shows a comparison between load-displacement curves of inorganic and composite coatings. In load-displacement plots, lower indentation depth indicates a higher hardness and a higher slope of unloading curve which indicates high stiffness of the sample [208]. The Ca-P coating showed the lowest indentation depth (around 83 nm) compared to composite coatings.

Moreover, in the case of Ca-P inorganic coating, a loading curve for indentation shows sudden displacements. This behaviour can be attributed to brittle failure and suggests the growth of micro cracks during loading or may be related to deboning or

delamination of coating [208]. On the other hand, the composite coatings had smooth indentation curves without any displacement, indicating no cracking and higher resistance to crack formation. In the composite materials, the polymer bridge resists crack formation and propagation [207]. Thus, by incorporating the polymer, the brittleness of the coating can be significantly reduced and the coating modulus can be adjusted to be close to that of Mg for optimum mechanical matching between substrate and coating. The increased coating ductility prevents or at least decreases the crack formation tendency.

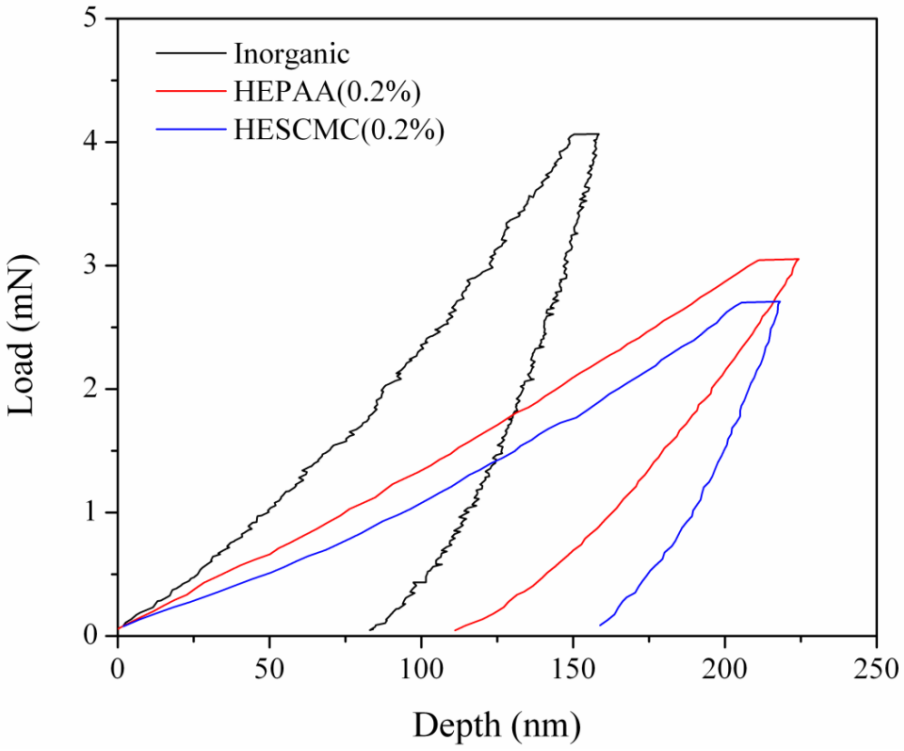


**Figure 6-18. Load-displacement curves in nano-indentation**

Fig.6-19 and Fig.6-20 show a comparison between mechanical properties of inorganic and composite coatings versus polymer content in the coating structure. Ca-P inorganic

coating shows high hardness (5.7 GPa) and Young's modulus (98 GPa). Incorporating polymer in the coatings reduced the inorganic content in the coating and consequently reduces both hardness and Young's modulus significantly. Young's modulus of HEPAA(0.2%) [With 9.05 wt.% polymer content] and HESCMS(0.2%) [With 4.24 wt.% polymer content] were very close to that of the Mg substrate at 50 GPa and 47 GPa, respectively. Similarity between mechanical properties of substrate and coating could be beneficial and significantly reduce the substrate-coating interface stress and concomitant failure.

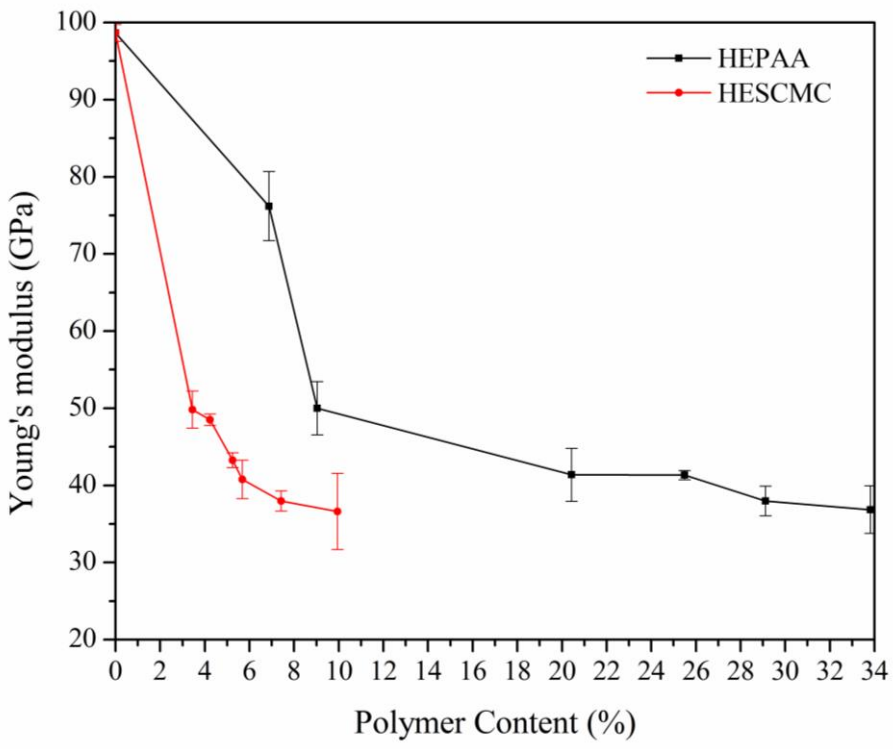


**Figure 6-19. Comparison between Young's moduli of coatings vs. polymer content in the coating**

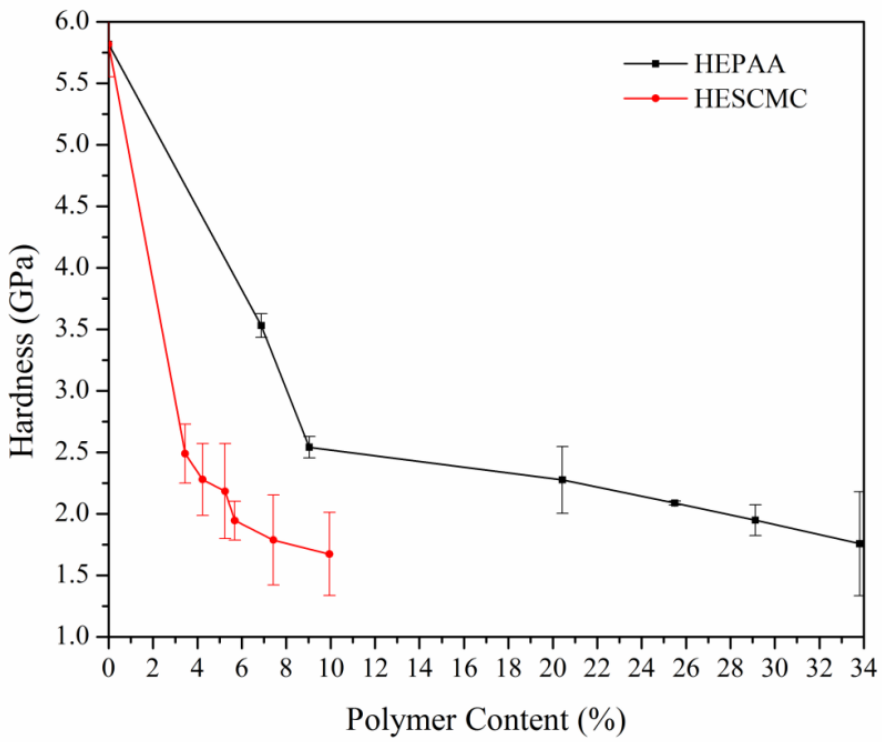


**Figure 6-20. Comparison between hardness of coatings vs. polymer content in the coating**

### 6.4.2 Scratch Test Results

Evaluation of the crack formation and failure mode in the coating was further investigated with scratch testing. Fig.6-21 shows the change in friction force ($F_f$) versus distance for inorganic and composite coatings. The Ca-P inorganic coating's graph showed an abrupt increase in friction force at 2584 mN which can be related to delamination or crack formation in the coating. On the other hand, the HESCMS composite coating graph indicated no major friction force fluctuations in the test, while the HEPAA composite coating showed a small increase in friction force at 2782 mN. In the scratch testing, friction force varied as different types of damage occur in the scratch track. Distinct changes in friction coefficient and friction force are indication

of damage event in the scratch test [209]. Fig.6-22 shows a comparison between friction coefficients (COF) of different coatings. COF of inorganic Ca-P coatings was higher compared to composite coating and fluctuated drastically. An abrupt increase in COF shows that the surface has experienced or undergone some damages such as coating delamination or micro cracking [209]. For the composite coatings, COF was relatively low and steady.

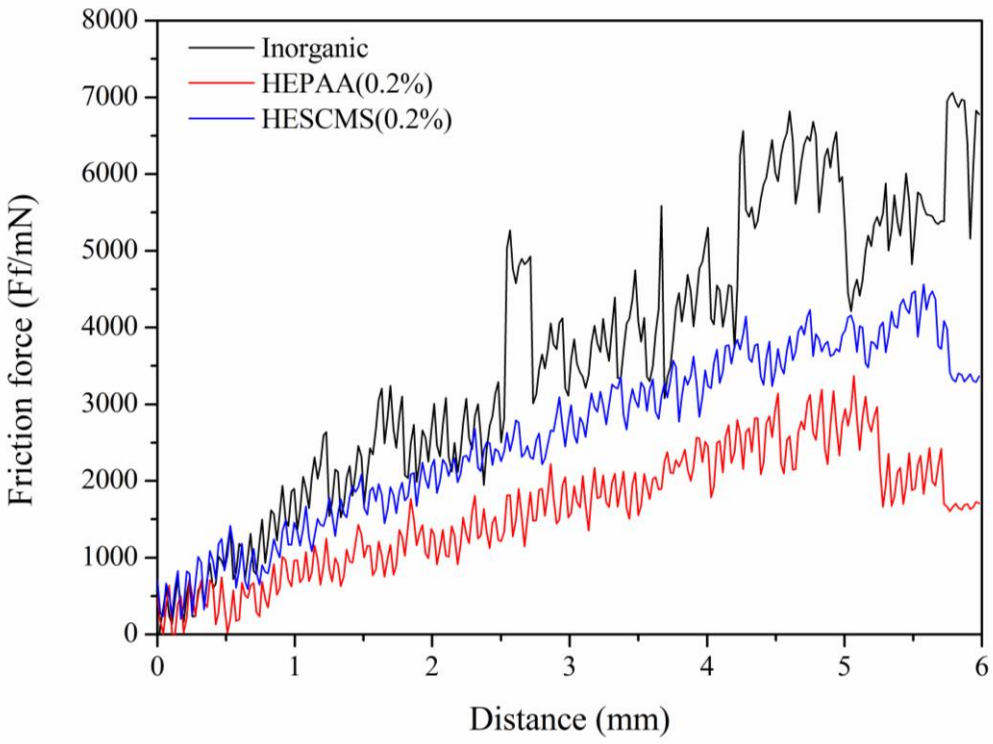


**Figure 6-21. Change in friction force vs. distance in the scratch test (Load was increased linearly over time)**

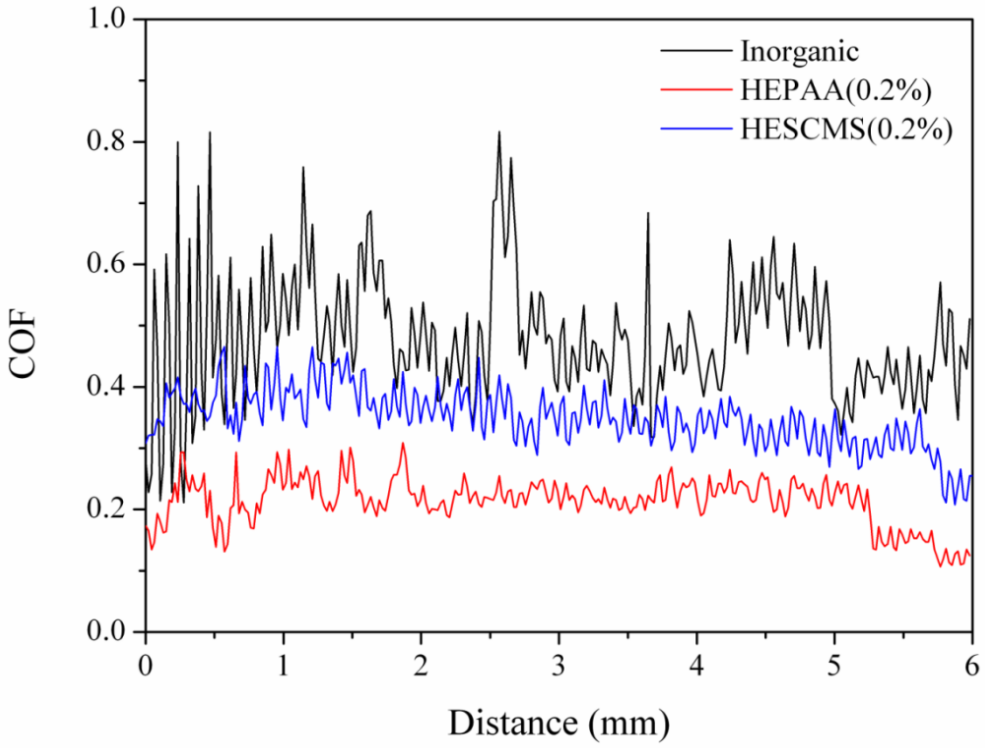


**Figure 6-22. Change in friction coefficient vs. distance in the scratch test**

Fig.6-23 shows optical micrographs of the coatings after the scratch test and Fig.6-24 shows the SEM micrograph of the coatings at higher magnification revealing the damage event during the scratch test. Coating failure was characterized by crack formation through the scratch path. According to Fig.6-23 the trackside spallation was observed for the Ca-P inorganic coating while the scratch paths were consistence and no damage was observed for the composite coatings. The delamination of the coating is characterized by the white portion along the scratch path in Fig.6-23 which was severe for Ca-P inorganic coating, but it was partial for the HEPAA composite coating. While, the HESCMS composite coating showed no delamination along the scratch path.

An examination of the sample's SEM images after the scratch test showed that different coating failures can be identified. The Ca-P inorganic coating clearly showed

crack formation and spallation of coating, however no crack formation was observed for the HEPAA and HESCMS composite coatings. Although, composite coatings showed partial coating's delamination which was minor compared to inorganic coating, suggesting that incorporation of polymer significantly affects the crack formation tendency.

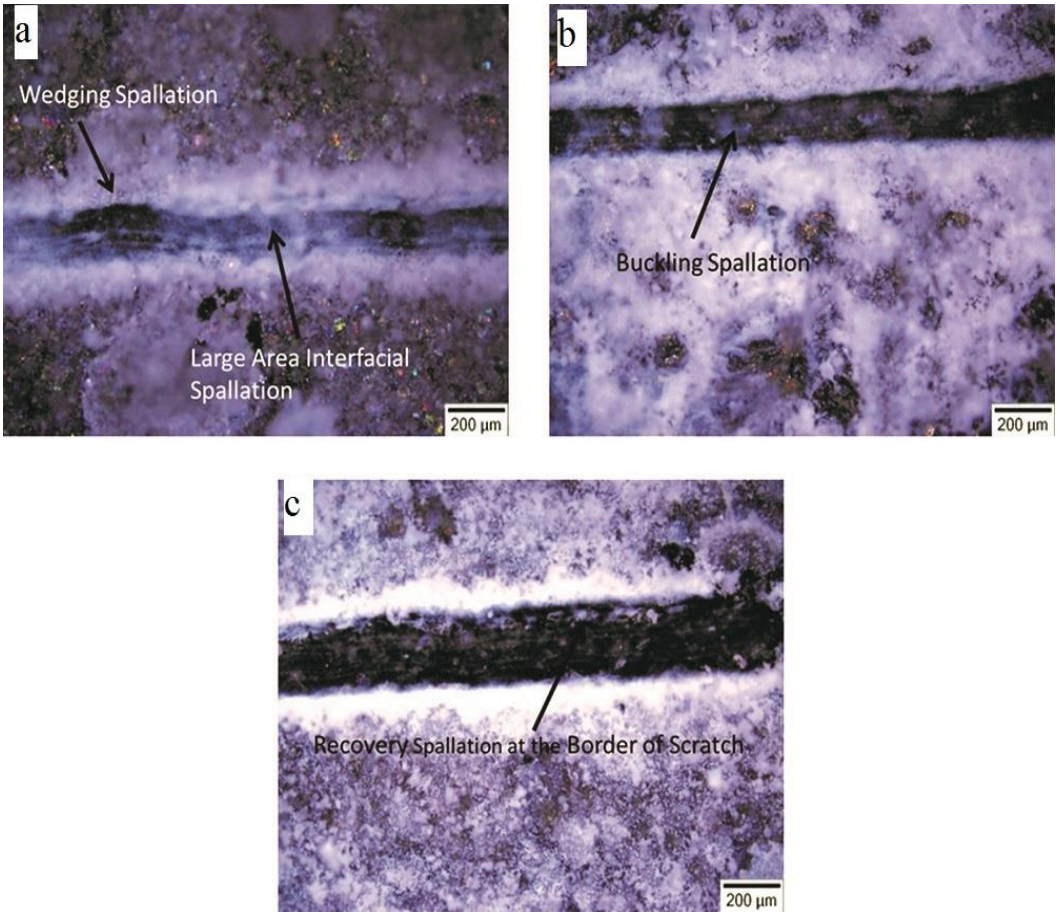


**Figure 6-23. Optical micrographs of scratch track: a) inorganic coating, b) HEPAA(0.2%) and c) HESCMS(0.2%)**

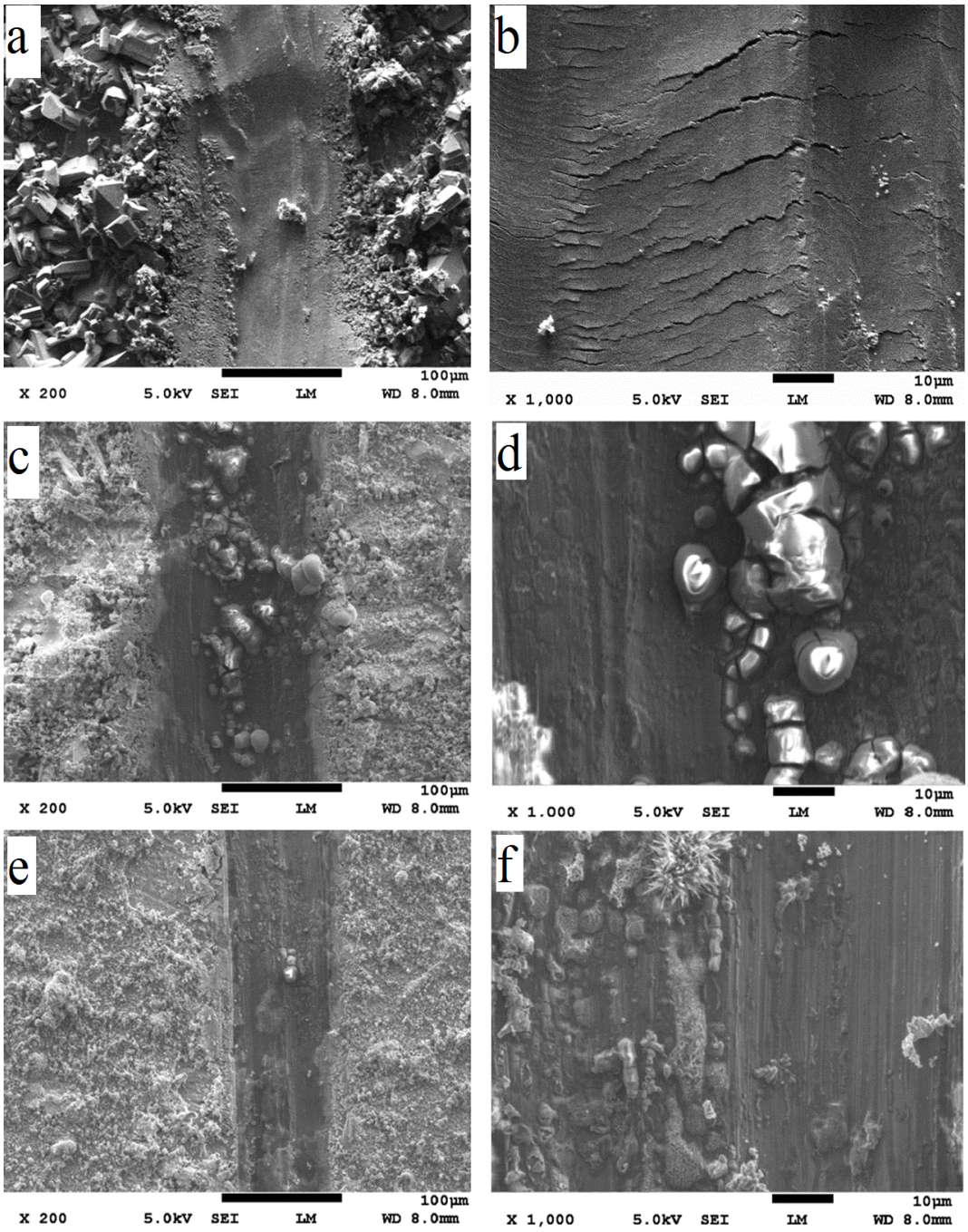


**Figure 6-24. SEM micrographs of scratch track: a), b) inorganic coating, c, d) HEPAA(0.2%) and e, f) HESCMS(0.2%)**

Nano-indentation and scratch test results showed that incorporation of the polymers can significantly improve the mechanical performance of the coatings. Based on nano-

indentation results, the use of a 0.2 wt.% polymer in the deposition bath (SCMS or PAA) adjusted Young's modulus of coating close to the Mg substrate [50 GPa for HEPAA(0.2%) and 47 GPa for the HESCMS(0.2%), compared to 98 GPa in the case of inorganic Ca-P coating and 41-47 GPa for Mg substrate]. Unlike an inorganic Ca-P coating, there was no significant change in COF or $F_f$ for the composite coatings showing no sign of crack formation.

### 6.4.3 Effect of Coatings on Mechanical Integrity of AZ31 Substrate

Biodegradable implants must maintain their mechanical integrity until bone healing is achieved. In order to determine the effect of coating on the delay of substrate disintegration, cylindrical bare and coated samples were immersed in SBF solution for up to 28 days. After each predetermined immersion time the compressive strength of bare and coated samples were measured.

Fig.6-25 shows the change in compressive strength of samples after immersion in a SBF solution, it is clear that uncoated samples suffered from a significant decrease in mechanical strength after 28 days immersion in a SBF solution. The compressive strength of bare substrate decreased from 452 MPa to 299 MPa, while in the case of inorganic coating, HEPAA(0.2%) and HESCMS(0.2%) coatings decreased from 452 MPa to 402, 393 and 397 MPa respectively. These results confirmed that the deposited protective and corrosion resistant coatings can significantly delay the initiation of mechanical strength degradation.

Photographs of bare and coated samples after 28 days immersion test are shown in Fig.6-26. The bare substrate had suffered from severe corrosion and the sample surface was irregular, while the corrosion level for coated samples was moderate and coatings still were preserved.

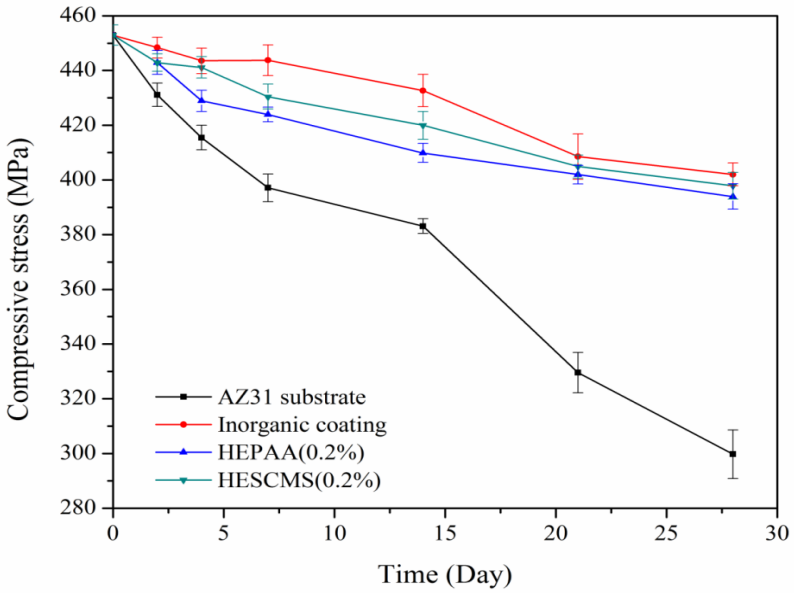


**Figure 6-25. Change in samples compression stress after an immersion test in SBF solution**

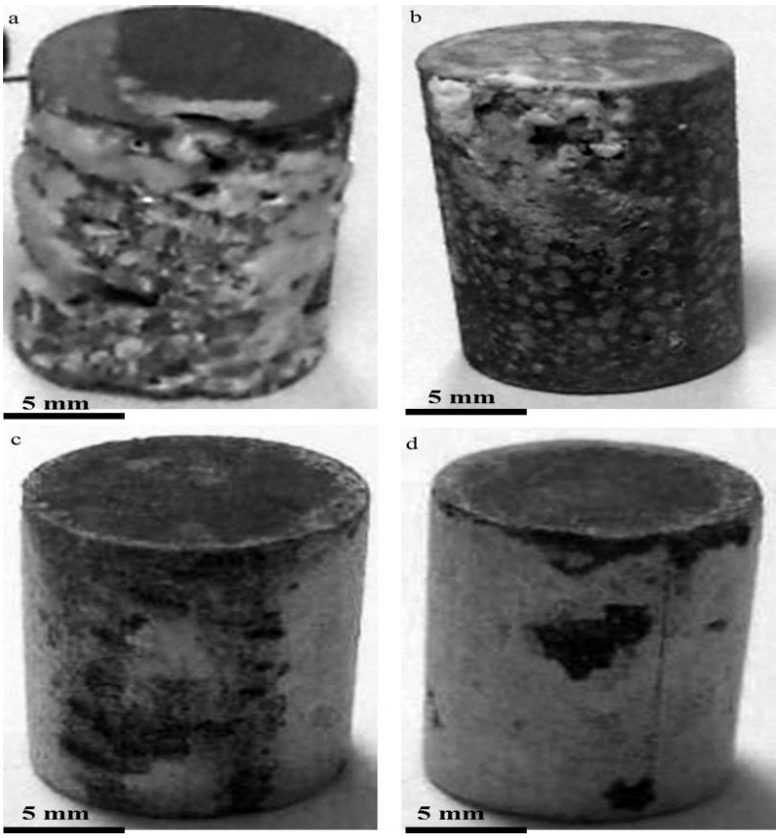


**Figure 6-26. Photographs of sample after 28 days immersion test: a) bare AZ31 substrate, b) inorganic coating, c) HEPAA(0.2%) and d) HESCM(0.2%)**

## 6.5 Summary

Corrosion performance of hydrothermally deposited inorganic Ca-P and composite coatings on the AZ31 alloy substrate were evaluated and compared to the bare substrate for potential biomedical application. The Ca-P coatings consisting of a mixture of bioactive and resorbable monetite and tricalcium phosphate improved the corrosion performance of Mg substrate up to 10,000 fold as measured by the corrosion current density. EIS results showed that the size of capacitance loops increased after applying the coating layers on Mg substrate and the capacitance loop's size was increased by increasing the deposition temperature. This was in parallel to the increase in charge transfer and polarization resistance which is a criterion for corrosion resistance enhancement and confirmed the results from potentiodynamic tests. The coating evaluation indicated that the corrosion resistance improved by increasing deposition temperature due to deposition of thicker layer at higher temperature. However, the EIS also revealed that coatings deposited at the highest temperature (190°C) did not behave the same way as coatings prepared at lower temperature by displaying an additional capacitive loop at medium frequency. Additionally, a potentiodynamic study indicated a lower level of corrosion protection for equivalent coating thickness when the deposition temperature was raised to 190 °C. This suggested that the coating structure and deposition mechanism may change above the 160 °C deposition temperature. The main factor in improving corrosion resistance was found to be increasing the coating thickness while the deposition temperature also played a factor. Thicker coating layers are expected to reduce the electrolyte access to the substrate and slow down the corrosion process. There appears to be an optimum deposition temperature at approximately 160 °C that can produce fairly thick coatings with good corrosion protection and stability.

In the case of composite coatings, a significant decrease (1000 fold) was observed in the corrosion rate of coated samples as compared to a bare alloy. The level of corrosion protection did not depend strongly on the polymer content of the coatings.

The incorporation of polymers reduced the Young's modulus and coating hardness significantly. With the appropriate polymer concentration, Young's modulus close to that of magnesium and bone can be achieved (approximately 50 GPa). Matching of the substrate and coating mechanical properties to the properties of bone tissue is expected to reduce interfacial stresses and potential interfacial failure such as delamination under loading. The composite nature of the coatings reduced cracking tendencies due to the increased ductility provided by the organic component.

# Chapter 7

# In Vitro Performance of Coatings and Deposition of Anti-Infective Coatings

## 7.1 Introduction

From Chapter 6 the corrosion resistance of the coatings appears to meet the implant application requirements. Since the interaction between the cells and tissues with biomaterials at the tissue-implant interface is a surface phenomenon, surface properties of implants play a major role in determining the biological response to the implant and the material response to the physiological conditions. Therefore, further studies were done to test the in vitro performance of the coatings in order to analyze the cell-coating interactions as well as coatings biocompatibility, which will be discussed in section 7.2 in detail.

Apart from controlling corrosion performance, anti-inflammatory and drug delivery of coatings need to be considered as well. Implantation of an orthopedic device in the body is always associated with a risk of microbial infection and biofilm formation [133, 210, 211]. When a bone becomes infected, the inner part (bone marrow) often swells. The infection can also spread outward from the bone to form a collection of infection in adjacent soft tissue, such as muscle. This phenomenon drastically reduces the patient's recovery process after implant surgery. Biofilms are extremely resistant to both the immune system and antibiotics, therefore inhibiting bacterial adhesion is essential to prevent implant-associated infection. In this chapter, a deposition of an anti-infective coating with a drug delivery ability and their antibacterial performance will be discussed (section 7.3).

## 7.2 *In Vitro* Tests

### 7.2.1 Direct *In Vitro* Test

Osteoblasts are important cells in the osseointegration of bone to the implant. They have the ability to synthesize and produce extracellular matrix and to control its

mineralization and regulate the ingrowth of bone to the implant. Osteoblasts are key cells with regard to implant performance, and assessing their behavior on a potential biomaterial may give insight into its likely biocompatibility [212].

The in vitro cellular responses to bare and coated samples were assessed with the use of MG63 osteoblastic cells. Fig.7-1 and Fig.7-2 show the typical cell-surface interaction after 1 day and 7 days incubation for the bare and coated samples. The results indicate a healthy morphology of cells and good interaction between cells and coated samples. The cells appear flattened and attach tightly to the sample surface suggesting high cell viability on coated surfaces. This confirmed that coated samples have good bioactivity and can provide an interface conducive for cell growth. Cell attachment is a complex process, affected by numerous aspects, such as cell behavior, material surface properties, and environmental factors. Material surface properties comprise the hydrophilicity, surface charge, surface roughness, softness and chemical composition of the biomaterial surface itself. Previous studies showed that cell adhesion is improved by increasing the surface hydrophilicity [213].

After 1 day, more cells were attached to the composite coatings compared to the inorganic coating. The contact angle results in the present work showed that both inorganic and composite coatings are super hydrophilic (the contact angle was below $10^{\circ}$), therefore, the higher cell attachment to the composite coatings surface cannot be justified by this factor. Another factor is surface charge; the higher cell attachment may be due to the presence of $COO^-$ functional groups on the surface of composite coatings. It is more likely that any difference in cell growth, such as proliferation, is influenced by the $COO^-$ functional group. Thevenot et al. [214] reported that the incorporation of negative charges may help adsorption of proteins which promote cell adhesion. Keselowsky et al. [215] reported that surfaces with differently chargeable functional groups ($CH_3$, OH, $COO^-$, and $NH_2$ groups) modulated MC3T3 adsorption and direct binding and specificity to control cell adhesion of osteoblasts to coated surfaces followed the trend: $OH > COO^- = NH_2 > CH_3$. Beside the surface charge,

surface stiffness is another factor that can affect the cell attachment. From mechanical properties results (in Chapter 6) the stiffness of composite coatings were much lower compared to inorganic coating (50 GPa for HEPAA(0.2%), 47GPa for HESCMS(0.2%) and 98 GPa for inorganic coating). The lower stiffness of composite coatings which are closer to bone stiffness, may improve the cell attachment [213]. Surface functional groups can influence cell growth, likely due to the fact that surface chemical functionality affects adsorbed protein and subsequent protein-cell interactions [214].

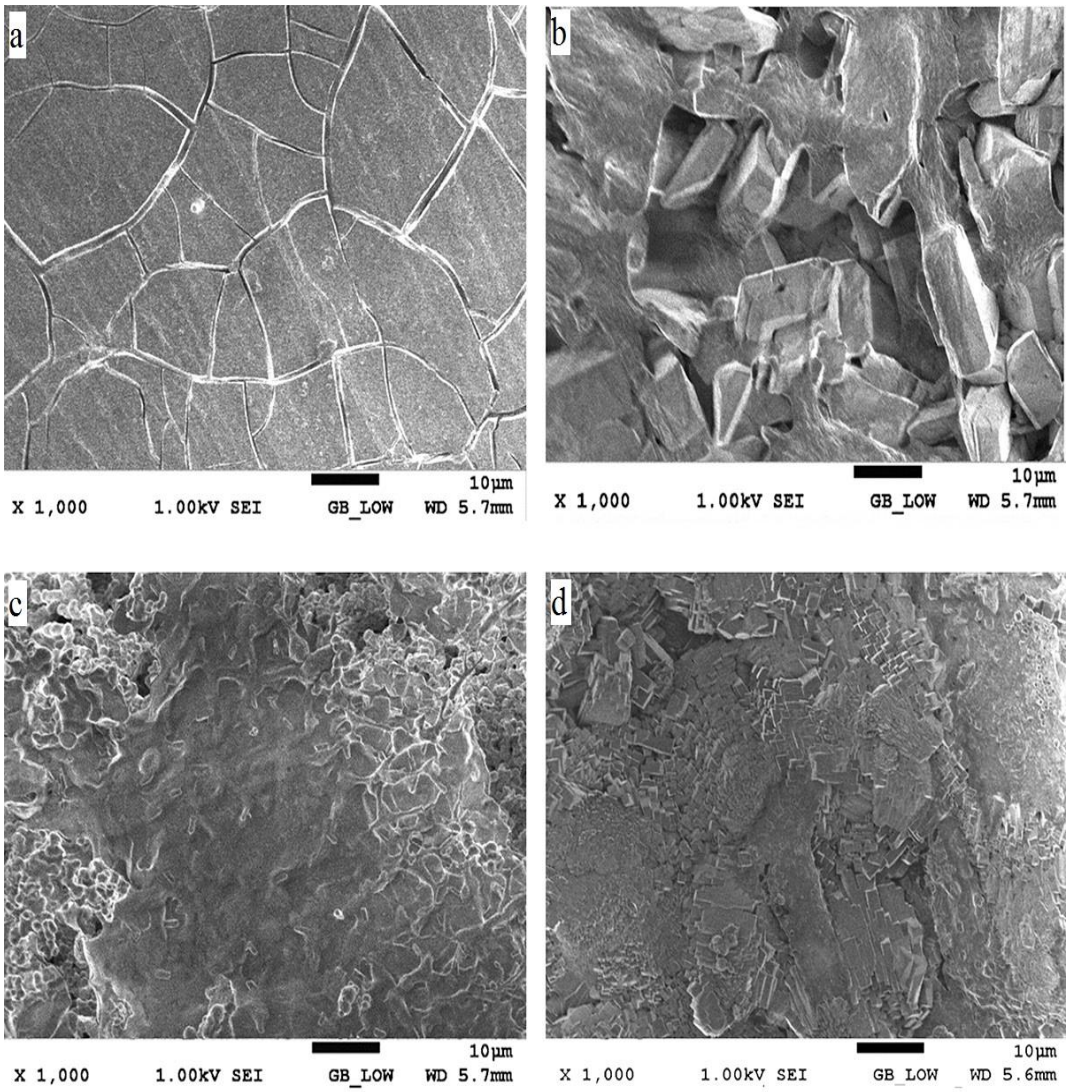


**Figure 7-1. Cell attachment after 1 day: a) AZ31 substrate, b) inorganic coating, c) HEPAA(0.2%) and d) HESCMS(0.2%)**

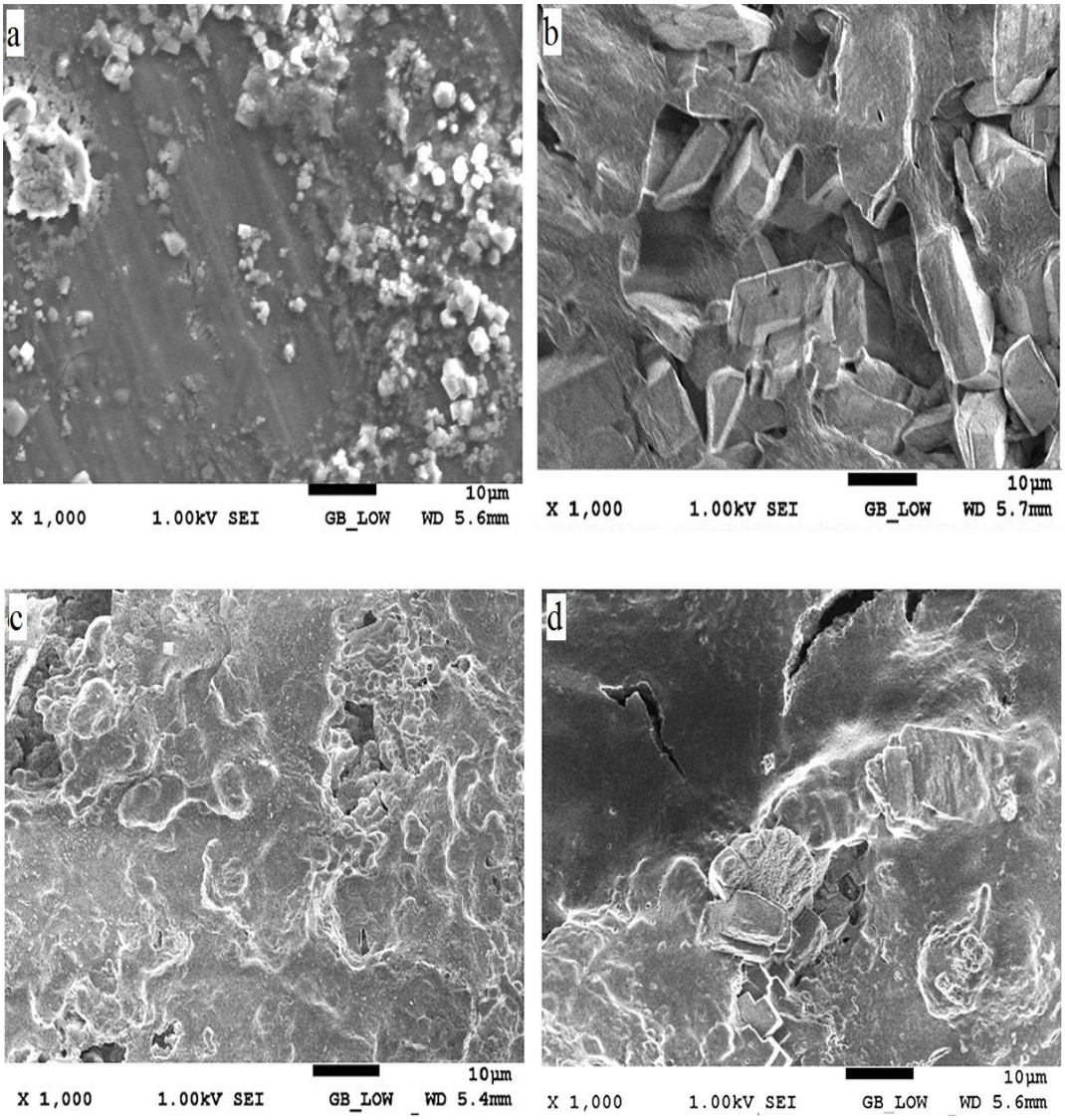


**Figure 7-2. Cell attachment after 7 days: a) AZ31 substrate, b) inorganic coating, c) HEPAA(0.2%) and d) HESCMS (0.2%)**

In comparison, the bare substrate had an adverse effect on cell attachment; few cells attached on the surface of the bare substrate and the attached cells did not show healthy morphology, which confirmed that the bare substrate did not have good bioactivity. This confirmed that surface modification of Mg substrate is essential for implant application.

The ultimate use of biomaterials in clinical purposes involves direct contact with the host tissues and cells. Therefore, the direct exposure of cells to the Mg alloy would be an important evaluation on cell-alloy interaction. This study suggested that the untreated Mg alloy surface is not favorable for cell attachment, which could impede the process for implant integration and remodeling process in the host. Coated samples have high potential to be used as implants for biomedical applications since they showed acceptable cell growth and cell attachment.

### 7.2.2 Indirect *In Vitro* Test

Another concern when using biodegradable alloys in biomedical applications is the cytotoxicity induced by their degradation products. Thus, cytotoxicity (cell viability) of bare and coated samples was assessed by means of an indirect test. Prior to cytotoxicity test, sample's extracts were added to the cell line and incubated for 1 and 7 days. After 1 and 7 days incubation, cell viabilities were measured by MTS [3-(4,5-dimethylthiazol-2-yl)-5-(3-carboxymethoxyphenyl)-2-(4-sulfophenyl)-2H-tetrazolium] test and the results are shown in Fig.7-3. All the extracts obtained from the coated samples exhibited no cytotoxicity to the cells. However, the byproduct of a bare substrate showed a moderate level of toxicity (the cell viability in the case of bare substrate was in the range 77-88 %).

The in vitro tests results indicated that although the byproduct of the bare substrate degradation showed low cytotoxicity, the bare substrate did not provide good bioactivity and cannot readily support cell growth. Thus, surface modification of AZ31 is shown to be essential for implant application.

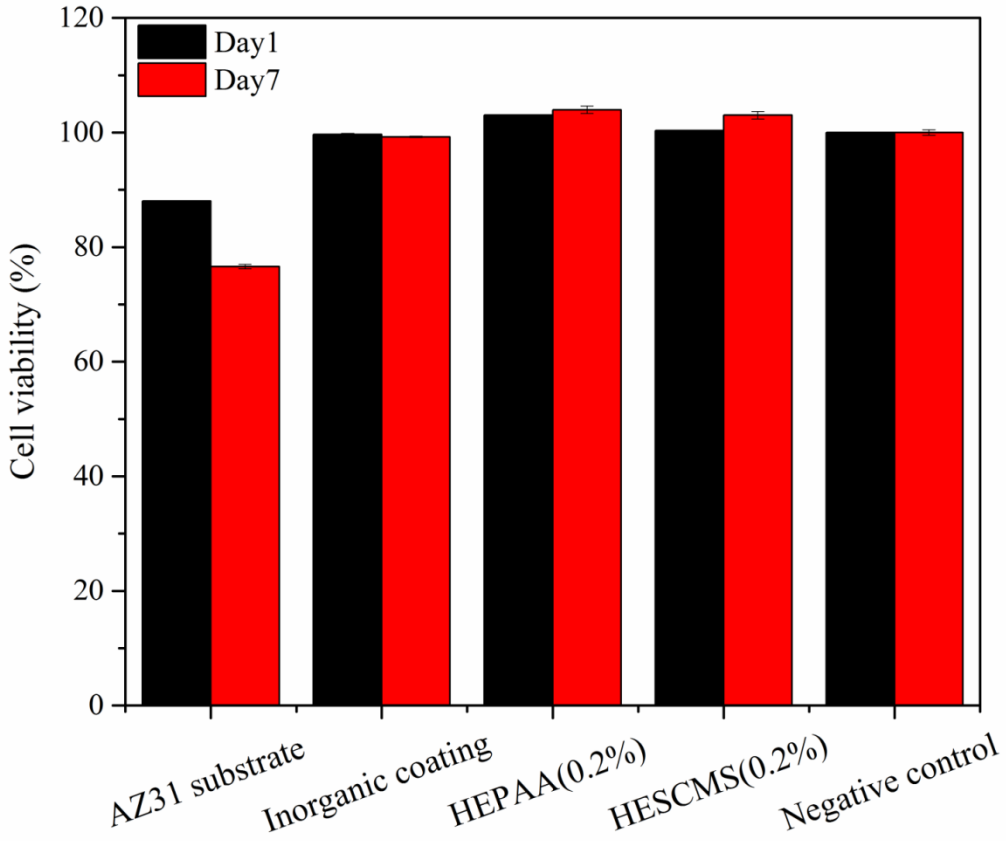


**Figure 7-3. Cell viability measured by MTS assay**

## 7.3 Anti-Infective Coatings with Local Drug Delivery Ability

Until now, Ca-P inorganic and Ca-P/Polymer composite coatings were successfully deposited on the AZ31 substrate by means of hydrothermal method, which offered good corrosion performance, mechanical properties, degradation behavior as well as cell attachments [174, 190, 216, 217]. Apart from that, inhibiting bacterial adhesion is essential to prevent implant-associated infection, because biofilms are extremely resistant to both the immune system and antibiotics. This could be achieved by using anti-infective coatings. An anti-infective coating could be developed by two means: first, incorporation of some ions such as silver (Ag) or copper (Cu), and second, by incorporating antibiotics such as tetracycline into the coatings [218, 219]. The second

method is preferred because by incorporating an antibiotic, the coating offers local drug delivery as well.

Systemic therapies can be used to treat implant-associated infections, but this method has a possible disadvantage of not being sufficiently effective due to impaired blood circulation and the need for a high concentration of antibiotics. Local drug delivery is a promising and effective procedure of delivering drug at the implantation site and seeks to prevent implant-associated infections by reducing the concentration of bacteria, and/or impeding bacterial adherence to the implant surface. Moreover, it has been proposed that a local delivery of an antibiotic can reduce the side effects and risk of overdose, also increasing the drug concentration that can be effectively delivered to a targeted site; in that way, a systemic administration of drug could be significantly reduced [220, 221].

### 7.3.1 Drug Release Measurement from Anti-Infective Coatings

A different concentration of TCH was incorporated into hydrothermally deposited inorganic Ca-P (HE160°C-3hr) and HEPAA(0.2%) composite coatings. TCH was loaded into the coating by using EPD technique. EPD is a fast, effective and low cost method which provides the possibility to incorporate different materials into the coatings in order to achieve controlled properties. Since drugs (antibiotics) are not stable at high temperature, it is not possible to incorporate TCH into the coating during the hydrothermal process in a single step. In this case, EPD deposition process at low temperature could be used with hydrothermal process for loading antibiotic into the pre-hydrothermally deposited coatings.

TCH is water soluble and hydrophilic and therefore, TCH is first encapsulate into the polymer solution (SCMS solution) in order to increase drug loading into the coating and prevent fast release of TCH. The release profile of TCH from the coatings into the

PBS solution is shown in Fig.7-4. For the both samples, an initial burst release was followed by a slow release (around 15-25 %) over a period of 10 days. The majority of release took place during the first 24 hours (75-85%) of immersion of samples in PBS solution. The fast drug release in the beginning is related to surface attached drug which followed by the slower release of the entrapped drug within the micropores present on the coated samples [222, 223]. Besides that, a further release of drugs could be a result from dissolution of an intermediate polymer layer (SCMS) which provided a new drug covered surface. The SCMS intermediate polymer layer also could act as a diffusion barrier to control the release rate of TCH into the solution.

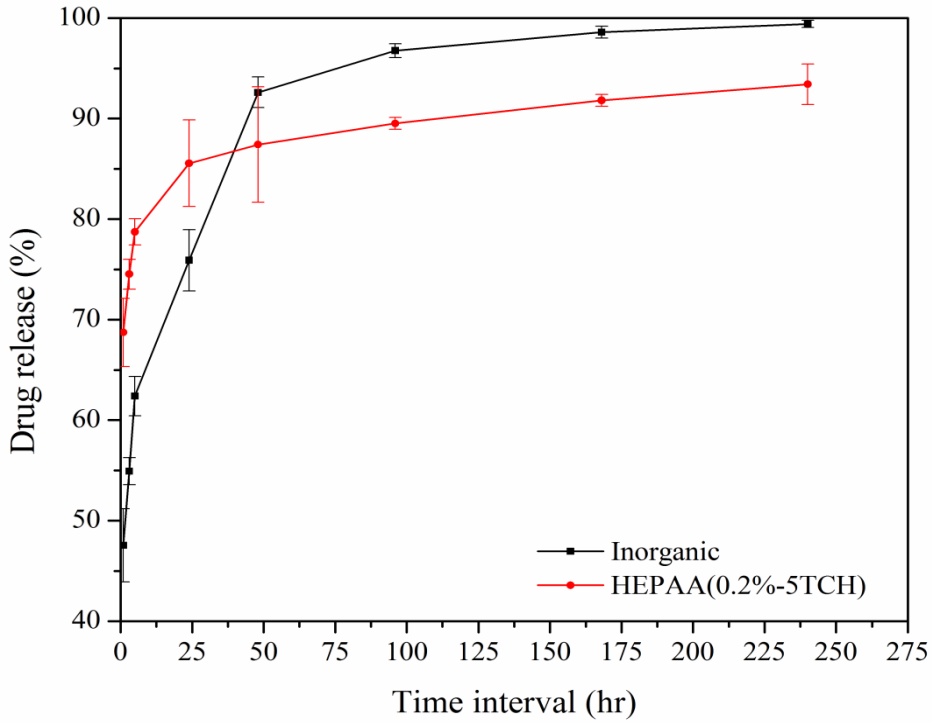


**Figure 7-4. Release profile of TCH over time from inorganic and composite coatings**

The release mechanism of the antibiotics can be described as a dissolution-diffusion phenomenon. Drug release could be affected by surface morphology and porosity. The

release of TCH from HEPAA(0.2%) composite coating was more sustained and after 250 hours around 90% of drug was released from the composite coating while in the case of inorganic coating after 250 hours almost 100% of the loaded drug was released into the PBS solution. A composite coating has a porous structure and drugs could entrap into the pores, and further release by diffusion from this pores. That may be a reason for more sustained release of TCH from a composite coating compared to an inorganic coating.

Fig.7-5 shows the release of TCH from HEPAA(0.2%) coatings with different amount of loaded TCH. The TCH release behavior was similar for all concentrations. The extent of release was proportional to the concentrations and the majority of release took place during the first 24 hours (around 70%).

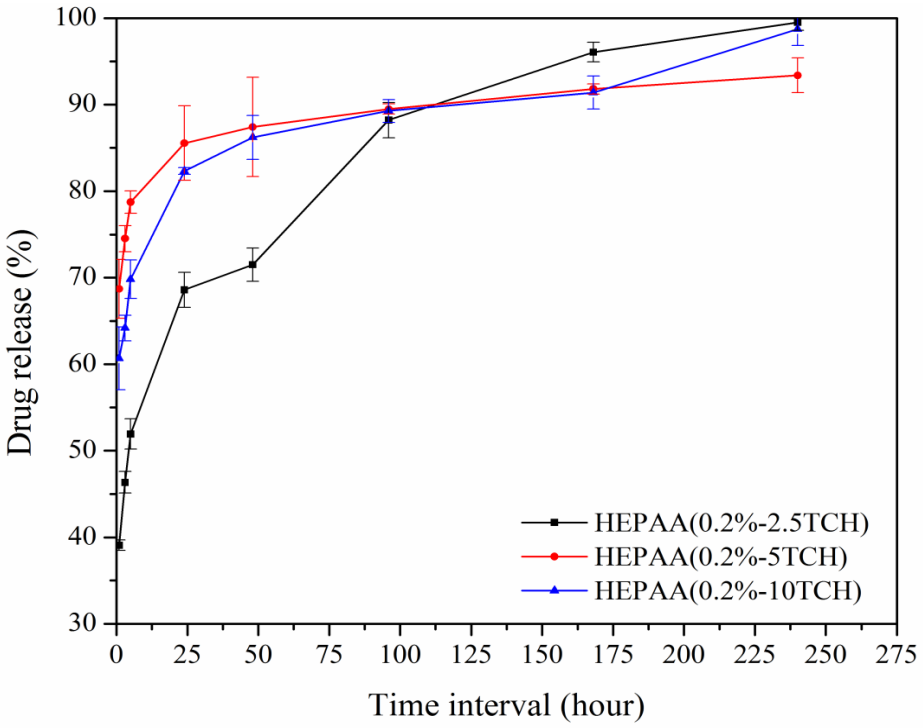


**Figure 7-5. Release profile of TCH over time for different incorporated concentration of drug**

From Fig.7-4 and Fig.7-5 the major amount of TCH loaded into the coating was released in the first 24 hours. This is considered as a fast release profile. Tissue engineering and drug delivery application are required continuous release of the drug; moreover, controlling the initial release of the drug could reduce the possibility of drug overdose and damaging the cells [224].

Therefore, in order to further control the drug release a top layer of SCMS polymer without the drug was applied on the previous coating as follows:

1- Deposition of a layer of SCMS/TCH for 2 min at 10 Volts by EPD
2- Deposition of an intermediate layer of SCMS polymer for 2 min at 10 Volts by EPD
3- Deposition of the second layer of SCMS/TCH for 2 min at 10 Volts
4- Deposition of a top layer of SCMS polymer for 2 min at 10 Volts by EPD

After that, the release profile for the new coatings was checked and the result is shown in Fig.7-6. The results showed that adding a top layer could significantly affect the drug release profile. Adding a top layer decreased the TCH release from 70% to 35% in the first 24 hours. Moreover, adding a top layer of polymer resulted in prolonger release of TCH. In this case the drug release sustained for around 500 hours, while for the coating without the top layer, almost the whole amount of the loaded TCH was released from the coatings after 250 hours.

For ideal drug delivery, antibacterial agents (antibiotics) should be released from the coating immediately after the implantation to prevent bacterial adhesion and infection in the implantation site, and followed by gradual and continuous release for a prolonged period [225]. The new coating with a top layer of polymer was controlled the initial release of TCH and was resulted in a sustained released of TCH for almost 20 days.

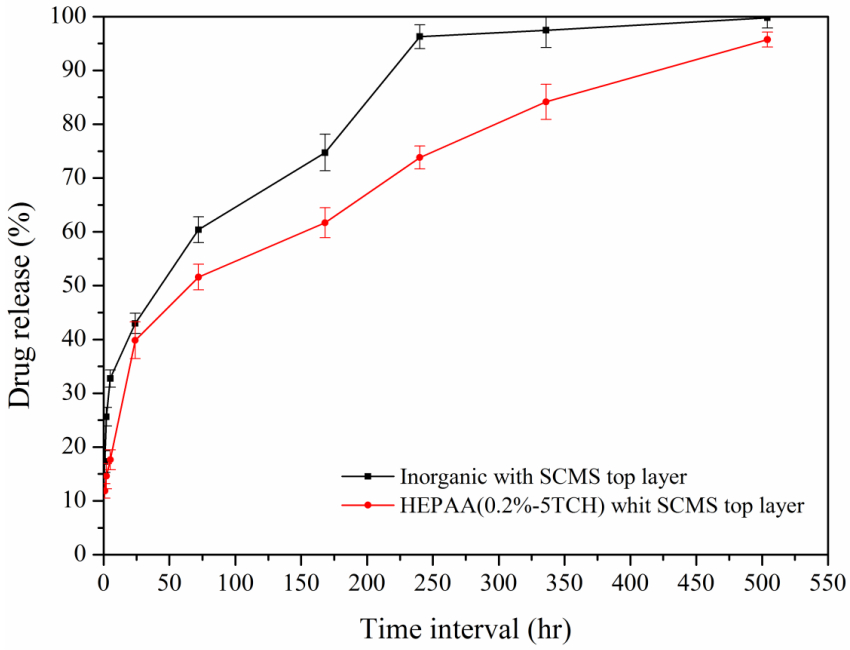


**Figure 7-6. A comparison of TCH release profile with and without polymer top layer**

### 7.3.2 Antibacterial Activity of Coatings

The antibacterial activity of the samples was investigated by conducting agar disk diffusion tests against gram positive S. aureus bacteria and measuring the zone of inhibition (ZOI) as shown in Fig.7-7 for inorganic and composite coatings. A comparison of antibacterial activity of HEPAA(0.2%) coatings with different amount of loaded TCH is shown in Fig.7-8. ZOI indicates the degree of sensitivity of bacteria to a drug. A color contrast around the samples is indicative of ZOI that resulted from a release of antibiotics into the solution which prevents bacterial growth. The size of ZOI for the composite coating was higher (19-23 mm) than inorganic coating (15-18 mm). The size of ZOI for both coatings was increased over time resulted from increased amount of released antibiotic from coatings.

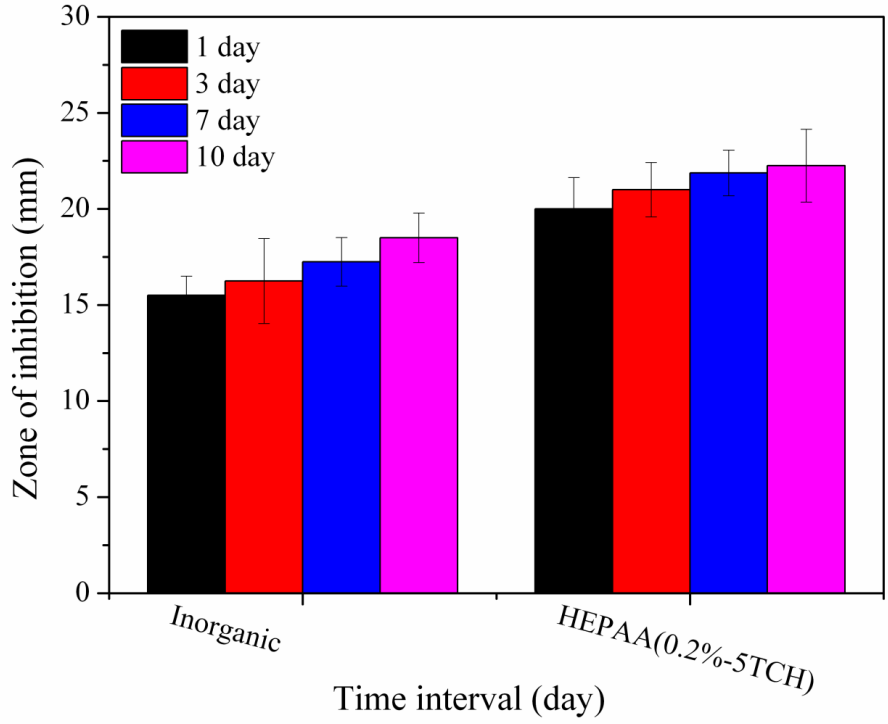


**Figure 7-7. A comparison in the size of ZOI for inorganic and composite coatings**

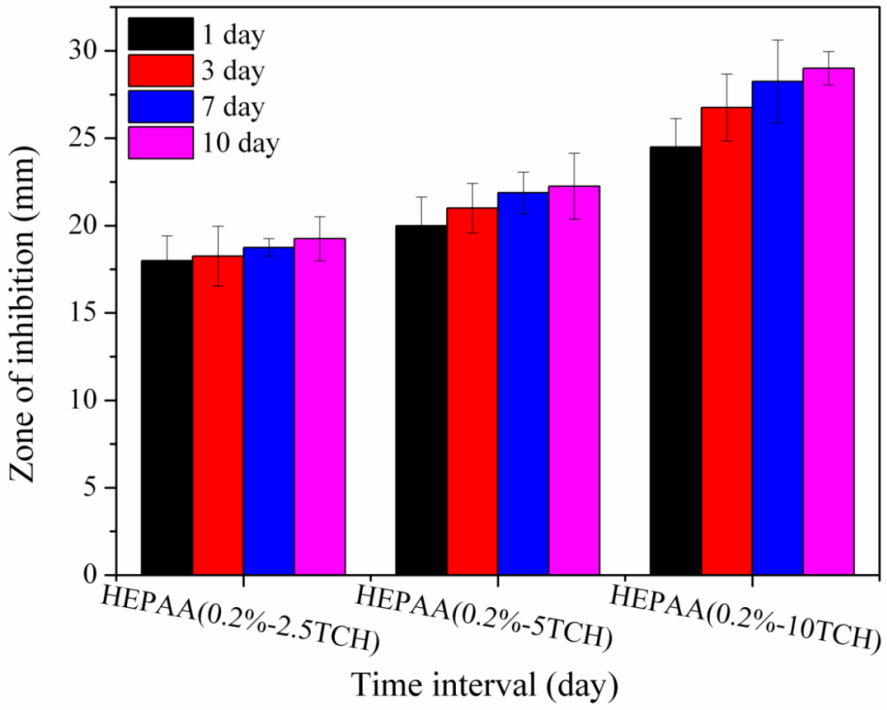


**Figure 7-8. A comparison in the size of ZOI for different amount of loaded TCH into the coating**

Photographs of the agar plates after antibacterial test are shown in Figures 7-9 to 7-12 for inorganic and composite coatings respectively. The PBS control did not develop a ZOI area against bacteria growth. The release of TCH from all samples showed a clear ZOI area. The bigger ZOI for the composite coating was a result from a higher amount of incorporated TCH into the composite coating. However, the inorganic coating was also capable of bacteria inhibition. The observed ZOI area confirmed that the quantity of TCH released from the coating exceeded the minimum inhibitory concentration (MIC) for the drug. The results showed that the obtained coatings could successfully prevent bacterial growth and can be used as the anti-infective coatings.

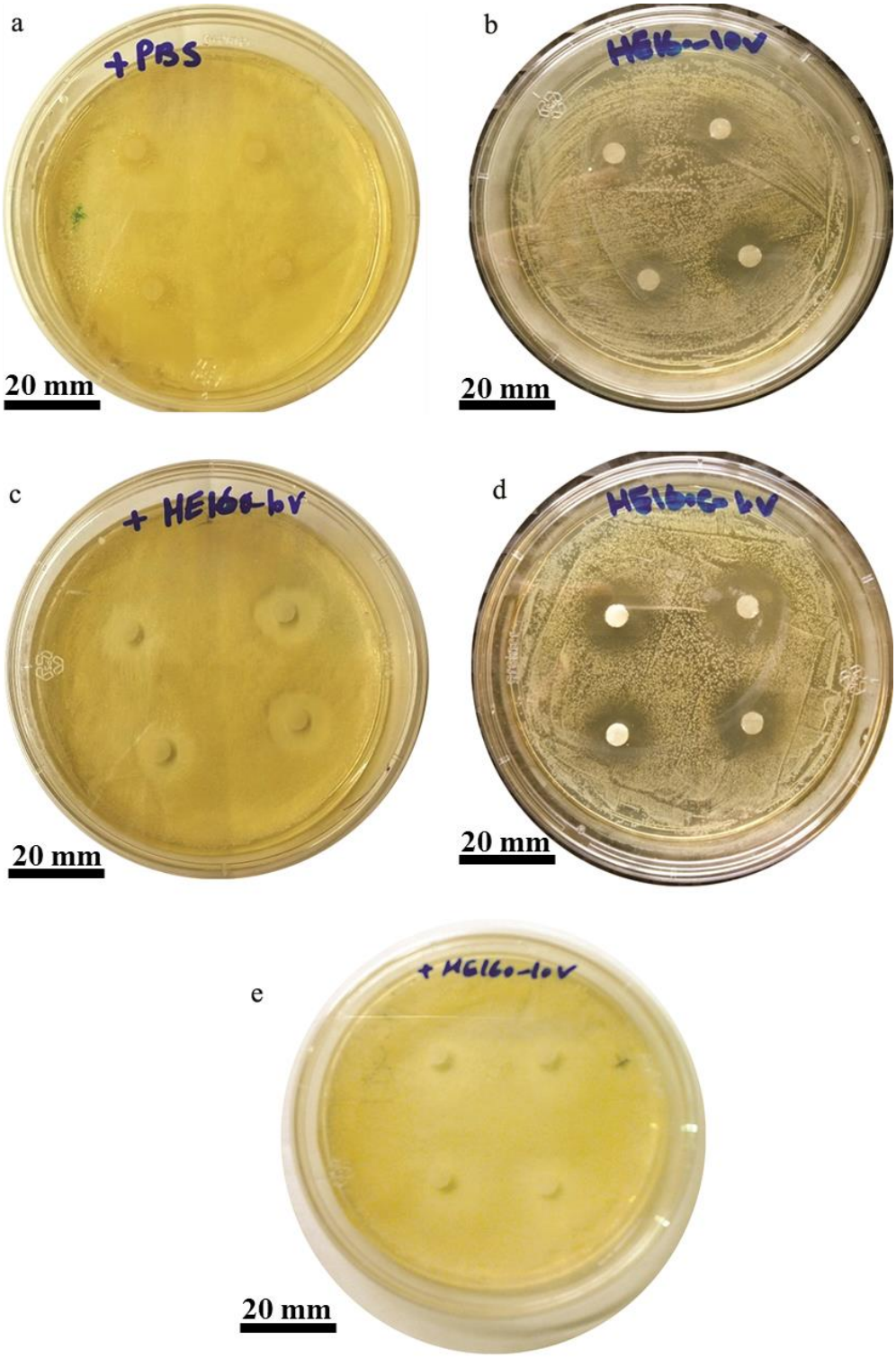


**Figure 7-9. Photographs of agar plate after antibacterial test for inorganic coating: a) PBS control, b) inorganic after 1 day, c) after 3 days, d) after 7 days and e) after 10 days**

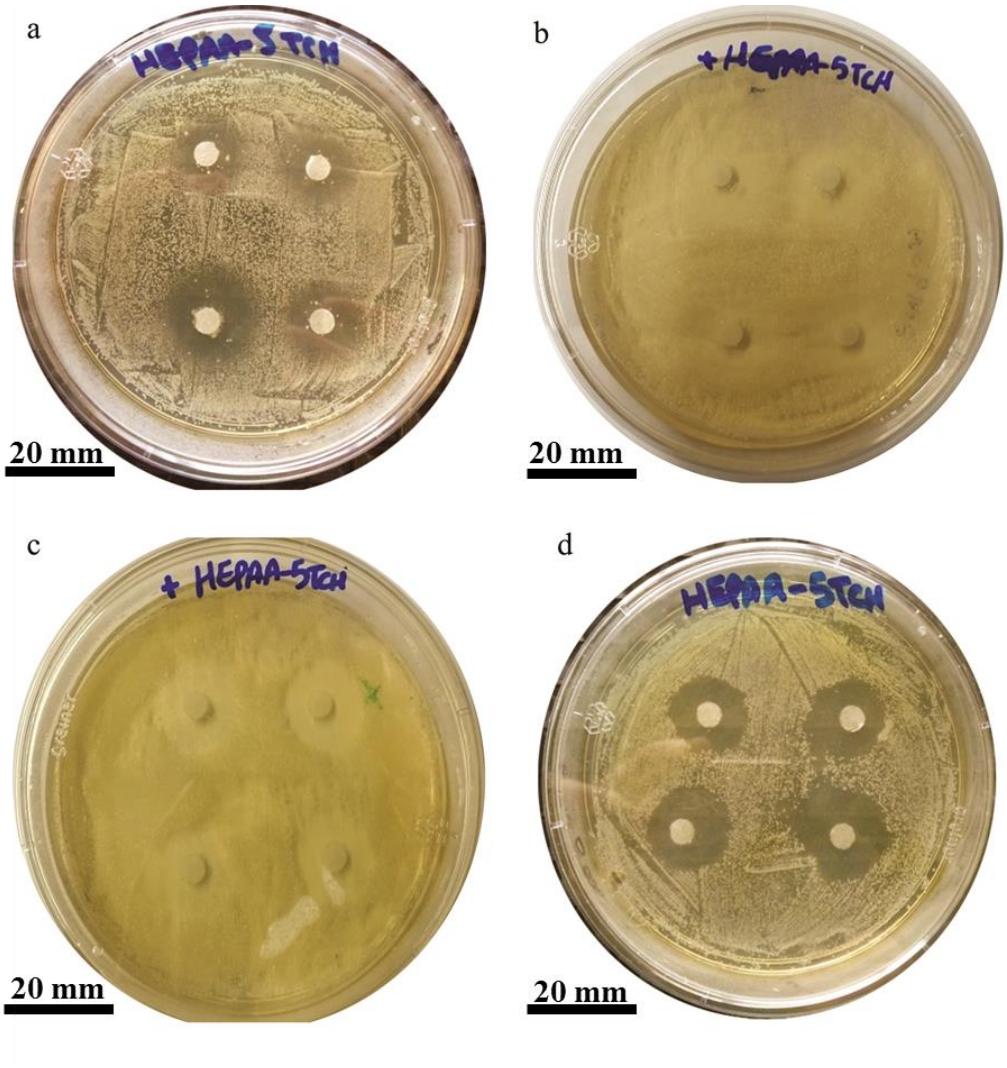


**Figure 7-10. Photographs of agar plate after antibacterial test for HEPAA(0.2%-5TCH) composite coating: a) after 1 day, b) after 3 days, c) after 7 days and d) after 10 days**

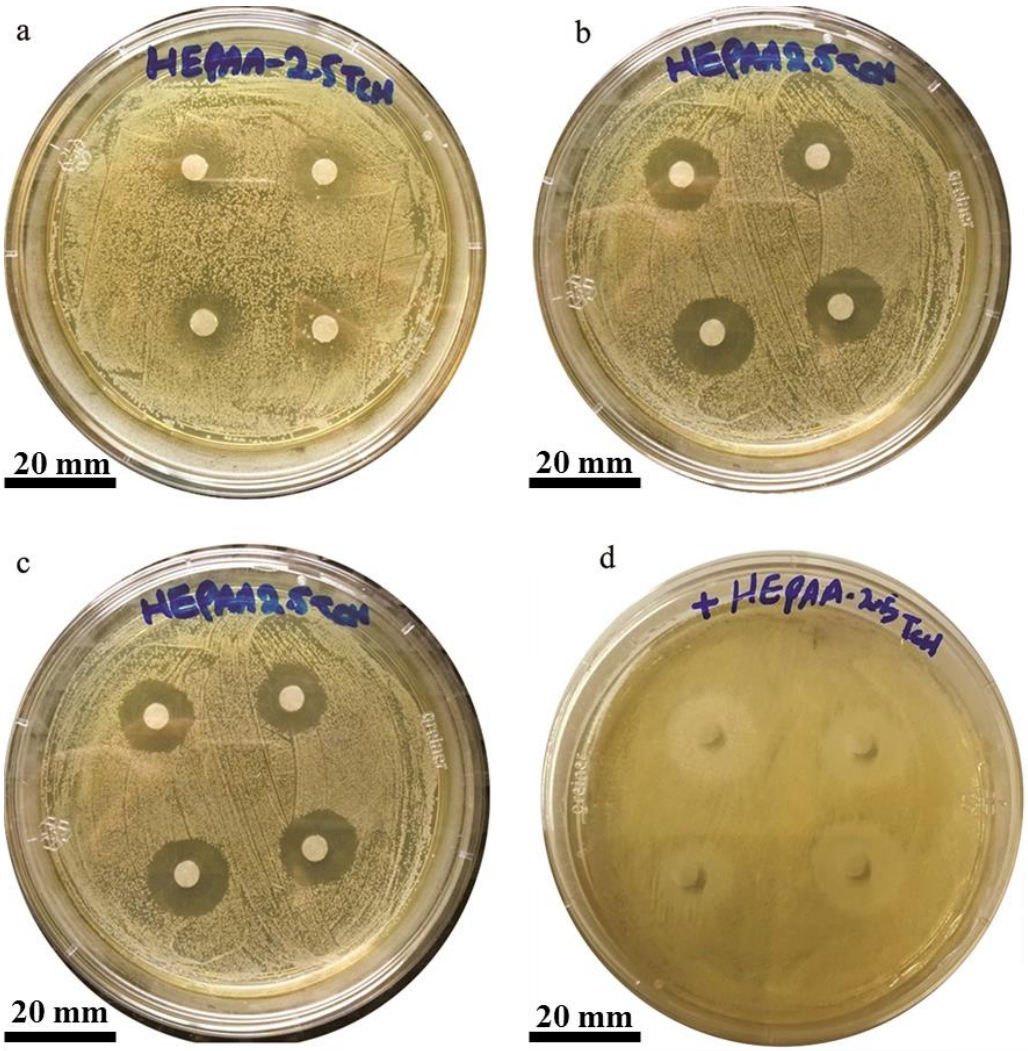


**Figure 7-11. Photographs of agar plate after antibacterial test for HEPAA(0.2%-2.5TCH) composite coating: a) after 1 day, b) after 3 days, c) after 7 days and d) after 10 days**

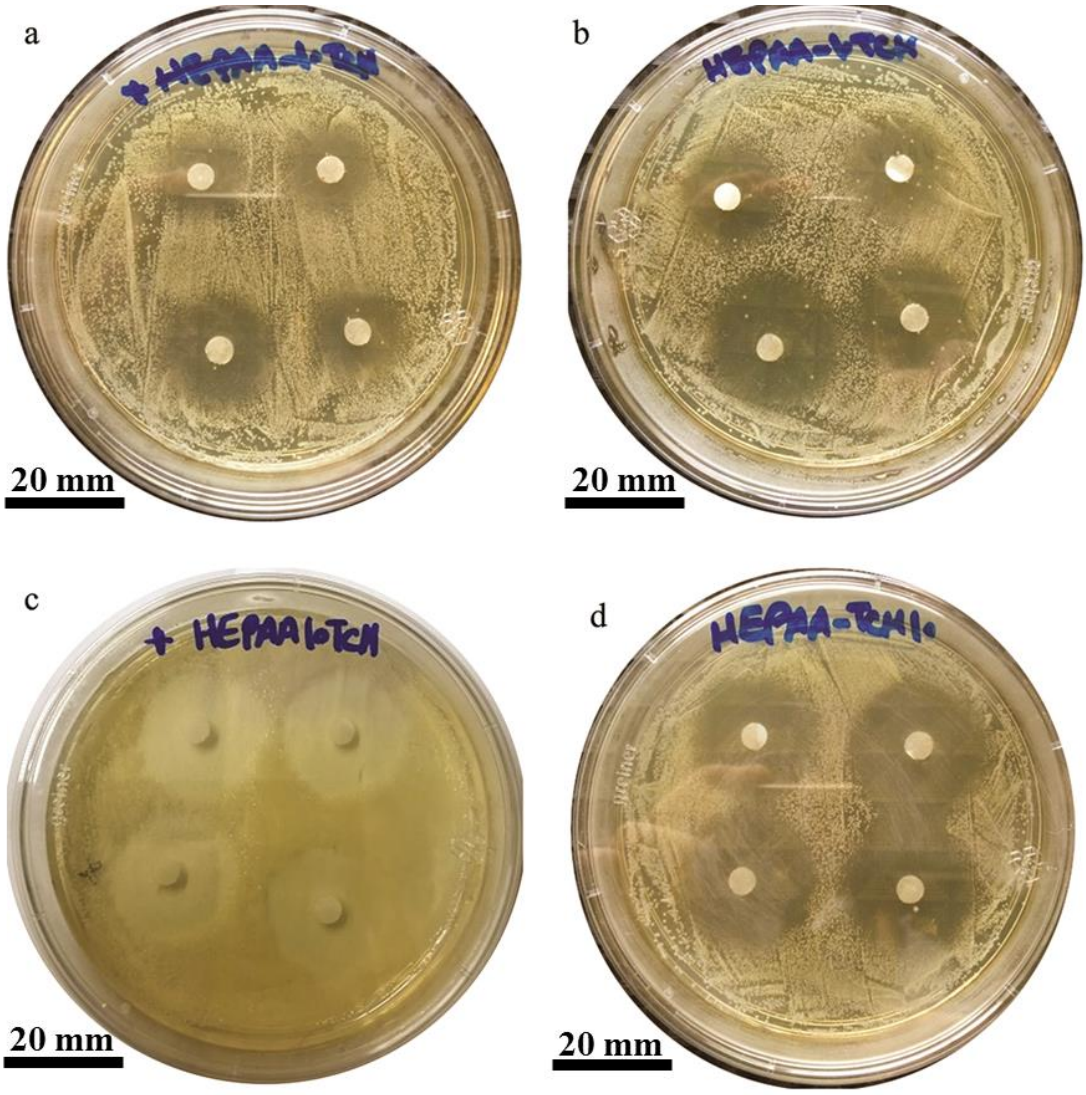


**Figure 7-12. Photographs of agar plate after antibacterial test for HEPAA(0.2%-10TCH) composite coating: a) after 1 day, b) after 3 days, c) after 7 days and d) after 10 days**

## 7.4 Summary

In vitro studies with MG63 cells confirmed that composite coatings provided a surface conducive for cell proliferation and did not have any cytotoxic effect. In comparison, the purely inorganic coating was found to support cell growth to a lesser extent while the uncoated AZ31 substrate displayed a modest level of cytotoxicity due to its degradation and associated change in pH at the surface.

Besides that, an anti-infective coating with drug delivery capability was successfully deposited by a combination of hydrothermal and EPD techniques. Since drugs are not stable at high temperature, it was not possible to incorporate drug into the coating during hydrothermal process. So it was beneficial to use an EPD method for incorporating different concentration of drug on the top of hydrothermally deposited coatings. The obtained coatings showed good antibacterial activity and drug release profile over time. The observed ZOI confirmed that the quantity of TCH released from the coatings exceeded the MIC for the drug. The results showed that obtained coatings could successfully prevent bacterial growth and can be used as the anti-infective coatings.

# Chapter 8

# Conclusions and Suggestions for Future Works

## 8.1 Conclusion

In this study, the possibility of deposition of biodegradable and biocompatible inorganic Ca-P and Ca-P/Polymer composite coatings on AZ31 magnesium alloy, Zn, Ti and SS substrates by means of hydrothermal process was investigated. The emphasis of the current work was on the deposition of biodegradable Ca-P phases, since Mg is designed to be biodegradable and the aim of surface modification of Mg substrate is only to delay the degradation of substrate until bone healing has been achieved and afterward coating needs to be dissolved and removed from the substrate. Therefore, there was no interest on the deposition of most common Ca-P phases like HA, but a focus on deposition of biodegradable monetite and tricalcium phosphate phases. The coatings were produced that close the gaps in terms of corrosion resistance, biocompatibility, and mechanical performance. The outcomes of the current project are as follow:

### 8.1.1 Deposition of Inorganic Ca-P Coatings

The hydrothermal process is an easy and low cost method for deposition of both inorganic and composite coatings. In the case of inorganic Ca-P coatings, it was found that deposition temperature and deposition time are important variables, which affect different coating's characteristics such as morphology, chemical composition, thickness and corrosion performance. Moreover, deposition temperature and deposition time showed a significant effect on coating deposition mechanism.

Deposited coatings at lower temperatures were mainly composed of the biodegradable monetite phase. However, increasing the deposition temperature resulted in a deposition of a higher amount of tricalcium phosphate and partial deposition of the calcium pyrophosphate phase, which are still considered as biodegradable phases compared to the HA phase.

A higher deposition temperature (190 °C) promoted the growth of a thick layer of $Mg(OH)_2$ on the AZ31 substrate which resulted in an increase in the coating thickness to around 400 µm (the thickness of deposited coating at 160 °C was around 60 µm). This significant increase in coating thickness consequently, decreased the coating adhesion to the substrate.

### 8.1.2 Deposition of Novel Ca-P/Polymer Composite Coatings

Novel Ca-P/Polymer composite coatings were successfully deposited in a single step on the AZ31 substrate by means of a hydrothermal process and reported for the first time in this project. In the case of composite coatings it was found that the polymer type strongly affects coating morphology and coating chemical composition. These differences resulted from polymer structure and molecular weight. Here we used two polymers (PAA and SCMS) with carboxylate functional group since $Ca^{2+}$ ions could cross link with carboxylic groups in the polymer structure and accelerate the deposition process. PAA with high carboxylate content concentration resulted in deposition of the tricalcium phase with nodular structures; while SCMC with a low carboxylate group acted as a crystal habit modifier and reduced the Ca-P crystal size; although, the crystal phase still remained as monetite phase which was similar to inorganic Ca-P coating.

### 8.1.3 Understanding the Deposition Mechanism of Coatings during the Hydrothermal Process

It was found that the successful deposition of coating during the hydrothermal process is strongly affected by substrate surface chemistry and metal-electrolyte interface reactions. Inorganic and composite coatings were successfully deposited on AZ31 and Zn substrates, and partially deposited on a SS substrate using the hydrothermal process. Deposition of the coating was mainly due to the substrate corrosion and consequently the pH change in the vicinity of the metal surface and promoting Ca-P precipitation on

the surface. The increase in pH and incorporation of $Mg^{2+}$ and $Zn^{2+}$ resulted in deposition and stabilization of the tricalcium phosphate phase followed by deposition of the monetite phase. A monetite phase is deposited at the lower bulk solution pH.

In the case of composite coatings, it was found that PAA polymer adsorption on AZ31 substrate in the initial step of deposition changed the deposition mechanism. In this case, increases in the local $Ca^{2+}$ concentration near the surface accelerated the deposition of composite coating. The Incorporation of a SCMS polymer did not alert the deposition mechanism compared to the inorganic coating.

### 8.1.4 Corrosion Performance of Hydrothermally Deposited Coatings

The main aim of the current project was to control the corrosion performance of AZ31 magnesium substrate for potential biomedical application. The biodegradable inorganic Ca-P and Ca-P/Polymer composite coatings improved the corrosion performance of the AZ31 substrate between 100-10,000 fold as measured by the corrosion current density. In the case of composite coatings, the level of corrosion protection did not depend strongly on the polymer content of the coatings.

From immersion test results, composite coatings showed a higher mass loss compared to inorganic coating. This difference resulted from an incorporation of the polymers into the coatings. Polymers have a higher degradation rate than Ca-P phases; therefore incorporating biodegradable polymers could increase the degradation rate of coating. In general, a combination of different factors like polymer content, polymer type, polymer molecular weight, coating morphology and coating crystal size define the real dissolution rate of a coating.

Different fracture types have different healing periods, for example healing period for a femoral shaft fracture is around 12 weeks, while the healing period for a humeral bone fracture is approximately 6-8 weeks. Therefore, by controlling different

parameters, coatings with different degradation rates could be deposited and be used for different bone fracture types.

### 8.1.5 Mechanical Properties of Hydrothermally Deposited Coatings

Ca-P coatings showed high Young's modulus, hardness and brittle behavior which resulted in crack formation during scratch and nano-indentation tests. Besides corrosion resistance, adjustable mechanical properties are another requirement for biomedical coatings in order to prevent early failure of the bone-implant interface. This aim was achieved by an incorporation of polymers into the coating structure and a deposition of composite coatings.

With the appropriate polymer concentration, Young's modulus close to that of Mg and bone was achieved (approximately 50 GPa). The composite nature of the coatings reduced cracking tendencies due to the increased ductility and prevented crack formation provided by the organic component.

### 8.1.6 Biocompatibility of Hydrothermally Deposited Coatings

Biocompatibility of coatings for biomedical applications is another concern which must be taken into consideration. In vitro studies with MG63 cells confirmed that both inorganic and composite coatings surface could support cell proliferation and growth and showed no cytoxicity effect, unlike uncoated AZ31 substrates which did not support cell attachment due to its degradation and associated change in pH at the surface. However, the composite coatings supported cell growth to higher extent, which was influenced by the $COO^-$ functional group in composite coatings structure.

### 8.1.7 Anti-infective Coatings

Implant infection is another aspect for biomedical coatings which needs to be considered. Anti-infective coatings were developed by incorporation of antibiotics into the coatings. The obtained coatings showed good antibacterial activity and sustained drug release profile over time. The obtained coatings successfully prevented bacterial growth and could be used as an anti-infective coatings with local drug delivery capability.

## 8.2 Suggestions for Future Works

### 8.2.1 In Vitro Study of Biomechanical Properties of Coated Samples

The ultimate goal of surface modification is to use a coated Mg substrate as an implant (as plate and screw, or rod) for bone fracture fixation. Therefore, the ability of coated AZ31 substrate as a bone fixation implant needs to be confirmed before use by conducting in vitro biomechanical tests.

In clinical applications, implant materials are subjected to different types of loads such as tension, compression, bending and shear forces, or even a combination of different loads depending on the implantation area.

In biomechanical testing, a simulated fixation test specimen such as a plate secured with screws is subjected to different loads, and the results demonstrate the real behavior and properties of a bone fixation implant. Since the bone fixation is biodegradable, its mechanical properties will change over time in the body. Therefore, it is necessary to perform biomechanical tests under wet condition in order to simulate real conditions and to better understand the mechanical performance of implant fixation. The biomechanical tests are depended on the implant fixation type and its applications can be divided as follows:

1- Static biomechanical tests including: tensile tests; bending tests; pull-out tests and shear tests
2- Cyclic biomechanical tests

### 8.2.2 In Vivo Studies of Coated Substrates

It is necessary to fully understand the nature of corrosion and biodegradation of hydrothermally deposited coatings in vivo condition before using them in practical applications. The biodegradation of material in vivo is a cell mediated process and is dependent on interface dynamics between material and environment, and caused by living systems such as microorganisms and cells.

Therefore, it is essential to evaluate the corrosion performance, biodegradation, as well as biocompatibility of coated samples in vivo and in animal models by using different techniques such as in vivo micro-computed tomography (μCT), blood examinations, histomorphological analysis and screening of degradation products.

# References

[1] Witte F, Fischer J, Nellesen J, Crostack HA, Kaese V, Pisch A, et al. In vitro and in vivo corrosion measurements of magnesium alloys. Biomaterials 2006; 27:1013-1018.
[2] Witte F, Hort N, Vogt C, Cohen S, Kainer KU, Willumeit R, et al. Degradable biomaterials based on magnesium corrosion. Current Opinion in Solid State and Materials Science 2008;12:63-72.
[3] Hornberger H, Virtanen S, Boccaccini AR. Biomedical coatings on magnesium alloys-a review. Acta Biomaterialia 2012;8:2442-2455.
[4] Salunke P, Shanov V, Witte F. High purity biodegradable magnesium coating for implant application. Materials Science and Engineering: B 2011;176:1711-1717.
[5] Song G, Song S. A possible biodegradable magnesium implant material. Advanced Engineering Materials 2007;9:298-302.
[6] Xu L, Yamamoto A. Characteristics and cytocompatibility of biodegradable polymer film on magnesium by spin coating. Colloids and Surfaces, Biointerfaces 2012;93:67-74.
[7] Zeng R, Dietzel W, Witte F, Hort N, Blawert C. Progress and challenge for magnesium alloys as biomaterials. Advanced Engineering Materials:B 2008;10:3-14.
[8] Salahshoor M, Guo Y. Biodegradable orthopedic magnesium-calcium (MgCa) alloys, processing, and corrosion performance. Materials 2012;5:135-155.
[9] Staiger MP, Pietak AM, Huadmai J, Dias G. Magnesium and its alloys as orthopedic biomaterials: A review. Biomaterials 2006;27:1728-1734.
[10] Witte F, Feyerabend F, Maier P, Fischer J, Stormer M, Blawert C, et al. Biodegradable magnesium-hydroxyapatite metal matrix composites. Biomaterials 2007;28:2163-2174.
[11] Kirkland NT, Birbilis N, Staiger MP. Assessing the corrosion of biodegradable magnesium implants: a critical review of current methodologies and their limitations. Acta Biomaterialia 2012;8:925-936.
[12] Song G. Control of biodegradation of biocompatable magnesium alloys. Corrosion Science 2007;49:1696-1701.
[13] Zhang S, Zhang X, Zhao C, Li J, Song Y, Xie C, et al. Research on an Mg-Zn alloy as a degradable biomaterial. Acta Biomaterialia 2010;6:626-640.
[14] Witte F. The history of biodegradable magnesium implants: a review. Acta Biomaterialia 2010;6:1680-1692.
[15] Seal CK, Vince K, Hodgson MA. Biodegradable surgical implants based on magnesium alloys-a review of current research. IOP Conference Series: Materials Science and Engineering 2009;4:1-5.
[16] Huiskes R, Weinans H, van Rietbergen B. The relationship between stress shielding and bone resorption around total hip stems and the effects of flexible materials. Clinical Orthopaedics and Related Research 1992;274:124-134.

[17] Niinomi M, Nakai M. Titanium-Based Biomaterials for Preventing Stress Shielding between Implant Devices and Bone. International Journal of Biomaterials 2011;1-10.
[18] Benli S, Aksoy S, Havıtcıoğlu H, Kucuk M. Evaluation of bone plate with low-stiffness material in terms of stress distribution. Journal of Biomechanics 2008;41:3229-3235.
[19] Hiromoto S, Tomozawa M. Hydroxyapatite coating of AZ31 magnesium alloy by a solution treatment and its corrosion behavior in NaCl solution. Surface and Coatings Technology 2011;205:4711-4719.
[20] Kirkland NT, Lespagnol J, Birbilis N, Staiger MP. A survey of bio-corrosion rates of magnesium alloys. Corrosion Science 2010;52:287-291.
[21] Lu W, Chen Z, Huang P, Yan B. Microstructure, corrosion resistance and biocompatibility of biomimetic HA-based Ca-P coatings on ZK60 magnesium alloy. International Journal of Electrochemical Science 2012;7:12668-12679.
[22] Wang J, Tang J, Zhang P, Li Y, Wang J, Lai Y, et al. Surface modification of magnesium alloys developed for bioabsorbable orthopedic implants: a general review. Journal of Biomedical Materials Research Part B, Applied Biomaterials 2012;100:1691-1701.
[23] Zhang Y, Zhang G, Wei M. Controlling the biodegradation rate of magnesium using biomimetic apatite coating. Journal of Biomedical Materials Research Part B, Applied Biomaterials 2009;89:408-414.
[24] Saris NE, Mervaala E, Karppanen H, Khawaja JA, Lewenstam A. Magnesium. An update on physiological, clinical and analytical aspects. Clinica Chimica Acta 2000;294:1-26.
[25] Pompa L, Rahman ZU, Munoz E, Haider W. Surface characterization and cytotoxicity response of biodegradable magnesium alloys. Materials Science and Engineering: C 2015;49:761-768.
[26] Brar HS, Wong J, Manuel MV. Investigation of the mechanical and degradation properties of Mg-Sr and Mg-Zn-Sr alloys for use as potential biodegradable implant materials. Journal of the Mechanical Behavior of Biomedical Materials 2012;7:87-95.
[27] Ma E, Xu J. Biodegradable alloys: The glass window of opportunities. Nature Materials 2009;8:855-857.
[28] Kirkland NT. Magnesium biomaterials: past, present and future. Corrosion Engineering, Science and Technology 2012;47:322-328.
[29] Chiu KY, Wong MH, Cheng FT, Man HC. Characterization and corrosion studies of fluoride conversion coating on degradable Mg implants. Surface and Coatings Technology 2007;202:590-598.
[30] Gray-Munro JE, Seguin C, Strong M. Influence of surface modification on the in vitro corrosion rate of magnesium alloy AZ31. Journal of Biomedical Materials Research Part A 2009;91:221-330.

[31] Hiromoto S, Tomozawa M. Corrosion behavior of magnesium with hydroxyapatite coatings formed by hydrothermal treatment. Materials Transactions 2010;51:2080-2087.
[32] Da Conceição TF, Scharnagl N, Dietzel W, Kainer KU. Controlled degradation of a magnesium alloy in simulated body fluid using hydrofluoric acid treatment followed by polyacrylonitrile coating. Corrosion Science 2012;62:83-89.
[33] Keim S, Brunner JG, Fabry B, Virtanen S. Control of magnesium corrosion and biocompatibility with biomimetic coatings. Journal of Biomedical Materials Research Part B, Applied Biomaterials 2011;96:84-90.
[34] Yun Y, Dong Z, Yang D, Schulz MJ, Shanov VN, Yarmolenko S, et al. Biodegradable Mg corrosion and osteoblast cell culture studies. Materials Science and Engineering: C 2009;29:1814-1821.
[35] Wang H, Shi Z. In vitro biodegradation behavior of magnesium and magnesium alloy. Journal of Biomedical Materials Research Part B, Applied Biomaterials 2011;98:203-209.
[36] Atrens A, Liu M, Zainal Abidin NI. Corrosion mechanism applicable to biodegradable magnesium implants. Materials Science and Engineering: B 2011;176: 1609-1636.
[37] Pourbaix M. Atlas of electrochemical equilibria in aqueous solutions. Houston, Tex.: National Association of Corrosion Engineers; 1974.
[38] Song GL, Atrens A. Corrosion mechanisms of magnesium alloys. Advanced Engineering Materials 1999;1:11-33.
[39] Xin Y, Hu T, Chu PK. In vitro studies of biomedical magnesium alloys in a simulated physiological environment: a review. Acta Biomaterialia 2011;7:1452-1459.
[40] Song G, Atrens A. Understanding magnesium corrosion-a framework for improved alloy performance. Advanced Engineering Materials 2003;5:837-858.
[41] Ghali E, Dietzel W, Kainer K-U. General and localized corrosion of magnesium alloys: A critical review. Journal of Materials Engineering and Performance 2004;13:7-23.
[42] Atrens A, Song G-L, Liu M, Shi Z, Cao F, Dargusch MS. Review of recent developments in the field of magnesium corrosion. Advanced Engineering Materials 2015;17:400-53.
[43] Doblaré M, García JM, Gómez MJ. Modelling bone tissue fracture and healing: a review. Engineering Fracture Mechanics 2004;71:1809-1840.
[44] Xue D, Yun Y, Schulz MJ, Shanov V. Corrosion protection of biodegradable magnesium implants using anodization. Materials Science and Engineering: C 2011;31:215-223.
[45] Li Z, Gu X, Lou S, Zheng Y. The development of binary Mg-Ca alloys for use as biodegradable materials within bone. Biomaterials 2008;29:1329-1344.
[46] Claes LE. Mechanical characterization of biodegradable implants. Clinical Materials 1992;10:41-46.

[47] Thomann M, Krause C, Bormann D, von der Höh N, Windhagen H, Meyer-Lindenberg A. Comparison of the resorbable magnesium alloys LAE442 and MgCa0.8 concerning their mechanical properties, their progress of degradation and the bone-implant-contact after 12 months implantation duration in a rabbit model. Materialwissenschaft und Werkstofftechnik 2009;40:82-87.
[48] Krause A, Höh N, Bormann D, Krause C, Bach FW, Windhagen H, et al. Degradation behaviour and mechanical properties of magnesium implants in rabbit tibiae. Journal of Materials Science 2010;45:624-632.
[49] Hagihara K, Shakudo S, Fujii K, Nakano T. Degradation behavior of Ca-Mg-Zn intermetallic compounds for use as biodegradable implant materials. Materials Science and Engineering C, Materials for Biological Applications 2014;44:285-292.
[50] Chen D, He Y, Tao H, Zhang Y, Jiang Y, Zhang X, et al. Biocompatibility of magnesium-zinc alloy in biodegradable orthopedic implants. International Journal of Molecular Medicine 2011;28:343-348.
[51] Chou DT, Hong D, Saha P, Ferrero J, Lee B, Tan Z, et al. In vitro and in vivo corrosion, cytocompatibility and mechanical properties of biodegradable Mg-Y-Ca-Zr alloys as implant materials. Acta Biomaterialia 2013;9:8518-8533.
[52] Ding Y, Wen C, Hodgson P, Li Y. Effects of alloying elements on the corrosion behavior and biocompatibility of biodegradable magnesium alloys: a review. Journal of Materials Chemistry B 2014;2:1912-1933.

[53] Tapiero H, Tew KD. Trace elements in human physiology and pathology: zinc and metallothioneins. Biomedicine and Pharmacotherapy 2003;57:399-411.
[54] Park RS, Kim YK, Lee SJ, Jang YS, Park IS, Yun YH, et al. Corrosion behavior and cytotoxicity of Mg-35Zn-3Ca alloy for surface modified biodegradable implant material. Journal of Biomedical Materials Research Part B, Applied Biomaterials 2012;100:911-923.
[55] Zainal Abidin NI, Martin D, Atrens A. Corrosion of high purity Mg, AZ91, ZE41 and Mg2Zn0.2Mn in Hank's solution at room temperature. Corrosion Science 2011;53:862-872.
[56] Zhang E, Yin D, Xu L, Yang L, Yang K. Microstructure, mechanical and corrosion properties and biocompatibility of Mg–Zn–Mn alloys for biomedical application. Materials Science and Engineering: C 2009;29:987-893.
[57] Wan Y, Xiong G, Luo H, He F, Huang Y, Zhou X. Preparation and characterization of a new biomedical magnesium-calcium alloy. Materials and Design 2008;29:2034-2037.
[58] Yang J, Cui F, Lee IS. Surface modifications of magnesium alloys for biomedical applications. Annals of Biomedical Engineering 2011;39:1857-1871.
[59] Paital SR, Dahotre NB. Calcium phosphate coatings for bio-implant applications: Materials, performance factors, and methodologies. Materials Science and Engineering: R 2009;66:1-70.

[60] Yang J, Cui FZ, Lee IS, Wang X. Plasma surface modification of magnesium alloy for biomedical application. Surface and Coatings Technology 2010;205: 182-187.
[61] Abdal-hay A, Dewidar M, Lim JK. Biocorrosion behavior and cell viability of adhesive polymer coated magnesium based alloys for medical implants. Applied Surface Science 2012;261:536-546.
[62] Van Phuong N, Lee K, Chang D, Kim M, Lee S, Moon S. Zinc phosphate conversion coatings on magnesium alloys: A review. Metals and Materials International 2013;19:273-281. [63] Chen XB, Birbilis N, Abbott TB. Review of Corrosion-Resistant Conversion Coatings for Magnesium and Its Alloys. Corrosion 2011;67:1-16.
[64] Liu B, Zhang X, Xiao GY, Lu YP. Phosphate chemical conversion coatings on metallic substrates for biomedical application: A review. Materials Science and Engineering: C 2015;47:97-104.
[65] Kouisni L, Azzi M, Zertoubi M, Dalard F, Maximovitch S. Phosphate coatings on magnesium alloy AM60 part 1: study of the formation and the growth of zinc phosphate films. Surface and Coatings Technology 2004;185:58-67.
[66] Gupta RK, Mensah-Darkwa K, Kumar D. Corrosion protective conversion coatings on magnesium disks using a hydrothermal technique. Journal of Materials Science and Technology 2014;30:47-53.
[67] Pereda MD, Alonso C, Gamero M, del Valle JA, Fernández Lorenzo de Mele M. Comparative study of fluoride conversion coatings formed on biodegradable powder metallurgy Mg: The effect of chlorides at physiological level. Materials Science and Engineering: C 2011;31:858-865.
[68] Ren M, Cai S, Liu T, Huang K, Wang X, Zhao H, et al. Calcium phosphate glass/$MgF_2$ double layered composite coating for improving the corrosion resistance of magnesium alloy. Journal of Alloys and Compounds 2014;591:34-40.
[69] Van Phuong N, Moon S. Comparative corrosion study of zinc phosphate and magnesium phosphate conversion coatings on AZ31 Mg alloy. Materials Letters 2014;122:341-344.
[70] Witte F, Fischer J, Nellesen J, Vogt C, Vogt J, Donath T, et al. In vivo corrosion and corrosion protection of magnesium alloy LAE442. Acta Biomaterialia 2010;6:1792-1799.
[71] Guang Ling S. Control of degradation of biocompatible magnesium in a pseudo-physiological environment by a ceramic like anodized coating. Advanced Materials Research 2007;29:95-98.
[72] Shi P, Ng WF, Wong MH, Cheng FT. Improvement of corrosion resistance of pure magnesium in Hanks' solution by microarc oxidation with sol–gel $TiO_2$ sealing. Journal of Alloys and Compounds 2009;469:286-292.
[73] Zhou X, Thompson Ge, Skeldon P, Wood GC, Shimizu K, Habazaki H. Film formation and detachment during anodizing of Al-Mg alloys. Corrosion Science 1999;41:1599-1613.

[74] Arurault L. Pilling-Bedworth ratio of thick anodic aluminium porous films prepared at high voltages in $H_2SO_4$ based electrolyte. Transactions of the Institute of Metal Finishing 2008;86:51-54.
[75] Kazanski B, Kossenko A, Zinigrad M, Lugovskoy A. Fluoride ions as modifiers of the oxide layer produced by plasma electrolytic oxidation on AZ91D magnesium alloy. Applied Surface Science 2013;287:461-466.
[76] Cao FH, Lin LY, Zhang Z, Zhang JQ, Cao CN. Environmental friendly plasma electrolytic oxidation of AM60 magnesium alloy and its corrosion resistance. Transactions of Nonferrous Metals Society of China 2008;18:240-247.
[77] Blawert C, Sah SP, Scharnagl N, Kannan MB. Plasma electrolytic oxidation/micro-arc oxidation of magnesium and its alloys. In: Narayanan S, Park TSN, Song IL, Lee MH, editors. Surface Modification of Magnesium and its Alloys for Biomedical Applications: modification and coating techniques. Woodhead Publishing Series in Biomaterials, 90 . Elsevier, Cambridge, UK 2015;2:193-234.
[78] Vu TN, Veys-Renaux D, Rocca E. Potential bioactivity of coatings formed on AZ91D magnesium alloy by plasma electrolytic anodizing. Journal of Biomedical Materials Research Part B: Applied Biomaterials 2012;100:1846-1853.
[79] Waterman J, Pietak A, Birbilis N, Woodfield T, Dias G, Staiger MP. Corrosion resistance of biomimetic calcium phosphate coatings on magnesium due to varying pretreatment time. Materials Science and Engineering: B 2011;176:1756-1760.
[80] Shadanbaz S, Dias GJ. Calcium phosphate coatings on magnesium alloys for biomedical applications: a review. Acta Biomaterialia 2012;8:20-30.
[81] Cui FZ, Yang JX, Jiao YP, Yin QS, Zhang Y, Lee IS. Calcium phosphate coating on magnesium alloy for modification of degradation behavior. Frontiers of Materials Science in China 2008;2:143-148.
[82] Chen XB, Kirkland NT, Krebs H, Thiriat MA, Virtanen S, Nisbet D, et al. In vitro corrosion survey of Mg–xCa and Mg–3Zn–yCa alloys with and without calcium phosphate conversion coatings. Corrosion Engineering, Science and Technology 2012;47:365-373.
[83] Duan K, Tang A, Wang R. A new evaporation-based method for the preparation of biomimetic calcium phosphate coatings on metals. Materials Science and Engineering: C 2009;29:1334-1337.
[84] Silva CCGe, Rigo ECdS, Marchi J, Bressiani AHdA, Bressiani JC. Hydroxyapatite coating on silicon nitride surfaces using the biomimetic method. Materials Research 2008;11:47-50.
[85] Stevens MM. Biomaterials for bone tissue engineering. Materials Today 2008;11:18-25. [86] Fathi MH, Salehi M, Saatchi A, Mortazavi V, Moosavi SB. In vitro corrosion behavior of bioceramic, metallic, and bioceramic-metallic coated stainless steel dental implants. Dental Materials 2003;19:188-198.
[87] Song YW, Shan DY, Han EH. Electrodeposition of hydroxyapatite coating on AZ91D magnesium alloy for biomaterial application. Materials Letters 2008;62:3276-3279.

[88] Abdeltawab AA, Shoeib MA, Mohamed SG. Electrophoretic deposition of hydroxyapatite coatings on titanium from dimethylformamide suspensions. Surface and Coatings Technology 2011;206:43-50.
[89] Eliaz N, Sridhar TM, Kamachi Mudali U, Raj B. Electrochemical and electrophoretic deposition of hydroxyapatite for orthopaedic applications. Surface Engineering 2005;21:238-242.
[90] Guan RG, Johnson I, Cui T, Zhao T, Zhao ZY, Li X, et al. Electrodeposition of hydroxyapatite coating on Mg-4.0Zn-1.0Ca-0.6Zr alloy and in vitro evaluation of degradation, hemolysis, and cytotoxicity. Journal of Biomedical Materials Research Part A 2012;100:999-1015.
[91] Lin DY, Wang XX. Preparation of hydroxyapatite coating on smooth implant surface by electrodeposition. Ceramics International 2011;37:403-406.
[92] Wen C, Guan S, Peng L, Ren C, Wang X, Hu Z. Characterization and degradation behavior of AZ31 alloy surface modified by bone-like hydroxyapatite for implant applications. Applied Surface Science 2009;255:6433-6438.
[93] Wang HX, Guan SK, Wang X, Ren CX, Wang LG. In vitro degradation and mechanical integrity of Mg-Zn-Ca alloy coated with Ca-deficient hydroxyapatite by the pulse electrodeposition process. Acta Biomaterialia 2010;6:1743-1748.
[94] Kannan MB. Enhancing the performance of calcium phosphate coating on a magnesium alloy for bioimplant applications. Materials Letters 2012;76:109-112.
[95] Roy A, Singh SS, Datta MK, Lee B, Ohodnicki J, Kumta PN. Novel sol-gel derived calcium phosphate coatings on $Mg_4Y$ alloy. Materials Science and Engineering: B 2011;176:1679-1689.
[96] Kannan MB, Wallipa O. Potentiostatic pulse-deposition of calcium phosphate on magnesium alloy for temporary implant applications-an in vitro corrosion study. Materials Science and Engineering: C 2013;33:675-679.
[97] Qiu X, Wan P, Tan L, Fan X, Yang K. Preliminary research on a novel bioactive silicon doped calcium phosphate coating on AZ31 magnesium alloy via electrodeposition. Materials Science and Engineering: C 2014;36:65-76.
[98] Kannan MB, Liyanaarachchi S. Hybrid coating on a magnesium alloy for minimizing the localized degradation for load-bearing biodegradable mini-implant applications. Materials Chemistry and Physics 2013;142:350-354.
[99] Jo JH, Kang BG, Shin KS, Kim HE, Hahn BD, Park DS, et al. Hydroxyapatite coating on magnesium with $MgF_2$ interlayer for enhanced corrosion resistance and biocompatibility. Journal of Materials Science-Materials in Medicine 2011;22:2437-2447.
[100] Alabbasi A, Bobby Kannan M, Blawert C. Dual layer inorganic coating on magnesium for delaying the biodegradation for bone fixation implants. Materials Letters 2014;124:188-191.
[101] Grubač Z, Metikoš-Huković M, Babić R. Electrocrystallization, growth and characterization of calcium phosphate ceramics on magnesium alloys. Electrochimica Acta 2013;109:694-700.

[102] Ren Y, Zhou H, Nabiyouni M, Bhaduri SB. Rapid coating of AZ31 magnesium alloy with calcium deficient hydroxyapatite using microwave energy. Materials Science and Engineering: C 2015;49:364-372.
[103] Chen Y, Mak AF, Wang M, Li J. Composite coating of bonelike apatite particles and collagen fibers on poly L-lactic acid formed through an accelerated biomimetic coprecipitation process. Journal of Biomedical Materials Research Part B, Applied Biomaterials 2006;77:315-322.
[104] Witte F, Calliess T, Windhagen H. Biodegradable synthetic implant materials. Clinical applications and immunological aspects. Orthopade 2008;37:125-130.
[105] Wong HM, Yeung KW, Lam KO, Tam V, Chu PK, Luk KD, et al. A biodegradable polymer-based coating to control the performance of magnesium alloy orthopaedic implants. Biomaterials 2010;31:2084-2096.
[106] Bumgardner JD, Wiser R, Gerard PD, Bergin P, Chestnutt B, Marini M, et al. Chitosan: potential use as a bioactive coating for orthopaedic and craniofacial/dental implants. Journal of Biomaterials Science, Polymer Edition 2003;14:423-438.
[107] Alabbasi A, Liyanaarachchi S, Kannan MB. Polylactic acid coating on a biodegradable magnesium alloy: an in vitro degradation study by electrochemical impedance spectroscopy. Thin Solid Films 2012;520:6841-6844.
[108] Cai K, Sui X, Hu Y, Zhao L, Lai M, Luo Z, et al. Fabrication of anticorrosive multilayer onto magnesium alloy substrates via spin-assisted layer-by-layer technique. Materials Science and Engineering: C 2011;31:1800-1808.
[109] Oosterbeek RN, Seal CK, Seitz JM, Hyland MM. Polymer–bioceramic composite coatings on magnesium for biomaterial applications. Surface and Coatings Technology 2013;236:420-428.
[110] Fan Y, Duan K, Wang R. A composite coating by electrolysis-induced collagen self-assembly and calcium phosphate mineralization. Biomaterials 2005; 26: 1623-1632.
[111] Gu XN, Wang X, Li N, Li L, Zheng YF, Miao X. Microstructure and characteristics of the metal-ceramic composite (MgCa-HA/TCP) fabricated by liquid metal infiltration. Journal of biomedical materials research Part B, Applied Biomaterials 2011;99:127-134.
[112] Kuroda K, Moriyama M, Ichino R, Okido M, Seki A. Formation and Osteoconductivity of Hydroxyapatite/Collagen Composite Films Using a Thermal Substrate Method in Aqueous Solutions. Materials Transactions 2009;50:1190-1195.
[113] Li W, Guan S, Chen J, Hu J, Chen S, Wang L, et al. Preparation and in vitro degradation of the composite coating with high adhesion strength on biodegradable Mg–Zn–Ca alloy. Materials Characterization 2011;62:1158-1165.
[114] Sun L, Berndt CC, Gross KA. Hydroxyapatite/polymer composite flame-sprayed coatings for orthopedic applications. Journal of Biomaterials Science, Polymer Edition 2002;13:977-990.

[115] Miao S, Weng W, Li Z, Cheng K, Du P, Shen G, et al. Electrolytic deposition of octacalcium phosphate/collagen composite coating on titanium alloy. Journal of Materials Science Materials in Medicine 2009;20:131-134.
[116] Ou KL, Chung RJ, Tsai FY, Liang PY, Huang SW, Chang SY. Effect of collagen on the mechanical properties of hydroxyapatite coatings. Journal of The Mechanical Behavior of Biomedical Materials 2011;4:618-624.
[117] He J, Huang T, Gan L, Zhou Z, Jiang B, Wu Y, et al. Collagen-infiltrated porous hydroxyapatite coating and its osteogenic properties: in vitro and in vivo study. Journal of Biomedical Materials Research Part A 2012;100:1706-1715.
[118] Zhao X, Hu T, Li H, Chen M, Cao S, Zhang L, et al. Electrochemically assisted co-deposition of calcium phosphate/collagen coatings on carbon/carbon composites. Applied Surface Science 2011;257:3612-3169.
[119] Shi Y, Qi M, Chen Y, Shi P. MAO-DCPD composite coating on Mg alloy for degradable implant applications. Materials Letters 2011;65:2201-2204.
[120] Zhang XX, Li Q, Li LQ, Zhang P, Wang ZW, Chen FN. Fabrication of hydroxyapatite/stearic acid composite coating and corrosion behavior of coated magnesium alloy. Materials Letters 2012;88:76-78.
[121] Li LH, Sankara Narayanan TSN, Kim YK, Kong YM, Park IS, Bae TS, et al. Deposition of microarc oxidation–polycaprolactone duplex coating to improve the corrosion resistance of magnesium for biodegradable implants. Thin Solid Films 2014;562:561-567.
[122] Ian J, Khalid A, Huinan L. Nanostructured hydroxyapatite/ poly(lactic-co-glycolic acid) composite coating for controlling magnesium degradation in simulated body fluid. Nanotechnology 2013; 24: 3751-3753.
[123] Guan RG, Johnson I, Cui T, Zhao T, Zhao ZY, Li X, et al. Electrodeposition of hydroxyapatite coating on Mg-4.0Zn-1.0Ca-0.6Zr alloy and in vitro evaluation of degradation, hemolysis, and cytotoxicity. Journal of Biomedical Materials Research Part A 2012;100:999-1015.
[124] Jamesh M, Kumar S, Sankara Narayanan TSN. Electrodeposition of hydroxyapatite coating on magnesium for biomedical applications. Journal of Coating Technology and Resarch 2012;9:495-502.
[125] Cui W, Beniash E, Gawalt E, Xu Z, Sfeir C. Biomimetic coating of magnesium alloy for enhanced corrosion resistance and calcium phosphate deposition. Acta Biomaterialia 2013;9:8650-8659.
[126] Jo JH, Hong JY, Shin KS, Kim HE, Koh YH. Enhancing biocompatibility and corrosion resistance of Mg implants via surface treatments. Journal of Biomaterials Applications 2012;27:469-476.
[127] Niu J, Yuan G, Liao Y, Mao L, Zhang J, Wang Y, et al. Enhanced biocorrosion resistance and biocompatibility of degradable Mg–Nd–Zn–Zr alloy by brushite coating. Materials Science and Engineering: C 2013;33:4833-4841.

[128] Chen S, Guan SK, Hou SS, Wang LG, Zhu SJ, Wang J, et al. Characterization and corrosion properties of Ti-O/HA composite coatings on Mg-Zn alloy. Surface and Interface Analysis 2011;43:1575-1580.
[129] Wu G, Gong L, Feng K, Wu S, Zhao Y, Chu PK. Rapid degradation of biomedical magnesium induced by zinc ion implantation. Materials Letters 2011;65:661-663.
[130] Kokubo T, Takadama H. How useful is SBF in predicting in vivo bone bioactivity?. Biomaterials 2006;27:2907-2915.
[131] Shi Z, Liu M, Atrens A. Measurement of the corrosion rate of magnesium alloys using Tafel extrapolation. Corrosion Science 2010;52:579-588.
[132] Kirkland NT, Birbilis N, Staiger MP. Assessing the corrosion of biodegradable magnesium implants: A critical review of current methodologies and their limitations. Acta Biomaterialia 2012;8:925-936.
[133] Pishbin F, Mouriño V, Gilchrist JB, McComb DW, Kreppel S, Salih V, et al. Single-step electrochemical deposition of antimicrobial orthopaedic coatings based on a bioactive glass/chitosan/nano-silver composite system. Acta Biomaterialia 2013;9:7469-7479.
[134] Chaudhry AA, Goodall J, Vickers M, Cockcroft JK, Rehman I, Knowles JC, et al. Synthesis and characterisation of magnesium substituted calcium phosphate bioceramic nanoparticles made via continuous hydrothermal flow synthesis. Journal of Materials Chemistry 2008;18:5900-5908.
[135] Suchanek WL, Byrappa K, Shuk P, Riman RE, Janas VF, TenHuisen KS. Mechanochemical-hydrothermal synthesis of calcium phosphate powders with coupled magnesium and carbonate substitution. Journal of Solid State Chemistry 2004;177:793-799.
[136] Han JK, Song HY, Saito F, Lee BT. Synthesis of high purity nano-sized hydroxyapatite powder by microwave-hydrothermal method. Materials Chemistry and Physics 2006;99:235-239.
[137] Hattori T, Lwadate Y. Hydrothermal Preparation of Calcium Hydroxyapatite Powders. Journal of the American Ceramic Society 1990;73:1803-1805.
[138] Liu HS, Chin TS, Lai LS, Chiu SY, Chung KH, Chang CS, et al. Hydroxyapatite synthesized by a simplified hydrothermal method. Ceramics International 1997;23:19-25.
[139] Liu D, Savino K, Yates MZ. Coating of hydroxyapatite films on metal substrates by seeded hydrothermal deposition. Surface and Coatings Technology 2011;205:3975-3986.
[140] Onoki T, Nakahira A, Tago T, Hasegawa Y, Kuno T. Novel low temperature processing techniques for apatite ceramics and chitosan polymer composite bulk materials and its mechanical properties. Applied Surface Science 2012;262:263-266.
[141] Onoki T, Yamamoto SY. Hydroxyapatite ceramics coating on magnesium alloy via a double layered capsule hydrothermal hot-pressing. Journal of the Ceramic Society of Japan 2010;118:749-752.

[142] Hiromoto S. Corrosion of Calcium Phosphate Coated AZ31 Magnesium Alloy under a Salt Spray Test. Materials Transactions 2012;53:700-706.
[143] Ng WF, Wong MH, Cheng FT. Stearic acid coating on magnesium for enhancing corrosion resistance in Hanks' solution. Surface and Coatings Technology 2010;204:1823-1830.
[144] Zhu Y, Wu G, Zhang Y-H, Zhao Q. Growth and characterization of $Mg(OH)_2$ film on magnesium alloy AZ31. Applied Surface Science 2011;257:6129-6137.
[145] Wang L, Nancollas GH. Calcium Orthophosphates: Crystallization and Dissolution. Chemical Reviews 2008;108:4628-4669.
[146] Touny A, Dawkins H, Zhou H, Bhaduri S. Hydrolysis of monetite/chitosan composites in α-MEM and SBF solutions. Journal of Materials Science: Materials in Medicine 2011;22:1101-1109.
[147] Tas AC. Monetite ($CaHPO_4$) Synthesis in Ethanol at Room Temperature. Journal of the American Ceramic Society 2009;92:2907-2912.
[148] Tortet L, Gavarri JR, Nihoul G, Dianoux AJ. Study of Protonic Mobility in $CaHPO_4{\cdot}2H_2O$ (Brushite) and $CaHPO_4$(Monetite) by Infrared Spectroscopy and Neutron Scattering. Journal of Solid State Chemistry 1997;132:6-16.
[149] Xu J, Butler IS, Gilson DFR. FT-Raman and high-pressure infrared spectroscopic studies of dicalcium phosphate dihydrate ($CaHPO_4{\cdot}2H_2O$) and anhydrous dicalcium phosphate ($CaHPO_4$). Spectrochimica Acta Part A: Molecular and Biomolecular Spectroscopy 1999;55:2801-2809.
[150] Chen J, Wang Y, Chen X, Ren L, Lai C, He W, et al. A simple sol-gel technique for synthesis of nanostructured hydroxyapatite, tricalcium phosphate and biphasic powders. Materials Letters 2011;65:1923-1926..
[140] Chen J, Wang Y, Chen X, Ren L, Lai C, He W, et al. A simple sol-gel technique for synthesis of nanostructured hydroxyapatite, tricalcium phosphate and biphasic powders. Materials Letters 2011;65:1923-1926.
[151] Chen J, Wang Y, Chen X, Ren L, Lai C, He W, et al. A simple sol-gel technique for synthesis of nanostructured hydroxyapatite, tricalcium phosphate and biphasic powders. Materials Letters 2011;65:1923-1926.
[152] Tonković M, Sikirić M, Babić-Ivančić V. Controversy about β-tricalcium phosphate. Colloids and Surfaces A: Physicochemical and Engineering Aspects 2000;170:107-112.
[153] Boanini E, Gazzano M, Bigi A. Ionic substitutions in calcium phosphates synthesized at low temperature. Acta Biomaterialia 2010;6:1882-1894..
[154] Lagier R, Baud CA. Magnesium whitlockite, a calcium phosphate crystal of special interest in pathology. Pathology, Research and Practice 2003;199:329-335.
[155] Morikawa H, Lee S, Kasuga T, Brauer DS. Effects of magnesium for calcium substitution in $P_2O_5$–CaO–$TiO_2$ glasses. Journal of Non-Crystalline Solids 2013;380:53-59.

[156] Shiryaev M, Safronova T, Putlyaev V. Calcium phosphate powders synthesized from calcium chloride and potassium hydrophosphate. Journal of Thermal Analysis and Calorimetry 2010;101:707-713.
[157] Galea LG, Bohner M, Lemaitre J, Kohler T, Muller R. Bone substitute: transforming beta-tricalcium phosphate porous scaffolds into monetite. Biomaterials 2008;29:3400-3407.
[158] Jinawath S, Pongkao D, Suchanek W, Yoshimura M. Hydrothermal synthesis of monetite and hydroxyapatite from monocalcium phosphate monohydrate. International Journal of Inorganic Materials 2001;3:997-1001.
[159] Desai TR, Bhaduri SB, Tas AC. A Self-Setting, Monetite ($CaHPO_4$) Cement for Skeletal Repair. Advances in Bioceramics and Biocomposites II, Ceramic Engineering and Science Proceedings 2008;27:61-69.
[160] Klammert U, Reuther T, Jahn C, Kraski B, Kübler AC, Gbureck U. Cytocompatibility of brushite and monetite cell culture scaffolds made by three-dimensional powder printing. Acta Biomaterialia 2009;5:727-734.
[161] Habibovic P, Gbureck U, Doillon CJ, Bassett DC, van Blitterswijk CA, Barralet JE. Osteoconduction and osteoinduction of low-temperature 3D printed bioceramic implants. Biomaterials 2008;29:944-953.
[162] Tamimi F, Torres J, Bassett D, Barralet J, Cabarcos EL. Resorption of monetite granules in alveolar bone defects in human patients. Biomaterials 2010;31:2762-2769.
[163] Zavgorodniy AV, Mason RS, LeGeros RZ, Rohanizadeh R. Adhesion of a chemically deposited monetite coating to a Ti substrate. Surface and Coatings Technology 2012;206:4433-4438.
[164] De Giglio E, Cafagna D, Ricci MA, Sabbatini L, Cometa S, Ferretti C, et al. Biocompatibility of poly(acrylic acid) thin coatings electro-synthesized onto TiAlV-based implants. Journal of Bioactive and Compatible Polymers 2010;25:374-391.
[165] De Giglio E, Cometa S, Cioffi N, Torsi L, Sabbatini L. Analytical investigations of poly(acrylic acid) coatings electrodeposited on titanium-based implants: a versatile approach to biocompatibility enhancement. Analytical and Bioanalytical Chemistry 2007;389:2055-2063.
[166] Ke Y. Preparation of carboxymethyl cellulose based microgels for cell encapsulation. Express Polymer Letters 2014;8:841-849.
[167] Shah N, R. PK. Formulation and Development of Hydrogel for Poly Acrylamide-Co-acrylic acid. Journal of Pharmaceutical Science and Bioscientific Research 2014;4:114-120.
[168] Butun S, Ince FG, Erdugan H, Sahiner N. One-step fabrication of biocompatible carboxymethyl cellulose polymeric particles for drug delivery systems. Carbohydrate Polymers 2011;86:636-643.
[169] Yokoi T, Kawashita M, Ohtsuki C. Effects of Monocarboxylic Acid Addition on Crystallization of Calcium Phosphate in a Hydrogel Matrix. Materials Science and Engineering 2011;18:1-5.

[170] Xie L, Wang L, Jia X, Kuang G, Yang S, Feng H. Effects of glutamic acid shelled PAMAM dendrimers on the crystallization of calcium phosphate in diffusion systems. Polymer Bulletin 2010;66:119-132.
[171] Yokoi T, Kawashita M, Ohtsuki C. Biomimetic mineralization of calcium phosphates in polymeric hydrogels containing carboxyl groups. Journal of Asian Ceramic Societies 2013;1:155-162.
[172] McNeill IC, Sadeghi SMT. Thermal stability and degradation mechanisms of poly(acrylic acid) and its salts: Part 1-Poly(acrylic acid). Polymer Degradation and Stability 1990;29:233-246.
[173] Ahmad N, Wahab R, Al-Omar SY. Thermal decomposition kinetics of sodium carboxymethyl cellulose: Model-free methods. European Journal of Chemistry 2014;5:247-251.
[174] Kaabi Falahieh Asl S, Nemeth S, Tan MJ. Hydrothermally deposited protective and bioactive coating for magnesium alloys for implant application. Surface and Coatings Technology 2014;258:931-937.
[175] Fujishiro Y, Sato T, Okuwaki A. Coating of hydroxyapatite on metal plates using thermal dissociation of calcium-EDTA chelate in phosphate solutions under hydrothermal conditions. Journal of Materials Science: Materials in Medicine 1995;6:172-176.
[176] Li X, Ito A, Sogo Y, Wang X, LeGeros RZ. Solubility of Mg-containing β-tricalcium phosphate at 25 °C. Acta Biomaterialia 2009;5:508-517.
[177] Kashima DP, Rakngarm A. Calcium phosphate film coating on titanium substrate by electrochemical deposition. Journal of Metals, Materials and Minerals 2008;18:27-31.
[178] Ban S, Matsuo K, Mizutani N, Hasegawa J. Hydrothermal-electrochemical deposition of calcium phosphates on various metals. Dental Materials Journal 1999;18:259-270.
[179] Xiong J, Li Y, Hodgson PD, Wen Ce. Nanohydroxyapatite coating on a titanium–niobium alloy by a hydrothermal process. Acta Biomaterialia 2010;6:1584-1590.
[180] Shaw; BA, Wolfe RC. Corrosion of Magnesium and Magnesium-Base Alloys. ASM Handbook,Corrosion:Materials (ASM International) Published 2005;13B:205 - 227.
[181] Zhang XG. Corrosion of Zinc and Zinc Alloys. ASM Handbook,Corrosion: Materials (ASM International) Published 2005;13B:402-417.
[182] Schutz RW. Corrosion of Titanium and Titanium Alloys. ASM Handbook,Corrosion: Materials (ASM International) Published 2005;13B:252-299.
[183] Beverskog B, Puigdomenech I. Pourbaix Diagrams for the Ternary System of Iron-Chromium-Nickel. Corrosion 1999;55:1077-1087.

[184] Badawy WA, Hilal NH, El-Rabiee M, Nady H. Electrochemical behavior of Mg and some Mg alloys in aqueous solutions of different pH. Electrochimica Acta 2010;55:1880-1887.
[185] Chevalier NR. Do Surface Wetting Properties Affect Calcium Carbonate Heterogeneous Nucleation and Adhesion?. The Journal of Physical Chemistry C 2014;118:17600-17607.
[186] Wang M, Zhang Y, Zheng H, Lin X, Huang W. Investigation of the Heterogeneous Nucleation on Fractal Surfaces. Journal of Materials Science and Technology 2012;28:1169-1174.
[187] Zhang Y, Wang M, Lin X, Huang W. Effect of Substrate Wettability and Surface Structure on Nucleation of Crystal. Journal of Materials Science and Technology 2012;28:859-864.
[188] Zhang Y, Wang M, Lin X, Huang W. Effect of Substrate Surface Microstructure on Heterogeneous Nucleation Behavior. Journal of Materials Science and Technology 2012;28:67-72.
[189] Wang M, Zhu SF, Zhang Y, Lin X, Huang WD. Researches on the Nucleation Behaviors of $NH_4Cl$ Crystal on Coarse Aluminum Surfaces. Materials Science Forum 2010;654-656:1343-1346.
[190] Kaabi Falahieh Asl S, Nemeth S, Tan MJ. Mechanism of calcium phosphate deposition in a hydrothermal coating process. Surface and Coatings Technology 2015;270:197-205.
[191] Liu ZX, Wang XM, Wang Q, Shen XC, Liang H, Cui FZ. Evolution of calcium phosphate crystallization on three functional group surfaces with the same surface density. CrystEngComm 2012;14:6695-6701.
[192] Zhang S, Cao F, Chang L, Zheng J, Zhang Z, Zhang J, et al. Electrodeposition of high corrosion resistance Cu/Ni–P coating on AZ91D magnesium alloy. Applied Surface Science 2011;257:9213-9220.
[193] Fan J, Qiu X, Niu X, Tian Z, Sun W, Liu X, et al. Microstructure, mechanical properties, in vitro degradation and cytotoxicity evaluations of Mg-1.5Y-1.2Zn-0.44Zr alloys for biodegradable metallic implants. Materials Science and Engineering C, Materials for Biological Applications 2013;33:2345-2352.
[194] Creager S. Solvents and Supporting Electrolytes. In: Zoski CG, editor. Handbook of Electrochemistry. Amsterdam: Elsevier; 2007,4:57-72.
[195] Yao Z, Jiang Z, Wang F. Study on corrosion resistance and roughness of micro-plasma oxidation ceramic coatings on Ti alloy by EIS technique. Electrochimica Acta 2007;52:4539-4546.
[196] Conde A, de Damborenea J. Evaluation of exfoliation susceptibility by means of the electrochemical impedance spectroscopy. Corrosion Science 2000;42:1363-1377.
[197] Razavi M, Fathi M, Savabi O, Mohammad Razavi S, Hashemi Beni B, Vashaee D, et al. Controlling the degradation rate of bioactive magnesium implants by

electrophoretic deposition of akermanite coating. Ceramics International 2014;40:3865-3872.
[198] Ballerini G, Bardi U, Bignucolo R, Ceraolo G. About some corrosion mechanisms of AZ91D magnesium alloy. Corrosion Science 2005;47:2173-2184.
[199] Inoue H, Sugahara K, Yamamoto A, Tsubakino H. Corrosion rate of magnesium and its alloys in buffered chloride solutions. Corrosion Science 2002;44:603-610.
[200] Wang Y, Lim CS, Lim CV, Yong MS, Teo EK, Moh LN. In vitro degradation behavior of M1A magnesium alloy in protein-containing simulated body fluid. Materials Science and Engineering: C 2011;31:579-587.
[201] Perez RA, Kim HW, Ginebra MP. Polymeric additives to enhance the functional properties of calcium phosphate cements. Journal of Tissue Engineering 2012;3:1-20.
[202] Bigi A, Bracci B, Panzavolta S. Effect of added gelatin on the properties of calcium phosphate cement. Biomaterials 2004;25:2893-2899.
[203] Félix Lanao RP, Leeuwenburgh SCG, Wolke JGC, Jansen JA. In vitro degradation rate of apatitic calcium phosphate cement with incorporated PLGA microspheres. Acta Biomaterialia 2011;7:3459-3468.
[204] Legeros RZ. Biodegradation and bioresorption of calcium phosphate ceramics. Clinical Materials 1993;14:65-88.
[205] Alexis F. Factors affecting the degradation and drug-release mechanism of poly(lactic acid) and poly[(lactic acid)-co-(glycolic acid)]. Polymer International 2005;54:36-46.
[206] Xin-bo X, Xie-rong Z, Chun-li Z, Ping L, Yun-bo F. Influence of hydrothermal temperature on hydroxyapatite coating transformed from monetite on HT-C/C composites by induction heating method. Surface and Coatings Technology 2009;204:115-119.
[207] Zhang J, Liu W, Schnitzler V, Tancret F, Bouler JM. Calcium phosphate cements for bone substitution: Chemistry, handling and mechanical properties. Acta Biomaterialia 2014;10:1035-1049.
[208] Bhushan B, Gupta BK, Azarian MH. Nanoindentation, microscratch, friction and wear studies of coatings for contact recording applications. Wear 1995;181-183, Part 2:743-58.
[209] ASTM C1624-05, Standard Test Method for Adhesion Strength and Mechanical Failure Modes of Ceramic Coatings by Quantitative Single Point Scratch Testing, ASTM International, West Conshohocken, PA, 2015, www.astm.org.
[210] Van De Belt H, Neut D, Schenk W, van Horn JR, van der Mei HC, Busscher HJ. Infection of orthopedic implants and the use of antibiotic-loaded bone cements. A review. Acta Orthopaedica Scandinavica 2001;72:557-571.
[211] Hetrick EM, Schoenfisch MH. Reducing implant-related infections: active release strategies. Chemical Society Reviews 2006;35:780-789.
[212] Yan T, Tan L, Xiong D, Liu X, Zhang B, Yang K. Fluoride treatment and in vitro corrosion behavior of an AZ31B magnesium alloy. Materials Science and Engineering: C 2010;30:740-748.

[213] Chang HI, Wang Y. Cell Responses to Surface and Architecture of Tissue Engineering Scaffolds. In Eberil D, editor. Regenerative Medicine And Tissue Engineering-Cells and Biomaterials, In Tech 2011; 569-588.
[214] Thevenot P, Hu W, Tang L. Surface chemistry influence implant biocompatibility. Current Topics in Medicinal Chemistry 2008;8:270-280.
[215] Keselowsky BG, Collard DM, García AJ. Surface chemistry modulates fibronectin conformation and directs integrin binding and specificity to control cell adhesion. Journal of Biomedical Materials Research Part A 2003;66:247-259.
[216] Kaabi Falahieh Asl S, Nemeth S, Tan MJ. Novel biodegradable calcium phosphate/polymer composite coating with adjustable mechanical properties formed by hydrothermal process for corrosion protection of magnesium substrate. Journal of Biomedical Materials Research Part B: Applied Biomaterials 2015.In press.
[217] Kaabi Falahieh Asl S, Nemeth S, Tan MJ. Improved corrosion protection of magnesium by hydrothermally deposited biodegradable calcium phosphate coating. Materials Chemistry and Physics 2015;161:185-193.
[218] Gallo J, Holinka M, Moucha CS. Antibacterial Surface Treatment for Orthopaedic Implants. International Journal of Molecular Sciences 2014;15:13849-13880.
[219] Knetsch MLW, Koole LH. New Strategies in the Development of Antimicrobial Coatings: The Example of Increasing Usage of Silver and Silver Nanoparticles. Polymers 2011;3:340-366.
[220] Hum J, Boccaccini AR. Bioactive glasses as carriers for bioactive molecules and therapeutic drugs: a review. Journal of Materials Science Materials in Medicine 2012;23:2317-2333.
[221] Mourino V, Boccaccini AR. Bone tissue engineering therapeutics: controlled drug delivery in three-dimensional scaffolds. Journal of the Royal Society 2010;7:209-227.
[222] Kenawy ER, Bowlin GL, Mansfield K, Layman J, Simpson DG, Sanders EH, et al. Release of tetracycline hydrochloride from electrospun poly(ethylene-co-vinylacetate), poly(lactic acid), and a blend. Journal of Controlled Release 2002;81:57-64.
[223] Park YJ, Lee YM, Park SN, Lee JY, Ku Y, Chung CP, et al. Enhanced guided bone regeneration by controlled tetracycline release from poly(L-lactide) barrier membranes. Journal of Biomedical Materials Research 2000;51:391-397.
[224] Karuppuswamy P, Reddy Venugopal J, Navaneethan B, Luwang Laiva A, Ramakrishna S. Polycaprolactone nanofibers for the controlled release of tetracycline hydrochloride. Materials Letters 2015;141:180-186.
[225] Wu P, Grainger DW. Drug/device combinations for local drug therapies and infection prophylaxis. Biomaterials 2006;27:2450-2467.

# List of Publications

## Peer-Reviewed Journal Papers

1- S. Kaabi Falahieh Asl, S. Nemeth, and M.J. Tan, ”Deposition of Novel biodegradable Ca-P/Polymer composite coating by hydrothermal process”, Journal of Biomedical Materials Research: Part B - Applied Biomaterials, 2015.In press.

2- S. Kaabi Falahieh Asl, S. Nemeth, and M.J. Tan, ”Improved corrosion protection of magnesium by hydrothermally deposited biodegradable calcium phosphate coating”, Materials Chemistry and Physics, 2015; 161:185-193.

3- S. Kaabi Falahieh Asl, S. Nemeth, and M.J. Tan, ”Mechanism of calcium phosphate deposition in a hydrothermal coating process”. Surface and Coatings Technology, 2015; 270:197-205.

4- S. Kaabi Falahieh Asl, S. Nemeth, and M.J. Tan, ”Hydrothermally deposited protective and bioactive coating for magnesium alloys for implant application”, Surface and Coatings Technology, 2014; 258:931-937.

5- S. Kaabi Falahieh Asl, S. Nemeth, and M.J. Tan, ”Electrophoretic deposition of hydroxyapatite coatings on AZ31 magnesium substrate for biodegradable implant applications”, Progress in Crystal Growth and Characterization of Materials, 2014; 60: 74-79.

## Conference Presentations

1- S. Kaabi Falahieh Asl, A.R. Boccaccini, S. Nemeth and M.J. Tan, ”Deposition of Polymer/Bioactive glass (Polymer/BG) coatings with local drug delivery capability by means of electrophoretic deposition”, 6th ICMOBT, 6-10 December 2015, Waikoloa, Hawaii, USA.

2- S. Kaabi Falahieh Asl, S. Nemeth and M.J. Tan, ”Coating Modulus and Crack Resistance Improvement with Calcium Phosphate-Polymer Composites on Magnesium Substrate for Implant Application”, 6th ICMOBT, 6-10 December 2015, Waikoloa, Hawaii, USA.

3- S. Kaabi Falahieh Asl, S. Nemeth, and M.J. Tan, ”Mechanical Properties and Deposition Mechanism of Hydrothermally Deposited Calcium Phosphate Coating”, ICMAT2015 & IUMRS-ICA, 28 June-03 July 2015, Singapore.

4- S. Kaabi Falahieh Asl, S. Nemeth, and M.J. Tan, ”Control the Corrosion of Magnesium for Implant Application by Hydrothermally Deposited Biodegradable Calcium Phosphate Coating”, 227th ECS Meeting, 24-28 May 2015, Chicago, USA.

5- S. Kaabi Falahieh Asl, S. Nemeth, and M.J. Tan, ”Hydrothermal Deposition of Bioresorbable Coating on AZ31 Magnesium for Implant Application”, 41st ICMCTF, 28 April-02 May 2014, San Diego, California, USA.

6- S. Kaabi Falahieh Asl, S. Nemeth, and M.J. Tan, “Electrophoretic Deposition of Hydroxyapatite Coatings on AZ31 Magnesium Substrate for Biodegradable Implant Applications”, 7th ICMAT, 30 June-05 July 2013, Singapore.